Investigating the neural correlates of urge and the modulatory effects of median nerve stimulation in the context of Tourette syndrome

Mairi Houlgreave, MSc. BSc.

Thesis submitted to the University of Nottingham for the degree of Doctor of Philosophy.

Acknowledgements

First of all, I would like to thank my supervisors Stephen Jackson and Matt Brookes for this opportunity and for their support, guidance and discussions throughout my PhD. I would also like to thank the members of both the Jackson and Brookes lab groups, in particular: Kat D, for showing me the ropes and for all the hours of MR-scanning; Barbara, for showing me all things related to MNS; Caitlin, for being my office buddy and scan assistant; Daisie, for showing me how to scan and analyse MEG data; and Elena, Ryan and Niall for all things OPM-related despite them not making it into my thesis. Also, thank you to Cesar and Eneko for teaching me how to use PFM, for all the python coding and for welcoming me to BCBL and Donostia in December 2021; Adam, for all your help with MR-spectroscopy and the analysis pipeline; Penny, for your guidance and discussions on PFM analysis; Valerie, for the real-time urge monitor code; and Rosa and Sue, for setting up the scans for the urge-to-blink study. Thank you to Jen, Hannah, Joanna, Kat G, Izzy and Erika for your encouragement while I wrote this thesis.

Importantly, I'd like to thank my friends and family for all your love and support. Mum, Dad, Chris, Fi, George and Jon, thank you for being the type of people who talk about science over dinner, for proof reading and for generally making everything that much easier. Peter, Jenny, and Jim, thank you for welcoming me into your home for the first 2 years of my degree. Mariana, thank you for being my climbing buddy and for supporting me during our lunchtime chats pre-covid and our video calls thereafter. Joe, thank you for keeping me calm, for endless cups of tea and for always doing the dishes.

Finally, I would like to thank everyone who volunteered to participate in my studies – I literally couldn't have done it without you.

Contents

List of Figures

List of Tables

Abbreviations

AAL	Automated anatomical labelling
ACC	Anterior cingulate cortex
ADHD	Attention deficit hyperactivity disorder
AIC	Akaike information criterion
AMD	Absolute mean displacement
AP	Action potential
APB	Abductor pollicis brevis
ATP	Adenosine triphosphate
ATS	Activation time series
BIC	Bayesian information criterion
BOLD	Blood oxygen level dependent
Cho	Choline
CRLB	Cramér–Rao lower bounds
CSF	Cerebrospinal fluid
CSTC	Cortico-striato-thalamo-cortical
cTBS	Continuous theta burst stimulation
DA	Dopamine
DBS	Deep brain stimulation
DLPFC	Dorsolateral prefrontal cortex
EEG	Electroencephalography
EMD	Empirical mode decomposition
EMG	Electromyography
EPSP	Excitatory postsynaptic potential
ERD	Event-related de-synchronisation
FA	Fractional anisotropy
FD	Framewise displacement
FDR	False discovery rate
FID	Free induction decay
FLIRT	FMRIB's linear image registration tool
fMRI	Functional magnetic resonance imaging
FoV	Field of view
FSI	Fast-spiking interneurons
FWHM	Full width at half maximum

GABA	Gamma-aminobutyric acid
GLM	General linear model
Gln	Glutamine
Glu	Glutamate
GM	Grey matter
HRF	Haemodynamic response function
H_0	Null hypothesis
H_1	Alternative hypothesis
HT	Hilbert transform
ICA	Independent component analysis
IFG	Inferior frontal gyrus
IMF	Intrinsic mode function
IPSP	Inhibitory postsynaptic potential
ISI	Inter-stimulus interval
ITPC	Inter-trial phase coherence
LCMV	Linear-constraint minimum-variance
LICI	Long-interval cortical inhibition
MCC	Mid-cingulate cortex
MCFLIRT	Motion correction with FMRIB's linear image registration tool
ME-ICA	Multi-echo independent component analysis
MEG	Magnetoencephalography
MEP	Motor evoked potential
MESPFM	Multi-echo sparse paradigm free mapping
MFG	Middle frontal gyrus
MNI	Montreal neurological institute
MNS	Median nerve stimulation
MPRAGE	Magnetisation-prepared rapid acquisition with gradient echo
MRBD	Movement-related beta desynchronisation
MR	Magnetic resonance
MRI	Magnetic resonance imaging
MRS	Magnetic resonance spectroscopy
MSN	Medium spiny neurons
NAA	N-acetylaspartate

NAcc	Nucleus accumbens
NIBS	Non-invasive brain stimulation
OCD	Obsessive compulsive disorder
OPM	Optically pumped magnetometers
PCC	Posterior cingulate cortex
PFC	Prefrontal cortex
PFM	Paradigm free mapping
PMBR	Post-movement beta rebound
PO	Parietal operculum
PSP	Postsynaptic potential
PU	Premonitory urge
PUTS-R	Premonitory urge for tics scale – revised
R2*	Transverse relaxation rate
RF	Radio frequency
RMT	Resting motor threshold
ROI	Region of interest
rTMS	Repetitive transcranial magnetic stimulation
SD	Standard deviation
SEF	Sensory evoked field
SEM	Standard error of the mean
SEP	Sensory evoked potential
SERF	Spin-exchange relaxation
SFG	Superior frontal gyrus
SICI	Short-interval cortical inhibition
SMA	Supplementary motor area
SMG	Supramarginal gyrus
SNR	Signal-to-noise ratio
SNr	Substantia nigra
SQUID	Superconducting quantum interference devices
SSEP	Steady-state evoked potential
tACS	Transcranial alternating current stimulation
tCr	Total creatine
tDCS	Transcranial direct current stimulation
TE	Echo time
TI	Inversion time

TMS	Transcranial magnetic stimulation
TR	Repetition time
TS	Gilles de la Tourette syndrome
tSNR	Temporal signal-to-noise ratio
Vmax	Maximum compliance voltage
WM	White matter
YGTSS	Yale global tic severity scale

Abstract

Tourette syndrome (TS) is a neurodevelopmental, hyperkinetic disorder characterised by the enduring presence of both motor and phonic tics. Premonitory urge (PU) is thought to be a negative reinforcer of tic expression in TS. Tic expression during fMRI scanning is required as an overt marker of increased urge-to-tic, however this can lead to a loss of large amounts of data due to head movement.

The first aim of this thesis was to validate a model free approach to investigate PU. In Chapter 3, I examined the urge-to-blink in healthy volunteers, an analogous behaviour that can be expressed overtly in the MRI scanner. The task involved alternating blocks of "Okay to blink" and "Suppress", during which participants continuously reported their subjective urge-to-blink. Subjective urge scores were found to be correlated with activity in the right posterior and ventral-anterior insula, mid-cingulate and occipital cortices. Blink suppression was associated with activation in the dorsolateral prefrontal cortex, cerebellum, right dorsal-anterior insula, mid-cingulate cortex and thalamus. Therefore, different regions within the right insula contribute to the urge-for-action and suppression networks. In Chapter 4, I reanalysed the same data using a paradigm free mapping approach, which identified activation within the insula and cingulate areas without prior specification of task timing.

The second part of this thesis explored the modulatory effects of rhythmic median nerve stimulation (MNS), a non-invasive stimulation method which has shown potential for reducing tics and urges in TS. In Chapter 5, using MEG I investigated whether rhythmic MNS could be used to entrain oscillations at frequencies associated with sensorimotor inhibition. I demonstrated a frequency specific increase in both amplitude and intertrial phase coherence in the contralateral sensorimotor cortex during rhythmic but not arrhythmic stimulation. I used linear modelling of a template sensory evoked potential (SEP) and empirical mode decomposition to show that these effects were due to entrainment and not purely steady-state SEPs. In Chapter 6, I investigated the effects of MNS on neuro-metabolite concentrations in the contralateral sensorimotor cortex using magnetic

resonance spectroscopy. I demonstrated an initial increase in glutamate compared to baseline during rhythmic but not arrhythmic stimulation but no difference in the difference-from-baseline measures between the two stimulation conditions. These results suggest that despite entrainment of oscillations during rhythmic MNS, there aren't large difference in the tonic neuromodulatory effects of rhythmic and arrhythmic stimulation.

Publications

Houlgreave MS, Morera Maiquez B, Brookes MJ, Jackson SR. The oscillatory effects of rhythmic median nerve stimulation. Neuroimage. 2022 May 1;251:118990. doi: 10.1016/j.neuroimage.2022.118990. Epub 2022 Feb 11. PMID: 35158022.

Houlgreave MS, Morera Maiquez B, Dyke K, Jackson G, Jackson S. (2022). Chapter Thirteen - Entrainment of movement-related brain oscillations to improve symptoms in Tourette syndrome. In Cavanna A.E., Lavoie M.E. (Ed.). *International Review of Movement Disorders* (Volume 4, pp. 349-361). Academic Press. https://doi.org/10.1016/bs.irmvd.2021.11.006.

Chapter 1: Thesis Overview and General Introduction

Key words:

Beta Oscillations, Cortico-Striato-Thalamo-Cortical (CSTC) Pathway, Dopamine (DA), Functional Magnetic Resonance Imaging (fMRI), Gamma-Aminobutyric Acid (GABA), Gilles de la Tourette syndrome (TS), Insula, Magnetoencephalography (MEG), Medium Spiny Neurons (MSNs), Mid Cingulate Cortex (MCC), Mu-Alpha Oscillations, Premonitory Urge (PU), Striatum, Tics, Tourette syndrome.

1.1 Thesis Overview

This thesis focuses on Tourette syndrome. In particular, the use of novel neuroimaging techniques and analyses to explore the brain regions involved in its hallmark symptoms and the reasons why rhythmic peripheral nerve stimulation may act to reduce these symptoms. Specifically, in this thesis I validated a novel model free approach to investigate premonitory urge in disorders such as Tourette syndrome and explored the modulatory effects of rhythmic median nerve stimulation, a novel non-invasive brain stimulation method which has shown potential for reducing tics and urges in Tourette syndrome.

Chapter 1 explores the pre-existing literature relating to the neural correlates of tics and urges, sensorimotor oscillations, and non-invasive brain stimulation. The main conclusions of this review are: 1) different regions are thought to be involved in tics, premonitory urge, and tic suppression, but due to the issues related to movement during conventional neuroimaging techniques, these networks are difficult to separate. 2) Rhythmic median nerve stimulation at a frequency associated with sensorimotor inhibition reduces the frequency and intensity of tics in Tourette syndrome. Its efficacy is hypothesised to be due to the entrainment of oscillations within primary sensorimotor regions. Chapter 2 describes the neuroimaging and stimulation techniques used during this thesis: magnetoencephalography, functional magnetic resonance imaging, magnetic resonance spectroscopy and median nerve stimulation.

Chapter 3 explores the brain regions involved in the urge-to-blink and blink suppression in healthy subjects. This was investigated by asking participants to continuously rate their urge-to-blink during a blink suppression functional magnetic resonance imaging paradigm. The results demonstrated that different regions within the insula were involved in blink suppression and the urge-to-blink. The mid-cingulate cortex and the supplementary motor area were active during both blinking and the suppression of blinking, suggesting that these regions may decide whether a suppressed movement is released.

Continuous rating of subjective urge affected the fMRI signal due to movement and attention to urge, therefore in Chapter 4 the same fMRI data is analysed using a model free approach called paradigm free mapping. This demonstrated that activation within the insula and cingulate regions could be identified without the need for subjective urge ratings. The analysis of the urge-to-blink allowed this analysis technique to be validated using a behaviour which could be overtly expressed in the scanner before it is used to investigate urge in Tourette syndrome patients whilst they suppress their tics. Unfortunately, a planned fMRI experiment using paradigm free mapping to identify the regions involved in the urge-to-tic could not be completed during this thesis due to university restrictions on face-to-face testing and closure of the magnetic resonance (MR) scanning facilities during the COVID-19 pandemic.

In Chapter 5, healthy participants received rhythmic median nerve stimulation at both 12 and 20Hz during an MEG scan to explore whether this resulted in the entrainment of targeted brain oscillations. The oscillatory amplitude and inter-trial phase coherence showed a frequency specific increase which was restricted to the contralateral sensorimotor hand region. Using a linear regression model and empirical mode decomposition, we demonstrated that these results could not be solely explained by steady state evoked potentials, suggesting that entrainment had taken place. Using magnetic resonance spectroscopy, we explored whether this stimulation resulted in similar neurometabolite concentration changes to that of voluntary movement. The results of Chapter 6 showed

an initial increase in glutamate during rhythmic stimulation but no change in GABA. However, when the difference-from-baseline measures were compared there were no differences between the effects of rhythmic and arrhythmic stimulation on glutamate and GABA concentration.

Over the course of this thesis, I address the following questions:

1. What are the neural correlates of premonitory urge? And can these regions be identified without knowledge of when the urge is high?

2. Does rhythmic MNS result in the entrainment of movement-related brain oscillations in the contralateral sensorimotor cortex?

3. Does rhythmic MNS result in changes to Glutamate and GABA concentrations in the contralateral sensorimotor cortex?

1.2 Gilles de la Tourette Syndrome

1.2.1 Clinical Presentation

Gilles de la Tourette syndrome (TS) is a neurodevelopmental, hyperkinetic disorder characterised by the enduring presence of multiple motor tics and at least one phonic tic (*Diagnostic and Statistical Manual of Mental Disorders*, 2013). For a diagnosis of TS, these tics must onset before the age of 18, and be present for at least a year (*Diagnostic and Statistical Manual of Mental Disorders*, 2013). TS was first described in a case study by Itard in 1825 before being fully characterised using 9 patients by Gilles de la Tourette in 1885 (Gilles de la Tourette, 1885; Itard, 1825). This disorder is now thought to affect approximately 1% of young people, with estimates ranging from 0.4-3.8% depending on the sample analysed and the diagnostic methods used (Robertson, 2008). Diagnoses of TS show a higher prevalence in males (5.2:1), although this distinction decreases with age (3:1) (Freeman et al., 2000).

Tics are fast, repetitive, and involuntary movements (*Diagnostic and Statistical Manual of Mental Disorders*, 2013; Robertson, 2011). In general, simple motor tics such as forceful blinking first become apparent between the ages of 4 and 6, followed by simple phonic tics, such as forceful coughing, between the ages of 5 and 7 (Bloch & Leckman, 2009; G. M. Jackson et al., 2015; Leckman et al., 1998). Simple tics are brief in duration and appear to be meaningless whereas complex tics, which can develop with age, are longer and more coordinated (Jankovic, 1997; Leckman et al., 1989). Examples of complex tics include echopraxia (echolalia) which involves imitating a movement (vocalisation), palipraxia (palilalia) where the patient repeats their own action (vocalisation) and copropraxia (coprolalia) where a socially inappropriate movement (vocalisation) is performed (S. C. Cohen et al., 2013).

Tics wax and wane in their frequency, but generally increase when the patient is anxious, tired or excited and decrease when focussed on a goal-directed activity (Conelea & Woods, 2008; Jankovic, 1997; Leckman, 2002). TS has a developmental time course where, in general, the severity of tics increases until around the age of 10 before beginning to decrease

with age (Bloch et al., 2006; Leckman et al., 1998). Interestingly, it has been proposed that only 22% of patients continue to have severe tics in adulthood (Bloch et al., 2006; Pappert et al., 2003). However, some of the most disruptive symptoms in patients often come from the disorders that present comorbidly (Freeman et al., 2000; Sukhodolsky et al., 2007). It is thought that only approximately 10% of cases are 'pure' TS, with there being on average 2 comorbidities per patient (Freeman et al., 2000). The most commonly associated co-occurring disorders are attention deficit hyperactivity disorder (ADHD) (mean: 60%, range: 33-91%) and obsessive-compulsive disorder (OCD) (mean: 27%, range: 2-66%) (Freeman et al., 2000). Due to the overlap in symptomatology and the high rates of comorbidity between these disorders, it may be that there is a common disruption within the cortico-striato-thalamo-cortical (CSTC) circuitry during development (see 1.2.2 Pathophysiology).

Despite outwardly appearing to be a movement disorder, TS is thought to be caused by dysfunction of both the sensorimotor and paralimbic systems (Bohlhalter et al., 2006). This is due to the experience of premonitory urge (PU) in the majority of sufferers (Kwak et al., 2003), although children under the age of 10 do not tend to report these sensations (Leckman et al., 1993). These urges precede tics and are often described as an 'urge-to-move' or the need to repeat an action until it feels 'just right' (Kwak et al., 2003). However, these urges do not necessarily precede every tic the patient has (Ganos et al., 2012). Unlike other movement disorders, tics can be briefly suppressed although this results in an amplification of the aversive sensation until the action is performed (Kwak et al., 2003). Many patients believe that tics are a voluntary response to these sensations and as a result, do not believe they would tic if these urges weren't present (Kwak et al., 2003). The question remains as to whether tics and PUs are independent processes. Do PUs act as negative reinforcement for tic behaviour (Capriotti et al., 2014), or do they arise due to the act of tic suppression (S. R. Jackson et al., 2011)?

1.2.2 Pathophysiology

The pathophysiology of TS is theorised to involve striatal disinhibition within the CSTC pathway (Figure 1.1) (Albin et al., 1989; Leckman et al., 2006). The CSTC circuitry consists of multiple parallel loops with different cortical targets: sensorimotor, limbic, and associational (Alexander et al., 1986; Leckman et al., 2010). Projections from cortical neurons converge on medium spiny neurons (MSNs) within the striosomal and matrisomal compartments of the striatum (Leckman, 2002). Limbic and pre-limbic cortical regions send input to striosomal MSNs, while sensorimotor regions project to matrisomal MSNs (Leckman, 2002).

These basal ganglia circuits are involved in the formation of habits; therefore, it may be that tics are reinforced by inappropriate habit formation in response to urges (Albin & Mink, 2006; Graybiel, 2008; S. R. Jackson et al., 2011; Leckman & Riddle, 2000). This theory involves hyper-dopaminergic activity arising in the substantia nigra (SNr) (Leckman et al., 2010). The levels of dopamine (DA) agonist which can induce stereotypies in rats can be predicted by the ratio of neuronal activation in the striosomes relative to the matrix, suggesting that an imbalance in these two striatal compartments could lead to tic-like behaviours (Canales & Graybiel, 2000). Pharmacological manipulation of DA levels through D2 receptor blockade and monoamine transporter inhibition has been shown to result in tic suppression through a decrease in DA activity (Scahill et al., 2006). Although DA is clearly implicated, multiple neurotransmitters and neuromodulators are involved in transmission within the CSTC pathways; therefore it is likely that multiple systems are disrupted (Singer & Minzer, 2003).

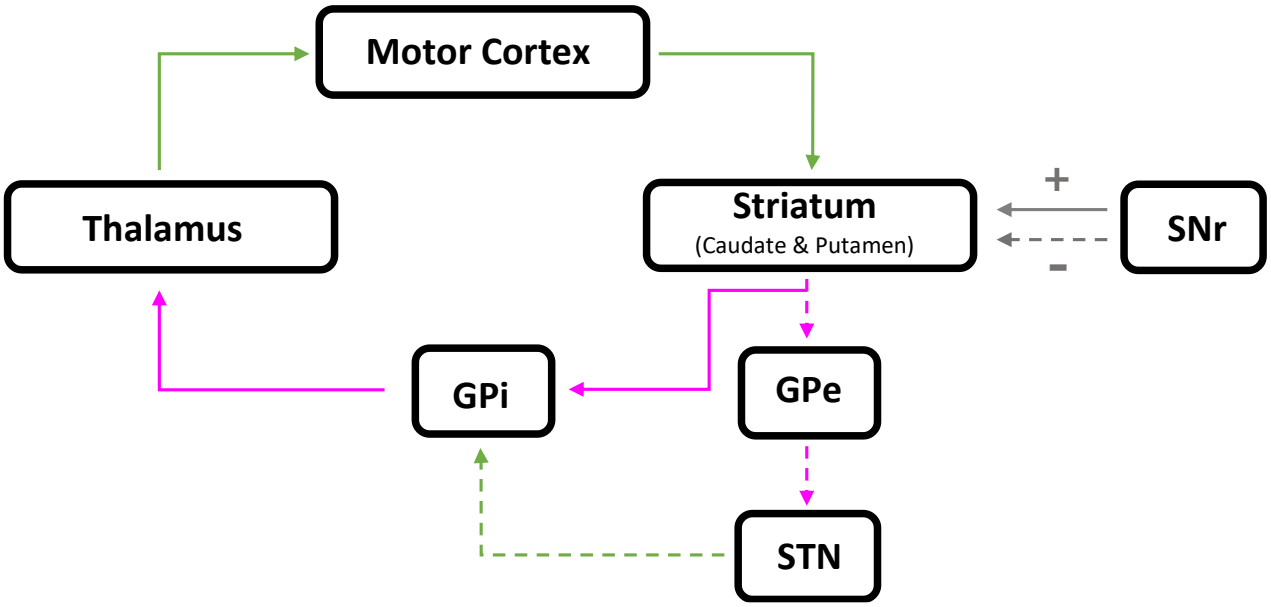

Figure *1.1* *Basic diagram depicting the basal ganglia motor circuits.*

Solid arrows represent an excitatory direct pathway and dashed arrows represent an inhibitory indirect pathway. Green signifies glutamatergic transmission, magenta signifies GABAergic transmission and grey signifies dopaminergic (+ = D1 receptor (excitatory); - = D2 receptor (inhibitory)). (Substantia nigra, SNr; Globus pallidus externus, GPe; Globus pallidus internus, GPi; Sub-thalamic nucleus, STN).

Striatal disinhibition could arise from overactivation of matrisomal MSNs which receive information from both sensorimotor and associational regions relating to a given body-part (Graybiel et al., 1994). If matrisomes become activated repeatedly, such as through reduced intra-striatal inhibition, the result would be repetitive stereotyped movement of a given body part (Mink, 2001). Post-mortem studies have revealed a reduction in both parvalbumin expressing GABA-ergic (gamma-aminobutyric acid) and cholinergic interneurons within the striatum, largely restricted to sensorimotor regions (Kalanithi et al., 2005; Kataoka et al., 2010). Fast-spiking interneurons (FSIs), also known as parvalbumin expressing interneurons, would normally cause widespread inhibition of MSNs within the dorsolateral striatum (Leckman et al., 2006). A lack of MSN inhibition could result in an increased influence of sensorimotor inputs to the striatum, leading to cortical disinhibition (Figure 1.2) (Leckman et al., 1993).

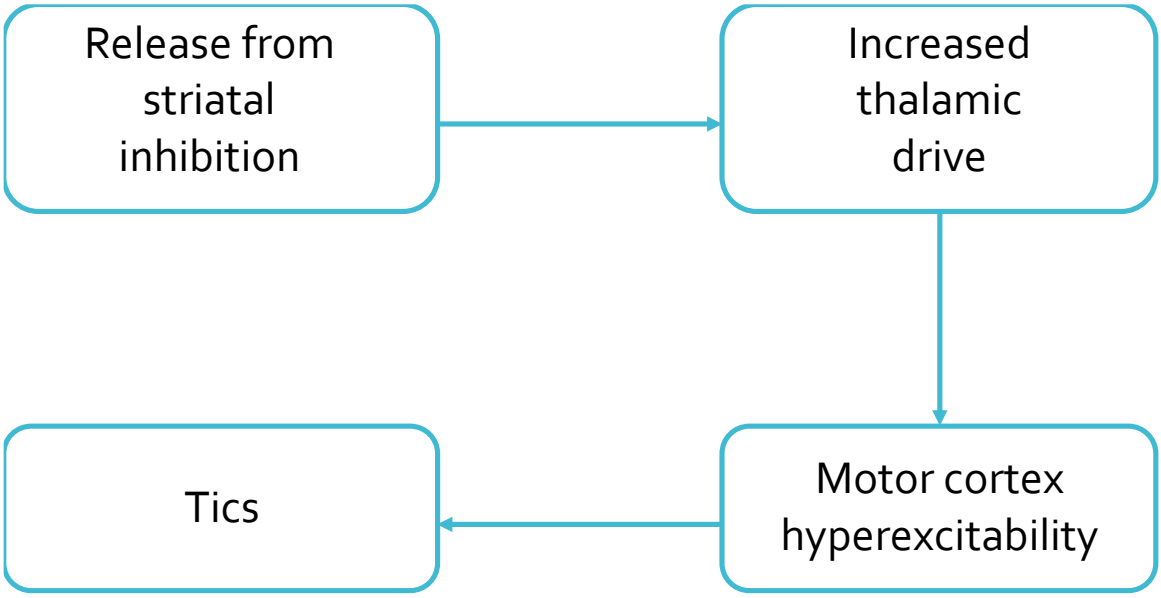

Figure 1.2. *A flow diagram showing the effects of striatal disinhibition in the context of tic generation.*

The striatum can be split into three anatomical regions, the putamen, caudate nucleus, and nucleus accumbens (NAcc) (Figure 1.3). When bicuculline, a $GABA_A$ antagonist, is injected into the dorsolateral putamen of primates they begin to display tic-like movements similar to the motor tics seen in humans with tic disorders (McCairn et al., 2009). Furthermore, injection of the same antagonist into the NAcc (ventral striatum) induces vocalisations in primates (McCairn et al., 2016). These findings suggest that the signal to tic may originate in the striatum of the basal ganglia. Therefore, these animal studies further support the idea of striatal dysfunction caused by reduced inhibition in TS leading to hyperexcitability of the motor cortex.

As the basal ganglia are deep structures, many techniques focus on the cortical effects of the pathology as they are easier to investigate. Transcranial magnetic stimulation (TMS) has been used to show reduced short-interval intracortical inhibition (SICI; a measure of inhibition via $GABA_A$ receptors) in resting TS patients which is suggestive of disinhibition of the motor cortex (Heise et al., 2010; Ziemann et al., 1997). However, the resting motor threshold (RMT) of young children with TS is significantly

higher compared to children of the same age without TS, indicating that a higher intensity of stimulation is required to produce a similar amplitude motor evoked potential (MEP; a measure of corticospinal excitability) (Pépés et al., 2016). Age was shown to be a significant predictor of RMT (Pépés et al., 2016), and in adulthood there is thought to be no difference in RMT compared with healthy controls (Heise et al., 2010). Moreover, there is a reduction in MEP amplitude increase during movement preparation in TS patients, which is suggestive of cortical hypoexcitability (Draper et al., 2015; Heise et al., 2010; S. R. Jackson et al., 2013). Those TS patients who reported lower tic severity show the largest MEP amplitude increases, while those with high tic severity show a lack of MEP amplitude increases prior to a movement (Draper et al., 2015). Similarly, there is a negative association between motor tic severity scores and input-output recruitment (IO) curve slopes (a curve showing MEP amplitudes associated with increasing stimulation intensities) (Pépés et al., 2016). As many patients will have a reduced severity of tic-related symptoms in adulthood, it is important to bear in mind that some of the differences seen may relate to compensation rather than pathology.

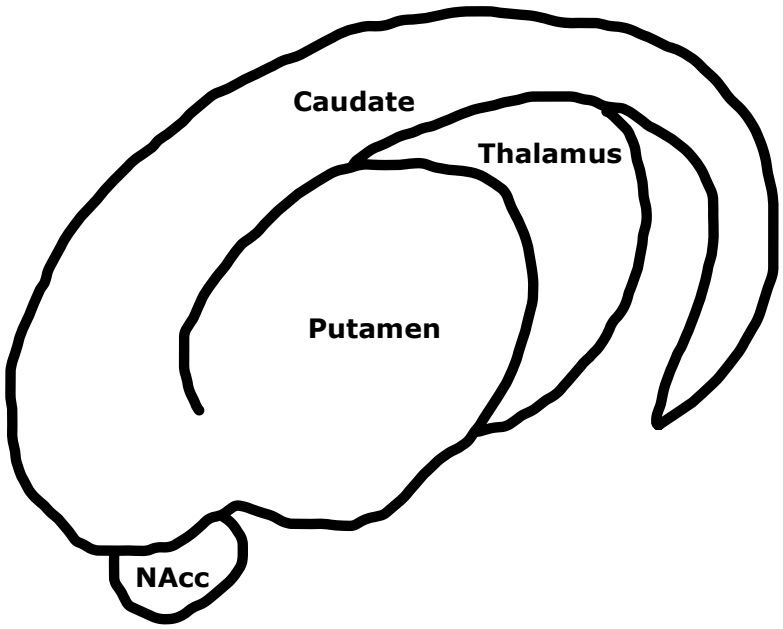

Figure 1.3. *The location of the striatum relative to the thalamus.*
Drawing based on figures in (Ferré et al., 2018; Williams, 2016).

Overall, the findings discussed in this section suggest that overactivation of matrisomal MSNs within the striatum leads to stereotyped movements, potentially through overlearning of habitual behaviours in response to urges. This disinhibition is likely to involve disruption to multiple neurotransmitter and neuromodulator systems including an increase in dopaminergic activation and a reduction in intra-striatal inhibition. Ultimately, striatal disinhibition will have widespread effects throughout the CSTC circuits and other brain regions through its synaptic connections, leading to the generation of tics.

1.2.3 Anatomical correlates of tics and premonitory urge

There are relatively few neuroimaging studies looking at the neural correlates of tic generation. This is largely due to the difficulty in scanning patients during a tic as conventional imaging techniques rely on the brain staying in the same position throughout the scan. One of the most influential studies to look at this research topic is Bohlhalter and colleagues who looked at the change in blood oxygen level dependent (BOLD) activity 2s before a tic and at tic onset (Bohlhalter et al., 2006). Before a tic there were significant increases in activity in the anterior cingulate cortex (ACC), insula, parietal operculum (PO), supplementary motor area (SMA), putamen and thalamus. In contrast, at tic onset the sensorimotor cortex, cerebellum and superior parietal lobule were significantly active (Bohlhalter et al., 2006). Similar patterns of activation preceding tics have been shown in other functional magnetic resonance imaging (fMRI) studies (Neuner et al., 2014; Wang et al., 2011). Although this research highlights the regions involved in tic generation, research into the dynamic interactions of these regions prior to and during tics is limited by the artifacts induced by movement and muscle activity in techniques with a high temporal resolution, like electroencephalography (EEG) and magnetoencephalography (MEG) (Morera Maiquez et al., 2022) (See 1.3.2 for further discussion).

One notable feature of TS, which distinguishes it from other movement disorders, is the preceding urge sensation. Urges, such as those experienced by TS patients are covert behaviours, and therefore

identification of urge-related activity in the brain can be difficult. One approach is to focus on the changes in the BOLD response prior to a tic, the other is to ask participants to suppress their tics throughout, leading to a build-up of urge sensations. When looking at the timeframe prior to a tic, along with activation of pre-motor regions, Bohlhalter and colleagues also found increased activation in paralimbic regions, including the insula, which they hypothesised to be involved in feelings of premonitory urge (Bohlhalter et al., 2006). A meta-analysis by Jackson and colleagues identified brain regions commonly active in fMRI studies looking at the urge to urinate, yawn, swallow, and tic. From their findings they propose that the urge-to-act may be generated by a loop involving the anterior insula, the mid-cingulate cortex (MCC) and the mid-insula (S. R. Jackson et al., 2011). Interestingly, the insula is associated with interoceptive processing (Craig, 2002, 2009), while the MCC is involved in motor responses (Caruana et al., 2018). These findings indicate that different networks are involved in the generation of tics and urges, suggesting that their generation may not be codependent (S. R. Jackson et al., 2020).

An fMRI study exploring the neural correlates of tic suppression described a decrease in subcortical activity, except in the caudate nucleus, and an increase in activity in cortical regions (Peterson et al., 1998). Chiefly, there was a decrease in activity in the ventral globus pallidus, putamen, and mid thalamus, but an increase in the right mid frontal cortex and right ACC. In addition, a study comparing the regions involved in ocular tic suppression in TS and blinking in healthy controls highlighted the increased activity in limbic regions, including the ACC, in TS patients compared to controls during action suppression (van der Salm et al., 2018). Meanwhile, there was increased involvement of sensorimotor regions such as the SMA and MCC during the successful inhibition of blinks. Furthermore, blink suppression, but not tic suppression was associated with increased activation in the right inferior frontal gyrus (IFG), which is thought to be a key region in the motor response inhibition network (Aron et al., 2004, 2014). Better understanding of the brain regions involved in successful tic suppression could help identify therapeutic targets for future interventions.

1.2.4 Management

The symptoms of TS can have a large impact on quality of life (Jalenques et al., 2012). Tics can cause physical exhaustion and pain due to their involuntary repetitive nature or as a result of secondary harm (Conelea et al., 2013; Freeman et al., 2000; Fusco et al., 2006). Tics are also disruptive affecting both academic and social performance (Conelea et al., 2013).

As the cortico-striato-thalamo-cortical system is implicated in both TS and the learning of habits, it has been theorised that the repetitive actions seen in TS are as a result of overlearning of habitual behaviours (Graybiel, 2008). This relates to the urges felt prior to a tic, it may be that patients with TS have overlearned actions needed to relieve these urges, and as such a negative reinforcement loop has been established (S. R. Jackson et al., 2011). Therefore, one common form of behavioural therapy is 'habit reversal training', which involves training the patient to be aware of the urge-to-tic and to perform a socially acceptable competing action to reduce feelings of urge (Azrin & Nunn, 1973). However, the availability of behavioural interventions is limited by the number of trained providers and the travel time, particularly for patients living in rural areas (Himle et al., 2010; Woods et al., 2010). Other interventions involve medication with antipsychotics, but these are associated with a large number of side effects such as fatigue, depression and in extreme cases dyskinesias (Budman, 2014; Jagger et al., 1982). Deep brain stimulation (DBS) of the thalamus or globus pallidus is a potential option for some patients with severe, refractory TS (Savica et al., 2012; X. H. Zhang et al., 2016). Although DBS can result in a significant decrease in symptoms, the procedure is invasive and carries large post-operative risks such as infection (X. H. Zhang et al., 2016). Therefore, the development of new non-invasive treatments to reduce brain activity involved in tic generation is important.

1.2.5 Non-invasive Brain Stimulation in TS

A decrease in motor cortex excitability is linked with a better ability to voluntarily suppress tics (Ganos et al., 2018). Therefore, non-invasive stimulation of the sensorimotor regions, using techniques known to result

in cortical inhibition, may decrease the occurrence of both motor and vocal tics. As such, multiple inhibitory paradigms using various stimulation techniques have been researched to see if they are effective in decreasing tic symptoms.

In transcranial direct current stimulation (tDCS) current is passed between an anode and a cathode placed on the scalp. When the stimulation is cathodal, the effects are inhibitory (Finisguerra et al., 2019). Following five daily sessions of 2mA cathodal tDCS over the left motor cortex in two adult TS patients there was a significant reduction in tics (Mrakic-Sposta et al., 2008). Similarly, ten patients receiving 1mA cathodal tDCS to the SMA showed significantly lower impairment following stimulation compared to sham (Dyke et al., 2019). However, no significant effect of the interaction between time and stimulation was seen, which may be due to there being only one session of stimulation. In contrast, after a period of 5 days with twice daily 2mA cathodal stimulation over the SMA and pre-SMA, all three patients exhibited an increase in tic frequency (Behler et al., 2018).

Repetitive TMS (rTMS) of the SMA at 1Hz has been shown to cause significant decreases in Yale Global Tic Severity Scale (YGTSS) scores and the severity of tic symptoms (Kwon et al., 2011). A similar paradigm showed that these effects can persist for 6 months in the majority of participants (Le et al., 2013). Interestingly, both studies describe an increase in bilateral RMT over time which suggests a spread of stimulation effects to connected cortical regions (Kwon et al., 2011; Le et al., 2013). Continuous theta burst stimulation (cTBS), a specific form of rTMS, of the SMA has also been trialled due to the reduced duration and intensity of stimulation compared with 1Hz rTMS (S. W. Wu et al., 2014). However, there was no difference in the effect on tic symptoms when sham and active conditions were compared, but there was a significant reduction in BOLD activity within the bilateral motor cortices and SMA during a motor task following cTBS.

Although some paradigms of non-invasive brain stimulation have shown promise, they are limited by the need for patients to attend clinics as the

devices used are not easily transported and a trained professional is required to deliver the treatment.

1.3 Neural Oscillations

Neural oscillations are rhythmic patterns of neuronal activity. When large populations of cortical neurons are synchronously active, their firing frequency becomes observable through electrophysiological techniques like EEG or MEG, which have a temporal resolution in the milliseconds range. Recordable oscillations arise when there is synchronised current flow along the dendrites within a neuronal population. An increase in EEG/MEG power (the magnitude of the signal) may arise from an increase in the number of neurons participating in the oscillation and/or an increase in their phase synchrony (Pfurtscheller & Lopes Da Silva, 1999). Neural oscillations are characterised by their frequency and are typically split into 5 bands: delta (1-4Hz), theta (5-7Hz), alpha (mu-alpha in the sensorimotor network) (8-12Hz), beta (13-30Hz) and gamma (>30Hz).

1.3.1 Oscillatory dynamics of voluntary movement

Beta oscillations arising in the contralateral sensorimotor cortex are known to desynchronise before and during movement (movement-related beta desynchronisation (MRBD)) and are associated with motor planning and movement-related activation (Pfurtscheller, 1981; Salmelin et al., 1995). Conversely, following movement, there is an increase in synchronisation in the contralateral cortex in comparison to rest, which is known as the post-movement beta rebound (PMBR). This rebound is associated with reduced corticospinal excitability (R. Chen et al., 1998). Like beta, mu-alpha event-related desynchronisation (ERD) is seen over the contralateral sensorimotor cortex during movement planning and motor tasks (Pfurtscheller & Aranibar, 1979; Pfurtscheller & Berghold, 1989).

1.3.2 Disruption to oscillations in disease states

Pathological changes to beta oscillations can be seen in Parkinson's disease, where a reduced magnitude of desynchronisation may relate to the reduced ability to initiate movement (Brown, 2007). Therefore, it would be natural to assume an increase in the amplitude of desynchronisation in disorders characterised by a hyperexcitability of movement, however there is evidence that mu-alpha and beta do not desynchronise prior to tics in Tourette's patients (Morera Maiquez et al.,

2022). Furthermore, Niccolai and colleagues recently described oscillatory changes occurring prior to tics recorded during a Go/No-Go experiment (Niccolai et al., 2019). When comparing the same timepoint in tic and non-tic trials there is a significant increase in beta power between -650ms and -500ms before a tic, which may relate to stronger motor urges, but there is no difference in power compared to baseline during the -500ms before a tic (Niccolai et al., 2019). As desychronisation is generally measured in comparison to baseline or through data standardisation, these findings could relate to a heightened excitability of the motor cortex in TS patients at baseline, meaning unwanted movements are easier to initiate. Or it may be that this reflects the involuntary nature of tics, indicating a lack of motor planning before the movement is performed. Nevertheless, a recent study found that when told not to suppress their tics patients showed less beta desynchronisation during voluntary movements (Zapparoli et al., 2019). This modulation was not evident when patients were asked to suppress their tics, suggesting that beta oscillations are disrupted in TS and that the mechanism of tic suppression brings these oscillations back under control.

Non-invasive brain stimulation (NIBS) techniques provide a mechanism by which we can temporarily manipulate these brain oscillations to see what effect this has on behaviour. Rhythmic stimulation is thought to cause progressive synchronisation of the activity of neuronal assemblies through a process known as entrainment (Thut, Veniero, et al., 2011). A key study used transcranial alternating-current stimulation (tACS) over the motor cortex at 20Hz during a visuomotor task resulting in a decrease in the velocity of movement in healthy participants (Pogosyan et al., 2009). Furthermore, Joundi and colleagues found that tACS stimulation at beta frequency caused a decrease in the peak rate and the rate of development of force during both 'Go' and 'No-Go' conditions of the Go/No-Go task (Joundi et al., 2012). The increased reduction in force during 'No-Go' compared to 'Go' trials serves as evidence of the possible benefit in the use of beta frequency NIBS for the reduction of motor tics in TS, as these 'No-Go' trials involved a failure to inhibit movement (Joundi et al., 2012). Interestingly, a technique involving non-invasive peripheral nerve

stimulation, rhythmic median nerve stimulation (MNS), has recently been shown to decrease tic frequency in patients (Morera Maiquez, Sigurdsson, et al., 2020). The stimulation was delivered at 10Hz (mu-alpha frequency). Importantly, this technique has the potential to be developed into a portable technique for use outside the clinic (Morera Maiquez, Sigurdsson, et al., 2020). These findings suggest that entrainment of sensorimotor regions using frequencies associated with the inhibition of movement could prove therapeutically useful in reducing the frequency and severity of tic symptoms in TS patients.

Chapter 2: Techniques and Methodology

2.1 Magnetoencephalography

2.1.1 Biophysical origin of the signal

MEG is a non-invasive technique for the measurement of brain electrophysiology in humans (D. Cohen, 1968, 1972). The magnetic fields that are measured using this technique are mainly generated by the current flow along pyramidal cells in the cortex. Pyramidal cells are directional, with apical dendrites orientated towards the cortical surface meaning they form an 'open field' (Schomer et al., 2018). As magnetic fields are perpendicular to the current flow, MEG sensors can only measure the magnetic field of tangential primary currents because, unlike those orientated radially, these currents are positioned such that their fields are measurable outside the scalp according to the right-hand rule (Sarvas, 1987) (Figure 2.1). Due to the convoluted structure of the cortex only the nadirs of the sulci and apices of the gyri have a large radial component and therefore signals generated at the majority of cortical sites can be measured (Hillebrand & Barnes, 2002).

At excitatory synapses, binding of the neurotransmitter (e.g. glutamate) to ligand-gated ion channels on the postsynaptic membrane causes an influx of Na^+ resulting in depolarisation of the apical dendrites (Bear et al., 2016). This increase in membrane potential is termed an excitatory post-synaptic potential (EPSP), as a result the neuron will be closer to the threshold for firing an action potential (AP) (Bear et al., 2016). Conversely at an inhibitory synapse, neurotransmitter (e.g. GABA) binding causes an influx of Cl^- resulting in an inhibitory post-synaptic potential (IPSP) which hyperpolarises the post-synaptic cell (Bear et al., 2016). The intracellular current set up by these post-synaptic potentials (PSPs) will flow from the apical dendrites to the soma, through ionic diffusion down their concentration gradient (Figure 2.1) (Bear et al., 2016). The apical dendrites can be thought of as a dipole, with the positive pole where the neuron is initially depolarised and the negative pole where the current is flowing towards (Bear et al., 2016).

For the generated magnetic field to be detected by MEG there needs to be synchronous activation of a large number of neurons. As APs are short in duration (milliseconds), PSPs (tens of milliseconds) are thought to contribute more to the magnetic fields measured by MEG as they are more likely to be synchronously active (Schomer et al., 2018). Furthermore, while APs display 'all or nothing' responses, with increased firing frequency denoting increased activation once its threshold has been surpassed, PSPs temporally summate in order to determine whether or not to trigger an AP. The summed PSPs within a pyramidal cell form one dipole and, because within an area of cortex all the pyramidal cells are orientated in the same direction, these can be treated as a single dipole when firing synchronously (Nunez & Srinivasan, 2006).

However, the magnetic field resulting from neuronal activity is only of the order of 10^{-12}T while the signals from other physiological sources are around 10^{-11}T (Vrba, 2002). Furthermore, the steady magnetic field resulting from the Earth is 10^{-4}T. As a result, the devices used to detect the signal for MEG recordings need to be sensitive to small deviations in the magnetic field surrounding the head.

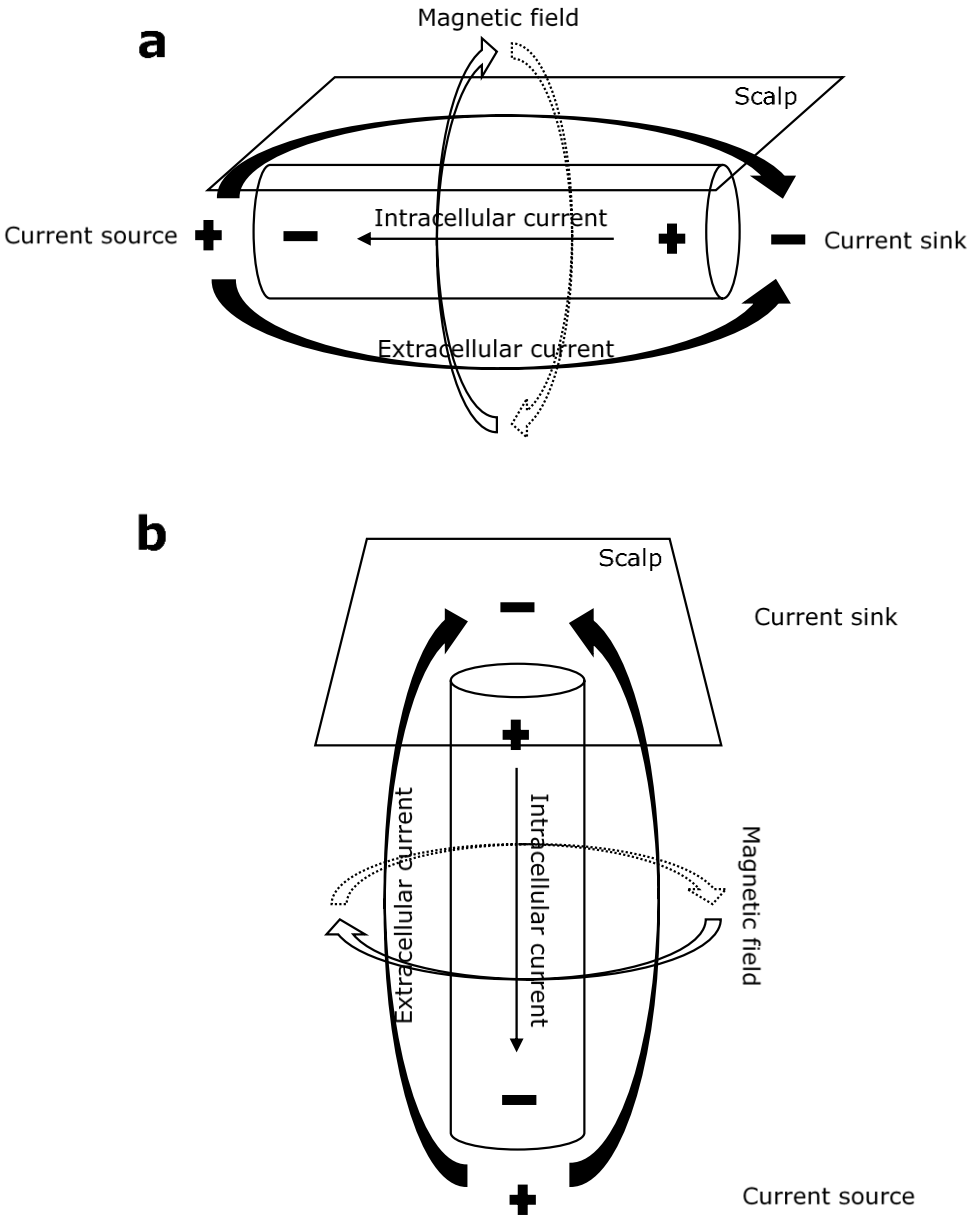

Figure 2.1. *Tangential and radially oriented primary currents.*

In MEG the magnetic field is only measurable when the dipole is orientated tangential to the scalp (a) rather than radial (b).

2.1.2 SQUIDs

Conventional MEG uses cryogenic sensors called superconducting quantum interference devices (SQUIDs) (Zimmerman et al., 1970). It is the SQUID's superconducting properties that allow detection of small variations in the magnetic field. When the temperature of a superconductor is maintained below its transition point, the electrical resistance becomes zero and current will flow indefinitely (Hansen et al., 2010; Hook & Hall, 1991). In MEG, SQUIDs are bathed in a dewar of liquid helium (~4K) in order to maintain the temperature below the transition point (~5K) (Muthukumaraswamy, 2014). It is theorised that superconductive properties at low temperatures stem from the formation of Cooper pairs (bound electron pairs), meaning all electron pairs within the superconductor exist in the same state (Hook & Hall, 1991). Therefore, all these Cooper pairs can be described by the same macroscopic wavefunction (Hansen et al., 2010; Hook & Hall, 1991). A SQUID is a ring composed of two superconductors separated by an insulating barrier meaning that two Josephson junctions are formed (Hämäläinen et al., 1993). The use of Josephson junctions, which allow tunnelling of Cooper pairs, allows us to measure the dynamic resistance across the SQUID without destroying the superconductivity (Hansen et al., 2010). In the presence of a static magnetic field a shielding current will be induced on the surface of the SQUID which is dependent on the magnitude of the field (Hansen et al., 2010). If a known bias current is applied then the magnetic field will induce a change in voltage across the ring which is measurable (Hansen et al., 2010).

Each SQUID in the MEG is coupled to a pickup coil which is situated near to the scalp (D. Cohen, 2009). When a magnetic field passes through the pickup coil it will induce a small electric current which is proportional to the strength of the magnetic field. A set bias current is passed through the SQUID and any change in the flow of this current caused by a change in the magnetic field causes the voltage measured across the SQUID to change (Hansen et al., 2010; R. Kleiner et al., 2004). A feedback circuit then equalises this magnetic field flux via current input and the voltage change is recorded by the MEG via a preamp. In the CTF 275-channel

system, axial gradiometers are used as the pickup coils (Schomer et al., 2018). Gradiometers consist of two magnetometers (wire loops which measure the magnetic field) positioned in opposing orientations: the coil closest to the scalp is the pickup coil and further away is a compensation coil (Hämäläinen et al., 1993; Hansen et al., 2010). An axial gradiometer will measure the spatial gradient of the magnetic field, radial to the scalp, between the two magnetometers (Hansen et al., 2010). A large signal from far away will affect both coils equally meaning an opposing current within the second magnetometer will cancel the current in the pickup coil (Hämäläinen et al., 1993; Hansen et al., 2010). Whereas for small, local changes in the magnetic field a current will only be induced in the pickup coil.

2.1.3 Noise reduction

The need for SQUIDs to be supercooled means that the sensors cannot be placed directly on the scalp resulting in a lower signal to noise ratio (SNR) (Muthukumaraswamy, 2014). Sources of interference will cause changes in the magnetic field which are several orders of magnitude larger than that of spontaneous brain activity. To reduce the effects of environmental noise the room in which the MEG scan takes place is magnetically shielded (D. Cohen, 2009). Additionally, the previously mentioned gradiometers can further reduce the effects because both magnetometers within a gradiometer will be equally affected by external noise (Muthukumaraswamy, 2014). Therefore, the difference between the measurements reflects the magnetic field of the measured dipole. Furthermore, we can combine the outputs of the axial gradiometers with a reference array to create a third-order synthetic gradiometer to improve noise reduction (Vrba & Robinson, 2001).

2.1.4 Movement and co-registration

As a standardised helmet is used for MEG recordings, the position of the head in relation to the sensors is dynamically measured. Fiducial coils are positioned on the bilateral preauricular points and the nasion of the participant and their magnetic signals are recorded (Schomer et al., 2018). If there is too much head movement, then the localisation of sources could be affected (Handy, 2009; Stolk et al., 2013).

Following the MEG scan, we localise where points on the participant's head are in relation to the fiducial coils, using a Polhemus FASTRAK 3D digitiser. A stylus is placed into each of the fiducial coils to record their location in relation to a transmitter box. Then points are recorded across the scalp, forehead, nose and eye sockets.

As we are interested in the activity of the sources rather than the activity measured at the sensors, a structural T_1-weighted magnetisation-prepared rapid acquisition with gradient echo (MPRAGE) sequence image is collected using either a 3T or 7T magnetic resonance imaging (MRI) scanner. The fiducials used during the MEG scan can be seen in both the Polhemus data and the head model reconstructed from the MRI image (Whalen et al., 2008). During co-registration points on the surface of the digitised head will be matched with those on the MRI head model by minimising a measure of the distance between them; the iteration with the lowest error will be selected (Figure 2.2) (Whalen et al., 2008). Many iterations are required to ensure the solution is not due to a local minimum (Whalen et al., 2008). The result is that the locations of the MEG sensors, fiducial points and the neuroanatomy will be defined within the same co-ordinate system to allow the sources to be modelled in relation to the sensors.

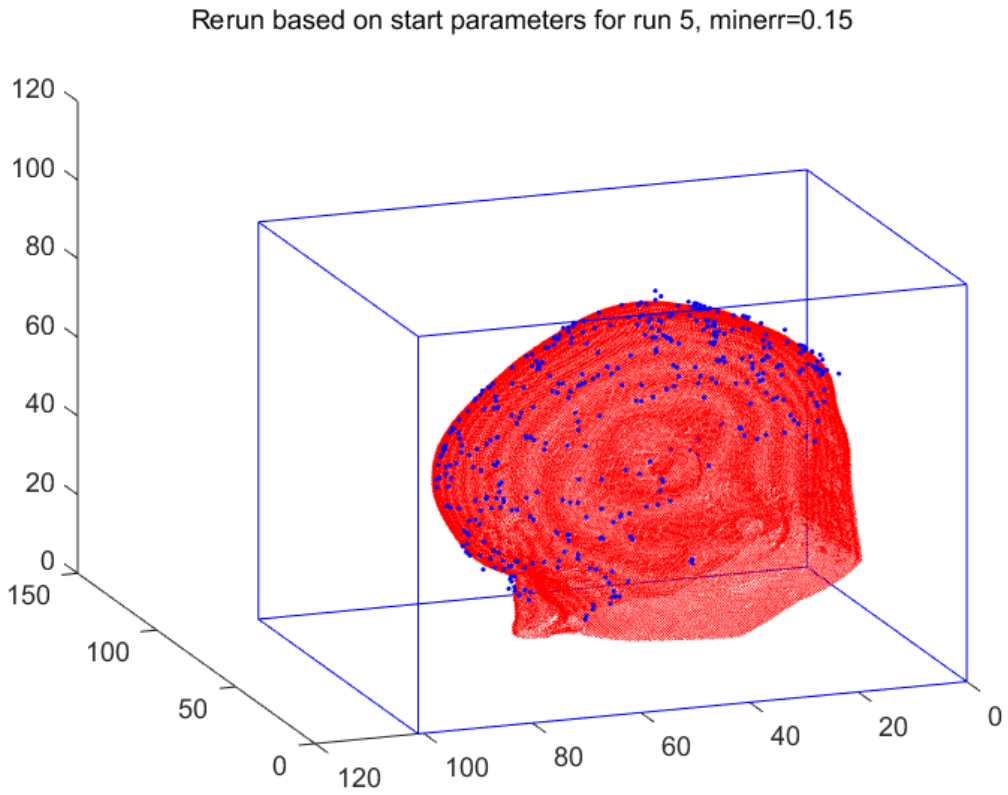

Figure 2.2. *Co-registration of participant data.*

An example of the best outcome for minimising the error between the digitised head surface and the head model from the magnetic resonance image.

2.1.5 The forward problem

Each MEG sensor measures the magnetic field produced by multiple sources. MEG data can be analysed at the sensor level but, as this thesis involves an interest in the neural generators of the measured oscillations, state-space modelling is required. The forward problem in source localisation relates to modelling the signal which would be measured by the MEG system for a source dipole at a given location. In order to compute this, it is assumed that the head can be modelled as a sphere with uniform electrical conductivity and that the magnetic field caused by many synchronized PSPs can be modelled as a single dipole (Nunez & Srinivasan, 2006; Sarvas, 1987).

The Biot-Savart law (1) describes the magnetic field $\boldsymbol{B}(\boldsymbol{r})$ measured outside of the head at sensor $\boldsymbol{r}$ (Sarvas, 1987). Where *G* is a conductor, μ_0 is the permeability (ability to sustain the development of a magnetic field) of free space, $\boldsymbol{J}$ is the total current, $\boldsymbol{r}'$ is the source and dv' is the differential volume element.

$$\boldsymbol{B}(\boldsymbol{r}) = \frac{\mu_0}{4\pi}\int_{\mathrm{G}} \boldsymbol{J}(\boldsymbol{r}') \times \frac{(\boldsymbol{r}-\boldsymbol{r}')}{|\boldsymbol{r}-\boldsymbol{r}'|^3} dv' \qquad (1)$$

The total current includes both the primary (intracellular) and volume currents (Mosher et al., 1999; Sarvas, 1987). If we substitute in these currents, we can show that the volume currents can be thought of as a set of currents on the surface of the head using the Geselowitz formula (Geselowitz, 1967; Sarvas, 1987). As the MEG only measures the radial component of the magnetic field, generated by tangential dipoles, we can ignore these volume currents as they will not contribute to the signal (Mosher et al., 1999; Sarvas, 1987).

2.1.6 The inverse problem

(Sarvas, 1987; Sekihara et al., 2007)

The inverse problem involves the issue of calculating the dipole distribution given the data measured. There are an infinite number of solutions to this problem because we do not know the location, orientation, size or number of the dipoles (Sarvas, 1987).

If we assume that the head can be modelled as a sphere (2). Where V is the volume and $b(\boldsymbol{r},t)$ represents the measured data at sensor $\boldsymbol{r}$ at time t. $L(\boldsymbol{r},\boldsymbol{r}')$ represents the forward model i.e., what would be measured at sensor $\boldsymbol{r}$ when there is a dipole at source $\boldsymbol{r}'$. $Q(\boldsymbol{r}',t)$ corresponds to the strength of the dipole at source $\boldsymbol{r}'$ at a given time t.

$$b(\boldsymbol{r},t) = \int_V L(\boldsymbol{r},\boldsymbol{r}')\, Q(\boldsymbol{r}',t)\, dV + e(\boldsymbol{r},t) \qquad (2)$$

This calculation is repeated for every voxel in the brain, where *M* is the total number of voxels (3).

$$b(\boldsymbol{r},t)=\left[\sum_{m=1}^{M} L(\boldsymbol{r},\boldsymbol{r'_m})\,Q(\boldsymbol{r'_m},t)\right]+e(\boldsymbol{r},t) \qquad (3)$$

As matrices, the lead field contains *N* channels and *M* voxels (4). Here, b is the measured MEG signal and q is the dipole strength.

$$\begin{bmatrix} b_1(t) \\ b_2(t) \\ \vdots \\ b_N(t) \end{bmatrix} = \begin{bmatrix} L_{1,1} & \cdots & L_{1,M} \\ L_{2,1} & \cdots & L_{2,M} \\ \vdots & \ddots & \vdots \\ L_{N,1} & \cdots & L_{N,M} \end{bmatrix} \begin{bmatrix} q_1(t) \\ \vdots \\ q_M(t) \end{bmatrix} + \begin{bmatrix} e_1(t) \\ e_2(t) \\ \vdots \\ e_N(t) \end{bmatrix} \qquad (4)$$

The aim is to minimise the error e in the inverse solution.

2.1.7 Beamforming

(Sarvas, 1987; Sekihara et al., 2007; Vrba & Robinson, 2001)

To estimate the contribution of each source within the brain to the measured signal (Hansen et al., 2010), we calculate the solution with the maximum-probability for each voxel in turn, this is achieved by applying a beamforming spatial filter (5). Where $\hat{q}(\boldsymbol{r}',t)$ is the estimate of the dipole strength at source $\boldsymbol{r}'$ at a given time t. The magnitude of a given dipole is calculated by the linear weighted sum of the measurements from every sensor, with the sensors proximal to the source being weighted higher than those distally placed, essentially acting as a spatial filter (6) (Hansen et al., 2010). In beamforming the weighting parameters w^T are dependent on both the lead field l (i.e. what would be measured at each sensor for a dipole at a given location) and the measured covariance between sensor timecourses C (6). The covariance between sensors accounts for the fact that the signal from a given source in the brain will be measured by multiple sensors causing correlations between the measured signals (Hansen et al., 2010). This spatial covariance is essentially cancelled by multiplying the lead fields by the inverted covariance matrix C^{-1} (Hansen et al., 2010). The covariance matrix is made invertible through regularisation, which adds noise into the signal so that the matrix is no longer rank deficient (Hansen et al., 2010). Beamforming tends to mis-localise sources to the centre of the brain and so we normalise the weights w_z^T to prevent this (7).

$$\hat{q}(\boldsymbol{r}', t) = w^T(\boldsymbol{r}')\, b(t) \tag{5}$$

$$w^T = \frac{l^T(\boldsymbol{r}')\, C^{-1}}{l^T(\boldsymbol{r}')\, C^{-1}\, l(\boldsymbol{r}')} \tag{6}$$

$$w_Z^T(\boldsymbol{r}') = \frac{l^T(\boldsymbol{r}')C^{-1}}{\sqrt{l^T(\boldsymbol{r}')\, C^{-2}\, l(\boldsymbol{r}')}} \tag{7}$$

The electrical field induced at a given source can then be calculated (8).

$$\hat{q}(r', t)^2 = w^T(r')\, C(t)\, w(r') \tag{8}$$

Followed by calculation of the dipole power where Σ is the noise covariance matrix (9).

$$Z = \frac{w^T(r')\, C(t)\, w(r')}{w^T(r')\, \Sigma\, w(r')} \tag{9}$$

The output of this calculation is a pseudo-Z-statistic Z for each voxel. To see how power changes in relation to task, we use the pseudo-T-statistic (10). Where ${}^{(a)}\hat{Q}_\theta^2$ and ${}^{(c)}\hat{Q}_\theta^2$ are the power estimates for the active and control conditions, respectively, and ${}^{(a)}\hat{v}_\theta^2$ and ${}^{(c)}\hat{v}_\theta^2$ are their corresponding noise power estimates (Vrba & Robinson, 2001).

$$T = \frac{{}^{(a)}\hat{Q}_\theta^2 - {}^{(c)}\hat{Q}_\theta^2}{{}^{(a)}\hat{v}_\theta^2 + {}^{(c)}\hat{v}_\theta^2} \tag{10}$$

2.1.8 Why MEG?

With MEG the localisation of deep sources is problematic as according to the inverse-square law the magnetic field decays with increasing distance from the underlying source (Hillebrand & Barnes, 2002) and currents induced by radial dipoles cannot be measured. But, unlike in EEG where the signals measured are affected by the conductivity of the overlying tissue (Cheyne, 2013), the MEG signal shows less spatial smearing meaning the models used for source localisation are less complex (Muthukumaraswamy, 2014). Furthermore, of particular importance when recording data from patients with movement disorders, EEG is more susceptible to muscle artefacts.

2.2 Functional Magnetic Resonance Imaging

2.2.1 The MR signal

Certain atomic nuclei demonstrate magnetic resonance when exposed to strong magnetic fields and we take advantage of this in MRI (Chappell et al., 2020). There is an abundance of hydrogen atoms in the human body as almost two-thirds of its composition is water (Huettel et al., 2014). When a magnetic field is applied hydrogen atoms, hereon referred to as protons, are electrically charged and have a spin, resulting in a magnetic moment (Huettel et al., 2014). Normally protons do not have a preferred orientation and so there is no net magnetisation, but under a strong applied magnetic field (B_0) the protons align with its axis in either a parallel or antiparallel orientation (Hashemi et al., 2018). In MRI, this field is established using a supercooled superconducting coil and, due to the strength of the field used, a higher proportion of spins exist in the lower energy parallel state causing net magnetisation, *M*, along the axis of the applied magnetic field (Chappell et al., 2020).

In the presence of the B_0 field individual protons will precess, but not in phase, and so there is no net effect (Mazumder & Dubey, 2013). If the protons are knocked out of alignment with the B_0 field using an oscillating magnetic field they will undergo nuclear magnetic resonance, and the net magnetisation will precess around the B_0 axis at a frequency which is proportional to its strength (Chappell et al., 2020). This is known as the Larmor or resonant frequency (ω_0), which is in the radiofrequency (RF) range (Chappell et al., 2020). The now precessing net magnetisation can induce a time-varying current in the RF coil through electromagnetic induction, which can be measured (Chappell et al., 2020). To shift the alignment away from the B_0 axis we generate a current in the RF coil that oscillates at the Larmor frequency, the same as the precession rate of the protons, in order to generate a time-varying magnetic field (B_1) (Chappell et al., 2020). The Larmor frequency is 127.74 MHz at 3T and 298.06 MHz at 7T (Chappell et al., 2020; Sprawls, 2000). On delivery of a 90° RF pulse, the net magnetisation tips away from the B_0 axis (longitudinal plane) into the transverse plane (Hashemi et al., 2018; Sprawls, 2000). Following this

pulse, we can measure the net magnetisation through the current it induces in the RF coil (Chappell et al., 2020).

However, without any spatial encoding the signal we receive would include the sum influence from all the protons within the scanner bore (Chappell et al., 2020). In MRI we can switch on and off 3 independent gradient coils to generate magnetic fields that vary with location along the bore in the x, y and z directions (Chappell et al., 2020). Therefore, for slice-selection each location along the bore (z axis) experiences a different B_0 field and so protons in each area will have a slightly different resonant frequency (Chappell et al., 2020). As such the RF pulse can be tuned to a specific range of frequencies for each slice of the image. Therefore, the frequency components of the received signal encode the position which can be identified through the Fourier Transform (Chappell et al., 2020).

For structural MRI images we measure the time taken for the protons to realign with the B_0 axis (longitudinal relaxation (T_1)); the difference in relaxation rate between tissue types gives the MRI contrast (Sederman, 2015; Sprawls, 2000). Following excitation with the RF pulse the signal recorded will have no longitudinal component, but it will have a large transverse component as we have flipped the net magnetisation into the transverse plane (Chappell et al., 2020). The longitudinal component will recover according to the time constant T_1, as the protons realign with the B_0 field (Chappell et al., 2020). The *repetition time* (TR) is the time we wait between excitation of the same slice (Chappell et al., 2020). We can select a TR where the longitudinal component has not fully recovered and the partial recovery will be different in each tissue type, giving a T_1-weighted image (Chappell et al., 2020).

2.2.2 Blood Oxygen Level Dependent signal

Action potential firing is an energy intense process which necessitates adenosine triphosphate (ATP), which is generated through aerobic respiration (Huettel et al., 2014). Therefore, neuronal activation results in an increase in the supply of oxygenated blood – the haemodynamic response (Glover, 2011). Haemoglobin within the blood is diamagnetic

when oxygen is bound, whereas deoxyhaemoglobin is paramagnetic and therefore disturbs the local magnetic field (Hashemi et al., 2018). fMRI measures deviations in the MR signal relating to the haemodynamic response (Huettel et al., 2014). In active regions there is an oversupply of oxygenated blood meaning there will be a higher ratio of oxy- to deoxyhaemoglobin, resulting in an increase in the BOLD signal.

In contrast to structural MRI images, functional MRI involves measuring the time taken for the protons to realign with the XY axis (transverse dephasing (T_2*)). As the precession frequency of a proton is affected by the magnetic field it experiences (Hashemi et al., 2018), proton spins will diphase depending on the oxygen content of the tissue due to deoxyhaemoglobin being paramagnetic. This loss of phase coherence means the decay of the transverse component will be faster than expected in regions with a high ratio of deoxyhaemoglobin. The BOLD signal is determined by the transverse relaxation time which is measured by the RF coil. As such voxels containing oxygenated tissue will have a higher BOLD signal (Chavhan et al., 2009). The *echo time* (TE) is the time we wait before acquiring the signal after an RF pulse; an appropriate TE is required in order to maximise the contrast in the signal received from different tissues (Chappell et al., 2020).

The spatial resolution of fMRI is high due to the selectivity of delivery of oxygenated blood. Therefore, the technique is ideal for the identification of regions activated by a task. However, as the signal relies on cerebral blood flow and oxygenation it is indirect, meaning the changes in the BOLD signal simply correlate with the changes in neuronal activation within a given area (Loued-Khenissi et al., 2019). For the same reasons, fMRI has a low temporal resolution due to the sluggish nature of the haemodynamic response (~20 seconds to return to baseline with a peak at around 5 seconds) (Poldrack et al., 2011).

2.2.3 Conventional fMRI analysis

2.2.3.1 The General Linear Model

A general linear model (GLM) (12) is used to model the BOLD signal measured during the experimental paradigm (Poldrack et al., 2011).

$$Y = B_1 X_1 + \epsilon \tag{12}$$

Where Y is the measured BOLD signal, B is the beta coefficient (how much a given predictor contributes to the signal), X is a predictor such as the stimulus onset times and ϵ is the error. The aim of the GLM is to find the weights for our predictor variables which minimise the error between our model and the measured BOLD signal.

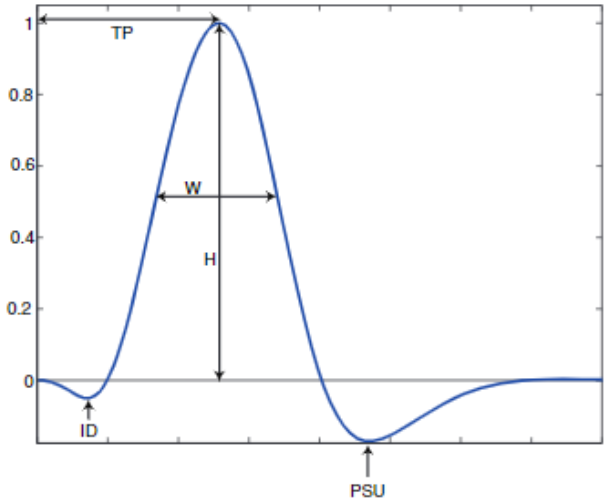

***Figure 2.3**. The shape of the haemodynamic response function.*

Initial dip, ID; Time to peak, TP; Width, W; Height, H; Post-stimulus undershoot, PSU. Image taken from Poldrack et al., 2011.

The haemodynamic response function (HRF) is the expected change in BOLD signal following presentation of a stimulus (Figure 2.3). The initial dip corresponds to the initial increase in deoxygenated blood when neurons begin firing in response. The peak corresponds to the oversupply of oxygenated blood to the active region. The BOLD signal is approximated by a linear time-invariant system for which we assume that the HRF is the same for the same stimulus, therefore we can shift it across time in accordance with the stimulus onset times (Poldrack et al., 2011). We also assume that where these signals overlap they can be summed linearly and

that the neural and BOLD signals scale by the same factor (Poldrack et al., 2011).

2.2.3.2 Estimating the BOLD signal

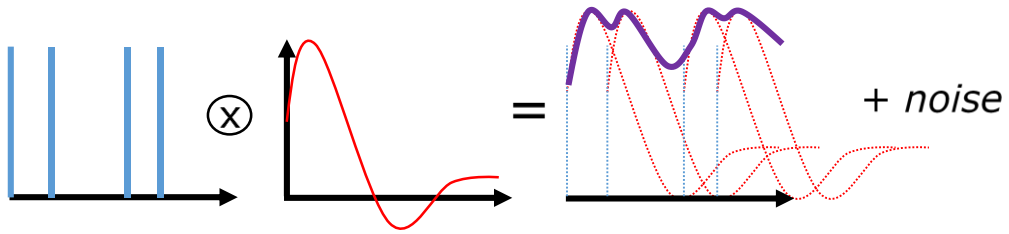

Figure 2.4. *Estimation of the BOLD signal.*

The stimulus onset times (blue) are convolved with the haemodynamic response function (red) to estimate the BOLD signal (purple).

The canonical HRF is defined by two gamma functions: one to model the stimulus response and one to describe the undershoot (Poldrack et al., 2011). This HRF is convolved with the stimulus onset times to model the BOLD timeseries (Figure 2.4). To create a better statistical model we include nuisance parameters, such as the regressors defined during motion correction, to account for other variance in the data. Inclusion of these should reduce model error and increase the detection power (Poldrack et al., 2011). We also use approaches such as smoothing (2.2.3.4), high-pass filtering (2.2.3.5) and prewhitening (2.2.3.5) to improve the signal-to-noise ratio.

2.2.3.3 Co-registration and motion correction

MRI assumes that a given voxel corresponds to the same region of tissue throughout the scan (Poldrack et al., 2011). This assumption can be violated by movement. Where movement is subtle and correlates with the task paradigm it can cause statistical differences at the edges of the brain where voxels that did not originally correspond to a region of brain tissue now do (Poldrack et al., 2011). To account for this, motion correction techniques are applied during pre-processing during which images from the timeseries are realigned to a reference image (usually the middle volume) using an affine transformation (Poldrack et al., 2011). A cost function will be incorporated into the method used to minimise the difference between the reference and current image (Poldrack et al.,

2011). Interpolation is then used to construct the new timeseries (Drobnjak, 2007). During this correction 6 motion parameters will be estimated (3 translational: x, y, z; 3 rotational: yaw, pitch, roll) (Poldrack et al., 2011). The sum of the absolute temporal derivatives of these parameters gives the framewise displacement (FD) (*Brain Mapping Unit Wiki*, 2018). Timepoints where FD values exceed a given threshold can be entered into the GLM so that the motion effects will not confound the analysis. During motion correction the absolute mean displacement (AMD) is calculated. Runs where participants display AMD values above a certain threshold (usually half a voxel size) can be excluded due to the likelihood that high levels of motion will have affected the quality of the data (Poldrack et al., 2011).

2.2.3.4 Spatial smoothing and spatial normalisation

To improve the signal-to-noise ratio the higher frequency information is removed from the image (Poldrack et al., 2011). Furthermore, smoothing reduces the effect of individual variation in region location on the activation pattern at the group level (Poldrack et al., 2011). The usual method is to convolve the data with a 3D Gaussian kernel where the extent of the smoothing is determined by the distribution width (Poldrack et al., 2011).

In order to average the data across subjects we transform the data into Montreal Neurological Institute (MNI) space (Poldrack et al., 2011). The structural MRI scans are pre-processed using brain extraction to skull-strip the images. An affine transformation is then used to register the aligned subject brain, following the motion correction procedure, to the MNI template.

2.2.3.5 Noise correction

In fMRI data there is a low-frequency drift, although whether the cause is physiological or scanner related is uncertain (Poldrack et al., 2011). Nevertheless, this is a noise signal that we do not want to affect our results. Therefore, a high-pass filter is applied.

The data are also temporally autocorrelated, which violates the assumptions for the GLM (Poldrack et al., 2011). To account for this, the

GLM is initially run overlooking the autocorrelation and the residuals from this are used to estimate the noise in the data (Poldrack et al., 2011). Prewhitening is then applied to remove the temporal autocorrelation from the GLM (12):

$$WY = WB_1X_1 + W\epsilon \quad (13)$$

where W is the whitening matrix. This whitening matrix will transform the data to temporally decorrelate the noise, and therefore make it white noise.

2.2.3.6 Cluster-level inference

During the first level of the analysis, we use the GLM to model the BOLD signal change for each subject run separately, giving the average response to the stimulus of interest in that run. At the second level, we average these first-level effects across runs within the subject. Finally at the third-level, mixed effects analysis is used to average across subjects.

In fMRI, we expect that regions which are larger than a single voxel will become activated during the task (Poldrack et al., 2011). Also, the spatial extent of activation is smoothed and oversampled, depending on the template image used, during pre-processing (Poldrack et al., 2011). Therefore, we use 'cluster-level inference' to identify clusters that are significantly activated following estimation of the BOLD response. First a cluster forming threshold is applied to identify groups of continuous voxels, within the Z-statistic map, which are then defined as clusters (Poldrack et al., 2011). The significance value of this cluster is then ascertained based on the size of the cluster using Gaussian random field theory (Friston et al., 1994; Nichols & Hayasaka, 2003). Through this approach multiple comparisons are corrected for using the family-wise error (FWE) rate.

2.3 Magnetic Resonance Spectroscopy

Magnetic resonance spectroscopy (MRS) uses MR hardware to non-invasively quantify chemical compounds within a predefined area of tissue (Juchem & Rothman, 2014). As previously described in the section on fMRI (2.2.1), the resonant frequency of protons exposed to a static magnetic field depends on the strength of the MRI scanner. At 7T the Larmor frequency is ~300 MHz. However, if the proton is bound to a compound the spin frequency will differ due to shielding by neighbouring electrons. This is referred to as the chemical shift (Juchem & Rothman, 2014). Where more than one proton is present in a molecule, the magnetic field generated by one can affect the field experienced by its neighbour causing multiple peaks to be seen in the chemical's spectrum. This is known as J-coupling (Figure 2.5) (Faghihi et al., 2017). The peaks of the spectrum will scale based on the number of protons spinning at a particular frequency and therefore the peaks scale with the amount of a given metabolite (Juchem & Rothman, 2014). When compared to a reference frequency (such as total creatine), the chemical shift is no longer dependent on the applied magnetic field (Juchem & Rothman, 2014).

For single voxel MRS, three radiofrequency pulses are delivered while an x, y or z slice gradient is applied (Figure 2.6). These should intersect at the voxel of interest (Faghihi et al., 2017; Frydman, 2009). Only protons within the target voxel will receive all 3 pulses, and spoiler gradients will dephase the precession of protons outside the target voxel (Juchem & Rothman, 2014).

As the abundance of these molecules is infinitesimal compared to the water content of the body, water suppression is applied to allow their quantification (Juchem & Rothman, 2014). To further aid in quantification, scanners with a higher field strength can be used to maximise the separation between metabolites and the water peak. This will also improve the SNR (Frydman, 2009). Furthermore, shimming can be applied to increase the homogeneity of the field within the scanner. Shimming involves the use of coils which produce magnetic fields that oppose any inhomogeneities in the environment (Faghihi et al., 2017). Eddy currents

induced within the scanner bore by the changing magnetic field gradients can also cause artifacts in the baseline spectrum which in turn can make it difficult to identify metabolite peaks (Juchem & Rothman, 2014). By running an additional acquisition without water suppression, the phase modulation of the eddy currents can be calculated due to the high SNR of the water peak, allowing artifact correction (Juchem & Rothman, 2014).

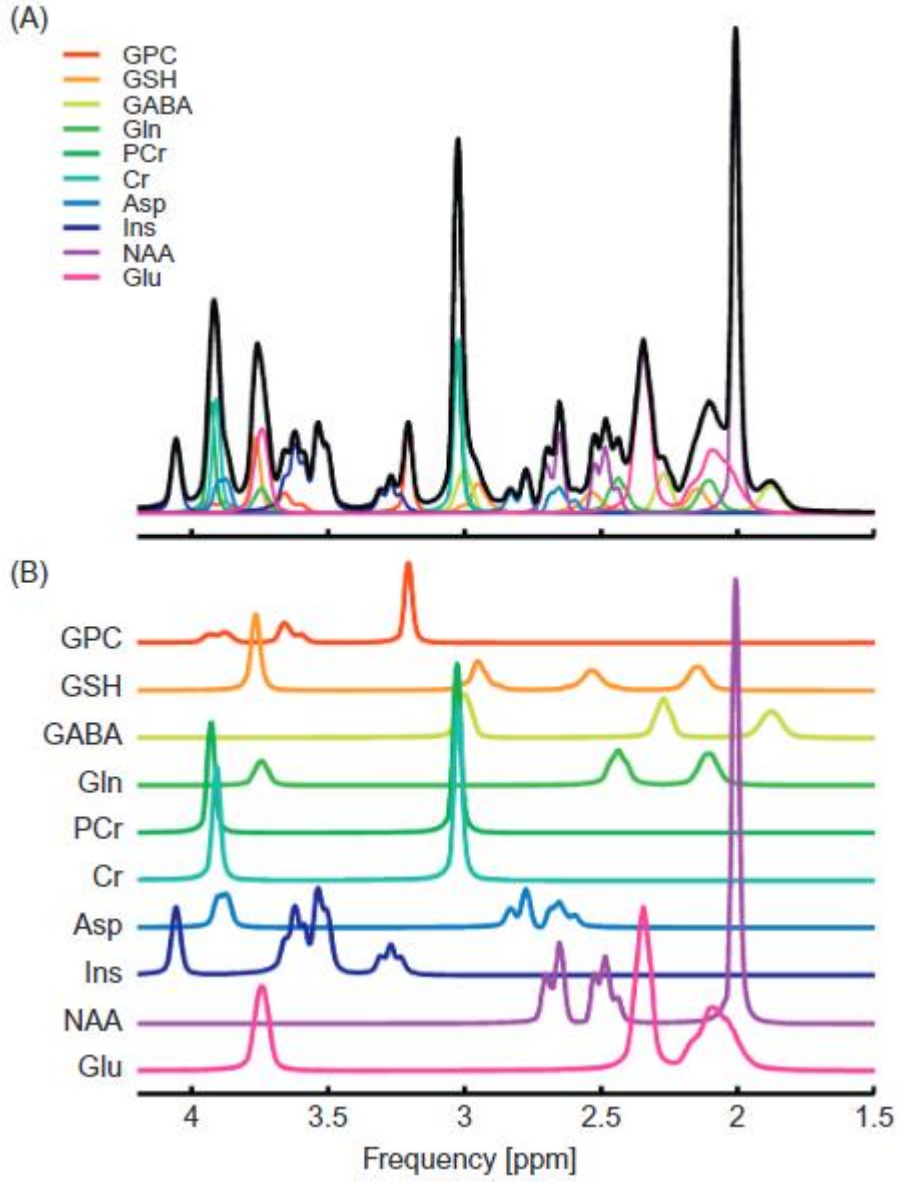

Figure 2.5. *The ^{1}H MR spectra.*

(A) The ^{1}H MR spectra (black) is the linear sum of all the spectra of the metabolites measured. (B) The individual spectra scale depending on metabolite concentration, J-coupling is responsible where spectra contain multiple peaks. (glycerophosphocholine, GPC; glutathione, GSH; glutamine, Gln; phosphocreatine, PCr; creatine, Cr; aspartate, Asp; myo-inositol, Ins; N-acetylaspartate, NAA; glutamate, Glu). Figure taken from Juchem and Rothman (2014).

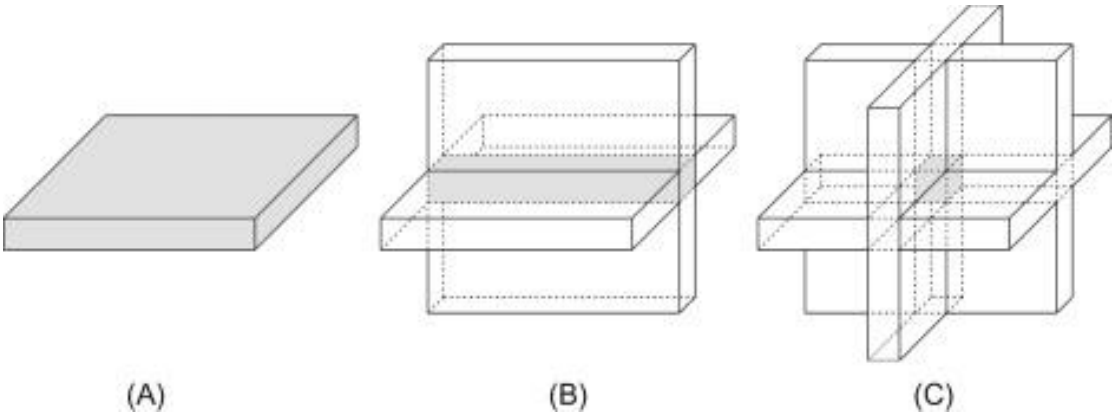

Figure 2.6. *Single voxel MRS.*

A radiofrequency pulse in the x plane selects a slice (A), when this intersects with a pulse along the y plane a column is selected (B) and finally with 3 radiofrequency pulses in different planes only protons within the voxel at the intersect will be targeted (C). Figure take from Juchem and Rothman (2014).

2.3.1 Measuring GABA

GABA is the main inhibitory neurotransmitter in the central nervous system. Phasic inhibition involves synaptic neurotransmission where vesicular GABA is released into the synaptic cleft following depolarisation of the pre-synaptic bouton (Brickley & Mody, 2012). The short-lived binding of GABA to post-synaptic receptors leads to a brief hyperpolarisation of the post-synaptic cell. However, GABA is also present extracellularly and can bind to extrasynaptic receptors for prolonged periods to provide tonic inhibition (Brickley & Mody, 2012). When using MRS there is no way to determine the concentration of intra- and extracellular GABA separately (Stagg, Bachtiar, et al., 2011). Stagg and colleagues found no relationship between MRS measures of GABA and TMS measures of synaptic $GABA_A$ (SICI) or $GABA_B$ (long-interval intracortical inhibition (LICI)), suggesting that synaptic GABA doesn't make up a large proportion of the concentration measured during MRS (Stagg, Bestmann, et al., 2011). Interestingly, the slope produced during a protocol involving 1ms interstimulus interval SICI correlated with MRS-GABA (Stagg, Bestmann, et al., 2011). As a $GABA_A$ agonist did not block the effect of this SICI protocol as they do with longer interstimulus intervals, the authors hypothesised that MRS-GABA is more likely a measure of tonic rather than

phasic inhibition, although conclusive evidence is yet to be found (Stagg, Bestmann, et al., 2011; Ziemann et al., 1996).

2.3.2 Ultra-high field MRS

The use of 7T MRS is beneficial when the metabolite of interest is GABA as there is signal overlap with glutamate (Glu), glutamine (Gln), creatine, and N-acetylaspartate (NAA) at lower field strengths, which is minimised by the reduction of peak width at higher strengths (Puts & Edden, 2012). Furthermore, GABA is present in relatively low concentrations, meaning the high signal-to-noise ratio of 7T MR aids in its quantification (Puts & Edden, 2012).

2.3.3 GABA-edited sequences

GABA has three multiplets in its spectrum which arise from effects on the magnetic fields experienced by the three methylene groups due to their close proximity to one another (Puts & Edden, 2012). These signals are coupled to one another and so the use of a pulse that selectively inverts one of these multiplets (e.g. 1.9ppm) means the other peaks (e.g. 3.0ppm) will also be affected, but the signals from overlapping metabolite signals will not (Juchem & Rothman, 2014; Puts & Edden, 2012). Therefore, subtracting the spectra from two scanning sessions, one with and one without selective inversion (j-difference editing), will maximise the GABA signal and minimise the signal arising from other metabolites (Juchem & Rothman, 2014; Puts & Edden, 2012). Although subtraction artifacts can arise if there are movement differences between the experiments, the effects should be minimal in healthy controls (Puts & Edden, 2012).

2.4 Median Nerve Stimulation

The median nerve is a division of the brachial plexus (Murphy & Morrisonponce, 2022). This nerve provides motor innervation to the forearm and hand, in addition to sensory innervation of the medial forearm, palm, thumb, index and middle fingers and a portion of the ring finger (Murphy & Morrisonponce, 2022). Sensory information is conveyed via the medial lemniscus pathway, where the fibres synapse in the cuneate nucleus, thalamus and finally the primary somatosensory cortex (Passmore et al., 2014). Median nerve stimulation (MNS) is a non-invasive technique which can manipulate neural activity through electrical stimulation of the median nerve. Stimulation of the median nerve above the motor threshold can evoke a sensory evoked potential/field (SEP/SEF) (Baumgartner et al., 1991; Kakigi, 1994) and induce mu/beta desynchronisation followed by a beta rebound (Neuper & Pfurtscheller, 2001; Salenius et al., 1997; Salmelin & Hari, 1994).

Throughout this thesis, stimulation is delivered to the electrodes positioned on the distal forearm (Figure 2.7) using a Digitimer constant current stimulator model DS7A (Digitimer Ltd, UK) (Figure 2.8) to activate the abductor pollicis brevis (APB) using rectangular pulses with a width of 0.2ms. The anode is placed distally and the cathode proximally with electrode gel being used to aid conduction. The stimulation intensity is increased until the motor threshold has been reached and a visible thumb movement is seen. It is important to ensure that the participant does not find this intensity painful. During combined MNS-MEG, triggers can be sent at the start of each trial, via the parallel port, to the data acquisition computer which will aid in the definition of active and control windows during data analysis.

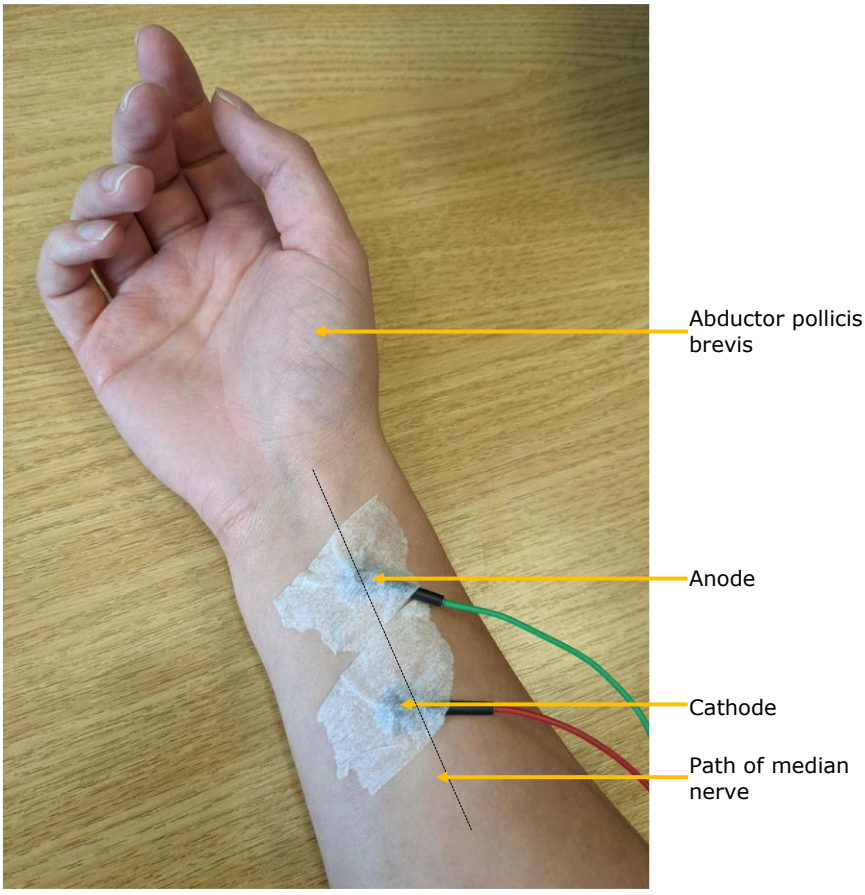

Figure 2.7. *Placement of MNS electrodes.*
Electrodes are placed over the median nerve, with the cathode placed proximally.

Figure 2.8. *The Digitimer Constant Current STIMULATOR model DS7A.*

Chapter 3: Using subjective urge ratings to identify the neural correlates of the urge-to-blink

3.1 Introduction

In contrast to other movement disorders, many TS patients can temporarily suppress their tics (Robertson, 2011). However, the majority of patients experience unpleasant sensations which build in intensity until the tic is released (Kwak et al., 2003; Leckman et al., 1993). These urges can manifest as sensations of pressure, itching, numbness or aching (Kwak et al., 2003; Woods et al., 2005), and are often used in behavioural therapies to predict and pre-empt tics (Azrin & Nunn, 1973). Despite being a common symptom in the adolescent and adult TS population, children under the age of 10 do not tend to report feelings of PU (Leckman et al., 1993). It is unknown whether this indicates that urges are not necessary for tic generation, as tics can also occur during sleep (Cohrs et al., 2001), or if this finding is simply due to the complex language needed to describe these feelings (Leckman et al., 1993). One key mechanistic question is whether tics are voluntary and function to alleviate PU (Leckman et al., 1993), which could act as a negative reinforcer of tic behaviour (Capriotti et al., 2014), or whether urges arise due to the act of suppression, much like the sensation experienced when suppressing a yawn (S. R. Jackson et al., 2011).

Previous research into the generation of tics and PU has suggested the involvement of separate networks. An fMRI study by Bohlhalter and colleagues showed that the primary sensorimotor cortex and the cerebellum are active at tic onset (Bohlhalter et al., 2006). Whereas the insula and premotor regions are active just before a tic, suggesting either an involvement in PU or in movement preparation (Bohlhalter et al., 2006). A recent study found that the grey matter value of voxels in the posterior right insula showed a negative association with motor tic severity scores (S. R. Jackson et al., 2020). Whereas a region in the anterior dorsal/mid insula was positively correlated with PU scores, suggesting that different portions of the insula may have different roles in tics and urges (S. R.

Jackson et al., 2020). It has been theorised that the urge-to-act may involve a loop comprising the anterior insula, the MCC and the mid-insula (S. R. Jackson et al., 2011), where activation of this pathway would lead to urge sensation, initiation of an action in response to the urge and finally assessment of whether the urge has been fulfilled.

Research looking at smoking behaviour showed that patients with brain injuries involving the insula were more likely to report a reduction in the urge-to-smoke compared to smokers with damage in other loci (Naqvi et al., 2007). Furthermore, sensations such as scratching, numbness, and warmth in distinct body parts can be elicited with direct stimulation of the contralateral insula (Penfield & Faulk, 1955). The anterior insula is known to be involved in interoceptive processing; therefore PU may manifest due to increased awareness of internal sensations (Craig, 2002, 2009). Similarly, it has been proposed that the mid-insula has a role in subjective feelings relating to movement and therefore could establish whether the urge-to-act has been fulfilled (Craig, 2009; S. R. Jackson et al., 2011). On the other hand, complex motor responses can be evoked by stimulation of the anterior MCC, which demonstrates that the region could have a role in the execution of actions performed in response to an urge (Caruana et al., 2018; S. R. Jackson et al., 2011).

The neural correlates of the urge-to-move have also been investigated in healthy participants in paradigms involving the suppression of common behaviours, such as blinking and yawning (Berman et al., 2012; Lerner et al., 2009; Mazzone et al., 2010; Nahab et al., 2009; Yoon et al., 2005). These behaviours give rise to an urge similar to those described by TS patients. Data from such experiments are analysed to identify associated regions either through block comparison or through attempts to model the expected pattern of urge (Berman et al., 2012; Botteron et al., 2019). A variety of areas including the cingulate cortex, insulae, prefrontal cortex (PFC) and temporal gyri show activation associated with urges (Berman et al., 2012; Lerner et al., 2009; Mazzone et al., 2010; Nahab et al., 2009; Yoon et al., 2005). Using a meta-analytic approach, Jackson and colleagues showed that there is an overlap in activity in the MCC and the

right insula during the urge-to-act in healthy participants for a variety of behaviours and the urge-to-tic in patients (S. R. Jackson et al., 2011). Therefore, when investigating the network involved in PU, blinking can be used for analogous investigation in healthy controls (S. R. Jackson et al., 2011).

The issue with investigating PU is that, due to their temporal correlation, it is hard to distinguish urge from the motor preparation before a tic is performed. Furthermore, due to the need for participants to remain still during fMRI studies, paradigms usually involve tic suppression. Whilst suppression allows feelings of urge to be isolated from those of tic generation, it also means that there are no observable events which can be used to determine when feelings of urge are high and, mechanisms involved in tic suppression will be present in the results.

To separate the networks involved in urge and action suppression, we will investigate the urge-to-blink in healthy controls performing a blink suppression paradigm. Subjects will be asked to continuously rate feelings of urge so that the BOLD signal can be modelled based on these subjective ratings, to allow us to identify a network associated with urge. We will also compare 'Okay to blink' and blink suppression blocks to highlight regions involved in action suppression, where we expect to show activation in the right IFG (Aron et al., 2004, 2014). Understanding the regions involved in the suppression of actions and the related experience of PU may help us to understand disorders such as TS, where this process is disrupted (Lerner et al., 2009).

3.2 Methods

3.2.1 Participants

Twenty-two healthy participants were screened for counter indications for MRI, use of medication and history of neurological or psychiatric disorders. One participant (male, 21 years old, right-handed) was excluded prior to analysis due to a technical issue which led to loss of their fMRI data and one participant (female, 28 years old, right-handed) was excluded during analysis due to excessive movement. Handedness for the remaining

twenty subjects (13 female, mean age (± standard deviation (SD)) = 28 ± 5.2 years) was determined using the Edinburgh Handedness Inventory (18 right-handed, 1 left-handed, 1 ambidextrous) (Oldfield, 1971). Subjects gave informed consent and the experimental paradigm received local ethics committee approval.

3.2.2 Behavioural Task

All subjects underwent three 7-minute fMRI runs of the same task. The task was based on Psychopy code used in a previous study by Brandt and colleagues which recorded real-time urge ratings (Brandt et al., 2016; Peirce et al., 2019). Eyeblinks during each run were captured using a MR compatible camera "12M-i" with integrated LED light mounted on the head coil (MRC systems GmbH) (half frame rate=60Hz). A projected screen displaying the task was visible by a mirror positioned above the participants' eyes (Figure 3.1). For the first 30 seconds an instruction was displayed to move a MR compatible trackball (Cambridge Research Systems) (sampling rate of 10Hz) randomly using their right-hand ('Random'). This was followed by alternating 60 second runs of 'Okay to blink' and 'Suppress'; during these conditions participants continuously rated their urge-to-blink on a scale of 0-100 while following instructions to either blink normally or to suppress their blinks respectively. For the last 30 seconds of the run the 'Random' baseline was repeated. Participants were instructed to pay attention to the instructions displayed at the top of the screen and during the 'Suppress' condition to return to suppressing their blinks should any escape blinks occur (Berman et al., 2012; Lerner et al., 2009; Stern et al., 2020). Previous studies have shown that 60s of action suppression is achievable and induces feelings of urge (Lerner et al., 2009; Stern et al., 2020). The order of 'Okay to blink' and 'Suppress' blocks was randomly counterbalanced to reduce order effects, with 50% of participants starting with suppression following the initial baseline. All participants moved the rollerball using their right hand regardless of hand dominance.

SPSS version 27.0 was used for statistical analysis of behavioural data. Differences between blocks were calculated using paired t-tests. The

behavioural blink data did not meet the assumptions for parametric testing and therefore a Wilcoxon signed-rank test was used. The level for significance was one-tailed and set at $p \leq 0.05$.

Before image analysis, the urge data were down-sampled from 10Hz to 1Hz and then standardised. This process was completed for the random and experimental conditions for each run in each subject separately.

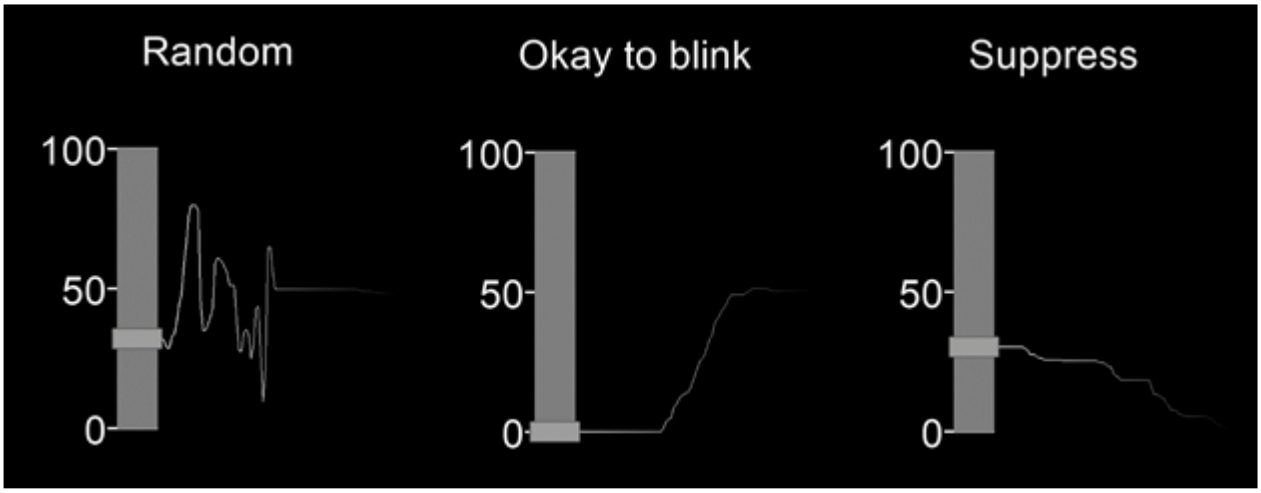

Figure 3.1. *The real-time urge task display.*

A figure displaying the real-time urge monitor, with urge rated on a scale of 0-100 and instructions for each condition displayed above.

3.2.3 Temporal relationship between urge and blinks

To investigate whether urge intensity was associated with the likelihood of blink occurrence, we followed a method similar to that used by Brandt and colleagues (2016). The Z-scores were calculated using the urge data from each run separately after the data were down-sampled from 10Hz to 1Hz. For the binary logistic regression, the standardised (Z-score) urge scores were concatenated across participants into separate okay-to-blink and suppress timeseries. Blink occurrence per second was binarized such that the occurrence of a blink was recorded rather than the number of blinks.

To look at the changes in urge around a blink, we extracted 5-seconds before and after each blink. The blinks for the first 5s of each block were discarded to allow the level of urge to adjust and the last 5s of blinks were discarded so that the average urge around blinks would not be affected by

the change in block. These data were averaged to give a single time-series for each participant for the suppression and okay to blink blocks separately. The peak latency, skewness and excess kurtosis of these distributions were investigated using one-sample t-tests to investigate the temporal characteristics of urge using MATLAB (MATLAB R2020a, Mathworks, Natick, MA). Where data failed tests for normality a Wilcoxon signed-rank test was used. Curvilinear regression analysis was applied using SPSS version 27.0, to investigate whether the average urge intensities (Z-score) around the blink in each condition followed a quadratic relationship.

3.2.4 Image Acquisition

The fMRI data were acquired using a Philips 3T Ingenia MRI scanner (Philips Healthcare, Best, The Netherlands) with a 32-channel head coil situated in the Sir Peter Mansfield Imaging Centre, Nottingham UK. Multi-echo sequencing was completed using matrix size = 64x64; FOV = 192x192x135mm; 45 slices; in-plane resolution 3mm; TR = 1800ms; TE = 12ms, 35ms, 58ms; flip angle = 80°; bandwidth = 2150.8khz. The functional T2* weighted scan was followed by a structural MP2RAGE image scan acquired using matrix size = 256x256, FOV = 192x192x135mm, 1mm cubed isotropic resolution, TR = 7.1ms, TE = 3.11ms, flip angle = 80°.

3.2.5 Image Preprocessing

Runs with an absolute mean displacement above 1.5mm were discarded, resulting in all 3 runs from one participant (female, 28 years old, right-handed), 1 run from five participants and 2 runs from one participant being removed from the analysis. One further run from one participant was removed due to loss of video data meaning the blink timings could not be defined. The SNR of the fMRI timeseries (tSNR) for each run was calculated using an in-house MATLAB app (MATLAB R2018b, Mathworks, Natick, MA) (https://github.com/nottingham-neuroimaging/qa/tree/master/fMRI_report_app) (Figure A.1 in Appendix A). If found, scans with a tSNR below 30 would have been excluded.

The first echo for each fMRI run was motion corrected using MCFLIRT (motion correction with FMRIB's linear image registration tool) using the middle volume as the reference (M. Jenkinson et al., 2002). This same transformation was then applied to echoes 2 and 3. Next, multi-echo independent component analysis (ME-ICA) was run using Tedana with the Akaike information criterion (AIC) method being used to select the components (Community et al., 2022; DuPre et al., 2021; Kundu et al., 2012, 2013). Rica was used to visualize and manually classify any components that had been misclassified or ignored by Tedana (Uruñuela, 2021). After, Tedana was rerun using a list of the manually accepted components. The resulting de-noised datasets were then pre-processed using FSL (FMRIB software library) (M. Jenkinson et al., 2012). Pre-processing involved the use of a high-pass filter to remove any signals below 0.0083Hz from the fMRI data. Images were spatially smoothed using a Gaussian kernel of 5mm FWHM (full width at half maximum) to increase the signal-to-noise ratio and to account for any major anatomical differences between subjects. Following pre-processing, activation maps for the first echo were normalised to MNI space and the same transformation was then applied to the second and third echoes. It is assumed that the activation of voxels in the ventricles is due to noise, therefore the principal components of activation within voxels containing cerebrospinal fluid (CSF) were computed. The five largest components were then removed from the data during de-trending (Cox, 1996; Cox & Hyde, 1997).

3.2.6 Standard Image Analysis

Using AFNI, the three echoes were optimally combined to produce a weighted average fMRI dataset (Cox, 1996; Cox & Hyde, 1997). ICA-based de-noising was implemented during preprocessing rather than including the standard and extended motion parameters in the GLM as regressors of no interest. Volumes with a frame-wise displacement above 0.9mm were scrubbed.

Within the FSL GLM design matrix, three boxcar models were used to define the onset and durations of each ‘Random’, ‘Suppress’ and ‘Okay to

blink' block. Parametric regressors were defined for the standardised (Z-score) urge scores for the random baseline and experimental periods separately. A further regressor was used to define the onset times and durations for blinks. All regressors were convolved with a double-gamma HRF. In the first-level analysis, data from each run for each subject were analysed separately. Contrasts were set up to compare the 'Okay to blink' and 'Suppress' blocks ('Suppress' > 'Okay', 'Okay' > 'Suppress') and the experimental blocks where urge was rated continuously were compared to the baseline 'Random' condition to account for activity related to moving of the rollerball (urge > 'Random', 'Random' > urge). Finally, the activity relating to blinks and urge were compared to separate the activity relating to the blink from that of high urge (urge > blink, blink > urge). At the second-level, results from the first-level analysis were averaged across runs for each subject. Finally, at the third-level mixed effects analysis was used to average across subjects. The results were corrected at the cluster level with a Z threshold of 3.2 ($p<0.05$). Regions were identified using the Harvard-Oxford cortical and subcortical structural atlases, as well as the cerebellar atlas in MNI152 space after normalization with FLIRT (FMRIB's linear image registration tool).

3.3 Results

3.3.1 Behaviour

All blinks in each run were first annotated by one rater, then a random 60 second block from each run was annotated by a second rater using ELAN (MH, IM, KD), with an average agreement of 95.51% ± 10.13 (mean ± SD) (*ELAN*, 2019). Any blink discrepancies were discussed until there was agreement for all blink occurrences. The average number of blinks per minute in the 'Okay to blink' condition was 31.20 ± 3.63 (mean ± standard error of the mean (SEM)) while in the suppression condition this was significantly ($t_{(20)}$ = -4.249, $p<0.001$) lower with 5.12 ± 0.81 blinks. The average urge per minute was 22.79% ± 4.00 and 55.62% ± 3.42 for 'Okay to blink' and 'Suppress' blocks, respectively. The difference between the urge in the two conditions was highly significant ($t_{(20)}$ = -10.901, $p<0.001$). These findings indicate that participants successfully followed

instructions to suppress blinks and that this was associated with an increased urge-to-blink.

Figure 3.2 shows examples of runs from two different subjects, urge is shown to rise during the period of suppression, with urge temporarily decreasing following 'escape' blinks. However, while for some subjects urge flattened throughout periods where blinking was okay (Figure 3.2B), others reported small increases in urge prior to blinks (Figure 3.2A), although the magnitude this reached before a blink was released was lower than that seen in the suppression blocks.

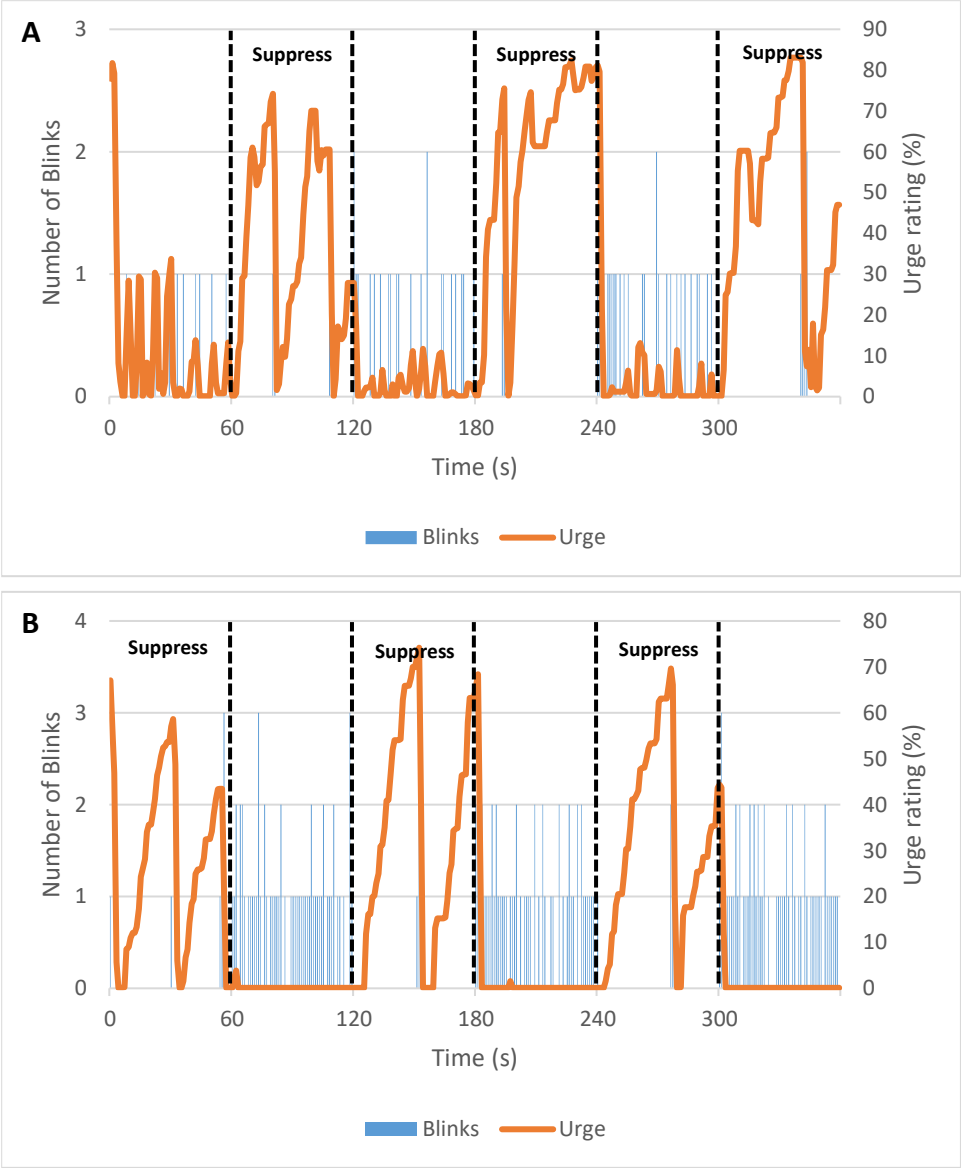

Figure 3.2. *The association between the urge-to-blink and blinking.*

Graphs displaying blink timings for individual task runs from two subjects alongside their subjective urge rating across time.

3.3.2 Temporal relationship between urge and blinks

A binary logistic regression showed that only 0.6% of the variance in blink occurrence during 'Okay to blink' could be explained by changes in subjective urge ratings (Cox & Snell $R^2 = 0.006$, $\chi^2(1) = 53.667$, $p < 0.001$; Exp(B) = 0.806, Wald(1) = 107.279, $p < 0.001$). Due to the scarcity of blinks in the 'Suppress' condition, all instances of blinks were classified as outliers by the model and so the data were not appropriate for this type of analysis.

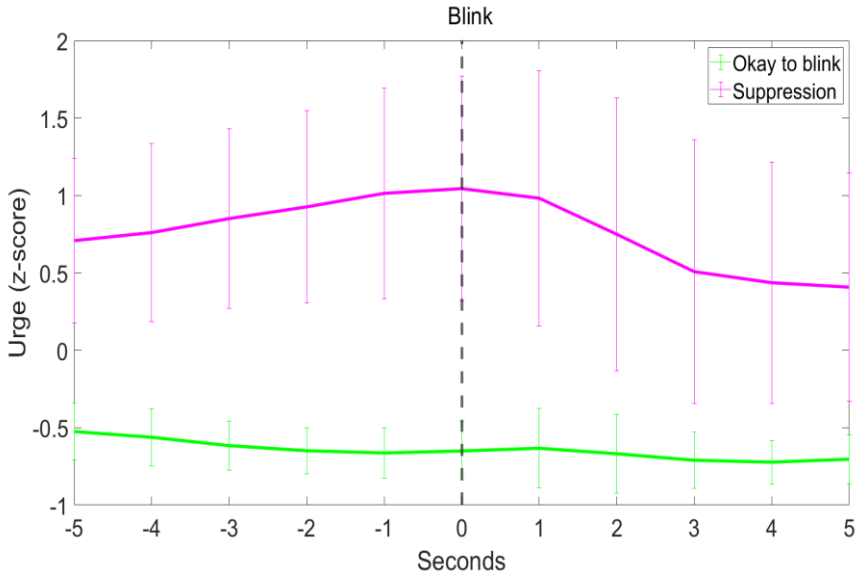

Figure 3.3. *The distribution of urge around a blink.*

A curvilinear regression showed that the mean urge around blinks followed a significant quadratic distribution over time in both the 'Okay to blink' ($F(2,8) = 27.279$, $p < 0.001$, Adjusted $R^2 = 0.840$) (Estimated urge = -0.661 - 0.017 * (time to blink) + 0.001 * (time to blink)^2) and 'Suppress' conditions ($F(2,8) = 26.192$, $p < 0.001$, Adjusted $R^2 = 0.834$)(Estimated urge = 0.948 - 0.038 * (time to blink) – 0.019 * (time to blink)^2).

In the 'Okay to blink' condition, urge intensity peaked significantly before the blink (-3.55 s ± 2.52 (mean ± sd), $z(19) = -3.68$, $p < 0.001$), whereas in the 'Suppress' condition urge peaked at blink onset (0.56 s ± 2.87, $z(17) = 0.89$, $p > 0.05$). There was no significant skew in the suppression condition (0.01 ± 0.75, $t(17) = 0.06$, $p > 0.05$) but in the free blinking condition, urges were slower to decrease than they were to increase before the peak (0.78 ± 0.62, $z(19) = 3.58$, $p < 0.001$). While there was no significant kurtosis in the 'Okay to blink' condition (2.84 ± 0.98, $z(19) = -1.57$, $p > 0.05$), the distribution of urge around the blink in the suppression condition was broader than that of a normal distribution (2.16 ± 1.27, $z(17) = -2.90$, $p < 0.01$). Two subjects were not included in the curvilinear regression and the temporal characteristics analysis for the 'Suppress' condition due to having no 'escape' blinks.

3.3.3 Block Analysis

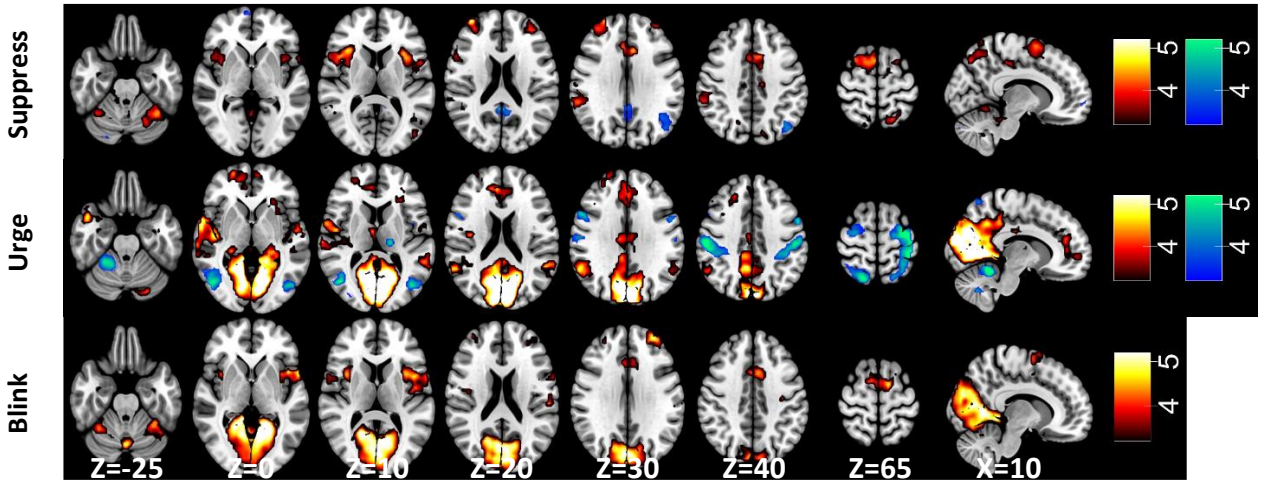

Figure 3.4. *BOLD response associated with blink suppression, urge-to-blink and blinking.*

Statistical maps overlaid onto the MNI152 brain showing significant activations for the (top) 'Suppress' > 'Okay' (red), 'Okay' > 'Suppress' (blue); (middle) Urge > 'Random' (red), 'Random' > Urge (blue); (bottom) Blink > Urge (red) contrast. Statistical maps were thresholded at Z=3.2 (p<0.05).

For the contrast of 'Suppress' > 'Okay to blink', significant activations were identified with peaks in the dorsolateral prefrontal cortex (DLPFC), lateral occipital cortex, cerebellum, opercular cortices, supramarginal gyrus (SMG) and posterior cingulate (PCC) (Figure 3.4). Notably, significant activations were found in the left primary somatosensory cortex, MCC, SMA and bilateral insulae. When contrasting 'Okay to blink' > 'Suppress', clusters were identified in the frontal orbital cortex, lateral occipital cortex, PCC, middle frontal gyrus and a small area in the cerebellum (Figure 3.4). Locations of clusters local maxima for all experimental block comparisons are defined within Table B.6 and Table B.7 in Appendix B.

3.3.4 Urge analysis

For the contrast of urge > 'Random', significant activations were identified in the medial occipital cortex, opercular cortex, ACC, bilateral insulae and cerebellum (Figure 3.4). When contrasting 'Random' > urge, clusters were identified in the bilateral sensorimotor cortices, lateral occipital cortex, cerebellum, left thalamus, opercular cortex and insulae (Figure 3.4). Locations of clusters local maxima for all urge comparisons are defined

within Table B.8 and Table B.9 in Appendix B. In Figure 3.5, the activations associated with the contrast urge > 'Random' are visualised alongside those associated with 'Suppress' > 'Okay to blink' and blink > urge showing an overlap between blinking and suppression in the MCC and SMA, while the ACC is associated with the urge-to-blink. Notably, there is a differentiation in insula involvement with a dorsal-anterior portion involved in suppression and blinking, a central portion involvement in blinking and posterior and ventral-anterior regions being active during feelings of urge-to-blink (Figure 3.5).

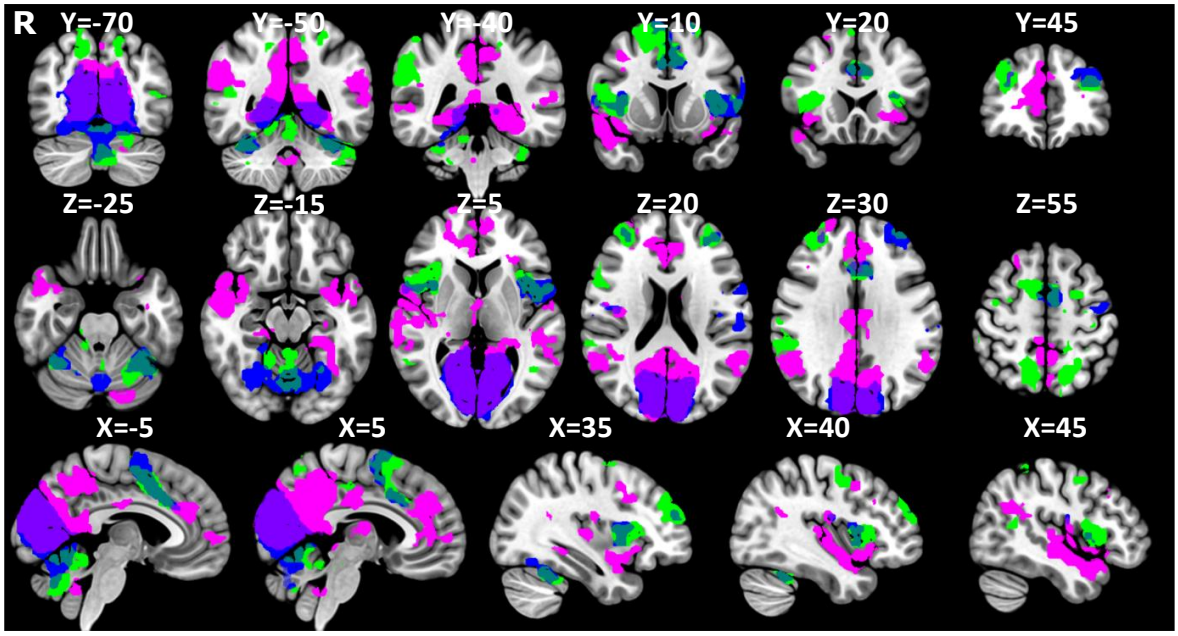

Figure 3.5. *Separate networks for urge-to-act and action suppression.*

Masks of significant activation for the 'Suppress' > 'Okay' (green), Urge > 'Random' (pink) and Blink > Urge (blue) contrasts overlaid onto the MNI152 brain.

3.3.5 Blink analysis

For the contrast blinks > urge, there were significant activations in the medial occipital cortex, MCC, opercular cortex, insulae, DLPFC, SMA and left primary sensorimotor cortex (Figure 3.4). No regions were identified by the urge > blinks contrast. Locations of clusters local maxima for the blinks > urge contrast are defined within Table B.10 in Appendix B.

3.4 Discussion

This fMRI study investigated the urge-to-blink using a conventional block analysis and a parametric model of subjective urge ratings, with the aim of disentangling the anatomical correlates of the urge-to-blink from those of action suppression.

3.4.1 Behavioural

Previous attempts to model the urge-to-blink have either employed a sawtooth model (Berman et al., 2012), where urge builds up linearly across the suppression block before decreasing, or an event-related model (Botteron et al., 2019), where urge decreases following escape blinks in the suppression block. Here, the representative examples of continuous urge ratings during the task show that blinking, particularly during suppression blocks, causes a temporary decrease in urge intensity. Therefore, although sawtooth models are likely better at approximating urge compared to a block analysis (Berman et al., 2012), they are still too simplistic as they do not consider escape blinks during suppression. More recent models which take account of these 'escape' blinks, such as the event-related approach suggested by Botteron and colleagues, more accurately represent real time urge ratings (Botteron et al., 2019). If applied to fMRI data, the model could theoretically identify neural correlates of the urge-to-blink relatively well. However, this approach would not be appropriate in the analysis of the urge-to-tic where overt expression of the behaviour would be suppressed during scanning, highlighting the need for continuous urge rating or another modelling approach. On the other hand, the process of reporting the continuous urge ratings could introduce confounds into the results due to movement and attention being directed towards feelings of urge.

During the suppression blocks, urge showed a quadratic relationship around blinks indicating that urge increases during suppression but diminishes after the blink. This is further supported by the urge peaking at blink onset. While the 'Okay to blink' blocks also showed a significant quadratic relationship, urge did not peak at blink onset. Furthermore, blink occurrence could not be predicted by the urge score in 'Okay to blink' blocks. This suggests that in the case of blinking in healthy participants, urge arises due to the act of suppression. Brandt and colleagues (2016) also found a significant quadratic distribution of urge in both the free to blink and suppress conditions. However, in contrast to our findings, they showed the peak in urge was coincident with the blink in the free blinking condition but prior to the blink in the suppress condition.

3.4.2 Urge-to-blink

The regions identified using the urge model included the insulae and ACC. These regions are commonly implicated in studies of urge, therefore the right insula and cingulate cortex are thought to be key nodes in the urge network (S. R. Jackson et al., 2011).

Activation of the insula has been linked to various urge sensations such as those related to ticcing (Bohlhalter et al., 2006; Neuner et al., 2014), blinking (Abi-Jaoude et al., 2018; Berman et al., 2012; Lerner et al., 2009) and yawning (S. R. Jackson et al., 2011). Patients with OCD show increased insula activity during early blink suppression compared to controls (Stern et al., 2020). Furthermore, PU severity has shown a negative association with the volume of left insular grey matter thickness in TS patients (Draper et al., 2016).

Subregions of the insula are thought to have differing functions (Kelly et al., 2012; Kurth et al., 2010). The posterior insula has a role in the initial processing of both noxious and non-noxious somatosensory stimuli (Ostrowsky et al., 2002), whereas the anterior insula integrates information from several functional systems to bring about interoceptive awareness (Craig, 2009; Kurth et al., 2010). In agreement with this concept of a functional division, our data suggest that the posterior insula is involved in the processing of urge sensations as has been theorised previously (Tinaz et al., 2015). Information is thought to flow in a hierarchical fashion from the posterior insula to the anterior insula, with initial sensory processing in the posterior portion and progressive integration of information in the anterior portion to give a final representation that incorporates all the task information (Craig, 2009; Craig et al., 2000). Here, the ventral-anterior insula was also associated with urge, and this subregion has been shown to be linked with emotional processing (Kelly et al., 2012; Kurth et al., 2010). Similarly, stimulation of the pregenual ACC has been shown to induce emotional, interoceptive and autonomic experiences (Caruana et al., 2018). Analysis of the functional connectivity of the insula has indicated that the ventral-anterior subregion is connected to the rostral ACC within a limbic network that is associated

with emotional salience detection (Cauda et al., 2011). On the other hand, the posterior insula is connected to sensorimotor regions within a network involved in response selection (Cauda et al., 2011). Therefore, it could be that somatosensory urges are processed by the posterior insula, and through integration of information in the ventral-anterior insula and ACC, these urges become emotionally salient, which perhaps draws attention to their uncomfortable nature. Meanwhile, functional connections between the posterior insula and sensorimotor regions, including the MCC and SMA, may lead to either the continuation of suppression or to the release of a blink in response to the urge sensation.

Along with the previously described regions, the medial occipital cortex was also shown to be involved in feelings of urge and during blinks. We hypothesise that this activation is specific to the urge-to-blink rather than the general urge network. Activation of the occipital cortex has been seen in previous studies looking at the urge-to-blink (Berman et al., 2012; Stern et al., 2020; Yoon et al., 2005), but it has not been described in relation to other forms of the urge-to-act (Bohlhalter et al., 2006; S. R. Jackson et al., 2011). This activation could be due to a loss of visual input during blinks (Nakano et al., 2013). However, as activation of this region is also seen when blinking in the dark (Golan et al., 2018), we think there may be a combined effect of the medial occipital cortex receiving motor efferents when a blink is likely to occur, for instance, when the urge-to-blink is high (Bristow et al., 2005).

We assumed that the regions which showed greater activity in the 'Random' > Urge contrast were associated purely with the movement of the rollerball device. As such this was used as an active baseline to tease apart activity related to urge from that of movement. However, participants moved the rollerball more during the random condition than they did during the experimental blocks, and as such this active baseline was not perfect. The higher activity seen in the cortical and cerebellar (lobules I-VI and VIII (Guell et al., 2018)) sensorimotor regions in the 'Random' > Urge contrast was likely due to this increased movement.

3.4.3 Suppression of action

A meta-analysis looking at the neural correlates of response inhibition identified the IFG (pars opercularis), SMG, SMA, MCC and bilateral insulae amongst other regions involved in action suppression (R. Zhang et al., 2017). These regions were also found to be active in our 'Suppress' > 'Okay' contrast, and the network bears a striking resemblance to the executive control network (Beckmann et al., 2005).

The 'Suppress' > 'Okay' contrast identified the dorsolateral PFC, which is thought to be involved in cognitive control (Miller & Cohen, 2001) and has previously been shown to be active to a higher degree in TS patients compared to healthy controls during blink inhibition (Mazzone et al., 2010). Therefore, this area may coordinate regions in a top-down manner to achieve the goal of blink suppression (Miller & Cohen, 2001). We also see that the activation of the insula/operculum extends into the IFG (pars opercularis), which is not surprising given its central role in the motor response inhibition network (Aron et al., 2004, 2014). More recently, Abi-Jaoude and colleagues found that the left DLPFC and left IFG showed higher activity in participants with fewer 'escape' blinks suggesting the regions play a role in successful suppression (Abi-Jaoude et al., 2018). The cerebellum has been hypothesised to have a complementary role in motor inhibition (Picazio & Koch, 2015). A TMS study showed that a conditioning pulse to the right lateral cerebellum 5-7ms prior to electrical stimulation of the left motor cortex resulted in a decrease in MEP amplitude (Ugawa et al., 1995). On the other hand, the higher cerebellar activity in lobules I-VI and VIII during suppression could be due to more variation in the urges being reported during these blocks, in comparison to when blinking was okay, meaning more hand movement was required to rate them (Guell et al., 2018).

As previously mentioned, the anterior insula is involved in multimodal integration and salience (Craig, 2009; Kurth et al., 2010). The activation seen during suppression was in the dorsal-anterior segment, which has been associated with cognitive processing (Kelly et al., 2012; Kurth et al., 2010). Notably, in a meta-analysis by Kurth and colleagues the dorsal-

anterior region was the site which was commonly active across task modalities except sensorimotor (Kurth et al., 2010). Therefore, it may be that suppression of an action involves integration of task information so that the automatic response to blink during periods of increased discomfort can be inhibited in blocks of suppression.

The insula and ACC (which includes the MCC in older descriptions) are theorised to be the limbic sensory and motor regions respectively (Craig, 2009; Craig et al., 2000) and are commonly co-active in studies of urge (Abi-Jaoude et al., 2018; Berman et al., 2012; Bohlhalter et al., 2006; S. R. Jackson et al., 2011; Lerner et al., 2009; Mazzone et al., 2010). The MCC has previously been suggested to have a role in selecting an action in response to urge sensations, as intra-cortical stimulation of the MCC induces complex motor responses (Caruana et al., 2018; S. R. Jackson et al., 2011). Movement can also be evoked though stimulation of the SMA (Fried et al., 1991), and in some cases it also induces feelings of urge, which may explain why its activation has frequently been associated with blink suppression (Berman et al., 2012; Lerner et al., 2009). As both the MCC and SMA were active during blinks as well as suppression blocks, these nodes may decide whether to release suppressed behaviours in response to feelings of urge. Similarly, blinks in suppression blocks may involve more influence from these pre-motor regions (Berman et al., 2012). This could be investigated in the future through comparison of blinks in suppress and free to blink conditions. Alternatively, activation of these regions during 'Suppress' blocks could relate to the effort participants exert to keep their eyes open (Lerner et al., 2009).

3.4.4 Blinking

Insular activation during blinks was restricted to the dorsal anterior insula and the mid-insula. As previously mentioned, the dorsal anterior activation may be linked with task-related integration of information, such as whether blinking was 'allowed' during the task block (Kurth et al., 2010). We hypothesise that the mid-insula activation is linked to the movement and sensory aspects of blinking due to its perceived role in somesthesis (Kelly et al., 2012; Kurth et al., 2010).

The DLPFC was active during blinks, which may relate to the task focusing on blinking and deciding when to blink in relation to this. This region has been shown to be more active during self-initiated blinks and therefore may relate to a conscious decision to blink (Van Eimeren et al., 2001). The DLPFC has not been identified in previous studies looking at the regions associated with blinking during a blink suppression paradigm (Berman et al., 2012; Lerner et al., 2009; Mazzone et al., 2010; Yoon et al., 2005), but most studies did not include event-related analysis of blinks and no studies have required participants to focus on their urges in order to give subjective ratings.

3.5 Conclusion

In summary, this study suggests that the urge-to-act network is composed of regions involved in sensory processing and salience, while the action suppression network includes regions involved in executive control and response inhibition. The main findings of this chapter are that separable regions within the insula contribute to different networks and there is a network overlap in the MCC and SMA that may act to determine when to perform a suppressed motor action. These are novel findings stemming from continuous measurement of urge, which allowed the two networks to be separated. The use of continuous subjective urge measurement could be used in fMRI studies involving disorders associated with urge such as TS, OCD, and addiction to investigate whether there is common disruption of the network associated with urge. Understanding what regions are involved in suppression and urge could also allow us to investigate how these regions interact before tics, as well as how they interact when a tic is successfully suppressed. However, the movement involved in this continuous urge rating affected the results due to activation of sensorimotor regions, meaning that we could not reliably ascertain whether these regions have a role in urge. Furthermore, the act of rating the urge itself could have affected how the participants experienced urge and therefore the BOLD response associated with it. A model free approach where the regions involved in urge and suppression could be identified

without the need for subjective urge ratings would be ideal. This approach is explored in Chapter 4.

Chapter 4: Validating the use of paradigm free mapping to identify the neural correlates of urge

4.1 Introduction

In the previous chapter, Chapter 3, we showed that the posterior and ventral-anterior insula, ACC and medial occipital cortex were involved in the urge-to-blink whilst the dorsal-anterior insula, DLPFC, MCC and SMA were involved in blink suppression. These regions were identified using a conventional GLM approach involving three boxcar models and a novel parametric regressor for continuous subjective urge ratings.

Conventional GLM involves averaging across many trials to increase the SNR, but this assumes that the response is the same for every trial and that the timings are known a priori to establish the hypothesised model. Events such as tics and urges in TS are not predictable and so the onset times cannot be specified in advance. These events also differ in duration and behaviour across time, therefore it may be inappropriate to average many events together.

Paradigm free mapping (PFM) is a deconvolution approach, where the neuronal activity which forms the basis of the BOLD response can be estimated without prior knowledge of event timings or durations by solving an inverse problem (Gaudes et al., 2013; Uruñuela et al., 2020). This is of particular interest for TS as tics and urges are spontaneous and vary in duration as well as in phenotype across time and between participants. Usually in fMRI studies looking at the neural correlates of TS, tics are identified post-hoc using video recordings, which is subjective and time-consuming. Regions involved in the urge-to-tic can then be identified by looking at regions that are active just before a tic, but this will also identify regions involved in tic generation. Furthermore, as a high proportion of fMRI data are lost during tics, for example due to concomitant head jerks, experiments usually involve tic suppression meaning that periods of high urge intensity are not overt.

Assuming a linear time invariant system, the BOLD response is assumed to be the neuronal signal convolved with the HRF (+ noise) (Poldrack et al., 2011). PFM works by deconvolving the fMRI signal using the HRF via regularised least-squares estimation to estimate the neuronal-related signal at each voxel (Figure 4.1) (Gaudes et al., 2013; Uruñuela et al., 2020). For each run we can assume that there will only be a few instances of significant BOLD activity in each voxel, therefore we can improve the accuracy of the deconvolution by regularising the estimates, for example maximising the sparsity of the activity-inducing signal (Gaudes et al., 2013).

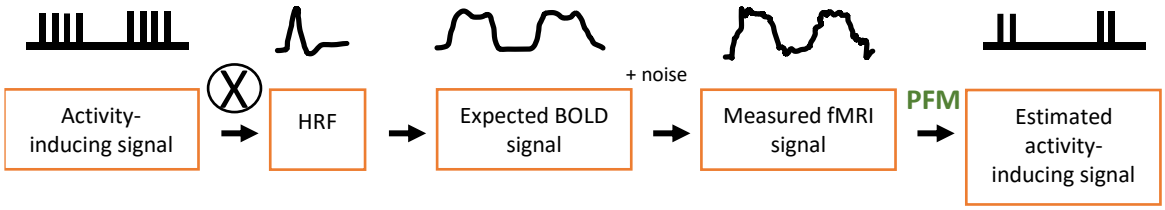

Figure 4.1. *Estimation of the activation timeseries.*

Paradigm free mapping (PFM) involves deconvolving the measured fMRI signal to estimate the activity-inducing signal using a haemodynamic response function (HRF) template (Uruñuela et al., 2021)*. (Figure based on flowchart from* (Uruñuela et al., 2021)).

In this chapter we will re-analyse the data collected in Chapter 3 using the multi-echo version of this sparse paradigm free mapping algorithm (MESPFM) (Caballero-Gaudes et al., 2019) in order to validate the approach before applying it to covert responses such as the urge-to-tic. It is expected that both the conventional and MESPFM analysis of urge will detect regions previously identified as being part of the urge network including the MCC and right insula (S. R. Jackson et al., 2011). If the same regions can be identified without specification of task timings, this would validate the use of MESPFM in fMRI studies involved in characterising urge networks in disorders such as TS and OCD. This is important for TS research as, due to the caveats of movement during conventional neuroimaging, moments of heightened urge cannot be identified, and networks involved in the urge-to-tic and tic suppression cannot be disentangled. Analysis using MESPFM could allow these networks to be separated without the need for continuous urge ratings. Therefore, in future, urge networks could be investigated without any confounds relating

to differing patterns of rollerball movement in different conditions when rating subjective feelings of urge (Chapter 3).

4.2 Methods

4.2.1 Preprocessing

The data were collected and initially preprocessed as described in sections 3.2.4 and 3.2.5 in Chapter 3 during a blink suppression task which involved continuous rating of the urge-to-blink (3.2.2). A summary diagram of these preprocessing steps and the following MESPFM analysis is shown in Figure 4.2. The remainder of the analysis was run using AFNI (Cox, 1996; Cox & Hyde, 1997) on the University of Nottingham's High-Performance Computer. The echoes were detrended using 4 Legendre polynomials, which removed irrelevant nonlinear trends from the data to allow more accurate prediction of the neuronal-related activity using the HRF. The signal percentage change was calculated by dividing the detrended data by the mean of the voxel data for that echo on a voxel-by-voxel basis. Then the data relating to the random baseline at the beginning and end of each run were removed, so that only the six 1-minute blocks of alternating blink suppression and rest remained.

Furthermore, a surrogate dataset was also created by shuffling the data from the six 1-minute blocks of alternating blink suppression and rest, before the signal percentage change was calculated. Shuffling of the data created a new dataset with the same temporal distribution as the original dataset but without the temporal relationships between the timepoints. Therefore, the shuffled dataset acts as a null distribution. If the activation in the original dataset is higher than that seen in the surrogate dataset, then it is unlikely to have happened by chance and can be considered significant.

4.2.2 Multi-echo sparse paradigm free mapping

For MESPFM, the regularization parameter was selected using the Bayesian Information Criterion (BIC) (Caballero-Gaudes et al., 2019). The BIC is a model selection method which assesses the goodness of fit of the model. Specifically, BIC will introduce an increasing penalty for more parameters being included in the model to prevent overfitting (Dziak et al., 2020). The

HRF used for the deconvolution was the SPM canonical HRF (Penny et al., 2007), and the model only considered changes in the transverse relaxation rate (R2*). R2* is a direct measure of the magnetic field inhomogeneity caused by the level of deoxyhaemoglobin in the blood.

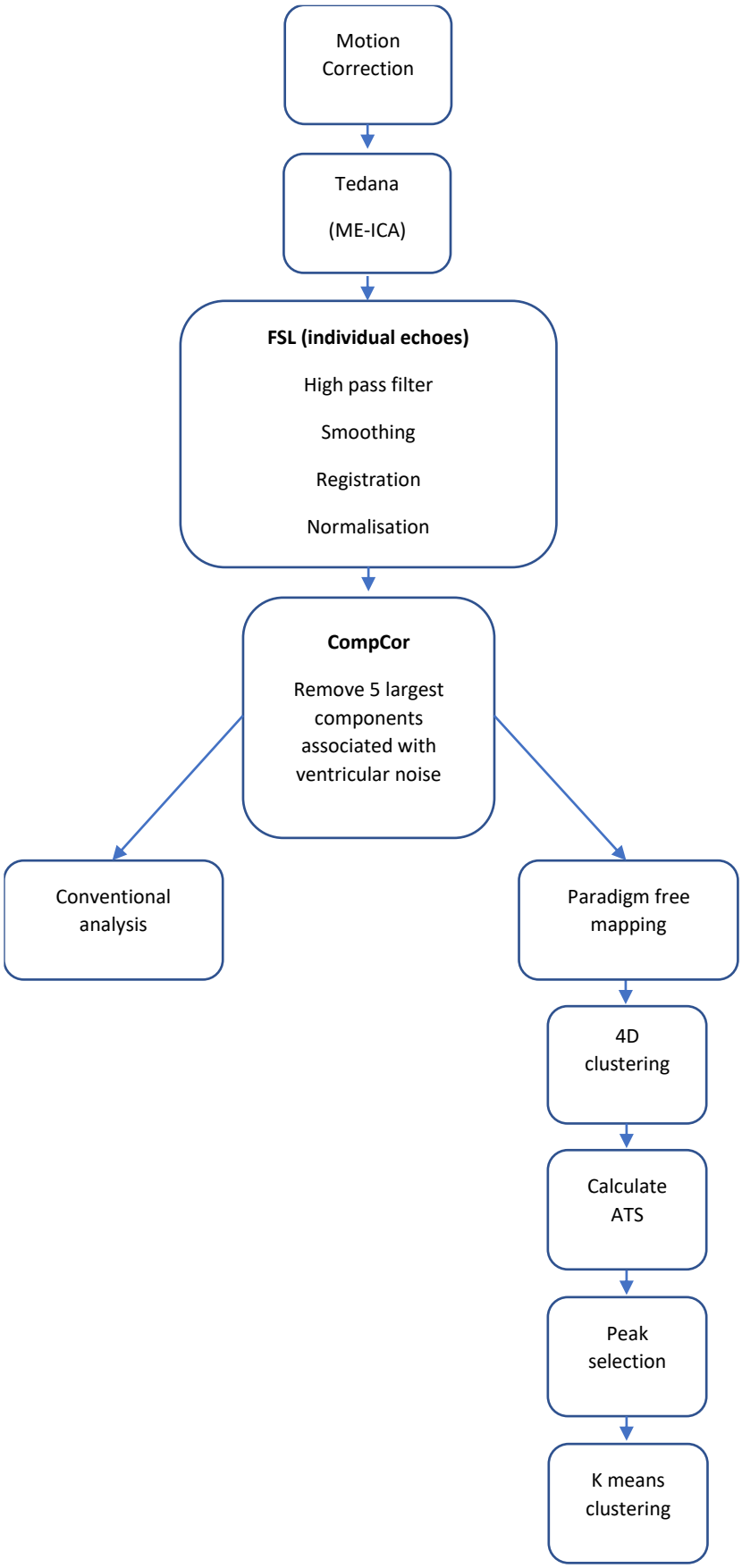

Figure 4.2. *A flow diagram depicting the analysis steps involved in the data preprocessing and the subsequent PFM.*

4.2.3 Activation time series

Following multi-echo sparse paradigm free mapping we performed spatiotemporal clustering using a sliding window approach. The sliding window consisted of 3 datapoints; the current datapoint and those either side. The current datapoint at each voxel was then substituted as the value of the largest absolute value within that window. The *3dmerge -1clust* AFNI (Cox, 1996; Cox & Hyde, 1997) function was used to cluster neighbouring voxels, with a minimum cluster size of 10. The spatiotemporal clustering mask was then applied to the original data in order to remove spurious, isolated activations that are likely false activations.

Then, an activation time series (ATS) (Gaudes et al., 2011) was computed by counting the number of voxels with a negative estimated R2* signal (i.e., a positive BOLD response) at each TR in our selected region of interest, the right insula. This mask of the right insula was created based on insular parcels from the Schaefer 1000 parcels 17 network atlas (Schaefer et al., 2018). Finally, we selected those peaks that had a higher number of activated voxels within the ROI compared with the shuffled dataset as any peaks higher than this are unlikely to have happened by chance. The ATS for the right insula is calculated to find the most relevant instances of activity, due to the regions hypothesised role in the urge-to-act network (Berman et al., 2012; S. R. Jackson et al., 2011; Lerner et al., 2009).

4.2.4 K-means clustering

Clustering was used to identify any patterns in the activation maps associated with the selected ATS peaks. The input was the matrix of pairwise distances between the activation maps associated with the selected ATS peaks. The metric used for calculating these pairwise distances was the Euclidean distance. This would help us to group together regions which were coactive. K-means clustering aims to separate the data into k clusters, here k was chosen using consensus clustering (J. Wu et al., 2015). The selected ATS maps would be assigned to the cluster that minimised the distance between the datapoints and their cluster centroids.

For the consensus clustering, k-means clustering was applied to 80% of the data with k values in the range 2 to 15 with 100 iterations per k. The k with the highest consensus value was selected. The consensus value is the average proportion of times that any pair of datapoints were assigned to the same cluster across the runs, giving a value between 0 and 1.

The K-means algorithm was run 50 times with different centroid seeds with the number of clusters determined by the consensus clustering. Finally, the voxelwise Z-scores for the activation maps for each cluster were calculated.

We then compared the cluster maps with the urge, suppression and blink GLM-based maps found in Chapter 3 to identify which they most closely represented. To do this the Z-scores of the identified MESPFM-clusters were multiplied by -1 to account for the maps showing the estimated R2* rather than the BOLD signal. Next the MESPFM-maps were thresholded at Z = 3.2 to make them comparable to the GLM-based maps from Chapter 3. Then, the MESPFM-clusters along with the GLM-based maps from Chapter 3 ('Suppress' > 'Okay to blink', blinks, Urge > Baseline) were binarized to create masks of the significant positive activation. Each MESPFM-cluster mask was then summed with each GLM-based cluster mask from Chapter 3 separately. These summed masked were thresholded to keep only those voxels where there was an overlap in activation. The highest overlap between the GLM-based masks and the MESPFM-cluster mask was used to determine which GLM-based map from Chapter 3 the cluster most represented. The percentage of overlapping voxels within the GLM-based masks is reported.

4.3 Results

Figure 4.3 demonstrates the single-run detection of activation within the right insula from a representative subject. Figure 4.3A shows the framewise displacement of the subject during this run, whilst Figure 4.3B shows the interpolated urge scores and blink frequencies per TR. Activation peaks within the right insula which surpass the threshold are shown in

Figure 4.3C and are not associated with increases in framewise displacement (Figure 4.3A). All other runs from all participants are in Appendix C (page 184). Whilst all runs showed activation in the right insula, not all runs showed activation which surpassed the threshold set by the shuffled dataset.

Consensus clustering determined that 3 clusters gave the most stable solution with a consensus value of 0.60140. The unthresholded K-means output maps (k = 3) are shown in Figure 4.4, Figure 4.5 and Figure 4.6. The thresholded K-means output maps are shown in Figure 4.7. The thresholded activation map for Cluster 1 reveals significant activation in the SMA, paracingulate cortex, ACC, bilateral insulae, bilateral frontal opercular cortices, right IFG pars opercularis, bilateral frontal orbital cortices, right postcentral gyrus, right superior parietal lobule, and both medial and lateral occipital areas. Similarly, Cluster 2 involves activation of the SMA, paracingulate cortex, right insula, right frontal opercular cortex, bilateral IFG pars opercularis, right frontal orbital cortex, bilateral superior frontal gyri (SFG), right middle frontal gyrus (MFG), bilateral DLPFC, left postcentral gyrus, bilateral superior parietal lobules, and both medial and lateral occipital areas. Finally, Cluster 3 shows activation in the SMA, paracingulate cortex, ACC, right insula, bilateral frontal opercular cortices, bilateral SFG, bilateral DLPFC, left sensorimotor cortex, bilateral superior parietal lobule, and both medial and lateral occipital regions.

All three MESPFM-cluster masks show activation within the right dorsal-anterior insula, paracingulate cortex, SMA, and medial and lateral occipital cortices (Figure 4.7). Figure 4.7 shows the results from both the MESPFM analysis and the conventional GLM analysis performed in Chapter 3. The largest overlap between all 3 thresholded cluster maps was with the regions shown to be active during suppression (Table 4.1).

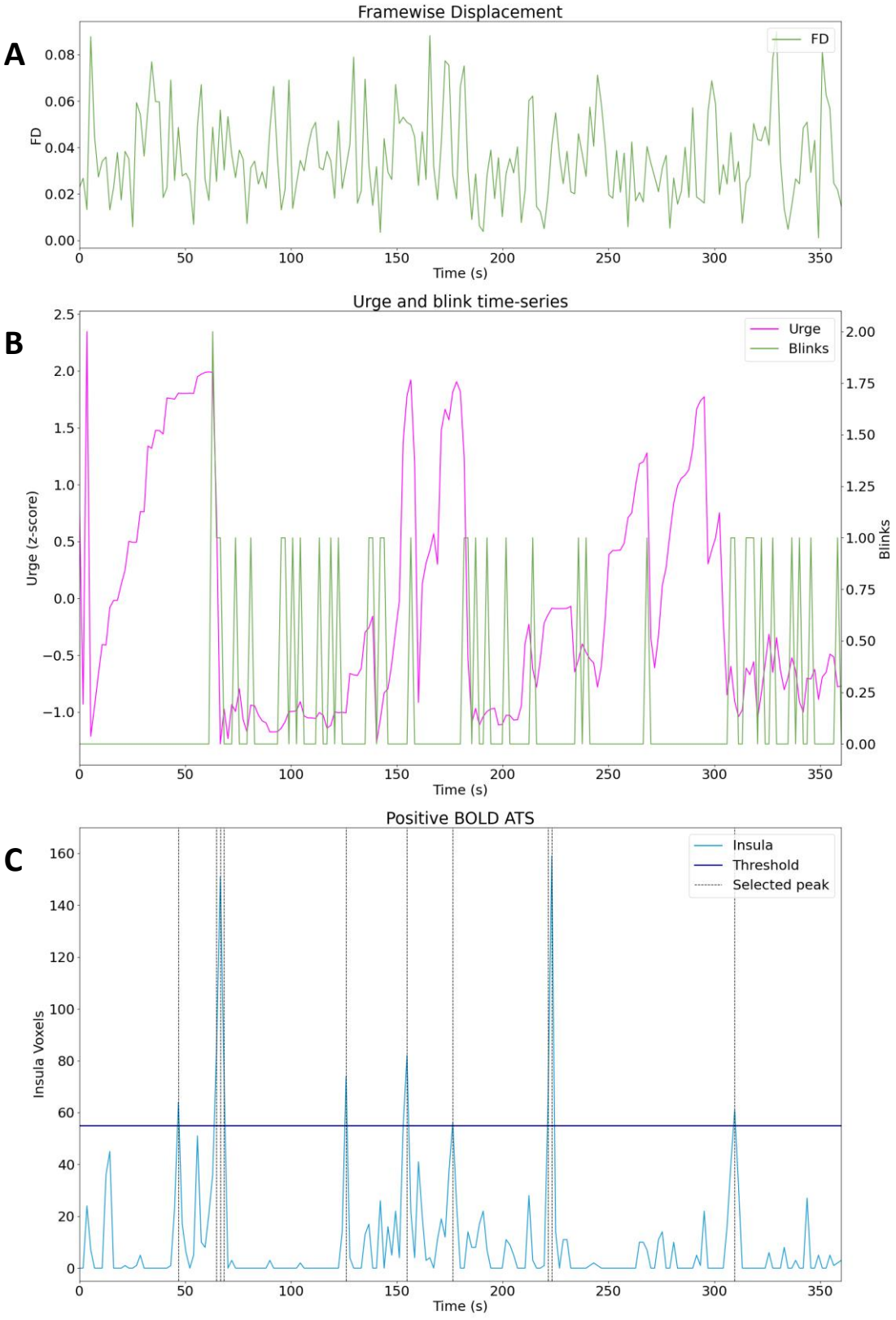

Figure 4.3. *The activation timeseries from a representative subject.*

A) Framewise displacement of the subject during the run; B) The interpolated urge scores and blink frequencies per TR.; C) All positive BOLD (negative R2) activations within the right insula with the threshold set by the shuffled dataset.*

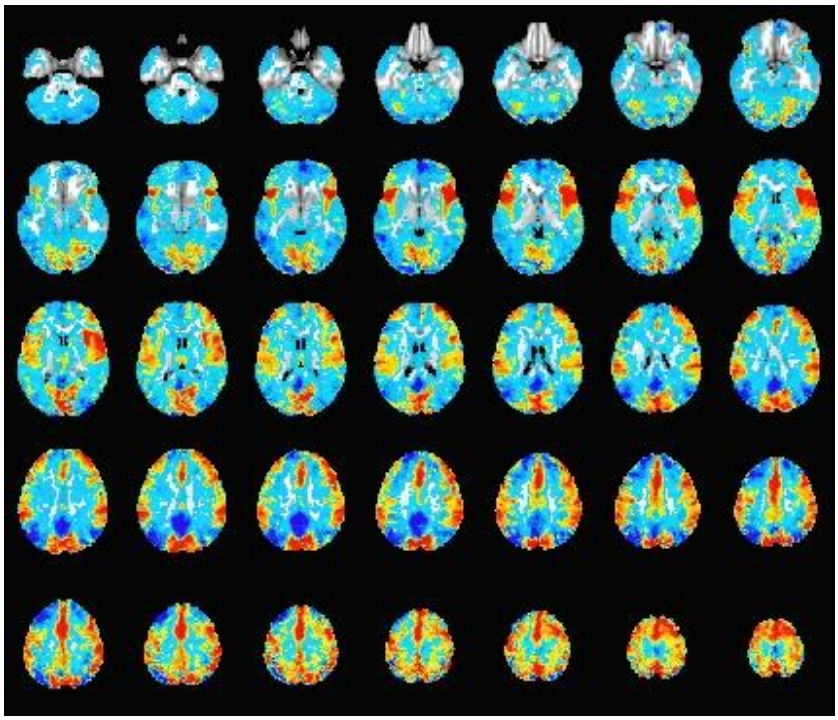

Figure 4.4. *Cluster 1*

Activation was identified in the SMA, paracingulate cortex, ACC, bilateral

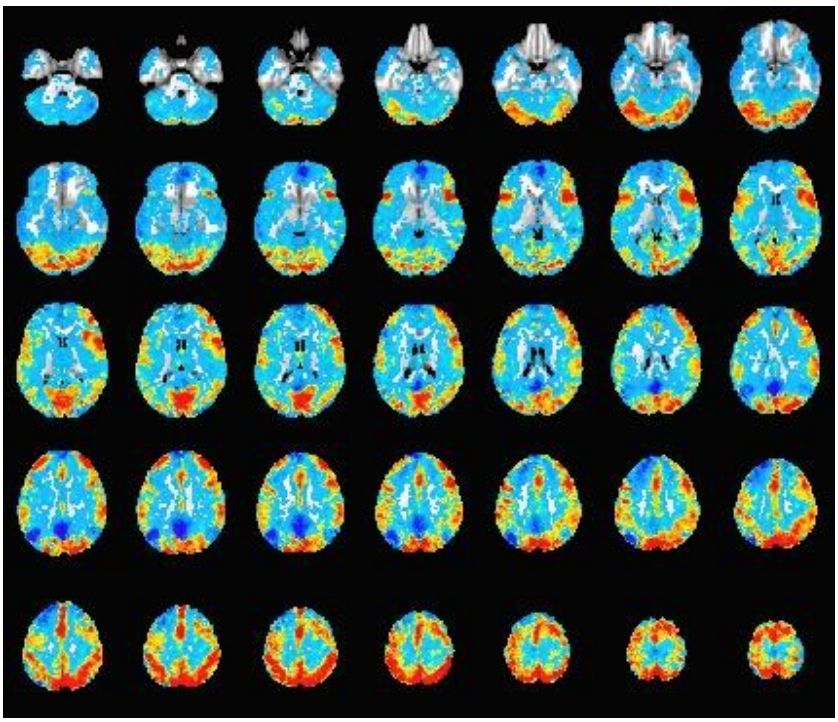

Figure 4.5. *Cluster 2*

Activation was identified in the SMA, paracingulate cortex, right insula, bilateral DLPFC, and both medial and lateral occipital areas.

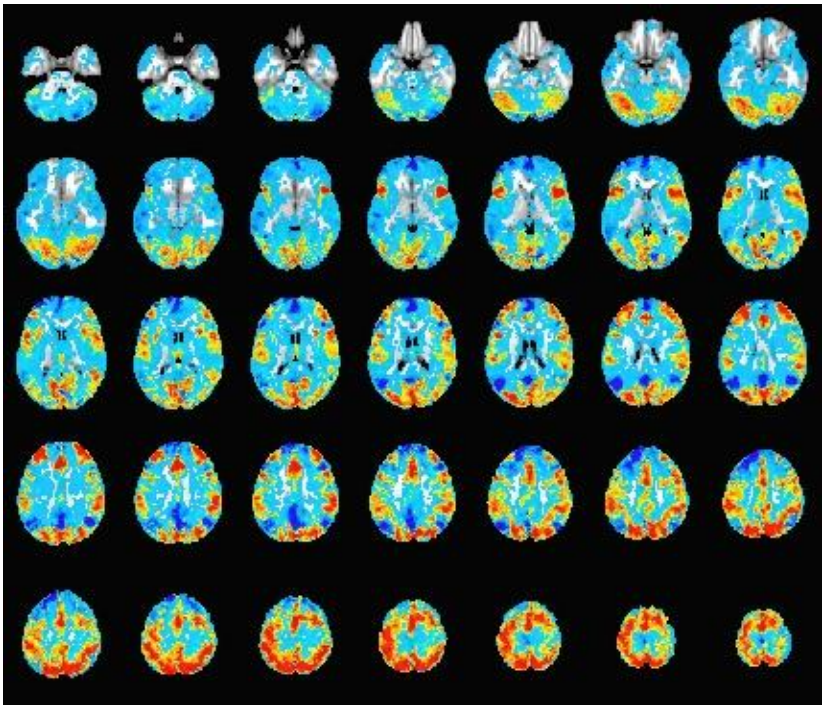

Figure 4.6. *Cluster 3*

Activation was identified in the SMA, paracingulate cortex, ACC, right insula, bilateral DLPFC, and both medial and lateral occipital regions.

Table 4.1. *Percentage overlaps of the MESPFM-cluster masks with the GLM-based cluster masks (Chapter 3). The largest overlap for each MESPFM cluster is highlighted in bold.*

	GLM-based suppression cluster	GLM-based urge cluster	GLM-based blink cluster
MESPFM cluster 1	**7.24%**	2.01%	4.48%
MESPFM cluster 2	**6.01%**	1.66%	2.49%
MESPFM cluster 3	**8.04%**	1.08%	2.68%

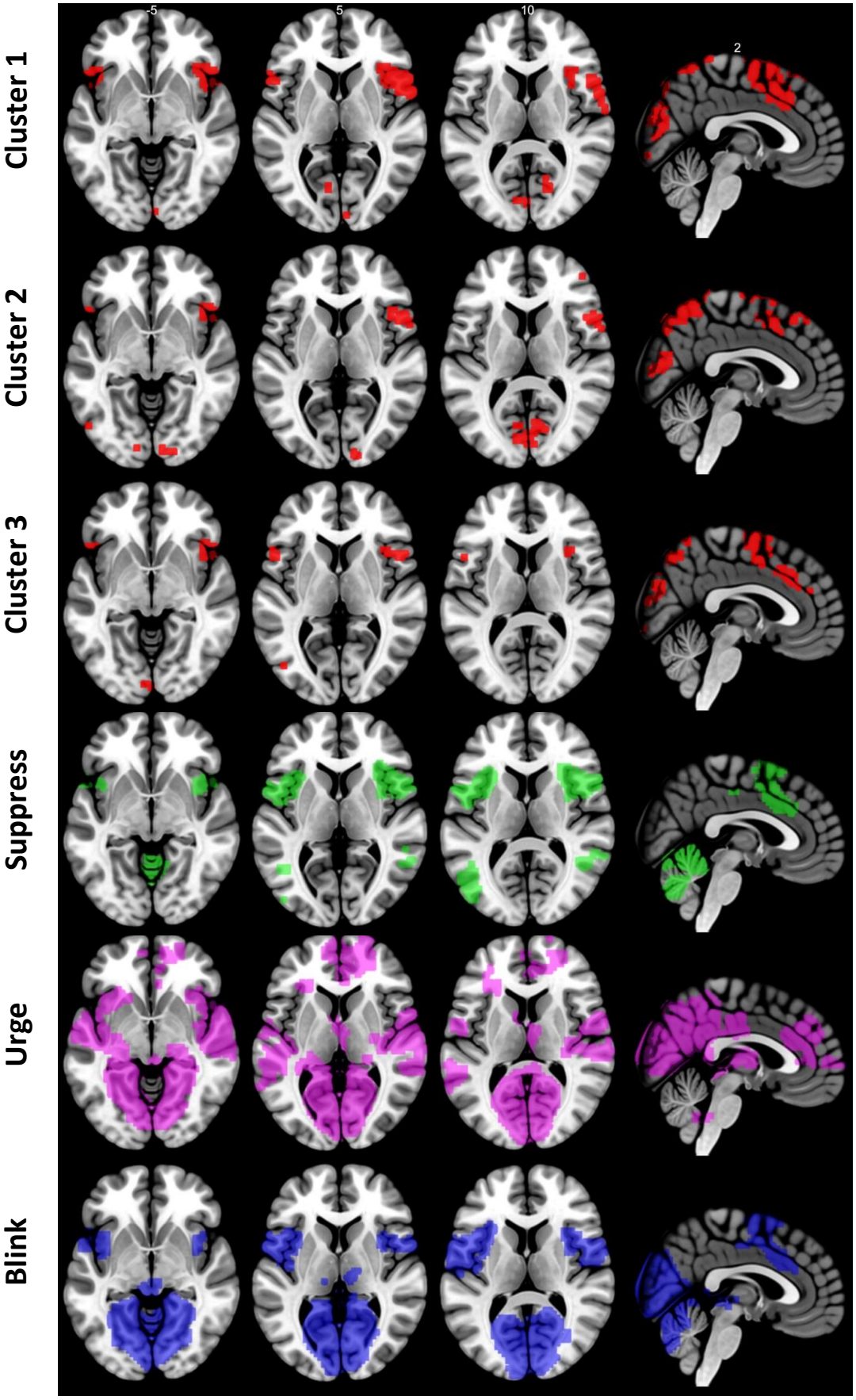

Figure 4.7. *Comparison of the masks generated during the multi-echo sparse paradigm free mapping (Clusters 1-3) and the conventional general linear model analysis (Suppression, Urge, Blink) (thresholded at Z = 3.2).*

4.4 Discussion

In this chapter, we aimed to analyse the data collected in Chapter 3 without prior specification of timings to validate whether MESPFM can be used to identify neuronal activity in an action suppression paradigm without prior specification of event timings. Neuronal activation was identified within the right insula, cingulate areas, SMA and medial occipital cortex. These regions were found to be commonly active during suppression when data were analysed using a conventional GLM approach (Chapter 3). The mid-cingulate cortex and the right insula have previously been identified as being active during the urge-to-act in healthy participants and the urge-to-tic in TS patients (S. R. Jackson et al., 2011).

All three clusters found with MESPFM showed similar activation of the right anterior insula and cingulate regions. The right insula was chosen as our region of interest for the estimation of the activation timeseries due to its consistent activation in fMRI studies of urge (Berman et al., 2012; S. R. Jackson et al., 2011; Lerner et al., 2009). However, in Chapter 3 we demonstrated that different portions of the right insula were active during suppression, urge and blinks. This is also shown in the activation timeseries shown in Appendix C (page 184), where activations of the insula were seen throughout the experiment regardless of task block. As the chosen activation maps relate to the activation seen during the corresponding timepoint we cannot separate suppression from feelings of urge if they happen simultaneously. Interestingly, in Chapter 3 we demonstrated that urge peaks at blink onset in the suppression blocks but not in the 'Okay to blink' blocks, suggesting that in healthy participants the urge-to-blink arises due to the act of suppression. Perhaps in future, separate insula ROIs can be used to estimate activation timeseries after the MESPFM analysis to examine if it is possible to cluster activation relating to suppression, urge and blinking separately. As this work is a precursor for research looking at the urge-to-tic, it would be useful to see if the same separable regions of the insula can be identified during a tic suppression paradigm when analysed using the conventional GLM approach.

For future work, we would ideally increase the sensitivity, while maintaining the specificity, of the MESPFM algorithm to detect BOLD events that will, in turn, result in selecting more peaks in the activation timeseries. This would give us more data across subjects and runs, and potentially allow us to separate the urge and suppression networks without the requirement for continuous subjective urge ratings. Recent developments of the MESPFM algorithm allow the use of the stability selection technique to avoid the selection of the regularisation parameter used to estimate the activity-inducing signal (here, we used BIC which provides very high specificity) (https://pyspfm.readthedocs.io/en/latest/index.html). The stability selection technique involves subsampling the data and solving the regularisation path for a range of regularisation parameters for multiple subsamples of the data. Then, stability selection calculates the probability of a TR containing a neuronal-related BOLD event, which should make the results more robust as opposed to when the regularisation parameter is fixed.

To conclude, this Chapter validates the use of MESPFM as a model-free approach to analyse fMRI data collected during action suppression paradigms where the event timings are unknown as might be the case during tic suppression in TS patients. Using the MESPFM approach, we were able to identify regions previously identified as being involved in the urge-to-act. The clusters identified showed an overlap with the regions involved in action suppression as shown by conventional analysis of the same data (Chapter 3).

Chapter 5: Exploring entrainment induced by rhythmic median nerve stimulation

This work has previously been reported in:

Houlgreave MS, Morera Maiquez B, Brookes MJ, Jackson SR. The oscillatory effects of rhythmic median nerve stimulation. Neuroimage. 2022.

doi: 10.1016/j.neuroimage.2022.118990.

5.1 Introduction

In the contralateral sensorimotor cortex, neural oscillations in the 8-30 Hz range are suppressed during movement and movement preparation, but following movement there is a beta rebound (13-30 Hz), meaning their amplitude is briefly higher than at rest (Jurkiewicz et al., 2006; Pfurtscheller et al., 1996). Corticospinal excitability is known to be increased when sensorimotor oscillations are suppressed and reduced during the post-movement beta rebound (R. Chen et al., 1998). Higher beta activity has also been associated with a slowing of newly initiated movements (Gilbertson et al., 2005). Therefore, beta synchrony is frequently thought of as a mechanism which promotes maintenance of the current motor set (Engel & Fries, 2010). However, a newer theory suggests that beta is a marker of motor readiness, whereby a low level of beta activity indicates a higher likelihood that a movement will be generated (N. Jenkinson & Brown, 2011). In a study investigating the roles of alpha (8-12 Hz) and beta oscillations through a novel saccade task a small positive correlation was found between saccade reaction time and contralateral sensorimotor beta power suggesting a role in somatosensory gating (Buchholz et al., 2014). On the other hand, alpha (mu-alpha in the sensorimotor cortex) synchrony has been linked to the inhibition of task irrelevant areas (Brinkman et al., 2014, 2016; Buchholz et al., 2014; Jensen & Mazaheri, 2010), with the network of regions involved in a task showing a desynchronisation of alpha oscillations (Haegens et al., 2010) and task-irrelevant regions showing an increase in alpha power (Brinkman et al., 2014; Buchholz et al., 2014). Various NIBS techniques have been shown to modulate these oscillatory rhythms as well as behaviour (Joundi

et al., 2012; Pogosyan et al., 2009; Thut, Veniero, et al., 2011). As a result, there is widespread interest in the use of these techniques as potential forms of therapy in a multitude of disorders.

An interesting avenue for therapy using NIBS is entrainment; the process though which neuronal assemblies become synchronised to a rhythmic stimulus train (Thut, Schyns, et al., 2011). Entrainment of oscillations in the 8-30 Hz range could prove therapeutically beneficial in patients with disorders characterised by sensorimotor hyperexcitability (Morera Maiquez, Sigurdsson, et al., 2020). Therefore, it is of interest that repetitive tACS at a frequency associated with periods of decreased corticospinal excitability can lead to a reduction in the velocity of movement (Pogosyan et al., 2009). In 2011, Thut and colleagues showed that rhythmic TMS of a parietal site at an individual's preferred alpha frequency caused region specific entrainment of brain oscillations (Thut, Veniero, et al., 2011). These findings were specific to rhythmic TMS and were not seen with arrhythmic or sham stimulation control conditions. Given that tACS can have similar oscillatory effects it is interesting that application of a topical anaesthetic can significantly reduce entrainment, suggesting that the effects of tACS may be due to stimulation of the somatosensory cortex via peripheral nerves rather than direct stimulation of the cortex itself (Asamoah et al., 2019). Stimulation was applied at the tremor frequency of healthy volunteers (~8.70 Hz), resulting in increasing tremor entrainment with increasing tACS amplitude. However, when a topical anaesthetic was applied to the scalp this significant increase in phase locking to the stimulation with increasing tACS amplitude was not seen. While there was still a trend for this effect the authors argue that this is more likely to be caused by an incomplete block of the peripheral nerves rather than a transcranial mechanism being involved. This suggests that there is potential for the entrainment effects seen with tACS to be replicated through rhythmic stimulation of peripheral nerves rather than the cortex. In fact, rhythmic MNS at 12 Hz and 19 Hz has been shown to cause a frequency specific increase in EEG power and inter-trial phase coherence (ITPC) over the contralateral sensorimotor cortex in healthy participants, which is not seen with arrhythmic stimulation (Morera

Maiquez, Jackson, et al., 2020; Morera Maiquez, Sigurdsson, et al., 2020). This suggests that rhythmic MNS may be able to entrain the sensorimotor cortex. Furthermore, when compared with no stimulation, delivery of 10 Hz rhythmic MNS has been shown to reduce the frequency of tics in TS patients (Morera Maiquez, Sigurdsson, et al., 2020). These are important findings as, unlike tACS and TMS, MNS is portable, cheaper and requires little training, making it an ideal technique to be used therapeutically outside of the clinic. An ideal therapeutic intervention would induce long-term clinically beneficial aftereffects. It has been shown that oscillatory aftereffects following entrainment protocols are prevalent (Veniero et al., 2015). However, these aftereffects are not necessarily localised to the entrained frequency and have been inconsistent between experiments stimulating using the same frequency (Veniero et al., 2015). As such, more work is needed to understand the potential therapeutic uses of rhythmic brain stimulation as well as the possible entrainment of brain oscillations and their aftereffects.

When a sensory stimulus (such as MNS) is delivered a transient, phase-locked electrical potential can be recorded over the sensorimotor cortex which is known as a SEP (Vialatte et al., 2010). When longer trains of rhythmic stimuli are delivered, we can record steady-state evoked potentials (SSEPs) which appear as a sustained response at the frequency of stimulation (Regan, 1989, as cited in (Vialatte et al., 2010)) (Regan, 1966). SSEPs are thought to either arise due to entrainment of a population of neurons (Herrmann, 2001) or due to linear superposition of SEPs in response to each pulse of the train (Capilla et al., 2011). Critically, both explanations could explain the increase in EEG/MEG power and ITPC at the frequency of stimulation (Capilla et al., 2011; Keitel et al., 2014). When refractoriness is taken into account there is compelling evidence for the superposition hypothesis (Capilla et al., 2011; Colon et al., 2012). Nevertheless, there is reason to believe both mechanisms coexist (Colon et al., 2012; Notbohm et al., 2016). Oscillating systems have a preferred frequency and when matched by the external stimulus train the system resonates (Colon et al., 2012; Herrmann, 2001; Notbohm et al., 2016; Vialatte et al., 2010). Therefore, at certain frequencies the signal recorded

could be largely because of entrainment rather than rhythmic SEPs (Colon et al., 2012). Hence, in our study we delivered trains of MNS at 12 and 20 Hz during concurrent MEG recording to investigate entrainment effects (adapted from (Morera Maiquez, Sigurdsson, et al., 2020)). There is evidence that stimulation at these frequencies can cause a slowing of voluntary movement. Reaction times during correct responses of a choice reaction time task were slowed by rhythmic 12Hz MNS (Morera Maiquez, Sigurdsson, et al., 2020), while 20Hz tACS has been shown to slow the initial and peak velocity of a movement (Pogosyan et al., 2009) as well as reduce the initial and peak force rate of movements (Joundi et al., 2012). As both entrainment and SSEPs would cause populations of neurons within the sensorimotor cortex to fire synchronously we would expect no difference in the online behavioural effects of these interventions. However, entrainment may make it easier to elicit long-term, clinically benificial effects. Replication of the entrainment effects of MNS in MEG is important to ensure validity of the findings, to investigate whether the effects of MNS are caused by entrainment or SSEPs, and to probe the regional effects of MNS in source rather than sensor space. In MEG the signal is less affected by the conductivity of the overlying tissue compared to EEG (Baillet, 2017; Cheyne, 2013), and therefore the models used for source localisation are simpler due to the lower level of spatial smearing (Muthukumaraswamy, 2014). Furthermore, compared to EEG, MEG has lower susceptibility to interference from non-neuronal sources such as muscles (Boto et al., 2019). Here we hypothesise that there will be entrainment of oscillations within the contralateral somatosensory cortex during rhythmic, but not arrhythmic, MNS. To conclude that rhythmic MNS induces entrainment we will need to show (i) a frequency and region-specific increase in instantaneous amplitude, (ii) synchronisation of the phase with the external source and (iii) that these effects are unlikely to be due to rhythmic evoked potentials. We expect no difference in the online effects of the stimulation at 12 and 20 Hz except for the frequency specificity.

5.2 Experimental Procedures

5.2.1 Subjects

Twenty healthy participants were recruited for the study. Nineteen participants were right-handed according to the Edinburgh Handedness Inventory (Oldfield, 1971). Participants gave informed consent and the experimental paradigm received local ethics committee approval (School of Psychology, University of Nottingham). Participants agreed that pre-existing structural MRI data (obtained within the Sir Peter Mansfield Imaging Centre, University of Nottingham) could be used by the researchers. One participant (female, 21 years old, right-handed) was excluded prior to analysis due to excessive movement during the MEG recording, leaving 19 usable datasets (aged 26.7 ± 3.6 years (mean ± SD); 11 female). A small inconvenience allowance was provided for volunteers for their participation.

5.2.2 Median Nerve Stimulation

Stimulation was delivered with electrodes (cathode proximal) positioned on the right forearm over the median nerve, using a Digitimer constant current stimulator model DS7A (Digitimer Ltd, UK). Pulse width was set at 0.2 ms and maximum compliance voltage (Vmax) was 400 V. Participants were seated and told to rest their forearm on the chair armrest to ensure the muscles were relaxed. The stimulation threshold was set at the minimum intensity required for a visible thumb twitch (mean ± SD) 9.1 ± 3.2 mA.

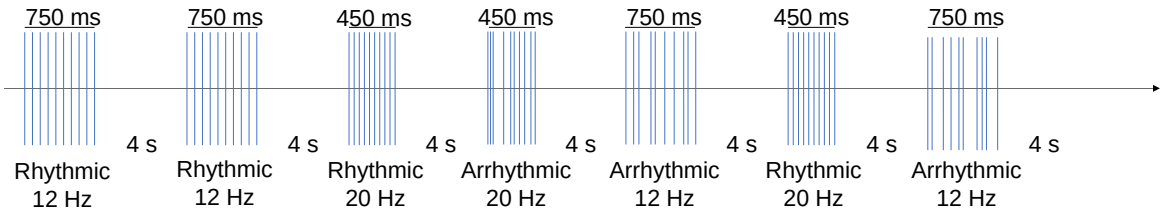

Figure 5.1. *Stimulation overview.*

A diagram showing an example of the trial setup for the MNS.

Four hundred trials of stimulation were delivered to the right median nerve during concurrent MEG recording, with a short break every 100 trials. Each trial consisted of 10 pulses delivered at the frequency of interest, rhythmic

12 Hz and 20 Hz in the test conditions. Arrhythmic controls were used to ensure that similar responses did not occur with random stimulation at the same average frequency. During the control trials the same number of pulses were delivered as in the test condition, but with a random inter-stimulus interval (ISI) which was on average the same as the rhythmic trials (but constrained to a minimum ISI of 0.01 s). The arrhythmic patterns were not the same for all trials or participants, however, the first pulse was always delivered at time 0 and the last pulse was always delivered at the end of the train (450 or 750 ms), regardless of the condition. For each of these 4 conditions, 100 trials were randomly delivered with an inter-trial interval of 4s using an in-house MATLAB script (MATLAB R2012a, Mathworks, Natick, MA) (Figure 5.1). The order of the 400 trials was randomised using the Psychtoolbox-3 function 'Shuffle' (M. Kleiner et al., 2007), and was different for every participant. Of note, here the right median nerve was chosen due to convention in the MNS literature, however we would expect no difference in the results for stimulation of the left median nerve except for the laterality of the effects.

5.2.3 EMG Measurement

To have an objective measure of the contractions caused by MNS, electromyography (EMG) electrodes were placed over the right abductor pollicis brevis (APB) muscle in a belly tendon montage. MEPs were recorded for twenty pulses of MNS at the intensity for a minimum thumb twitch, with 3s between each pulse. A Brainamp ExG (Brain Products GmbH, Gilching, Germany) was used to amplify the signal and Brain Vision Recorder (Brain Products GmbH, Gilching, Germany) was used to record the EMG data (bandpass filtered 10-2000 Hz, sampling rate 5 kHz). Peak-to-peak amplitudes were measured using an in-house MATLAB script to determine the baseline MEP amplitude (mean = 1219.13 μV, range = 52.10 - 7490.9 μV) (MATLAB R2017a, Mathworks, Natick, MA). EMG data from 6 individuals was not recorded due to technical issues.

5.2.4 MEG Data Acquisition

MEG data were collected at the Sir Peter Mansfield Imaging Centre, University of Nottingham using a 275-channel CTF MEG system (MISL,

Coquitlam, Canada) with participants in a seated position. The system was operated in a third order synthetic gradiometer configuration and data were sampled at 600 Hz. Fiducial marker coils were placed on the nasion and bilateral preauricular points of the participants, to track head movement in relation to the MEG sensors. A Polhemus FASTRAK (Polhemus Inc, Vermont) was used to digitise the participants' head shape and the relative positions of the fiducial markers. The data were examined by eye using commercial MEG data visualisation software (CTF MEG, Canada) and trials containing large artefacts were discarded, as were trials where the head moved more than 7 mm from its initial position. One occipital channel was removed during preprocessing in one subject. Following preprocessing there were on average (mean ± SD) 7 ± 8 rhythmic 20 Hz, 9 ± 10 arrhythmic 20 Hz, 8 ± 9 rhythmic 12 Hz and 8 ± 8 arrhythmic 12 Hz trials removed per subject. The data were then segmented such that an epoch started 1 s before stimulation and ended 3 s following the end of stimulation. The epoch lengths of alpha and beta trials were 4.75 s and 4.45 s, respectively. An anatomical MRI scan (1.0 mm^3 resolution, MPRAGE sequence) from each subject was used for co-registration to the digitised head shape.

5.2.5 Data Analysis

After pre-processing, a linear-constraint minimum-variance (LCMV) beamformer was applied to the data (Van Veen et al., 1997). Using FLIRT (FMRIB's Linear Image Registration Tool) (M. Jenkinson et al., 2012), a MNI (Montreal Neurological Institute) template brain was warped with respect to the subject's downsampled (4mm) anatomical scan, as was the AAL (Automated Anatomical Labelling) atlas (Tzourio-Mazoyer et al., 2002). This allowed the cortex to be parcellated into 78 regions and the coordinates of the centroids from each region to be determined for each individual (Gong et al., 2009). Covariance was calculated for the entire experimental time window within a 1-150 Hz frequency window (Brookes et al., 2008). The covariance matrix of the filtered data was regularised using the Tikhonov method, with the regularisation parameter set at 5% of the maximum singular value. The forward model was computed using dipole approximation and a multiple local spheres head model (Huang et

al., 1999; Sarvas, 1987). Dipoles were rotated in the tangential plane to determine the orientation which yielded the maximum signal-to-noise ratio. Beamformer weights were calculated for the centroid of each brain region resulting in 78 timecourses (O'Neill et al., 2017), which were filtered between 1 and 48 Hz.

5.2.6 Time Frequency Spectrograms

To visualise amplitude changes across the trial, time frequency spectrograms were calculated. Data were filtered into overlapping frequency bands spanning from 4 to 50 Hz to visualise the changes across frequency bands in the left somatosensory cortex as defined by the AAL atlas. The analytic signal for the data within each band was determined using a Hilbert transform (HT), the absolute value of which gave the instantaneous amplitude of the MEG signal at each point in time. Timecourses for each frequency band were then averaged across trials, before being normalised using the average amplitude during the control window (0.24-0.99 s for 12 Hz trials and 0.54-0.99 s for 20 Hz trials (length the same as the active time window for that condition)). Time frequency spectrograms were averaged across subjects.

We also calculated the average amplitude during the period of stimulation to investigate the differences between rhythmic and arrhythmic without averaging out the effects of the arrhythmic condition due to the random pulse timings. First the data were filtered into the frequency band of stimulation (11-13 Hz or 19-21 Hz). Then the data from each trial was normalised using the average amplitude during the control window for that trial. Next, we calculated the mean amplitude within the period of stimulation and finally averaged across trials and subjects. The average amplitude from the periods of rhythmic and arrhythmic stimulation were then compared using a one-tailed Wilcoxon signed rank test.

5.2.7 Inter-Trial Phase Coherence

The timeseries from the contralateral somatosensory cortex were filtered into the same frequency bands as were previously used for the time

frequency spectrogram calculation. Following a HT of the data, the ITPC was calculated using formula (14) below:

$$ITPC = \left| \frac{1}{N} \sum_{k=1}^{N} exp^{i * \phi k} \right| \quad (14)$$

Where N is the number of trials and ϕk is the phase angle in radians of the datapoint in the current trial.

5.2.8 Statistical Analysis

For both the instantaneous amplitude and ITPC, timecourses were filtered according to the frequency of stimulation (11-13 Hz or 19-21 Hz) using a bandpass least-square linear-phase FIR filter with a filter order of 200. These timecourses were then statistically compared using a one-tailed Wilcoxon signed rank test at each timepoint as the data failed the Kolmogorov-Smirnov test for normality. Multiple comparisons were corrected for using the false discovery rate (FDR) of 0.05 (Benjamini & Hochberg, 1995; Benjamini & Yekutieli, 2001; Groppe, 2020). The same method was used to compare the timecourses following each pulse of rhythmic and arrhythmic stimulation for the evoked potential analysis. Post-hoc timecourse analysis was completed in the same manner but with a two-tailed test. All timecourse plots show the standard error of the mean (SEM) (Martínez-Cagigal, 2020).

5.2.9 Sensory Evoked Potentials

Rhythmic sensory evoked potentials would lead to an increase in instantaneous amplitude and ITPC during rhythmic stimulation, providing an alternative mechanism to entrainment (Thut, Veniero, et al., 2011). To investigate whether this was the case, we looked at whether there was a full oscillation at the frequency of stimulation associated with each pulse of the rhythmic stimulation train to determine whether entrainment had occurred. To do this the beamformed signal was filtered between 11-13 Hz for the 12 Hz stimulation trials and 19-21 Hz for the 20 Hz stimulation trials. The data following the pulse timings (83.3 ms for the 12 Hz trials and 50 ms for the 20 Hz trials) were averaged for each of the 10 pulses

across all trials for every subject, before being averaged across subjects. The same method was used to look at the broadband (1-48 Hz) signal following each pulse, to investigate whether there was a SEP associated with each MNS pulse. Data from 1 participant were not included in the 20 Hz condition analysis due to a loss of data, meaning we were unable to determine which trials were deleted during preprocessing, and as such could not determine the pulse timings for the remaining trials.

We then took the average broadband (1 – 48 Hz) data from the first pulse of the rhythmic trials and used this as a template SEP for each subject, as this should be equivalent to the SEP seen with a single pulse of MNS. This will have negated the possibility of pulses happening in quick succession in the arrhythmic trials. Using the fitlm MATLAB function (MATLAB R2019a, Mathworks, Natick, MA), we linearly modelled the averaged data for each pulse of the rhythmic and arrhythmic trials in each subject individually using their template SEP. We hypothesised that if the rhythmic response were due to entrainment rather than rhythmic SEPs then the adjusted R-squared value would be significantly higher for the arrhythmic compared to the rhythmic pulses, as the model would explain more of the variance in the response. To compare the fit of the linear model we used a Friedman's two-way ANOVA with rhythmic and arrhythmic as the conditions and pulses for every subject as paired repeats. A non-parametric test was used as the data failed the Kolmogorov-Smirnov test for normality.

To further investigate whether the effects were due to entrainment or rhythmic SEPs, we used empirical mode decomposition (EMD) to decompose the mean trial data for each participant, associated with pulses 3-10 of the rhythmic 12Hz and 20Hz stimulation, into intrinsic mode functions (IMFs). Using the EMD python package (Quinn et al., 2021), we computed the IMFs. Then the 'good' oscillatory cycles, with an amplitude above 0.05, were identified. These cycles were then phase aligned and the phase-aligned instantaneous frequency was determined. The phase-aligned instantaneous frequency was calculated for every IMF, for each subject in each condition, and then the IMF with the average instantaneous

frequency closest to the frequency of stimulation was selected. Finally, a one-sample t-test was performed at every point in the phase cycle to compare the phase-aligned instantaneous frequency from all the good cycles in that IMF to the stimulation frequency. If entrainment had occurred, we would expect a constant instantaneous frequency at the stimulation frequency across instantaneous phase, as is the case with sinusoidal oscillations. Browns method was used to combine the p-values to determine whether there was a significant difference overall for that subject (Poole et al., 2016).

5.2.10 Individual frequency

The individual alpha and beta frequency for each subject were calculated based on all the conditions together (12 Hz and 20 Hz, rhythmic and arrhythmic), using a 2 second window within the rest period between trials. The MATLAB periodogram function was used to determine which frequency was associated with the maximum power peak within the frequency band of interest. We investigated the relationship between the absolute distance in Hz from the individual frequency and the mean amplitude at the frequency of stimulation using a Spearman's rank test, as the data failed the Kolmogorov-Smirnov test for normality.

5.2.11 Voxel-based beamformer

A LCMV beamformer was applied to the preprocessed data to allow comparison of the data in the active (20Hz [1s 1.45s]; 12Hz [1s 1.75s]) and passive (20Hz [0.54s 0.99s]; 12Hz [0.24s 0.99s]) windows, for rhythmic MNS at the frequency of stimulation (Van Veen et al., 1997). Beamformer weights were calculated for each voxel, to create a pseudo-T-statistic map for each condition. Covariance was calculated for the entire experimental time window in a frequency window set according to the frequency of stimulation (19-21Hz and 11-13Hz) (Brookes et al., 2008). The covariance matrix of the filtered data was regularised using the Tikhonov method, with the regularisation parameter set at 4% of the maximum singular value. Individual maps were sampled on a 4mm grid of the subject's anatomical scan. For the group average, individual maps were subsequently transformed to MNI coordinate space using FLIRT (M.

Jenkinson et al., 2012). The neural generator of the entrained oscillations was identified using the peak in the frequency band of interest on the pseudo-T-statistic map.

5.3 Results

All analyses were conducted on the contralateral (left) *somatosensory* cortex as defined by the AAL atlas. Results for similar analyses on the contralateral *motor* cortex can be found in Appendix D (Figure D.1 and Figure D.2).

5.3.1 Entrainment: Increase in Instantaneous Amplitude

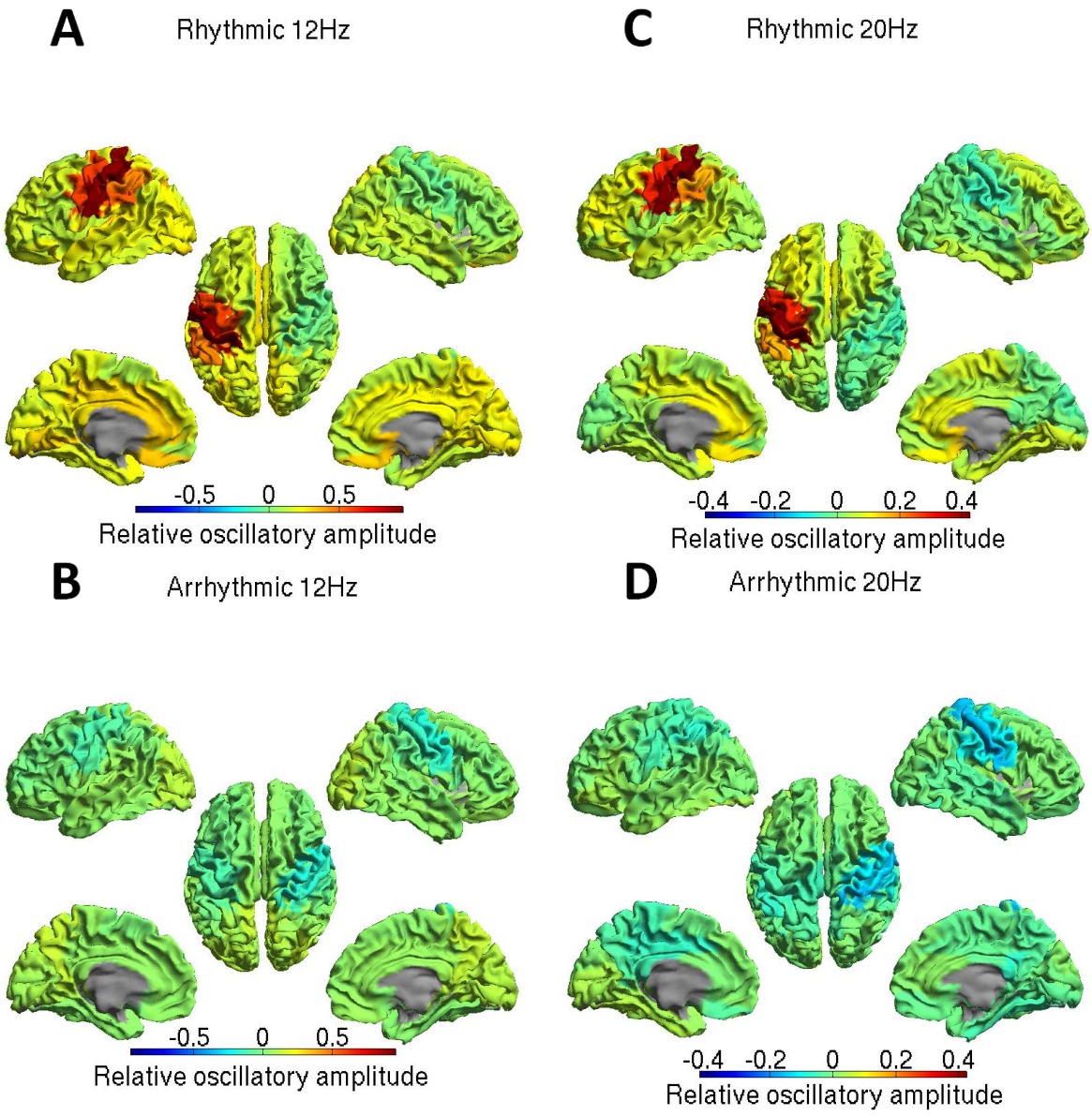

Figure 5.2. *Localisation of the source of oscillatory changes at the frequency of interest compared to baseline.*

Oscillatory amplitude for 78 cortical regions of the AAL atlas during A) rhythmic 12 Hz MNS, B) arrhythmic 12 Hz MNS, C) rhythmic 20 Hz MNS and D) arrhythmic 20 Hz MNS. (N = 19, standard deviation of signal during active window (1-1.75 s for 12 Hz trials 1-1.45 s for 20 Hz trials) minus control window (0.24-0.99 s for 12 Hz trials and 0.54-0.99 s for 20 Hz trials)).

During the delivery of 10 rhythmic pulses at 12 Hz, the source of the increase in oscillatory amplitude at 12 Hz (Figure 5.2A) was the contralateral sensorimotor cortex. This increase was not evident during arrhythmic stimulation where a decrease in amplitude was seen bilaterally

in the sensorimotor cortices (Figure 5.2B). Similarly, during the 20 Hz rhythmic condition the source of the increase in the oscillatory amplitude at 20 Hz (Figure 5.2C) was the contralateral sensorimotor cortex, which was not evident during arrhythmic stimulation at the same average frequency (Figure 5.2D). Therefore, the rest of our analysis will focus on the contralateral sensorimotor cortex.

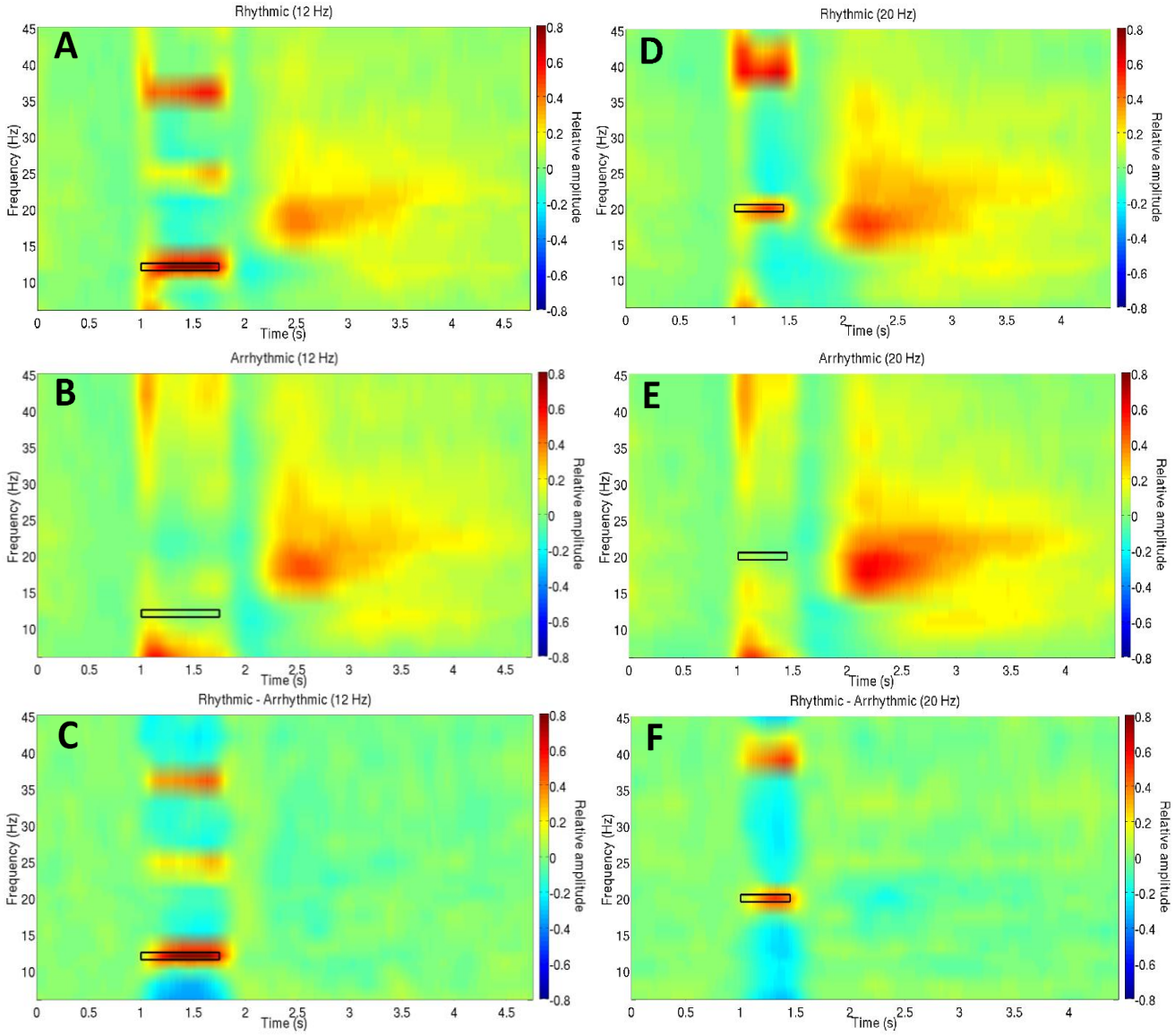

Figure 5.3. *Relative amplitude in the contralateral somatosensory cortex.*

(A-C) Time frequency spectrograms of relative amplitude changes when 12 Hz MNS was delivered between 1 and 1.75 s in either a A) rhythmic or B) arrhythmic pattern with C) showing the difference in amplitude between the two conditions. (D-F) Time frequency spectrograms of relative amplitude changes when 20 Hz MNS was delivered between 1 and 1.45 s in a D) rhythmic E) arrhythmic pattern with F) showing the difference in amplitude between the two conditions.

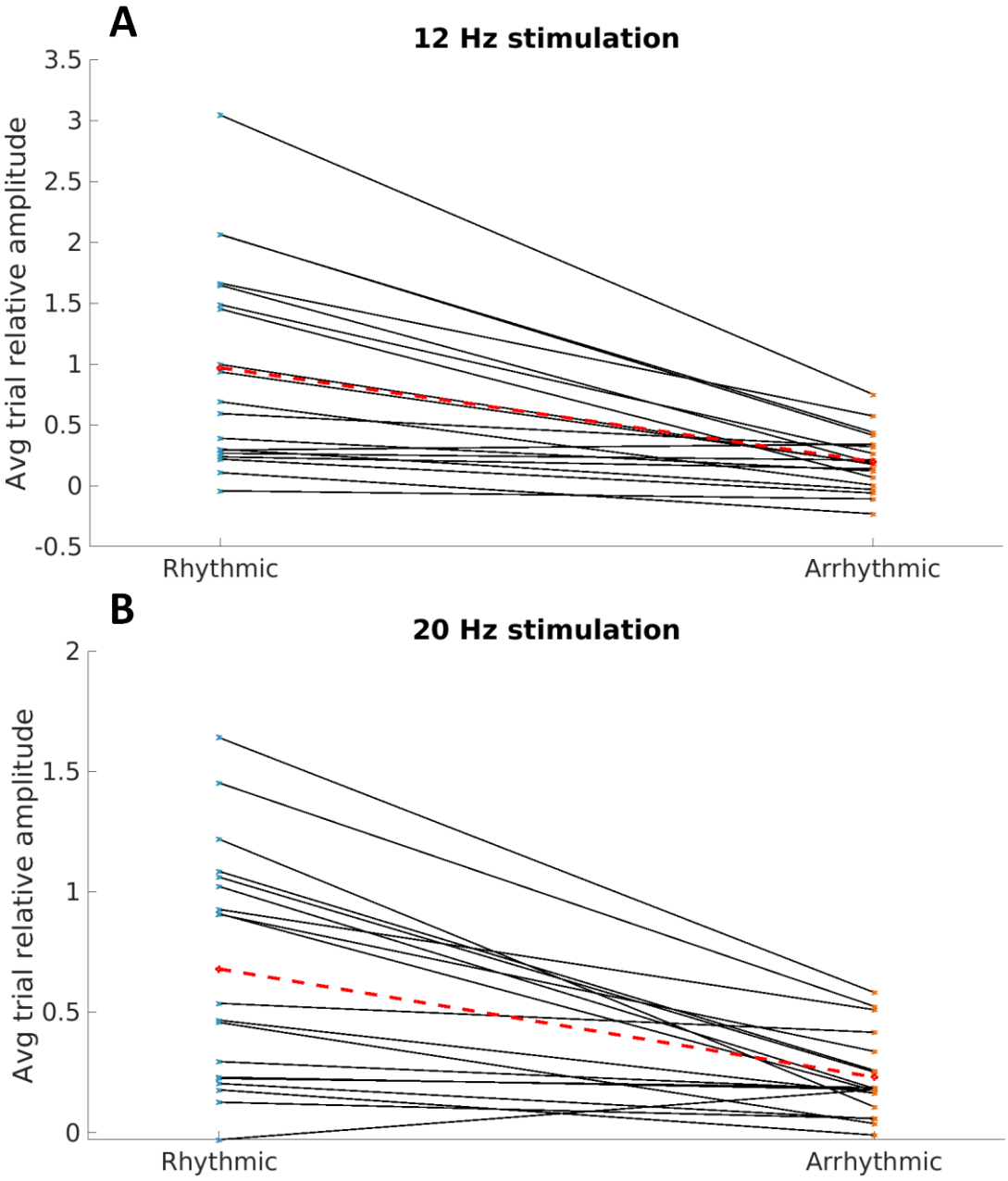

Figure 5.4. *Intra-subject comparison of average relative amplitude in the contralateral somatosensory cortex.*

A scatterplot contrasting the average relative amplitude across trials for subjects during rhythmic and arrhythmic patterns of A) 12 Hz (t=189, z=3.76, p=0.000084) and B) 20 Hz stimulation (t=182, z=3.48, p=0.00025).

Evidence of rhythmic entrainment comes from the time frequency spectrograms where there was an initial broadband increase in amplitude associated with the first pulse (1 s) of both rhythmic (Figure 5.3A, Figure 5.3D) and arrhythmic stimulation (Figure 5.3B, Figure 5.3E), which became specific to a narrowband around the frequency of stimulation during only rhythmic stimulation (Figure 5.3A, Figure 5.3D). This increase in amplitude returned to baseline shortly after the last pulse in the rhythmic condition. When the arrhythmic time frequency spectrogram is subtracted from the rhythmic time frequency spectrogram, it is evident that the difference between trials occurred only during the delivery of stimulation (Figure 5.3C, Figure 5.3F). The 12 Hz relative amplitude within the window of stimulation was significantly higher in the rhythmic condition compared to arrhythmic ($p \leq 0.05$ between 1093 and 1883 ms, FDR corrected). Similarly, the 20 Hz relative amplitude significantly increases within the window of stimulation in the rhythmic condition compared to arrhythmic ($p \leq 0.05$ between 1127 and 1557 ms, FDR corrected). As the arrhythmic condition involved pulses being delivered at different times during every trial, amplitude changes may have been averaged out during calculation of the time frequency spectrogram. Therefore, we calculated the average amplitude at the frequency of stimulation during the period that pulses were delivered for each trial before averaging across trials (Figure 5.4). This showed a significantly higher 20 Hz amplitude in the rhythmic compared to the arrhythmic condition ($t=182$, $z=3.48$, $p<0.001$). Analysis of the average amplitude across trials in the 12 Hz condition again showed significantly higher 12 Hz amplitude in the rhythmic condition ($t=189$, $z=3.76$, $p<0.001$).

5.3.2 Entrainment: Increase in Phase Coherence

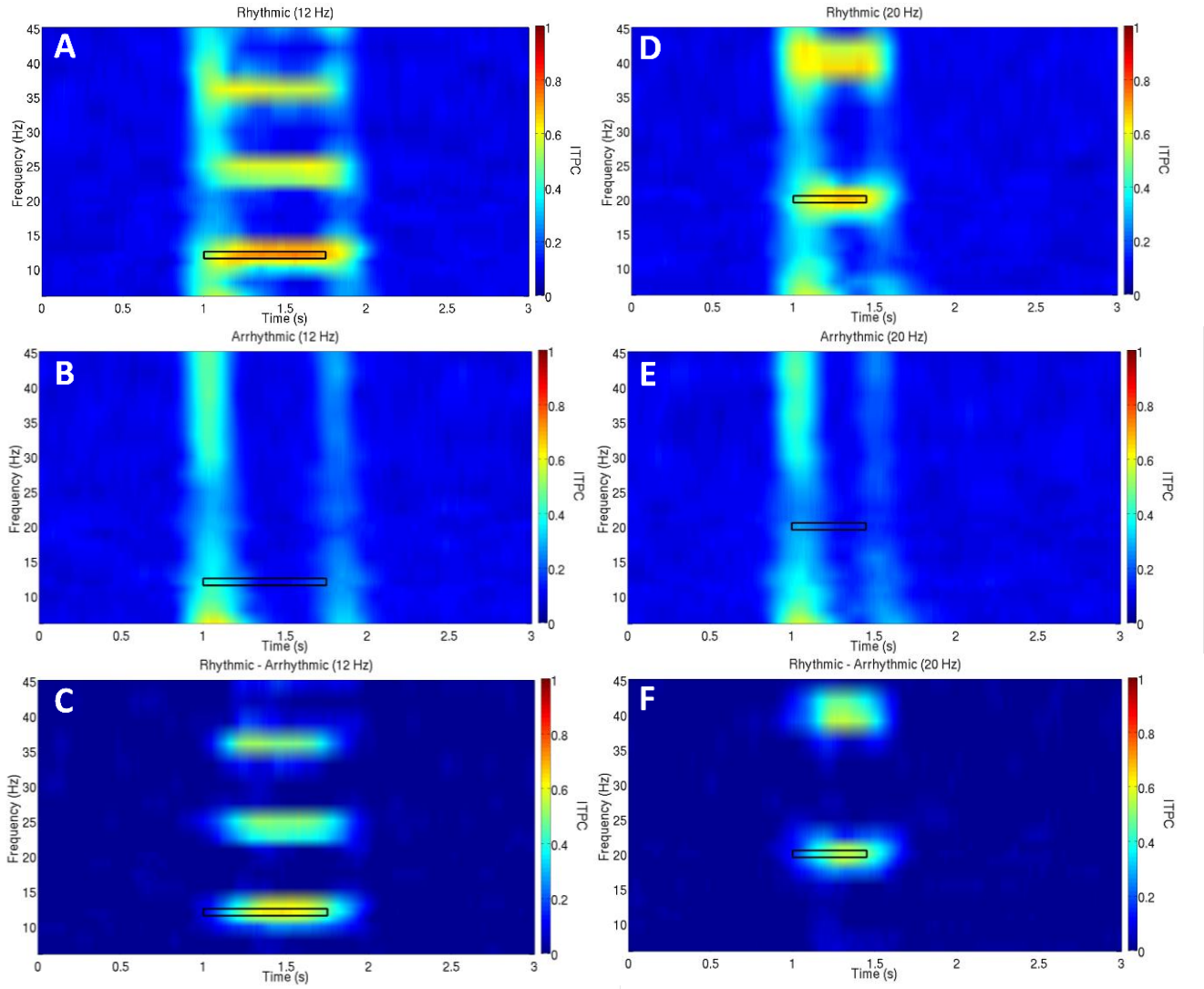

***Figure 5.5**. Inter-trial phase coherence in the contralateral somatosensory cortex.*

(A-C) Time frequency spectrograms of ITPC when 12 Hz MNS was delivered between 1 and 1.75 s in A) rhythmic B) arrhythmic pattern with C) showing the difference in ITPC between the two conditions. (D-F) Time frequency spectrograms of ITPC when 20 Hz MNS was delivered between 1 and 1.45 s in a D) rhythmic E) arrhythmic pattern with F) showing the difference in ITPC between the two conditions.

For both rhythmic and arrhythmic stimulation, there was an initial increase in ITPC across a wide range of frequencies (Figure 5.5). After the first stimulation pulse, this increase in ITPC was maintained in only the rhythmic condition and centred on the frequency of stimulation and its harmonics (Figure 5.5A, Figure 5.5D). The ITPC within the window of stimulation was significantly higher in the rhythmic condition compared to arrhythmic (12 Hz: $p \leq 0.05$ between 1047-1990 ms, FDR corrected) (20 Hz: $p < 0.05$ between 960-1700 ms and at 1703 ms, FDR corrected).

5.3.3 Entrainment: Hemispheric Specificity

To investigate whether the effect was hemisphere specific, as suggested by the results shown in Figure 5.2, we analysed the relative amplitude at the frequency of stimulation in the right and left somatosensory cortices during the rhythmic trials. The increase in relative amplitude during the 12 Hz rhythmic stimulation ($p \leq 0.05$ between 1105 and 1842 ms, FDR corrected) and the subsequent rebound ($p \leq 0.05$ for 3715-3960 ms, 4397-4405 ms and at 4417 ms, FDR corrected) was significantly higher in the left somatosensory cortex, which is contralateral to the stimulated arm. Similarly, the increase in amplitude in the left hemisphere during the 20 Hz rhythmic stimulation was significantly higher ($p \leq 0.05$ between 1152-1520 ms, FDR corrected), as was the subsequent rebound ($p \leq 0.05$ for 1993-3165 ms, 3168-3173 ms, 3223-3373 ms, 3632-3637 ms, 3643-3867 ms, 3875-3902 ms and 3968-4092 ms, FDR corrected).

5.3.4 Sensory Evoked Potentials

A possible explanation for the increase in instantaneous amplitude and ITPC seen during stimulation is that there was a SEP associated with each pulse of the MNS (Thut, Veniero, et al., 2011). Therefore, we investigated whether each rhythmic pulse was associated with a full oscillation at the frequency of stimulation and whether this could be explained by the filtering of an SEP (Figure 5.6). Each subplot contains the data following the pulse timings in each condition for a complete oscillation at the frequency of stimulation meaning a timeframe of 83.3 ms was used for the 12 Hz trials and 50 ms for the 20 Hz trials. As is evident in the frequency filtered data, a full oscillatory cycle was associated with each pulse of both the rhythmic and arrhythmic trains (Figure 5.6A, Figure 5.6C). However, this is less clear in the broadband 1-48 Hz data with a SEP being associated with the first pulse of the train (Figure 5.6B, Figure 5.6D). In Figure 5.6A and Figure 5.6C the timings were shifted by 20 ms to account for the approximate time it would take for the afferent volley to reach the cortex. The data in Figure 5.6B and Figure 5.6D were not shifted and the negative deflection at ~20 ms (N20 peak) reflects when the signal arrived in the primary somatosensory cortex (Passmore et al., 2014).

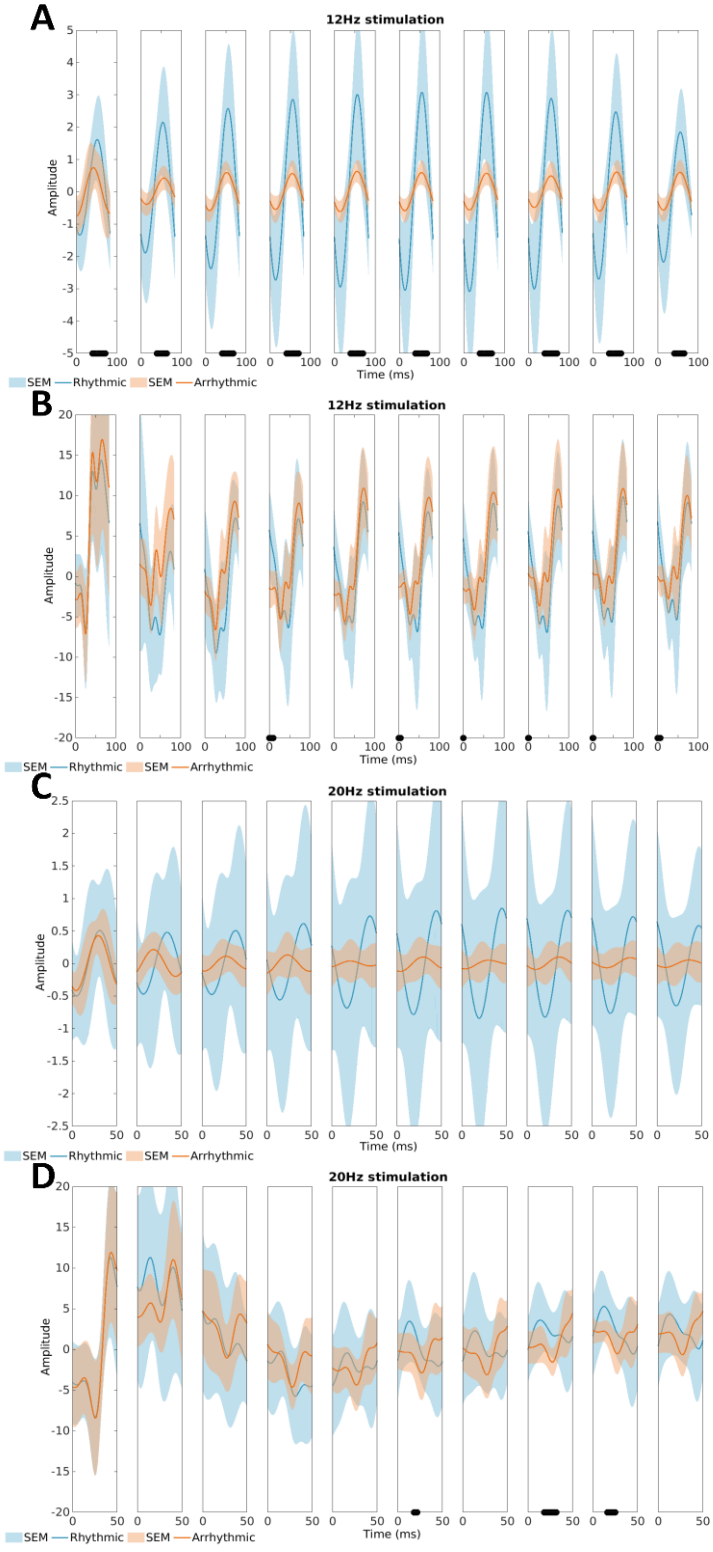

Figure 5.6. *Evoked components in the contralateral somatosensory cortex*

A) The 12 Hz oscillatory response to each pulse of the rhythmic and arrhythmic 12 Hz MNS.
B) The broadband (1-48 Hz) signal following each pulse of the rhythmic and arrhythmic 12 Hz MNS.
C) The 20 Hz oscillatory response to each pulse of the rhythmic and arrhythmic 20 Hz MNS.
D) The broadband (1-48 Hz) signal following each pulse of the rhythmic and arrhythmic 20 Hz MNS. A black line along the x-axis marks timepoints where a significant difference ($p \leq 0.05$) is seen (FDR corrected).

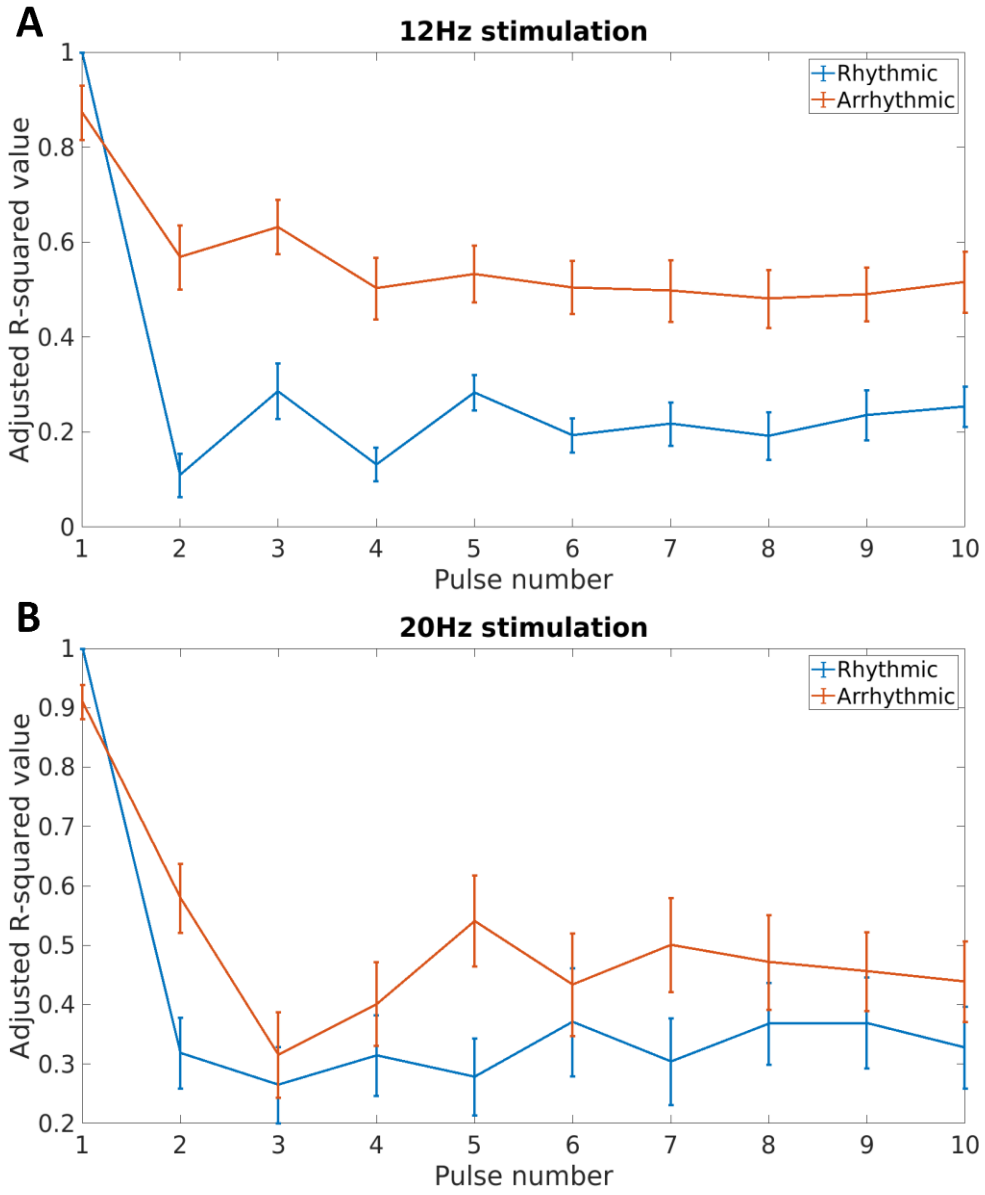

Figure 5.7. *Model fit when using a subject-specific template sensory evoked potential at each pulse.*

A figure showing the average adjusted R-squared values for each pulse of A) 12 Hz and B) 20 Hz stimulation with error bars showing the SEM.

To determine whether these effects were indeed due to entrainment rather than SEPs, we linearly modelled the responses to each pulse in each participant using the SEP associated with the first pulse of rhythmic stimulation as the template. Following the first pulse of stimulation the variability explained by the model decreased for both rhythmic and arrhythmic conditions (Figure 5.7). However, the variability explained in the arrhythmic trials was significantly higher than the rhythmic trials (12

Hz: $\chi^2(1) = 80.7$, $p < 0.001$; 20 Hz: $\chi^2(1) = 11.58$, $p < 0.001$). Examples of individual subject fits can be found in Appendix D (Figure D.3 and Figure D.4).

To further investigate these entrainment effects, we used EMD to decompose our data into IMFs. After selection of our frequency specific IMF, we compared the phase-aligned instantaneous frequency to the stimulation frequency at each phase of the oscillatory cycle. For the 12Hz rhythmic stimulation 15 out of the 19 subjects did not have an instantaneous frequency that was significantly different to 12 Hz ($p>0.05$), suggesting entrainment had occurred. For the 20Hz rhythmic trials, 5 subjects were excluded due to them having fewer than 2 'good' oscillatory cycles. Out of the 13 subjects included in the analysis 10 subjects did not have an instantaneous frequency that was significantly different to 20 Hz ($p>0.05$), suggesting entrainment occurred for those subjects.

5.3.5 Post-hoc Analyses

Due to the evidence of aftereffects seen in the paper by Morera and colleagues (Morera Maiquez, Sigurdsson, et al., 2020), we also investigated the mu-alpha (8-12 Hz) and beta (13-30 Hz) frequency band effects following both 12 Hz and 20 Hz stimulation. The only significant effect was in the mu-alpha (8-12 Hz) band during 20 Hz arrhythmic stimulation compared to rhythmic stimulation, indicating a greater degree of suppression in the rhythmic trials compared with the relative increase in mu-alpha instantaneous amplitude during 20 Hz arrhythmic stimulation as seen in Figure 5.3(D-F) ($p \leq 0.05$ for 1123-1353 ms and 1387-1487 ms, FDR corrected). There were no significant differences in the aftereffects of rhythmic and arrhythmic stimulation.

For completeness, we investigated the association between the absolute difference in individual frequencies from the stimulation frequency and the average amplitude at the frequency of stimulation (Figure 5.4). Individual frequencies were calculated using 2 s of data from the rest period between stimulation trains from all conditions (rhythmic and arrhythmic, 12 Hz and 20 Hz stimulation). The individual alpha frequency was 9.65 Hz ± 0.31

(mean ± SEM) (range: 8.00 – 12.00 Hz), while the individual beta frequency was 17.73 Hz ± 0.77 (mean ± SEM) (range: 13.00 – 25.20 Hz). There was no significant correlation between the difference from individual alpha frequency and the amplitude at 12 Hz during 12 Hz rhythmic stimulation (r_s=0.1116, p= 0.6492, N=19) nor the difference from individual beta frequency and the amplitude at 20 Hz during 20 Hz rhythmic stimulation (r_s=-0.0939, p= 0.7021, N=19).

As the beneficial effects of rhythmic MNS on tics were not restricted to the stimulated limb, as demonstrated in a recent paper by Morera and colleagues, we decided to investigate the spread of the effect using a voxel LCMV beamformer (Morera Maiquez, Sigurdsson, et al., 2020). This revealed that the source location of the amplitude increase during rhythmic stimulation was in the contralateral sensorimotor hand region (Figure 5.8).

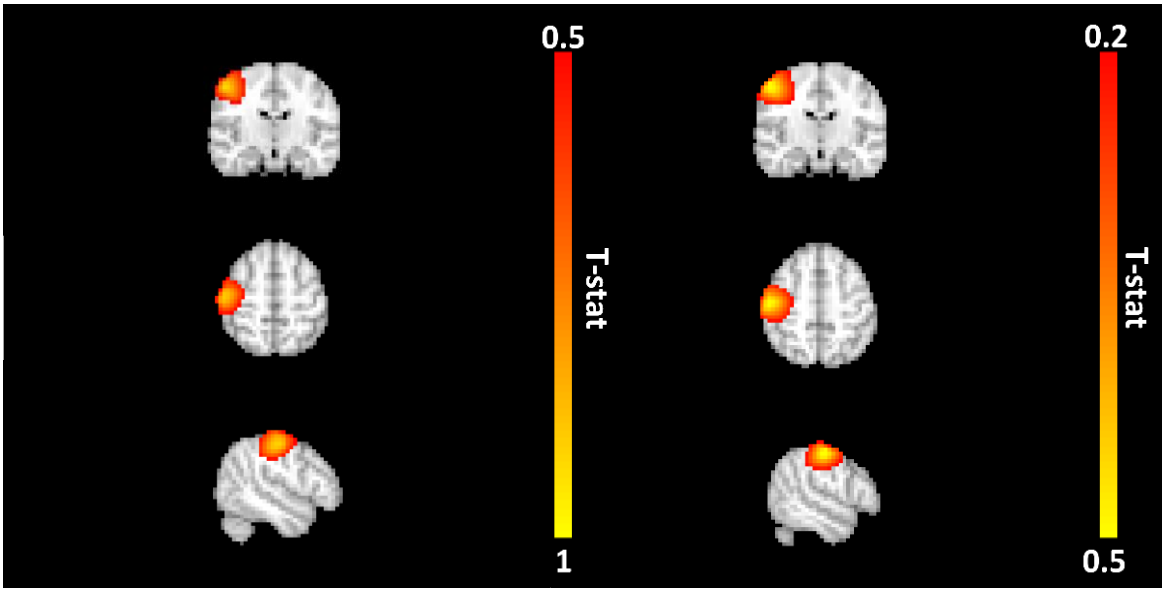

Figure 5.8. *Pseudo-T-statistical map*

A figure showing the average location of the amplitude increase during rhythmic stimulation at 12Hz (left) and 20Hz (right) localises to the contralateral sensorimotor hand region (MNI space) (neurological orientation).

5.4 Discussion

We investigated whether rhythmic MNS could be used to entrain oscillations at frequencies associated with sensorimotor inhibition, mu-alpha (12 Hz) and beta (20 Hz). Our results demonstrate that rhythmic 12

Hz stimulation resulted in an increase in the relative amplitude and ITPC at 12 Hz for the duration of the stimulation in the contralateral somatosensory cortex. Both findings can be split into two segments: 1) an increase in both amplitude and ITPC across a broad range of frequencies for the first pulse in both the rhythmic and arrhythmic trials; 2) an increase specific to the frequency of stimulation for the remainder of the pulse train, which was only seen in the rhythmic condition. We also show that for 12 Hz MNS, a template SEP fit the response to arrhythmic pulses significantly better than the response to rhythmic pulses in individual subjects. These effects were replicated in the 20 Hz condition. These results, and the evidence they provide as to whether MNS can entrain neuronal oscillations, are discussed below.

5.4.1 Steady-State Evoked Response

Thut et al., 2011 previously showed that ~10 Hz TMS caused an initial broadband increase in amplitude in both the rhythmic and arrhythmic stimulation conditions, before progressive entrainment was seen in the rhythmic condition (Thut, Veniero, et al., 2011). The authors proposed that the delivery of the first few pulses may have resulted in phase resetting of neural generators within the cortex whose frequencies of oscillation varied across a broad range of frequency bands (Thut, Veniero, et al., 2011). Therefore, phase resetting of these oscillators could have resulted in the initial broadband increase in amplitude. The subsequent pulses however will have only occurred in phase with generators oscillating in the alpha band leading to progressive synchronisation of oscillations at this frequency (Thut, Veniero, et al., 2011).

Here we show that MNS causes an initial broadband increase in relative amplitude, suggesting that peripheral stimulation triggers an initial phase reset of the neural generators within the contralateral somatosensory cortex regardless of the pattern of stimulation. In line with the theory of entrainment we see that the remainder of the rhythmic pulses cause a frequency specific increase in amplitude. This is also mirrored in the ITPC results, where the initial broadband increase aligns with the theory that numerous neural generators phase reset resulting in phase coherence

across trials. As the remaining rhythmic pulses are associated with an increased ITPC in the stimulated frequency band (and its harmonics) this shows that oscillations across trials are relatively more in phase during the stimulation suggesting synchronisation with the pulses of MNS. These findings are consistent with previous reports of a frequency specific increase in EEG power and ITPC during 12 and 19 Hz MNS (Morera Maiquez, Jackson, et al., 2020; Morera Maiquez, Sigurdsson, et al., 2020). However, one central issue in concluding that a rhythmic oscillatory response to a rhythmic stimulus is neural entrainment is whether the same data could be explained by rhythmic evoked potentials (For in-depth review please see (Thut, Schyns, et al., 2011; Zoefel et al., 2018)). If we deliver a stimulus at 12 Hz it is expected that we would see a response 12 times a second (Zoefel et al., 2018). An investigation of this possibility by Capilla and colleagues showed that the oscillatory response seen during rhythmic stimulus presentation can be modelled through linear superposition of evoked potentials, which casts doubt on the explanation of entrainment (Capilla et al., 2011). As both responses are expected to repeat at the same frequency, this makes it difficult to determine whether there is underlying entrainment (Zoefel et al., 2018). Furthermore, we would expect oscillations to continue after stimulation if entrainment had taken place (Thut, Schyns, et al., 2011; Zoefel et al., 2018). During entrainment oscillators become phase-aligned to the external source and, as phase is a free parameter, any change in phase alignment should only occur if the system is perturbed (Pikovsky et al., 2003). Here, we see a short-lived continuation of the increase in amplitude after the last pulse of MNS, but this could be due to an evoked potential associated with this last pulse.

Fitting a subject specific SEP template to each pulse demonstrated that at the individual subject level the model was significantly better at explaining the variability in the arrhythmic response compared to the rhythmic response. Also, for most subjects the phase-aligned instantaneous frequency of the selected IMF was not significantly different from the stimulation frequency. These results suggest that entrainment occurred. Furthermore, we demonstrated that the difference between the stimulation

frequency and the individual frequency was not associated with the amplitude of the response seen at the stimulation frequency. This contrasts with previous evidence that suggests that entrainment is strongest when delivered at the individual's preferred frequency (Romei et al., 2016). Preferred frequencies are usually identified during a separate experiment prior to intervention with NIBS to ensure there are no carryover effects from the stimulation. Therefore, the effect of distance of stimulation frequency from the individual's preferred frequency should be further investigated. The use of 12 Hz here rather than 10 Hz, which is the average alpha frequency, may have made it more difficult to induce entrainment effects, as the oscillatory frequency is more likely to be further from the individual alpha frequency. As 10 Hz MNS would be more tolerable compared with 20 Hz stimulation, the entrainment, and the long-term behavioural effects of this frequency of stimulation should also be explored.

Both evoked potentials and entrained oscillations are generated by synchronous firing of neuronal populations within the contralateral somatosensory cortex meaning these neurons are engaged in processing of the afferent input. As both 12 and 20 Hz stimulation have been shown to slow movement (Joundi et al., 2012; Morera Maiquez, Sigurdsson, et al., 2020; Pogosyan et al., 2009), we would expect no difference in the online behavioural effects of these stimulation frequencies. Recent research has already demonstrated the possibility that rhythmic 10 Hz MNS could be therapeutically beneficial in reducing tic frequency in Tourette syndrome patients (Morera Maiquez, Sigurdsson, et al., 2020). It is thought that there is a high level of 'sensorimotor noise' associated with the occurrence of tics in TS leading to a difficulty in discriminating between the signals preceding voluntary and involuntary movement (Ganos et al., 2015). Increasing synchronised firing of neuronal populations within the sensorimotor cortex through MNS may lead to a decrease in this noise. Alternatively, it is known that ~20 ms following median nerve stimulation there is a decrease in the amplitude of MEPs elicited by a TMS pulse to the contralateral motor cortex in a process known as short afferent inhibition (Tokimura et al., 2000). As there is thought to be a deficit in this form of

inhibition in Tourette syndrome patients it could be that continuous MNS compensates for this deficit and aids in the inhibition of tics and urges (Morera Maiquez, Sigurdsson, et al., 2020; Orth et al., 2005; Orth & Rothwell, 2009). It is therefore of interest as to whether arrhythmic stimulation also reduces the frequency of tics i.e., is the beneficial effect due to short afferent inhibition and/or a decrease in sensorimotor noise or is the rhythmicity of the stimulation important (Morera Maiquez, Sigurdsson, et al., 2020).

5.4.2 Aftereffects of Rhythmic Stimulation

The observance of a desynchronisation and rebound of sensorimotor oscillations following MNS trains is typical of that seen following one pulse of MNS (Pfurtscheller, 1981). The only significant difference in the effect seen here was a lower relative amplitude in the 8-12 Hz band during 20 Hz rhythmic stimulation compared to arrhythmic. We found no difference in aftereffects. This contrasts with recent findings which indicated that there was greater mu-alpha and beta desynchronization and increased beta rebound following 19 Hz arrhythmic stimulation (Morera Maiquez, Jackson, et al., 2020). On inspection of the data reported by Morera and colleagues, there is a short period of increased mu-alpha suppression towards the end of the stimulus train and for a short time following rhythmic stimulation, similar to what is seen in our data. This suggests that the typical mu-alpha band desynchronization seen during movement is maintained to a degree in the rhythmic condition. We hypothesise that the opposite effect of a synchronisation of mu-alpha oscillations during arrhythmic stimulation stems from the stimulation frequency containing components at both lower and higher frequencies to achieve an average frequency of 20 Hz. However, further findings by the same authors also describe greater beta desynchronization and increased beta rebound following 12 Hz arrhythmic stimulation (Morera Maiquez, Sigurdsson, et al., 2020). A potential factor for the difference in aftereffects seen is the subjective nature of the visible thumb twitch which may have led to participants in one study to experience higher intensities of stimulation. Ultimately further investigation into the aftereffects of rhythmic versus arrhythmic MNS is required. If possible future studies should ideally use

an objective method of thresholding, for example, through measurement of MEPs as is common practice with TMS.

5.4.3 Conclusion

To conclude, the evidence from this research suggests that endogenous oscillations within the somatosensory cortex can be entrained by 12 and 20 Hz rhythmic MNS. The behavioural effects of rhythmic peripheral nerve stimulation which have been demonstrated by Morera and colleagues are clinically important, however a better understanding of how these behavioural effects are produced is vital for fine-tuning their development as a therapeutic technique (Morera Maiquez, Sigurdsson, et al., 2020).

Chapter 6: Investigating neuro-metabolite changes in response to median nerve stimulation

6.1 Introduction

The previous chapter of this thesis (Chapter 5) demonstrated that rhythmic MNS, at 12 and 20Hz, resulted in an increase in both amplitude and phase synchronisation of oscillations, which was specific to the frequency of stimulation (Houlgreave et al., 2022; Morera Maiquez, Sigurdsson, et al., 2020). This modulation was restricted to the contralateral sensorimotor cortex and was not seen during arrhythmic stimulation (Houlgreave et al., 2022; Morera Maiquez, Sigurdsson, et al., 2020). This mechanism is of therapeutic interest as compared to periods of no stimulation, rhythmic application of 10Hz MNS has been shown to cause a substantial reduction in tic frequency in individuals with Tourette Syndrome (Morera Maiquez, Sigurdsson, et al., 2020). In contrast to TMS, MNS offers a relatively cheap and simple approach to modulating activity arising in sensorimotor regions which could easily be adapted into a therapeutic device for use at home for conditions, such as Tourette Syndrome, which are characterised by dysregulation within sensorimotor systems.

fMRI studies have shown that both unilateral movements and rhythmic MNS result in activation of cortical sensorimotor regions. During unilateral movements, there is activation in the contralateral sensorimotor cortex and deactivation of the ipsilateral sensorimotor cortex (Allison et al., 2000). Similarly, MNS at low frequencies (0.5-4Hz) causes activation of the contralateral primary sensory cortex, bilateral secondary sensory cortex, and the bilateral insula (Backes et al., 2000; Ferretti et al., 2007; Manganotti et al., 2009). Furthermore, this primary somatosensory cortex (S1) activation has been shown to increase with stimulation frequency, although this increase plateaus at 10Hz (Ferretti et al., 2007; Kampe et al., 2000; Manganotti et al., 2009).

Chen and colleagues used an fMRI localiser task to identify a voxel located in the motor cortex which was activated by a simple hand-clenching task

(C. Chen et al., 2017). Then using functional magnetic resonance spectroscopy (fMRS), they demonstrated a significant increase in Glu and glutamine in the voxel during the same task (C. Chen et al., 2017). Other fMRS studies have reported similar increases in Glu during motor tasks (Schaller et al., 2014; Volovyk & Tal, 2020). Meanwhile a significant decrease in GABA was reported (C. Chen et al., 2017). GABA is the main inhibitory neurotransmitter, however at any timepoint, the majority of GABA in the brain forms a metabolic pool while the minority is neurotransmitter (Rae, 2014). Therefore, MRS-GABA likely reflects tonic rather than phasic inhibition (Rae, 2014; Stagg, Bestmann, et al., 2011). On the other hand, glutamate is the main excitatory neurotransmitter, and a novel simultaneous fMRS/fMRI experiment has shown that MRS-Glu and fMRI-BOLD activation are significantly correlated over time (Ip et al., 2017). Therefore, MRS-Glu increases could reflect increases in glutamatergic neuronal firing (Ip et al., 2017).

fMRS is a powerful approach which allows non-invasive in vivo quantification of neurometabolites. Recent studies at ultra-high field (7T) in the visual (Boillat et al., 2020; Ip et al., 2017) and motor (C. Chen et al., 2017; Kolasinski et al., 2019) cortex have demonstrated the ability of fMRS to detect task related changes in metabolites such as Glu and GABA. With ultra-high field MRS, there is a higher SNR and the overlap between metabolites is lessened due to reduced peak widths meaning they are easier to quantify (Puts & Edden, 2012). This is useful for this study as we are interested in Glu and so the ability to separate its contribution from glutamine is important. Furthermore, as GABA is present in relatively low concentrations the higher SNR will aid in its quantification, as will the use of a GABA-edited sequence (Puts & Edden, 2012).

In this study we aimed to better understand the impact of repetitive MNS in healthy adults as a bridge to enhancing our knowledge into the therapeutic potential of MNS. While rhythmic MNS has been shown to influence oscillatory activity, we know little about its effects of neuro-metabolites, such as GABA and Glu. Given the neurometabolic changes associated with sensorimotor activation during movement (C. Chen et al.,

2017), we hypothesise that rhythmic and arrhythmic MNS at 10Hz may lead to an increase in Glu and a decrease in GABA concentration. This study aims to test this hypothesis using ultra-high field fMRS.

6.2 Methods

6.2.1 Participants

Seventeen healthy, unmedicated adults were recruited for this study. Two participants were excluded prior to data collection; one due to mild claustrophobia/nausea whilst in the scanner and another due to an inability to produce a sufficient muscle twitch using a comfortable MNS intensity. The remaining sample of 15 participants completed two scanning sessions in a counterbalanced order. These sessions were spaced by 10±8 days and the timing of the session held constant (i.e., if the first session was conducted in the morning so was the second) for all but one participant due to a change in availability. All participants were deemed right-handed using the Edinburgh Handedness inventory (Oldfield, 1971); mean participant age was 27±5 years and 8 were female. Participant demographics can be seen in Table 1. The study received ethical approval through the University of Nottingham School of Psychology committee.

Table 6.1. *Participant demographics for rhythmic and arrhythmic conditions.*

	N	Sex (m/f)	Age (years)	MNS intensity (mA)	Difference in intensity between sessions (mA)
Rhythmic	15	7/8	27.5±4.8	11.3±2.1	0.3±2.3
Arrhythmic	15	7/8	27.5±4.8	11.4±3.0	

Note – counterbalanced within subject design used. Data are presented as mean value ± sd.

6.2.2 MNS Stimulation paradigm

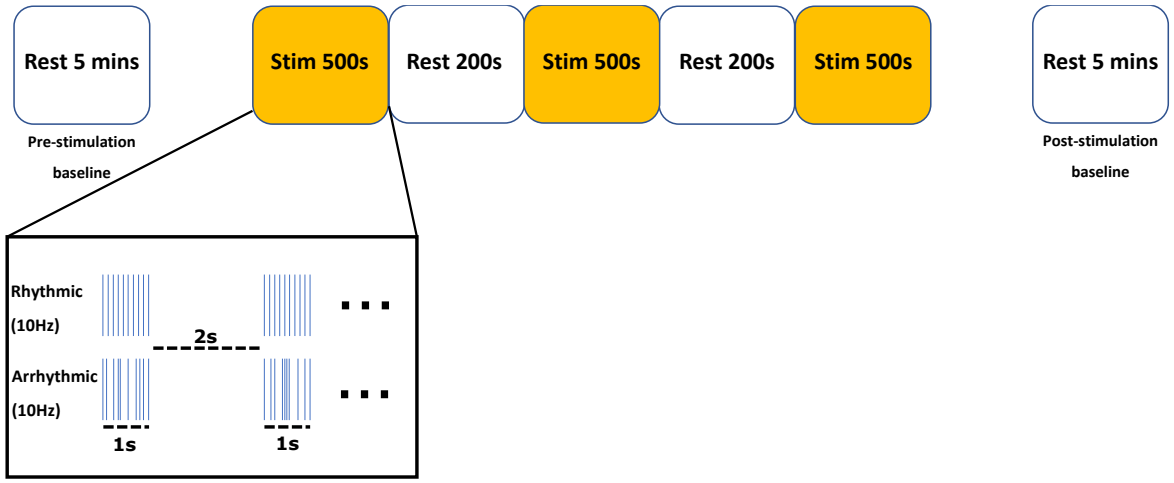

Figure 6.1. *A diagram demonstrating both the trial setup and the stimulation paradigm.*

Stimulation was delivered to the right median nerve using a Digitimer constant current stimulator model DS7A (Digitimer Ltd, UK). The maximum compliance voltage (Vmax) was set to 400V, and the pulse width was 0.2ms. The stimulation threshold for each participant was determined to be the minimum intensity which induced a visible thumb twitch (Table 6.1). During the stimulation blocks, which lasted 500s, stimulation was delivered at 10Hz for 1s followed by 2s of no stimulation (MATLAB R2017a, Mathworks, Natick, MA). Stimulation was not delivered constantly for the 500s to ensure participant comfort. The three stimulation blocks were interspersed with blocks of no stimulation lasting 200s. Each participant completed one session of rhythmic stimulation and one of arrhythmic stimulation. The arrhythmic session was used to investigate whether similar neurometabolic changes occurred when stimulation had a random interpulse interval but the same average frequency (minimum interpulse interval of 0.01s) (Figure 6.1).

6.2.3 MR acquisitions

The MRI data were acquired using a Philips 7T Achieva MRI scanner (Philips Healthcare, Best, The Netherlands) with a 32-channel radio frequency head coil situated in the Sir Peter Mansfield Imaging Centre, Nottingham UK. A pair of prism glasses were used to allow participants to view a nature documentary displayed on a screen outside of the scanner bore.

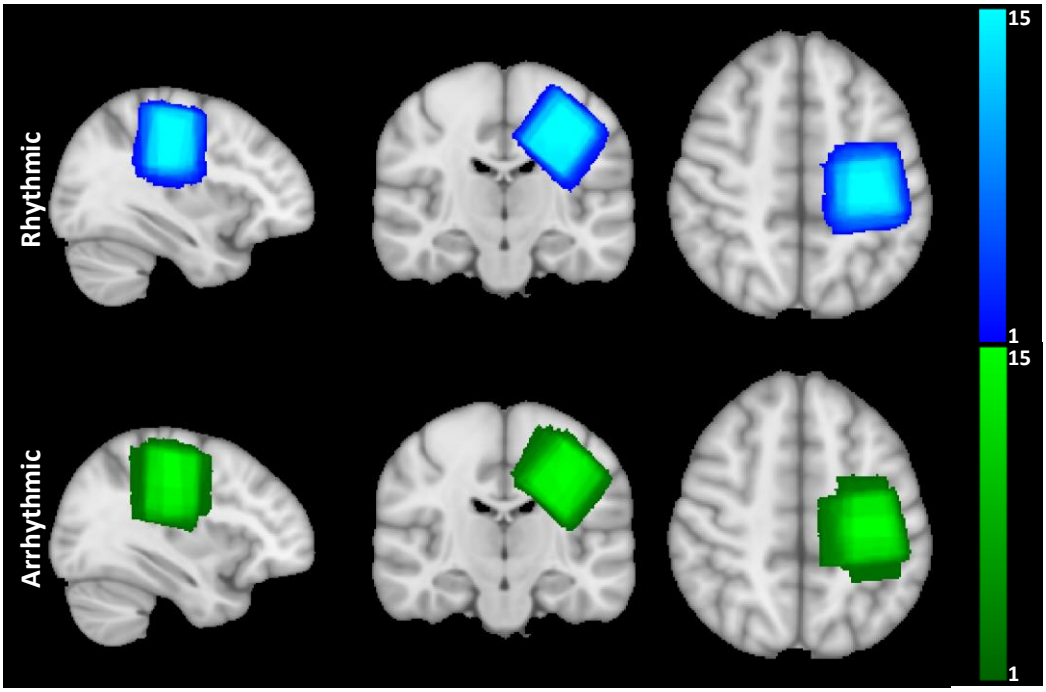

Figure 6.2. *MRS voxel (30×30×30mm^3) overlaps for the rhythmic and arrhythmic sessions centred on the hand knob of the contralateral sensorimotor cortex. Colourbars signify the number of subjects.*

T_1-weighted anatomical images were acquired using a MPRAGE sequence (TR/TE/TI=7.3/3.4/999.79ms, FA=8°, FOV=256×256×180mm^3, isotropic resolution=1mm^3) for tissue segmentation (using SPM12) and planning of the MRS voxel. ^{1}H MRS data were acquired from a voxel of interest (30×30×30mm^3) placed over the contralateral hand area (Figure 6.2) using a MEGA sLASER sequence optimised for GABA (TR/TE=4640/72ms, spectral width = 4kHz). Water suppression was achieved using VAPOR (variable pulse power and optimised relaxation delay) (Tkáč et al., 1999). B_0 shimming was accomplished using a vendor-provided second-order projection-based method.

Three consecutive MRS scans were performed during each experimental session. The MEGA sLASER parameters were identical for each, except for number of signals averaged and hence total scan time. Pre and post MNS scans occurred without stimulation and lasted approximately 5mins 20s and consisted of 64 averages consisting of on/off pairs. Scans taken during MNS in both the rhythmic and arrhythmic conditions lasted approximately 32mins 5s and consisted of a total of 410 averages consisting of on/off pairs. For two participants in one session, the voxel was replanned using a new MPRAGE following the pre-stimulation baseline due to movement at the beginning of the stimulation block.

6.3 Data analysis

The raw spectral data were processed using an in-house MATLAB script (available at https://github.com/aberrington/specReg) (MATLAB R2020a, Mathworks, Natick, MA). First, the raw data were coil combined and eddy current corrected before being split into ON (GABA editing) and OFF (no GABA editing) spectra. A template for spectral registration was defined as the mean of the OFF spectra for that participant. This template was used for spectral registration of the free induction decay (FID) data (Near et al., 2015). Spectra were rejected if the mean square error around the Choline (Cho) peak differed from the mean by more than 3 standard deviations. The aligned ON and OFF spectra were then subtracted to create a GABA difference spectrum.

For the fMRS stimulation scan, a block-wise averaging method was used with a block size of 54 pairs for the stimulation blocks and 21 pairs for the rest blocks. We obtained 5 datapoints for each subject session with one datapoint per block. For the pre- and post-stimulation scans we obtained 1 datapoint for each, consisting of 64 averages.

The GABA difference (edited on-off spectra) and off spectra were fitted in LCModel (Provencher, 2001). Shaped refocusing pulse information with interpulse timings and customised 2D density matrix simulations were utilised to generate metabolite basis spectra (Govind et al., 2015; Tkáč,

2008). The LCModel *nobase* control parameter was set to false to enable baseline fitting. The spectral range was set to 1.8-4.2ppm. The tCr and Glu concentrations were quantified using the LCModel output for the OFF spectra, while GABA was quantified using the difference spectra. Concentrations are presented as a ratio relative to tCr. Participants would have been excluded if the SNR of NAA (N-acetylaspartate) was less than 40 or if the linewidth of unsuppressed water was greater than 15Hz (0.05 ppm). The SNR was calculated using the FID-A MRS toolbox (https://github.com/CIC-methods/FID-A) (Simpson et al., 2017). One participant was excluded due to having noisy spectra (Female, 37 years, right-handed, 11.5 mA intensity for both conditions).

6.3.1 Statistical analysis

Changes in ratios were calculated with respect to the pre-stimulation baseline for that session. Bayesian one-sided paired sample T-tests were used to compare the pre-stimulation baseline with the stimulation blocks and post-stimulation block. Bayesian two-sided paired sample T-tests were used to compare the differences from the pre-stimulation baseline between the rhythmic and arrhythmic stimulation conditions. All statistical analyses were performed using JASP (JASP Team, 2022). A Bayes Factor of BF_{10} was used with a default Cauchy prior width of 0.707 due to there not being enough knowledge to inform the choice of a prior (Ly et al., 2020; Rouder et al., 2012). Following the analysis, a Bayes factor robustness check was carried out to ensure the Bayes factor was robust to a change in the prior. Where data failed the assumption of normality, a Bayesian Wilcoxon signed-rank test was used.

6.4 Results

Table 6.2. *Data quality metrics for all scans in the rhythmic and arrhythmic conditions (N=14).*

	Rhythmic baseline	Rhythmic post-stimulation	Rhythmic stimulation	Arrhythmic baseline	Arrhythmic post-stimulation	Arrhythmic stimulation
Linewidth of unsuppressed water peak (Hz)	11.1 ± 1.0	11.2 ± 0.9	10.9 ± 0.9	11.0 ± 1.4	11.3 ± 1.2	11.0 ± 1.0
SNR of NAA	281.8 ± 41.2	274.0 ± 35.4	693.7 ± 86.5	273.5 ± 51.5	259.4 ± 47.5	659.3 ± 114.0
GABA CRLB (%)	7.9 ± 2.3	7.9 ± 1.9	7.3 ± 1.3	7.8 ± 1.5	7.6 ± 1.6	7.6 ± 1.9
Glu CRLB (%)	3.4 ± 0.5	3.5 ± 0.5	3.4 ± 0.5	3.4 ± 0.6	3.4 ± 0.5	3.4 ± 0.5

Data are presented as mean value ± sd. SNR, signal-to-noise ratio; NAA, N-acetylaspartate; GABA, γ-aminobutyric acid; CRLB, Cramér–Rao lower bound; Glu, glutamate.

The data quality metrics of the MRS data including SNR, unsuppressed water linewidth and Cramér–Rao lower bounds (CRLBs) for Glu and GABA can be seen in Table 6.2. The low linewidth of the water peak implies that good shimming was achieved, and the high SNR suggests that the spectra fits were reliable. Figure 6.3 shows the quality of both the GABA and glutamate LCModel spectra fit at the individual-level, from a representative subject, and at the group-level during the fMRS stimulation blocks. To check that we could reliably fit glutamine from glutamate, we ensured that the pair-wise correlation coefficient for all scans was greater than -0.5.

Figure 6.2 shows reliable positioning of the MRS voxel over the contralateral hand area for both stimulation sessions. This voxel was composed of 67 ± 3% white matter (WM), 29 ± 3% grey matter (GM) and 4 ± 2% cerebrospinal fluid (CSF). Paired samples t-tests confirmed that there were no significant differences in voxel composition for WM, GM or CSF between rhythmic and arrhythmic sessions (all $p > 0.2$).

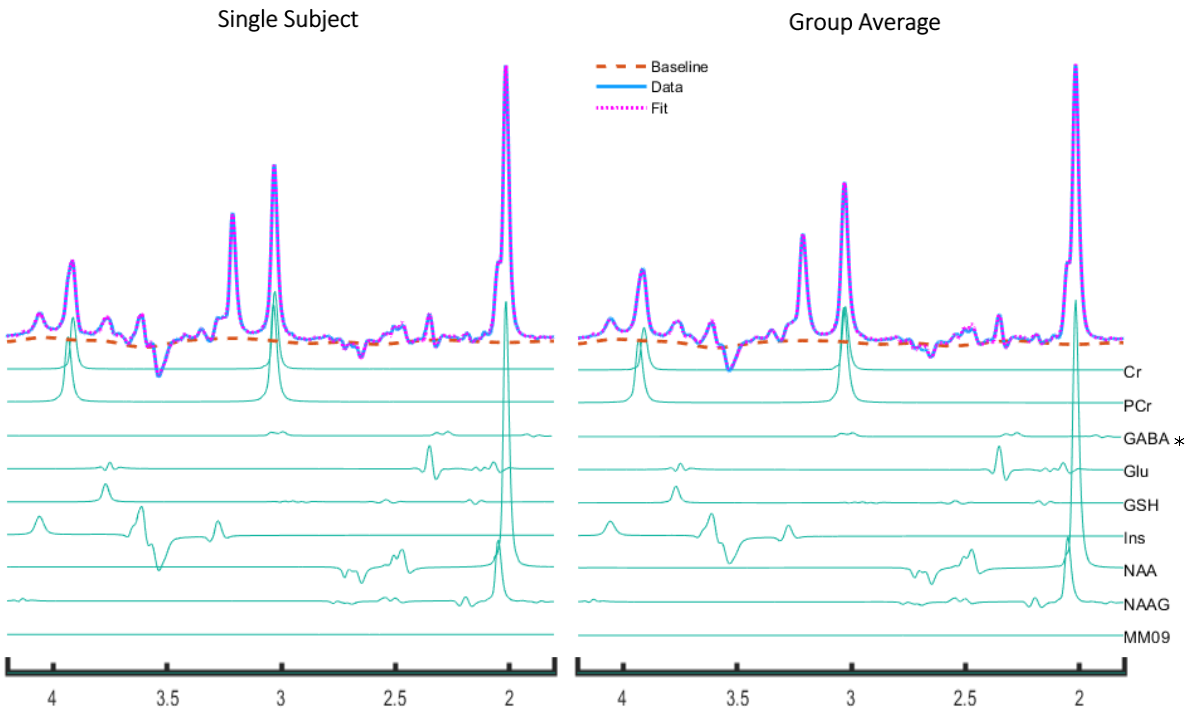

Figure 6.3. *Example spectra from an individual subject session (left) and the group average (right) showing the average spectra from the fMRS stimulation scan (orange) and the average LCModel fit (N = 14) (pink dashed line). (*GABA spectra were plotted based on the difference spectra).*

Table 6.3. *Concentration ratios for GABA/tCR and Glu/tCR for the different timepoints in the rhythmic condition.*

			Change during stimulation			Change during rest			Change post-stimulation	
	Baseline	**Stimulation**	**Abs**	**%**	**Rest**	**Abs**	**%**	**Post**	**Abs**	**%**
Glu /tCR	0.77 ±0.08	0.78 ±0.06	0.01 ± 0.03	1.36 ± 4.67	0.79 ± 0.07	0.02 ± 0.04	2.18 ± 4.86	0.78 ± 0.07	0.00 ± 0.03	0.80 ± 4.51
GABA /tCR	0.08 ±0.01	0.08 ±0.01	0.00 ± 0.02	-0.25 ± 23.51	0.09 ± 0.01	0.01 ± 0.02	13.75 ± 32.98	0.08 ± 0.02	0.00 ± 0.02	1.34 ± 28.12

The change in this ratio from the pre-stimulation baseline are reported as both absolute change (abs) and percentage change (%). Data are presented as mean value ± sd. N = 14.

Table 6.4. *Concentration ratios for GABA/tCR and Glu/tCR for the different timepoints in the arrhythmic condition.*

			Change during stimulation			Change during rest			Change post-stimulation	
	Baseline	**Stimulation**	**Abs**	**%**	**Rest**	**Abs**	**%**	**Post**	**Abs**	**%**
Glu /tCR	0.81 ±0.08	0.81 ±0.10	0.00 ±0.05	-0.25 ±5.80	0.82 ±0.09	0.01 ±0.04	1.23 ±4.92	0.81 ±0.09	0.00 ±0.03	0.34 ±3.71
GABA/ tCR	0.08 ±0.01	0.08 ±0.01	0.00 ±0.01	-2.48 ±14.50	0.08 ±0.01	0.00 ±0.01	5.19 ±16.40	0.08 ±0.02	0.00 ±0.02	5.22 ±22.38

The change in this ratio from the pre-stimulation baseline are reported as both absolute change (abs) and percentage change (%). Data are presented as mean value ± sd. N = 14.

Figure 6.4 shows the mean percentage change in metabolite levels from the pre-stimulation baseline, during the stimulation and post-stimulation blocks, for both the rhythmic and arrhythmic sessions. The GABA/tCR and Glu/tCR concentration ratios for the rhythmic and arrhythmic sessions are presented in Table 6.3 and Table 6.4, respectively.

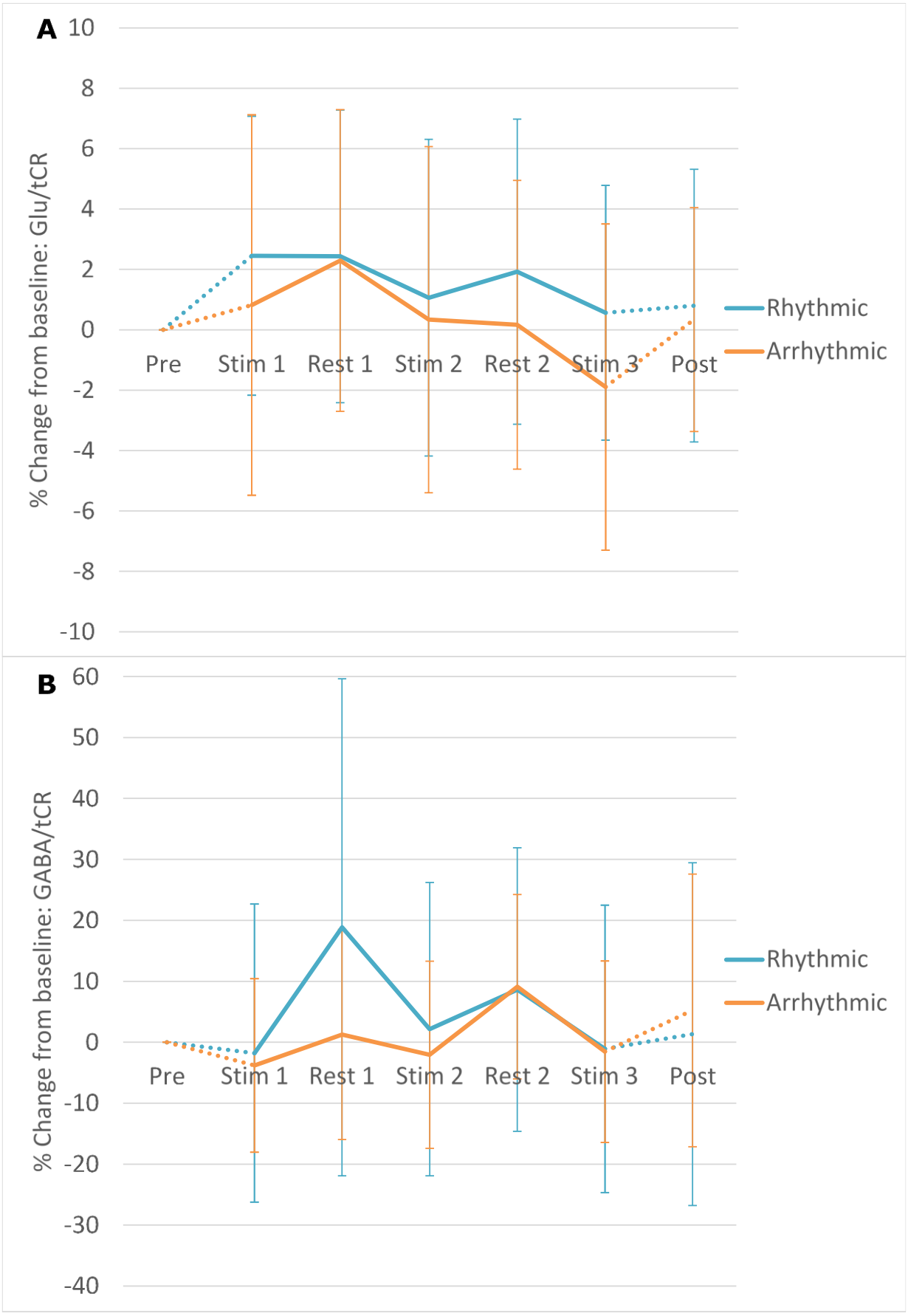

Figure 6.4. *The mean change from the pre-stimulation baseline in Glutamate (A) and GABA (B) for both the rhythmic (blue) and arrhythmic (orange) conditions (N = 14). The error bars represent the standard deviation.*

The use of Bayesian paired T-tests allowed us to determine whether there was evidence to support our hypothesis, that GABA would decrease and Glu would increase during MNS compared to the pre-stimulation baseline. BF_{10} values above 1 suggest that there is evidence to support the alternative hypothesis (H_1) while in contrast, values below 1 suggest that there is evidence to support the null hypothesis (H_0). Our analysis demonstrated that there is anecdotal evidence ($1 < BF_{10} < 3$) that rhythmic stimulation caused an increase in glutamate compared to baseline in the first (BF_{10} = 2.388, median effect size = -0.464) stimulation and rest (BF_{10} = 1.867, median effect size = -0.427) fMRS blocks (Table 6.5). There was also anecdotal evidence for an increase in glutamate during the first rest block (BF_{10} = 1.634, median effect size = -0.407) for the arrhythmic condition (Table 6.5). For both rhythmic and arrhythmic stimulation, the evidence against our hypothesis, that stimulation would cause a decrease in GABA compared to baseline, ranged from anecdotal to moderate ($1/10 < BF_{10} < 1$) (Table 6.6). When comparing the difference-from-baseline measures for the rhythmic and arrhythmic stimulation conditions, we found evidence to suggest that there is no difference in the effect of rhythmic and arrhythmic stimulation on Glu or GABA concentrations within the sensorimotor hand area (Table 6.7).

Table 6.5. *Bayes factors (BF_{10}) for the comparison of Glu/tCr concentrations between fMRS blocks in the rhythmic and arrhythmic conditions and the pre-stimulation baseline (N = 14).*

BF_{10}	Stimulation 1	Rest 1	Stimulation 2	Rest 2	Stimulation 3	Post-stimulation
Rhy	2.388*	1.867*	0.453ǂ	0.988ǂ	0.358ǂ	0.429ǂ
Arr	0.261ǂǂ	1.634*	0.333ǂ	0.300ǂǂ	0.135ǂǂ	0.352ǂ

*Rhy, rhythmic; Arr, arrhythmic; *, anecdotal evidence for H_1; ǂ, anecdotal evidence for H_0; ǂǂ, moderate evidence for H_0.*

Table 6.6. *Bayes factors (BF_{10}) for the comparison of GABA/tCr concentrations between fMRS blocks in the rhythmic and arrhythmic conditions and the pre-stimulation baseline (N = 14).*

BF_{10}	Stimulation 1	Rest 1	Stimulation 2	Rest 2	Stimulation 3	Post-stimulation
Rhy	0.652ǂ	0.110ǂǂ	0.301ǂǂ	0.138ǂǂ	0.565ǂ	0.354ǂ
Arr	0.961ǂ	0.259ǂǂ	0.585ǂ	0.106ǂǂ	0.464ǂ	0.169ǂǂ

Rhy, rhythmic; Arr, arrhythmic; ǂ, Anecdotal evidence for H_0; ǂǂ, moderate evidence for H_0.

Table 6.7. *Bayes factors (BF_{10}) for the comparison of the difference-from-baseline measures for the rhythmic and arrhythmic conditions (N = 14).*

Rhythmic vs Arrhythmic	BF10 Glu	BF10 GABA
Stimulation block 1	0.332ǂ	0.270ǂǂ
Rest block 1	0.272ǂǂ	0.697ǂ
Stimulation block 2	0.274ǂǂ	0.284ǂǂ
Rest block 2	0.387ǂ	0.281ǂǂ
Stimulation block 3	0.519ǂ	0.281ǂǂ
Post-stimulation	0.275ǂǂ	0.406ǂ

ǂ, anecdotal evidence for H_0; ǂǂ, moderate evidence for H_0.

6.5 Discussion

This fMRS study investigated the effects of rhythmic and arrhythmic MNS on neuro-metabolite concentrations in the contralateral sensorimotor cortex. We found that rhythmic, but not arrhythmic, MNS caused an initial increase in Glu. However, during the first rest block for both conditions there was an increase in Glu compared to baseline. Previous studies involving a motor task have also reported increases in Glu (C. Chen et al., 2017; Schaller et al., 2014; Volovyk & Tal, 2020). Conversely, neither stimulation condition effected the GABA concentration. Our results contrast with Chen et al. (2017), where a decrease in GABA was reported during a hand clenching task. However, changes in GABA have not been reliably reported. Another hand clenching task at 3T rather than 7T, reported an increase in Glu but no change in GABA (Volovyk & Tal, 2020). Furthermore, a pre-clinical study demonstrated an increase in Glu but no change in GABA in the contralateral S1 of mice during electrical hind paw stimulation

(Seuwen et al., 2019). Here we saw an initial increase in Glu which was not sustained. When the difference-from-baseline measures were compared there were no differences between the effects of rhythmic and arrhythmic stimulation on Glu and GABA concentration.

The only difference between the rhythmic and arrhythmic conditions was the rhythmicity of the stimulation. For both patterns of stimulation, each pulse of MNS will cause synchronous firing of neuronal populations within the contralateral somatosensory cortex meaning excited pyramidal cells will be releasing glutamate synchronously. Whilst there was no difference in the effects on Glu between the rhythmic and arrhythmic conditions, only rhythmic had evidence to support a rise in Glu during the first block of stimulation when compared to baseline. During the rhythmic stimulation the additional effects of entrainment may lead to the recruitment of more neurons. We speculate that this may result in a higher initial concentration of Glu in the rhythmic condition which may not be as evident in the arrhythmic condition. As previous research into the neurometabolic effects of movement largely focuses on cued rhythmic movements (C. Chen et al., 2017; Schaller et al., 2014), it would be interesting to see the effect on Glu when movements are cued arrhythmically. For both rhythmic and arrhythmic stimulation, the stimuli are occurring predictably every third second in the stimulation block. Glu has been shown to be lower during repetitive compared to novel trials (Apšvalka et al., 2015), and here we only found a significant increase in the initial blocks of stimulation. Therefore, it may be that in both conditions Glu reduces over time due to the repetitive nature of the stimulation. This adaptation has not been shown in previous MRS studies involving motor tasks (C. Chen et al., 2017; Schaller et al., 2014; Volovyk & Tal, 2020), but here the stimulation is at a high frequency and externally driven.

Our hypotheses for this study did not consider the entrainment effects of the rhythmic stimulation on sensorimotor oscillations (Houlgreave et al., 2022; Morera Maiquez, Sigurdsson, et al., 2020). GABA is thought to be involved in the generation of synchronised oscillations (Gonzalez-Burgos & Lewis, 2008). Previous electrophysiological studies have demonstrated a

clear relationship between GABA and oscillations within the sensorimotor cortex. Elevation of the effects of extracellular GABA, using transporter blocker tiagabine and extrasynaptic positive allosteric modulator gaboxadol, resulted in an increase in the power of all frequency bands up to and including beta oscillations (Nutt et al., 2015). Higher levels of resting MRS-GABA in the motor cortex have been associated with higher power during the post-movement beta rebound (Gaetz et al., 2011). Given this relationship between GABA and oscillatory activity, an increase in GABA related to entrainment may have been expected in the rhythmic condition (Spooner et al., 2022). However, the effects of entrainment are, by definition, restricted to the frequency of stimulation. During rhythmic MNS a desynchronisation of frequencies within the 8-30Hz range was still evident (Houlgreave et al., 2022; Morera Maiquez, Sigurdsson, et al., 2020). Moreover, any inhibitory effects of entrainment through MNS will be phasic. Phasic inhibition relates to synaptic GABA release leading to short-lived neuronal hyperpolarisation (Brickley & Mody, 2012). Whereas extrasynaptic GABA binding leads to a more long-lived tonic inhibition (Brickley & Mody, 2012). There is evidence to suggest that there is no association between MRS-GABA and TMS measures which are thought to reflect activity involving synaptic GABA in adults (Dyke et al., 2017; Stagg, Bestmann, et al., 2011; Tremblay et al., 2013). This suggests that MRS-GABA may be a measure of tonic rather than phasic inhibition. As such, increases in phasic GABAergic activity relating to MNS induced entrainment are unlikely to be quantifiable through MRS. However, it is worth noting that there is evidence for an association between MRS-GABA and TMS measures in paediatric populations (Harris et al., 2021).

One limitation of this study is that the stimulation was not constant during the stimulation blocks. Instead, the stimulation was delivered for 1 second followed by 2 seconds of no stimulation. This choice was made to ensure participant comfort during the experiment. However, we do not expect that any changes in the concentration of metabolites caused by the stimulation would return to baseline levels during the 2 second period of rest. Data from previous studies shows a gradual return of these metabolite concentrations to baseline following a movement task (C. Chen et al.,

2017), and a gradual increase in concentration during the task even when there were brief pauses between movements (Kolasinski et al., 2019). Another limitation is that the sizes and therefore SNR of the pre-stimulation baseline, rest blocks, stimulation blocks and post-stimulation blocks were not equivalent. As a result, the data may have been less variable in the stimulation blocks compared to the other experimental blocks, nevertheless, the Cramér–Rao lower bounds for Glu and GABA were similar across all scans.

To conclude, this chapter demonstrates that there is an initial increase in glutamate with rhythmic but not arrhythmic stimulation. However, there was no difference in the difference-from-baseline measures for Glu and GABA when the rhythmic and arrhythmic conditions were compared. Therefore, the neuromodulatory effects of rhythmic and arrhythmic stimulation are similar despite the entrainment seen with rhythmic stimulation. New evidence suggests that both rhythmic and arrhythmic stimulation may be effective in reducing tics in TS (Iverson et al., 2023; Morera Maiquez, Sigurdsson, et al., 2020). Hence the beneficial effects in patients are unlikely to be associated with tonic changes in concentrations of neurometabolites or entrainment and are more likely to be due to a decrease in neuronal noise caused by each pulse of the stimulation regardless of the pattern as theorised in Chapter 5.

Chapter 7: General Discussion

This thesis explores the neural correlates of premonitory urge and the effects of rhythmic median nerve stimulation. The first aim of this thesis was to identify the neural correlates of premonitory urge (Chapter 3) and to validate whether these regions could be identified through a model-free approach without prior specification of task timings (Chapter 4). The second aim of this thesis was to explore the oscillatory and neurometabolic effects of rhythmic median nerve stimulation in the contralateral sensorimotor cortex (Chapter 5, Chapter 6). In this chapter I will summarise the main findings of this thesis in the context of Tourette Syndrome research. For clarity, I will first focus on Chapters 3 and 4 in 'Identifying the neural correlates of premonitory urge', then Chapters 4 and 5 in 'The mechanism of rhythmic median nerve stimulation as a potential therapy for Tourette Syndrome'.

7.1 Identifying the neural correlates of premonitory urge

Premonitory urge is thought to be a negative reinforcer of tic expression in TS (Capriotti et al., 2014). Previous fMRI research of premonitory urge in TS has described the involvement of the insula, ACC, SMA, operculum, primary somatosensory cortex, putamen, and amygdala (Bohlhalter et al., 2006; Neuner et al., 2014; Wang et al., 2011). However, the analysis for these studies either focussed on the seconds before a tic, under the assumption that at these timepoints urge would be at its highest, or by comparing the activation during volitional tic performance to spontaneous tic performance (Bohlhalter et al., 2006; Neuner et al., 2014; Wang et al., 2011).

In Chapter 3 we use a blink suppression fMRI paradigm involving continuous subjective urge ratings to explore the neural correlates of the urge-to-blink, blink suppression and blinking. We identified activation of separable regions of the insula during different components of the paradigm, using a parametric model of the urge ratings, a block comparison of 'Suppress' versus 'Okay to blink' and blink-related activation. We propose that the posterior insula is involved in the initial

processing of the urge sensations, and that these feelings become conscious and emotionally salient through integration of information in the ventral-anterior insula (Craig, 2009; Craig et al., 2000; Kelly et al., 2012; Kurth et al., 2010). During suppression the dorsal-anterior insula may integrate task information to inhibit the automatic blink behaviour during periods of increased urge, due to this subregion being commonly active across task modalities (Kelly et al., 2012; Kurth et al., 2010). We theorised that activation of the mid-insula during blinks on the other hand may be linked to the sensorimotor components of the action (Kelly et al., 2012; Kurth et al., 2010).

In addition to the insula activation, both the MCC and SMA were active during suppression and blinks, whereas the ACC was active during feelings of urge. The MCC and insula are understood to be the limbic motor and sensory regions respectively (Craig, 2009; Craig et al., 2000), whereas the pregenual ACC is thought to be involved in emotional and interoceptive experiences (Caruana et al., 2018). A previous meta-analysis has shown an overlap in the right insula and MCC during the urge-to-act (S. R. Jackson et al., 2011). From these findings they suggested that the urge-to-act may be generated by a loop involving the anterior insula, the MCC and the mid-insula (S. R. Jackson et al., 2011). The posterior and mid-insula were thought to be involved in the processing of the somatosensory urge sensations, but that perception of these sensations was associated with the anterior insula. The MCC was hypothesized to initiate the action in response to the urge, whereas the mid-insula would assess whether the urge-to-act had been satisfied. Our data support this theory of an urge-to-act loop involving separable regions of the insula and the MCC. Based on the overlap between activation of the insula and MCC during the urge to swallow, yawn, urinate and tic, as shown in the meta-analysis by Jackson and colleagues (S. R. Jackson et al., 2011), we would expect a similar pattern of insula and cingulate cortex activation to what is shown here during the urge-to-tic.

Premonitory urges are covert, and therefore it is difficult to identify the neural correlates of urge. In TS there is an added difficulty that due to

conventional imaging techniques relying on the brain staying in the same position throughout the scan, we would lose large amounts of data due to motion artefacts if participants were asked to tic in the scanner. Therefore, in Chapter 4, we reanalysed the blink suppression paradigm data using a deconvolution approach called paradigm free mapping (Gaudes et al., 2013; Uruñuela et al., 2020). As blinks can be performed in the scanner without the issues associated with movement this allowed us to explore whether the same brain activity could be identified without prior specification of timing. We showed that activation within the right insula and cingulate regions can be identified using this approach. These regions have been consistently identified in research into the urge-to-act (Abi-Jaoude et al., 2018; Berman et al., 2012; Bohlhalter et al., 2006; S. R. Jackson et al., 2011; Lerner et al., 2009; Mazzone et al., 2010), however we weren't able to separately cluster regions involved in suppression and urge. The reasons for this will be described in 7.1.1.

7.1.1 Limitations and future work

A limitation of this study is that the movement caused by continuous urge rating resulted in activation of sensorimotor regions, making it difficult to determine whether these regions have a role in generating urge. Furthermore, participants may have experienced urge differently due to the instruction to rate the urge thereby potentially affecting the BOLD response associated with urge. However, these subjective urge rating are needed to validate the model free approach. Once validated PFM could be used to identify these regions without the need for subjective urge ratings.

In future, this study will be replicated in TS participants who will be asked to suppress their tics in the scanner and to continuously rate their self-estimated urge-to-tic. This will allow us to identify whether the same separable subregions of the insula are active during tic suppression and the urge-to-tic. We would expect that participants will tic during this suppression period and so participants with tics that are less likely to lead to a loss of data will be recruited for this study. However, this will lead to an unrepresentative subsample of TS patients. Therefore, we will also run a parallel study using wearable optically pumped MEG (OPM-MEG) (as

described in Appendix E (page 214)). During this study participants will be asked to alternately suppress and allow their tics. Analysis will focus on the regions identified from the fMRI study as being involved in the urge-to-tic (pilot data in Appendix E (page 220)). Similarly, healthy control participants will be asked to take part in a similar blink suppression paradigm in the OPM-MEG to explore the oscillatory dynamics of the urge-to-act.

A limitation of the paradigm free mapping analysis in Chapter 4 is that we could not separately cluster activity relating to suppression and urge. This may be because the urge-to-blink arises due to the act of suppression. However, the number of time points selected for the cluster analysis was relatively low. Therefore, in future, the use of the stability selection technique to select the lambda used to estimate the activity-inducing signal rather than the BIC may result in less sparse activation estimates. Having more data to cluster will allow us to determine whether the urge and suppression activation maps could be separated using PFM.

7.2 The mechanism of rhythmic median nerve stimulation as a potential therapy for Tourette Syndrome

A recent double-blind, sham-controlled clinical trial has shown a significant reduction in tic frequency and severity following rhythmic 10 Hz MNS in comparison to sham stimulation (50% of threshold) or the 'treatment as usual' control group (Maiquez et al., 2023). The mechanism of action has not been definitively shown, but it is hypothesised to be due to entrainment of oscillations within the sensorimotor cortex, with stimulation being delivered at a frequency associated with the inhibition of movement (Morera Maiquez, Sigurdsson, et al., 2020). In Chapter 5 we delivered trains of rhythmic and arrhythmic median nerve stimulation at 12 and 20 Hz whilst participants sat in an MEG scanner to explore the oscillatory effects of rhythmic MNS. We demonstrated a frequency specific increase in both amplitude and intertrial phase coherence in the contralateral sensorimotor cortex during rhythmic but not arrhythmic stimulation. This replicated previous findings by Morera Maiquez and colleagues (Morera Maiquez, Sigurdsson, et al., 2020). To determine whether these effects

were due to entrainment or steady-state sensory evoked potentials we used a subject specific template SEP and showed that this template was significantly better at explaining the variability in the arrhythmic condition compared to the rhythmic condition. Furthermore, we used empirical mode decomposition to decompose the mean trial data for each participant, associated with pulses 3-10 of the rhythmic 12Hz and 20Hz stimulation, into intrinsic mode functions (Quinn et al., 2021). For the majority of the participants, the phase-aligned instantaneous frequency of the selected intrinsic mode function was not significantly different from the stimulation frequency. These results suggest that entrainment occurred in the rhythmic condition.

In Chapter 6, we further explored the effects of median nerve stimulation by delivering rhythmic and arrhythmic 10 Hz median nerve stimulation during a magnetic resonance spectroscopy scan. There was an initial increase in glutamate in the rhythmic condition, which was not seen during the arrhythmic condition. However, there was no difference in the difference-from-baseline measures for the rhythmic and arrhythmic conditions. This suggests that there aren't large differences between rhythmic and arrhythmic stimulation on concentrations of the main excitatory (glutamate) and inhibitory (GABA) neurometabolites in the brain.

Recent research suggests that both rhythmic and arrhythmic MNS can significantly reduce the frequency of tics in TS (Iverson et al., 2023), suggesting that the beneficial effects are not due to entrainment of oscillations in the sensorimotor cortex. It is thought that there is a high level of 'sensorimotor noise' associated with the occurrence of tics in TS leading to a difficulty in discriminating between the signals preceding voluntary and involuntary movement (Ganos et al., 2015). Therefore, I hypothesise that increasing synchronised firing of neuronal populations through entrainment or the generation of sensory evoked potentials within the sensorimotor cortex may lead to a decrease in this noise.

7.2.1 Limitations and future work

The studies involving MNS are limited by the lack of a sham control. However, prior to the clinical trial (Maiquez et al., 2023), I analysed MEG data from two pilot participants and the data did not show an increase in amplitude at the frequency of stimulation during sham (50% of threshold) stimulation. Due to the lack of persistent change in neurometabolite concentration during rhythmic and arrhythmic stimulation we would also predict a lack of neurometabolite changes during sham stimulation. Another limitation is that the SNR of the pre-stimulation baseline, rest blocks, stimulation blocks and post-stimulation blocks were not equal. Therefore, the data in the baseline, rest and post-stimulation blocks may have been more variable than the stimulation blocks. However, the Cramér–Rao lower bounds for Glu and GABA were similar across all scans. We did not deliver stimulation constantly during the stimulation blocks. This was to ensure participant comfort. However, we do not expect that any changes in the concentration of metabolites caused by the stimulation would return to baseline levels during the 2 second period of rest (C. Chen et al., 2017; Kolasinski et al., 2019).

In future, a median nerve stimulation paradigm involving rhythmic, arrhythmic, sham and no stimulation conditions could be delivered to TS participants whilst being scanned using the wearable optically pumped MEG scanner (description of OPM-MEG in Appendix E (page 214)). The oscillatory changes within the sensorimotor cortices could be correlated with changes in the frequency and intensity of tics, while oscillatory changes in the insula could be correlated with changes in urge intensity. A similar study using OPM-MEG could be used to explore the dose-response curve of rhythmic MNS both on the frequency and intensity of tics and the entrainment within the contralateral sensorimotor cortex. Furthermore, as the rhythmicity of the stimulation does not appear to matter, suggesting the beneficial effects of stimulation are not purely due to entrainment, perhaps a behavioural study exploring the use of lower frequency stimulation on tics may be beneficial as lower frequencies would be more tolerable. To explore the neural noise hypothesis the 1/f noise could be

compared for TS participants before and after delivery of 10 Hz rhythmic and arrhythmic MNS (Adelhöfer et al., 2021; Münchau et al., 2021).

7.3 Overall conclusions

To conclude this thesis showed that the urge-to-act may be generated by a loop involving the posterior insula, the ventral-anterior insula and the ACC. The execution of the action in response to this urge is hypothesised to be generated by the MCC and SMA. Paradigm free mapping was able to identify activation within the right insula and cingulate during the blink suppression paradigm. However, different methods to select the lambda used to estimate the activity-inducing signal should be explored to reduce the sparsity of the activation estimates. Collection of fMRI data during a tic suppression paradigm where TS participants continuously rate their urge-to-tic will allow us to identify whether the same separable subregions of the insula are active during tic suppression and the urge-to-tic. This thesis also showed that there are differing neuronal effects of rhythmic and arrhythmic stimulation, however new research suggests they share a common mechanism which results in the reduction of tics in TS patients (Iverson et al., 2023). I propose that this may be due to a reduction in neural noise within the sensorimotor cortex. To further explore this hypothesis, I suggest comparison of the 1/f noise at baseline and post-stimulation to determine whether the protocol results in a reduction of noise and if this is seen for both rhythmic and arrhythmic stimulation (Adelhöfer et al., 2021; Münchau et al., 2021).

Bibliography

Abi-Jaoude, E., Segura, B., Cho, S. S., Crawley, A., & Sandor, P. (2018). The neural correlates of self-regulatory fatigability during inhibitory control of eye blinking. *Journal of Neuropsychiatry and Clinical Neurosciences*, *30*(4), 325–333. https://doi.org/10.1176/appi.neuropsych.17070140

Adelhöfer, N., Paulus, T., Mückschel, M., Bäumer, T., Bluschke, A., Takacs, A., Tóth-Fáber, E., Tárnok, Z., Roessner, V., Weissbach, A., Münchau, A., & Beste, C. (2021). Increased scale-free and aperiodic neural activity during sensorimotor integration-a novel facet in Tourette syndrome. *Brain Communications*, *3*(4). https://doi.org/10.1093/braincomms/fcab250

Albin, R. L., & Mink, J. W. (2006). Recent advances in Tourette syndrome research. In *Trends in Neurosciences* (Vol. 29, Issue 3, pp. 175–182). https://doi.org/10.1016/j.tins.2006.01.001

Albin, R. L., Young, A. B., & Penney, J. B. (1989). The functional anatomy of basal ganglia disorders. *Trends in Neurosciences*, *12*(10), 366–375. https://doi.org/10.1016/0166-2236(89)90074-X

Alexander, G. E., DeLong, M. R., & Strick, P. L. (1986). Parallel organization of functionally segregated circuits linking basal ganglia and cortex. *Annual Review of Neuroscience*, *VOL. 9*, 357–381. https://doi.org/10.1146/annurev.ne.09.030186.002041

Allison, J. D., Meador, K. J., Loring, D. W., Figueroa, R. E., & Wright, J. C. (2000). Functional MRI cerebral activation and deactivation during finger movement. *Neurology*, *54*(1), 135–135. https://doi.org/10.1212/WNL.54.1.135

Apšvalka, D., Gadie, A., Clemence, M., & Mullins, P. G. (2015). Event-related dynamics of glutamate and BOLD effects measured using functional magnetic resonance spectroscopy (fMRS) at 3T in a repetition suppression paradigm. *NeuroImage*, *118*, 292–300. https://doi.org/10.1016/j.neuroimage.2015.06.015

Aron, A. R., Robbins, T. W., & Poldrack, R. A. (2004). Inhibition and the right inferior frontal cortex. In *Trends in Cognitive Sciences* (Vol. 8, Issue 4, pp. 170–177). https://doi.org/10.1016/j.tics.2004.02.010

Aron, A. R., Robbins, T. W., & Poldrack, R. A. (2014). Inhibition and the right inferior frontal cortex: One decade on. In *Trends in Cognitive Sciences* (Vol. 18, Issue 4, pp. 177–185). https://doi.org/10.1016/j.tics.2013.12.003

Asamoah, B., Khatoun, A., & Mc Laughlin, M. (2019). tACS motor system effects can be caused by transcutaneous stimulation of peripheral nerves. *Nature Communications*, *10*(1), 1–16. https://doi.org/10.1038/s41467-018-08183-w

Azrin, N. H., & Nunn, R. G. (1973). Habit-reversal: A method of eliminating nervous habits and tics. *Behaviour Research and Therapy*, *11*(4), 619–628. https://doi.org/10.1016/0005-7967(73)90119-8

Backes, W. H., Mess, W. H., Van Kranen-Mastenbroek, V., & Reulen, J. P. H. (2000). Somatosensory cortex responses to median nerve stimulation: fMRI effects of current amplitude and selective attention. *Clinical Neurophysiology*, *111*(10), 1738–1744. https://doi.org/10.1016/S1388-2457(00)00420-X

Baillet, S. (2017). Magnetoencephalography for brain electrophysiology and imaging. In *Nature Neuroscience* (Vol. 20, Issue 3, pp. 327–339). https://doi.org/10.1038/nn.4504

Baumgartner, C., Sutherling, W. W., Di, S., & Barth, D. S. (1991). Spatiotemporal modeling of cerebral evoked magnetic fields to median nerve stimulation. *Electroencephalography and Clinical Neurophysiology*, *79*(1), 27–35. https://doi.org/10.1016/0013-4694(91)90153-U

Baumung, L., Müller-Vahl, K., Dyke, K., Jackson, G., Jackson, S., Golm, D., Münchau, A., & Brandt, V. (2021). Developing the Premonitory Urges for Tic Disorders Scale–Revised (PUTS-R). *Journal of Neuropsychology*, *15*(1), 129–142. https://doi.org/10.1111/jnp.12216

Bear, M. F., Connors, B. W., & Paridiso, M. A. (2016). *Neuroscience: exploring the brain* (Enhanced f). Jones & Bartlett Learning.

Beckmann, C. F., DeLuca, M., Devlin, J. T., & Smith, S. M. (2005). Investigations into resting-state connectivity using independent component analysis. *Philosophical Transactions of the Royal Society*

B: Biological Sciences, *360*(1457), 1001–1013. https://doi.org/10.1098/rstb.2005.1634

Behler, N., Leitner, B., Mezger, E., Weidinger, E., Musil, R., Blum, B., Kirsch, B., Wulf, L., Löhrs, L., Winter, C., Padberg, F., & Palm, U. (2018). Cathodal tDCS over motor cortex does not improve tourette syndrome: Lessons learned from a case series. *Frontiers in Behavioral Neuroscience*, *12*, 194. https://doi.org/10.3389/fnbeh.2018.00194

Benjamini, Y., & Hochberg, Y. (1995). Controlling the False Discovery Rate: A Practical and Powerful Approach to Multiple Testing. *Journal of the Royal Statistical Society: Series B (Methodological)*, *57*(1), 289–300. https://doi.org/10.1111/j.2517-6161.1995.tb02031.x

Benjamini, Y., & Yekutieli, D. (2001). The control of the false discovery rate in multiple testing under dependency. *Annals of Statistics*, *29*(4), 1165–1188. https://doi.org/10.1214/aos/1013699998

Berman, B. D., Horovitz, S. G., Morel, B., & Hallett, M. (2012). Neural correlates of blink suppression and the buildup of a natural bodily urge. *NeuroImage*, *59*(2), 1441–1450. https://doi.org/10.1016/j.neuroimage.2011.08.050

Bloch, M. H., & Leckman, J. F. (2009). Clinical course of Tourette syndrome. In *Journal of Psychosomatic Research* (Vol. 67, Issue 6, pp. 497–501). https://doi.org/10.1016/j.jpsychores.2009.09.002

Bloch, M. H., Peterson, B. S., Scahill, L., Otka, J., Katsovich, L., Zhang, H., & Leckman, J. F. (2006). Adulthood outcome of tic and obsessive-compulsive symptom severity in children with Tourette syndrome. *Archives of Pediatrics and Adolescent Medicine*, *160*(1), 65–69. https://doi.org/10.1001/archpedi.160.1.65

Bohlhalter, S., Goldfine, A., Matteson, S., Garraux, G., Hanakawa, T., Kansaku, K., Wurzman, R., & Hallett, M. (2006). Neural correlates of tic generation in Tourette syndrome: An event-related functional MRI study. *Brain*, *129*(8), 2029–2037. https://doi.org/10.1093/brain/awl050

Boillat, Y., Xin, L., van der Zwaag, W., & Gruetter, R. (2020). Metabolite concentration changes associated with positive and negative BOLD responses in the human visual cortex: A functional MRS study at 7

Tesla. *Journal of Cerebral Blood Flow and Metabolism*, *40*(3), 488–500. https://doi.org/10.1177/0271678X19831022

Boto, E., Holmes, N., Leggett, J., Roberts, G., Shah, V., Meyer, S. S., Muñoz, L. D., Mullinger, K. J., Tierney, T. M., Bestmann, S., Barnes, G. R., Bowtell, R., & Brookes, M. J. (2018). Moving magnetoencephalography towards real-world applications with a wearable system. *Nature*, *555*(7698), 657–661. https://doi.org/10.1038/nature26147

Boto, E., Holmes, N., Tierney, T. M., Leggett, J., Hill, R., Mellor, S., Roberts, G., Barnes, G., Bowtell, R., Brookes, M. J., Papanicolaou, A. C., Roberts, Timothy. P. L., & Wheless, J. W. (2020). Magnetoencephalography Using Optically Pumped Magnetometers. In *Fifty years of Magnetoencephalography: Beginnings, Technical Advances and Applications.* Oxford University Press USA. https://doi.org/10.1093/oso/9780190935689.003.0008

Boto, E., Seedat, Z. A., Holmes, N., Leggett, J., Hill, R. M., Roberts, G., Shah, V., Fromhold, T. M., Mullinger, K. J., Tierney, T. M., Barnes, G. R., Bowtell, R., & Brookes, M. J. (2019). Wearable neuroimaging: Combining and contrasting magnetoencephalography and electroencephalography. *NeuroImage*, *201*(March), 116099. https://doi.org/10.1016/j.neuroimage.2019.116099

Botteron, H. E., Richards, C. A., Nishino, T., Ueda, K., Acevedo, H. K., Koller, J. M., & Black, K. J. (2019). The urge to blink in Tourette syndrome. *Cortex*, *120*, 556–566. https://doi.org/10.1016/j.cortex.2019.07.010

Brandt, V. C., Beck, C., Sajin, V., Baaske, M. K., Bäumer, T., Beste, C., Anders, S., & Münchau, A. (2016). Temporal relationship between premonitory urges and tics in Gilles de la Tourette syndrome. *Cortex*, *77*, 24–37. https://doi.org/10.1016/j.cortex.2016.01.008

Brickley, S. G., & Mody, I. (2012). Extrasynaptic GABA A Receptors: Their Function in the CNS and Implications for Disease. In *Neuron* (Vol. 73, Issue 1, pp. 23–34). https://doi.org/10.1016/j.neuron.2011.12.012

Brinkman, L., Stolk, A., Dijkerman, H. C., De Lange, F. P., & Toni, I. (2014). Distinct roles for alpha- and beta-band oscillations during mental simulation of goal-directed actions. *Journal of Neuroscience*,

34(44), 14783–14792. https://doi.org/10.1523/JNEUROSCI.2039-14.2014

Brinkman, L., Stolk, A., Marshall, T. R., Esterer, S., Sharp, P., Dijkerman, H. C., de Lange, F. P., & Toni, I. (2016). Independent causal contributions of Alpha- and Beta-band oscillations during movement selection. *Journal of Neuroscience*, *36*(33), 8726–8733. https://doi.org/10.1523/JNEUROSCI.0868-16.2016

Bristow, D., Haynes, J. D., Sylvester, R., Frith, C. D., & Rees, G. (2005). Blinking suppresses the neural response to unchanging retinal stimulation. *Current Biology*, *15*(14), 1296–1300. https://doi.org/10.1016/j.cub.2005.06.025

Brookes, M. J., Vrba, J., Robinson, S. E., Stevenson, C. M., Peters, A. M., Barnes, G. R., Hillebrand, A., & Morris, P. G. (2008). Optimising experimental design for MEG beamformer imaging. *NeuroImage*, *39*(4), 1788–1802. https://doi.org/10.1016/j.neuroimage.2007.09.050

Brown, P. (2007). Abnormal oscillatory synchronisation in the motor system leads to impaired movement. In *Current Opinion in Neurobiology* (Vol. 17, Issue 6, pp. 656–664). https://doi.org/10.1016/j.conb.2007.12.001

Buchholz, V. N., Jensen, O., & Medendorp, W. P. (2014). Different roles of alpha and beta band oscillations in anticipatory sensorimotor gating. *Frontiers in Human Neuroscience*, *8*(JUNE), 1–9. https://doi.org/10.3389/fnhum.2014.00446

Budman, C. L. (2014). The role of atypical antipsychotics for treatment of Tourette's syndrome: An overview. In *Drugs* (Vol. 74, Issue 11, pp. 1177–1193). https://doi.org/10.1007/s40265-014-0254-0

Caballero-Gaudes, C., Moia, S., Panwar, P., Bandettini, P. A., & Gonzalez-Castillo, J. (2019). A deconvolution algorithm for multi-echo functional MRI: Multi-echo Sparse Paradigm Free Mapping. *NeuroImage*, *202*, 116081. https://doi.org/10.1016/J.NEUROIMAGE.2019.116081

Canales, J. J., & Graybiel, A. M. (2000). A measure of striatal function predicts motor stereotypy. *Nature Neuroscience*, *3*(4), 377–383. https://doi.org/10.1038/73949

Capilla, A., Pazo-Alvarez, P., Darriba, A., Campo, P., & Gross, J. (2011). Steady-state visual evoked potentials can be explained by temporal superposition of transient event-related responses. *PLoS ONE*, *6*(1), e14543. https://doi.org/10.1371/journal.pone.0014543

Capriotti, M. R., Brandt, B. C., Turkel, J. E., Lee, H. J., & Woods, D. W. (2014). Negative Reinforcement and Premonitory Urges in Youth With Tourette Syndrome: An Experimental Evaluation. *Behavior Modification*, *38*(2), 276–296. https://doi.org/10.1177/0145445514531015

Caruana, F., Gerbella, M., Avanzini, P., Gozzo, F., Pelliccia, V., Mai, R., Abdollahi, R. O., Cardinale, F., Sartori, I., Lo Russo, G., & Rizzolatti, G. (2018). Motor and emotional behaviours elicited by electrical stimulation of the human cingulate cortex. *Brain*, *141*(10), 3035–3051. https://doi.org/10.1093/brain/awy219

Cauda, F., D'Agata, F., Sacco, K., Duca, S., Geminiani, G., & Vercelli, A. (2011). Functional connectivity of the insula in the resting brain. *NeuroImage*, *55*(1), 8–23. https://doi.org/10.1016/j.neuroimage.2010.11.049

Chappell, M., Okell, T., & Jenkinson, M. (2020). *Short introduction to MRI Physics for Neuroimaging* (M. Jenkinson & M. Chappell, Eds.). Oxford University Press.

Chavhan, G. B., Babyn, P. S., Thomas, B., Shroff, M. M., & Mark Haacke, E. (2009). Principles, techniques, and applications of T2*-based MR imaging and its special applications. *Radiographics*, *29*(5), 1433–1449. https://doi.org/10.1148/rg.295095034

Chen, C., Sigurdsson, H. P., Pépés, S. E., Auer, D. P., Morris, P. G., Morgan, P. S., Gowland, P. A., & Jackson, S. R. (2017). Activation induced changes in GABA: Functional MRS at 7 T with MEGA-sLASER. *NeuroImage*, *156*, 207–213. https://doi.org/10.1016/j.neuroimage.2017.05.044

Chen, R., Yaseen, Z., Cohen, L. G., & Hallett, M. (1998). Time course of corticospinal excitability in reaction time and self- paced movements. *Annals of Neurology*, *44*(3), 317–325. https://doi.org/10.1002/ana.410440306

Cheyne, D. O. (2013). MEG studies of sensorimotor rhythms: A review. In *Experimental Neurology* (Vol. 245, pp. 27–39). https://doi.org/10.1016/j.expneurol.2012.08.030

Cohen, D. (1968). Magnetoencephalography: evidence of magnetic fields produced by alpha-rhythm currents. *Science (New York, N.Y.)*, *161*(3843), 784–786.

Cohen, D. (1972). Magnetoencephalography: Detection of the Brain's Electrical Activity with a Superconducting Magnetometer. *Science*, *175*(4022), 664–666.

Cohen, D. (2009). *The MEG made ridiculously simple*.

Cohen, S. C., Leckman, J. F., & Bloch, M. H. (2013). Clinical assessment of Tourette syndrome and tic disorders. In *Neuroscience and Biobehavioral Reviews* (Vol. 37, Issue 6, pp. 997–1007). https://doi.org/10.1016/j.neubiorev.2012.11.013

Cohrs, S., Rasch, T., Altmeyer, S., Kinkelbur, J., Kostanecka, T., Rothenberger, A., Rüther, E., & Hajak, G. (2001). Decreased sleep quality and increased sleep related movements in patients with Tourette's syndrome. *Journal of Neurology Neurosurgery and Psychiatry*, *70*(2), 192–197. https://doi.org/10.1136/jnnp.70.2.192

Colon, E., Legrain, V., & Mouraux, A. (2012). Steady-state evoked potentials to study the processing of tactile and nociceptive somatosensory input in the human brain. In *Neurophysiologie Clinique* (Vol. 42, Issue 5, pp. 315–323). https://doi.org/10.1016/j.neucli.2012.05.005

Community, T. tedana, Ahmed, Z., Bandettini, P. A., Bottenhorn, K. L., Caballero-Gaudes, C., Dowdle, L. T., DuPre, E., Gonzalez-Castillo, J., Handwerker, D., Heunis, S., Kundu, P., Laird, A. R., Markello, R., Markiewicz, C. J., Maullin-Sapey, T., Moia, S., Salo, T., Staden, I., Teves, J., … Whitaker, K. (2022). *ME-ICA/tedana: 0.0.12*. https://doi.org/10.5281/ZENODO.6461353

Conelea, C. A., & Woods, D. W. (2008). The influence of contextual factors on tic expression in Tourette's syndrome: A review. In *Journal of Psychosomatic Research* (Vol. 65, Issue 5, pp. 487–496). https://doi.org/10.1016/j.jpsychores.2008.04.010

Conelea, C. A., Woods, D. W., Zinner, S. H., Budman, C. L., Murphy, T. K., Scahill, L. D., Compton, S. N., & Walkup, J. T. (2013). The impact of tourette syndrome in adults: Results from the tourette syndrome impact survey. *Community Mental Health Journal*, *49*(1), 110–120. https://doi.org/10.1007/s10597-011-9465-y

Cox, R. W. (1996). AFNI: Software for analysis and visualization of functional magnetic resonance neuroimages. *Computers and Biomedical Research*, *29*(3), 162–173. https://doi.org/10.1006/cbmr.1996.0014

Cox, R. W., & Hyde, J. S. (1997). Software tools for analysis and visualization of fMRI data. *NMR in Biomedicine*, *10*(4–5), 171–178. https://doi.org/10.1002/(SICI)1099-1492(199706/08)10:4/5<171::AID-NBM453>3.0.CO;2-L

Craig, A. D. (2002). How do you feel? Interoception: The sense of the physiological condition of the body. *Nature Reviews Neuroscience*, *3*(8), 655–666. https://doi.org/10.1038/nrn894

Craig, A. D. (2009). How do you feel - now? The anterior insula and human awareness. In *Nature Reviews Neuroscience* (Vol. 10, Issue 1, pp. 59–70). https://doi.org/10.1038/nrn2555

Craig, A. D., Chen, K., Bandy, D., & Reiman, E. M. (2000). Thermosensory activation of insular cortex. *Nature Neuroscience*, *3*(2), 184–190. https://doi.org/10.1038/72131

Diagnostic and statistical manual of mental disorders: DSM-5 (5th ed). (2013). American Psychiatric Association.

Draper, A., Jackson, G. M., Morgan, P. S., & Jackson, S. R. (2016). Premonitory urges are associated with decreased grey matter thickness within the insula and sensorimotor cortex in young people with Tourette syndrome. *Journal of Neuropsychology*, *10*(1), 143–153. https://doi.org/10.1111/jnp.12089

Draper, A., Jude, L., Jackson, G. M., & Jackson, S. R. (2015). Motor excitability during movement preparation in Tourette syndrome. *Journal of Neuropsychology*, *9*(1), 33–44. https://doi.org/10.1111/jnp.12033

Drobnjak, I. (2007). *FMRI Simulator: Development and Applications*.

DuPre, E., Salo, T., Ahmed, Z., Bandettini, P. A., Bottenhorn, K. L., Caballero-Gaudes, C., Dowdle, L. T., Gonzalez-Castillo, J., Heunis, S., Kundu, P., Laird, A. R., Markello, R., Markiewicz, C. J., Moia, S., Staden, I., Teves, J. B., Uruñuela, E., Vaziri-Pashkam, M., Whitaker, K., & Handwerker, D. A. (2021). TE-dependent analysis of multi-echo fMRI with *tedana*. *Journal of Open Source Software*, *6*(66), 3669. https://doi.org/10.21105/JOSS.03669

Dyke, K., Jackson, G. M., Nixon, E., & Jackson, S. R. (2019). Effects of single-session cathodal transcranial direct current stimulation on tic symptoms in Tourette's syndrome. *Experimental Brain Research*, *237*(11), 2853–2863. https://doi.org/10.1007/s00221-019-05637-5

Dyke, K., Pépés, S. E., Chen, C., Kim, S., Sigurdsson, H. P., Draper, A., Husain, M., Nachev, P., Gowland, P. A., Morris, P. G., & Jackson, S. R. (2017). Comparing GABA-dependent physiological measures of inhibition with proton magnetic resonance spectroscopy measurement of GABA using ultra-high-field MRI. *NeuroImage*, *152*, 360–370. https://doi.org/10.1016/j.neuroimage.2017.03.011

Dziak, J. J., Coffman, D. L., Lanza, S. T., Li, R., & Jermiin, L. S. (2020). Sensitivity and specificity of information criteria. *Briefings in Bioinformatics*, *21*(2), 553. https://doi.org/10.1093/BIB/BBZ016

Engel, A. K., & Fries, P. (2010). Beta-band oscillations-signalling the status quo? In *Current Opinion in Neurobiology* (Vol. 20, Issue 2, pp. 156–165). https://doi.org/10.1016/j.conb.2010.02.015

Faghihi, R., Zeinali-Rafsanjani, B., Mosleh-Shirazi, M. A., Saeedi-Moghadam, M., Lotfi, M., Jalli, R., & Iravani, V. (2017). Magnetic Resonance Spectroscopy and its Clinical Applications: A Review. In *Journal of Medical Imaging and Radiation Sciences* (Vol. 48, Issue 3, pp. 233–253). https://doi.org/10.1016/j.jmir.2017.06.004

Ferré, S., Bonaventura, J., Zhu, W., Hatcher-Solis, C., Taura, J., Quiroz, C., Cai, N. S., Moreno, E., Casadó-Anguera, V., Kravitz, A. v., Thompson, K. R., Tomasi, D. G., Navarro, G., Cordomí, A., Pardo, L., Lluís, C., Dessauer, C. W., Volkow, N. D., Casadó, V., … Zwilling, D. (2018). Essential control of the function of the striatopallidal neuron by pre-coupled complexes of adenosine A2A-dopamine D2 receptor

heterotetramers and adenylyl cyclase. *Frontiers in Pharmacology*, *9*(APR), 243. https://doi.org/10.3389/fphar.2018.00243

Ferretti, A., Babiloni, C., Arienzo, D., Del Gratta, C., Rossini, P. M., Tartaro, A., & Romani, G. L. (2007). Cortical brain responses during passive nonpainful median nerve stimulation at low frequencies (0.5-4 Hz): An fMRI study. *Human Brain Mapping*, *28*(7), 645–653. https://doi.org/10.1002/hbm.20292

Finisguerra, A., Borgatti, R., & Urgesi, C. (2019). Non-invasive brain stimulation for the rehabilitation of children and adolescents with neurodevelopmental disorders: A systematic reviewnon-invasive brain stimulation for the rehabilitation of children and adolescents with neurodevelopmental disorders: A . *Frontiers in Psychology*, *10*(FEB), 135. https://doi.org/10.3389/fpsyg.2019.00135

Freeman, R. D., Fast, D. K., Burd, L., Kerbeshian, J., Robertson, M. M., & Sandor, P. (2000). An international perspective on Tourette syndrome: Selected findings from 3500 individuals in 22 countries. *Developmental Medicine and Child Neurology*, *42*(7), 436–447. https://doi.org/10.1017/S0012162200000839

Fried, I., Katz, A., McCarthy, G., Sass, K. J., Williamson, P., Spencer, S. S., & Spencer, D. D. (1991). Functional organization of human supplementary motor cortex studies by electrical stimulation. *Journal of Neuroscience*, *11*(11), 3656–3666. https://doi.org/10.1523/jneurosci.11-11-03656.1991

Friston, K. J., Worsley, K. J., Frackowiak, R. S. J., Mazziotta, J. C., & Evans, A. C. (1994). Assessing the significance of focal activations using their spatial extent. *Human Brain Mapping*, *1*(3), 210–220. https://doi.org/10.1002/hbm.460010306

Frydman, L. (2009). *MRS: in vivo spectroscopic imaging*. https://www.weizmann.ac.il/chemphys/assaf_tal/sites/chemphys.assaf_tal/files/uploads/lecture_x_-_spectroscopy_lucio.pdf

Fusco, C., Bertani, G., Caricati, G., & Della Giustina, E. (2006). Stress fracture of the peroneal bone secondary to a complex tic. *Brain and Development*, *28*(1), 52–54. https://doi.org/10.1016/j.braindev.2005.03.009

Gaetz, W., Edgar, J. C., Wang, D. J., & Roberts, T. P. L. (2011). Relating MEG measured motor cortical oscillations to resting γ-Aminobutyric acid (GABA) concentration. *NeuroImage*, *55*(2), 616–621. https://doi.org/10.1016/j.neuroimage.2010.12.077

Ganos, C., Asmuss, L., Bongert, J., Brandt, V., Münchau, A., & Haggard, P. (2015). Volitional action as perceptual detection: Predictors of conscious intention in adolescents with tic disorders. *Cortex*, *64*, 47–54. https://doi.org/10.1016/j.cortex.2014.09.016

Ganos, C., Kahl, U., Schunke, O., Kühn, S., Haggard, P., Gerloff, C., Roessner, V., Thomalla, G., & Münchau, A. (2012). Are premonitory urges a prerequisite of tic inhibition in Gilles de la Tourette syndrome? *Journal of Neurology, Neurosurgery and Psychiatry*, *83*(10), 975–978. https://doi.org/10.1136/jnnp-2012-303033

Ganos, C., Rocchi, L., Latorre, A., Hockey, L., Palmer, C., Joyce, E. M., Bhatia, K. P., Haggard, P., & Rothwell, J. (2018). Motor cortical excitability during voluntary inhibition of involuntary tic movements. *Movement Disorders*, *33*(11), 1804–1809. https://doi.org/10.1002/mds.27479

Gaudes, C. C., Petridou, N., Dryden, I. L., Bai, L., Francis, S. T., & Gowland, P. A. (2011). Detection and characterization of single-trial fMRI bold responses: Paradigm free mapping. *Human Brain Mapping*, *32*(9), 1400. https://doi.org/10.1002/HBM.21116

Gaudes, C. C., Petridou, N., Francis, S. T., Dryden, I. L., & Gowland, P. A. (2013). Paradigm free mapping with sparse regression automatically detects single-trial functional magnetic resonance imaging blood oxygenation level dependent responses. *Human Brain Mapping*, *34*(3), 501–518. https://doi.org/10.1002/hbm.21452

Geselowitz, D. B. (1967). On Bioelectric Potentials in an Inhomogeneous Volume Conductor. *Biophysical Journal*, *7*(1), 1–11. https://doi.org/10.1016/S0006-3495(67)86571-8

Gilbertson, T., Lalo, E., Doyle, L., Di Lazzaro, V., Cioni, B., & Brown, P. (2005). Existing motor state is favored at the expense of new movement during 13-35 Hz oscillatory synchrony in the human corticospinal system. *Journal of Neuroscience*, *25*(34), 7771–7779. https://doi.org/10.1523/JNEUROSCI.1762-05.2005

Gilles de la Tourette, G. E. A. B. (1885). Etude sur une affection nerveuse charactérisée par de l'incoordination motrice accompagnée d'écholalie et de coprolalie (jumping, latah, myriachit). *Archives de Neurologie (Paris)*, *9*(19–42), 19–42.

Glover, G. H. (2011). Overview of functional magnetic resonance imaging. In *Neurosurgery Clinics of North America* (Vol. 22, Issue 2, pp. 133–139). https://doi.org/10.1016/j.nec.2010.11.001

Golan, T., Grossman, S., Deouell, L. Y., & Malach, R. (2018). Widespread Suppression of High-Order Visual Cortex During Blinks and External Predictable Visual Interruptions. *BioRxiv*, 456566.

Gong, G., He, Y., Concha, L., Lebel, C., Gross, D. W., Evans, A. C., & Beaulieu, C. (2009). Mapping anatomical connectivity patterns of human cerebral cortex using in vivo diffusion tensor imaging tractography. *Cerebral Cortex*, *19*(3), 524–536. https://doi.org/10.1093/cercor/bhn102

Gonzalez-Burgos, G., & Lewis, D. A. (2008). GABA neurons and the mechanisms of network oscillations: Implications for understanding cortical dysfunction in schizophrenia. In *Schizophrenia Bulletin* (Vol. 34, Issue 5, pp. 944–961). https://doi.org/10.1093/schbul/sbn070

Govind, V., Young, K., & Maudsley, A. A. (2015). Corrigendum: proton NMR chemical shifts and coupling constants for brain metabolites. Govindaraju V, Young K, Maudsley AA, NMR Biomed. 2000; 13: 129-153. *NMR in Biomedicine*, *28*(7), 923–924. https://doi.org/10.1002/NBM.3336

Graybiel, A. M. (2008). Habits, rituals, and the evaluative brain. In *Annual Review of Neuroscience* (Vol. 31, Issue 1, pp. 359–387). https://doi.org/10.1146/annurev.neuro.29.051605.112851

Graybiel, A. M., Aosaki, T., Flaherty, A. W., & Kimura, M. (1994). The basal ganglia and adaptive motor control. *Science*, *265*(5180), 1826–1831. https://doi.org/10.1126/science.8091209

Groppe, D. (2020). *fdr_bh*. https://uk.mathworks.com/matlabcentral/fileexchange/27418-fdr_bh

Guell, X., Schmahmann, J. D., Gabrieli, J. D. E., & Ghosh, S. S. (2018). Functional gradients of the cerebellum. *ELife*, *7*, 1–22. https://doi.org/10.7554/eLife.36652

Haegens, S., Osipova, D., Oostenveld, R., & Jensen, O. (2010). Somatosensory working memory performance in humans depends on both engagement and disengagement of regions in a distributed network. *Human Brain Mapping*, *31*(1), 26–35. https://doi.org/10.1002/hbm.20842

Hämäläinen, M., Hari, R., Ilmoniemi, R. J., Knuutila, J., & Lounasmaa, O. V. (1993). Magnetoencephalography theory, instrumentation, and applications to noninvasive studies of the working human brain. *Reviews of Modern Physics*, *65*(2), 413–497. https://doi.org/10.1103/RevModPhys.65.413

Handy, T. C. (2009). *Brain Signal Analysis: Advances in Neuroelectric and Neuromagnetic Methods*. 271.

Hansen, P., Kringelbach, M., & Salmelin, R. (2010). MEG: An introduction to methods. In *MEG: An Introduction to Methods*. Oxford University Press. https://doi.org/10.1093/acprof:oso/9780195307238.001.0001

Harris, A. D., Gilbert, D. L., Horn, P. S., Crocetti, D., Cecil, K. M., Edden, R. A. E., Huddleston, D. A., Mostofsky, S. H., & Puts, N. A. J. (2021). Relationship between GABA levels and task-dependent cortical excitability in children with attention-deficit/hyperactivity disorder. *Clinical Neurophysiology*, *132*(5), 1163–1172. https://doi.org/10.1016/j.clinph.2021.01.023

Hashemi, R. H., Bradley, W. G., & Lisanti, C. J. (2018). *MRI: the basics* (4th ed.). Wolters Kluwer Health.

Heise, K. F., Steven, B., Liuzzi, G., Thomalla, G., Jonas, M., Müller-Vahl, K., Sauseng, P., Münchau, A., Gerloff, C., & Hummel, F. C. (2010). Altered modulation of intracortical excitability during movement preparation in Gilles de la Tourette syndrome. *Brain*, *133*(2), 580–590. https://doi.org/10.1093/brain/awp299

Herrmann, C. S. (2001). Human EEG responses to 1-100 Hz flicker: Resonance phenomena in visual cortex and their potential correlation to cognitive phenomena. *Experimental Brain Research*, *137*(3–4), 346–353. https://doi.org/10.1007/s002210100682

Hillebrand, A., & Barnes, G. R. (2002). A quantitative assessment of the sensitivity of whole-head MEG to activity in the adult human cortex.

NeuroImage, *16*(3 I), 638–650. https://doi.org/10.1006/nimg.2002.1102

Himle, M. B., Olufs, E., Himle, J., Tucker, B. T. P., & Woods, D. W. (2010). Behavior Therapy for Tics via Videoconference Delivery: An Initial Pilot Test in Children. *Cognitive and Behavioral Practice*, *17*(3), 329–337. https://doi.org/10.1016/J.CBPRA.2010.02.006

Holmes, N., Leggett, J., Boto, E., Roberts, G., Hill, R. M., Tierney, T. M., Shah, V., Barnes, G. R., Brookes, M. J., & Bowtell, R. (2018). A bi-planar coil system for nulling background magnetic fields in scalp mounted magnetoencephalography. *NeuroImage*, *181*, 760–774. https://doi.org/10.1016/j.neuroimage.2018.07.028

Hook, J. R., & Hall, H. E. (1991). *Solid state physics*.

Houlgreave, M. S., Morera Maiquez, B., Brookes, M. J., & Jackson, S. R. (2022). The oscillatory effects of rhythmic median nerve stimulation. *NeuroImage*, *251*. https://doi.org/10.1016/J.NEUROIMAGE.2022.118990

Huang, M. X., Mosher, J. C., & Leahy, R. M. (1999). A sensor-weighted overlapping-sphere head model and exhaustive head model comparison for MEG. *Physics in Medicine and Biology*, *44*(2), 423–440. https://doi.org/10.1088/0031-9155/44/2/010

Huettel, S. A., Song, A. W., & McCarthy, G. (2014). *Functional magnetic resonance imaging* (3rd ed.). Sinauer Associates, Inc., Publishers.

Ip, I. B., Berrington, A., Hess, A. T., Parker, A. J., Emir, U. E., & Bridge, H. (2017). Combined fMRI-MRS acquires simultaneous glutamate and BOLD-fMRI signals in the human brain. *NeuroImage*, *155*(December 2016), 113–119. https://doi.org/10.1016/j.neuroimage.2017.04.030

Itard, J. (1825). Memorie sur quelques fonctions involuntaries des appareils de la locomotion de la prehension et de la voix. *Archives of General Psychiatry*, *8*, 385–407.

Iverson, A. M., Arbuckle, A. L., Ueda, K., Song, D. Y., Bihun, E. C., Koller, J. M., Wallendorf, M., & Black, K. J. (2023). Peripheral nerve induction of inhibitory brain circuits to treat Tourette syndrome: A randomized crossover trial. *MedRxiv*, 2023.02.01.23285304. https://doi.org/10.1101/2023.02.01.23285304

Jackson, G. M., Draper, A., Dyke, K., Pépés, S. E., & Jackson, S. R. (2015). Inhibition, Disinhibition, and the Control of Action in Tourette Syndrome. In *Trends in Cognitive Sciences* (Vol. 19, Issue 11, pp. 655–665). https://doi.org/10.1016/j.tics.2015.08.006

Jackson, S. R., Loayza, J., Crighton, M., Sigurdsson, H. P., Dyke, K., & Jackson, G. M. (2020). The role of the insula in the generation of motor tics and the experience of the premonitory urge-to-tic in Tourette syndrome. *Cortex*, *126*, 119–133. https://doi.org/10.1016/j.cortex.2019.12.021

Jackson, S. R., Parkinson, A., Kim, S. Y., Schüermann, M., & Eickhoff, S. B. (2011). On the functional anatomy of the urge-for-action. In *Cognitive Neuroscience* (Vol. 2, Issues 3–4, pp. 227–243). https://doi.org/10.1080/17588928.2011.604717

Jackson, S. R., Parkinson, A., Manfredi, V., Millon, G., Hollis, C., & Jackson, G. M. (2013). Motor excitability is reduced prior to voluntary movements in children and adolescents with Tourette syndrome. *Journal of Neuropsychology*, *7*(1), 29–44. https://doi.org/10.1111/j.1748-6653.2012.02033.x

Jagger, J., Prusoff, B. A., Cohen, D. J., Kidd, K. K., Carbonari, C. M., & John, K. (1982). The epidemiology of Tourette's syndrome: A pilot study. *Schizophrenia Bulletin*, *8*(2), 267–278. https://doi.org/10.1093/schbul/8.2.267

Jalenques, I., Galland, F., Malet, L., Morand, D., Legrand, G., Auclair, C., Hartmann, A., Derost, P., & Durif, F. (2012). Quality of life in adults with Gilles de la Tourette Syndrome. *BMC Psychiatry*, *12*(1). https://doi.org/10.1186/1471-244X-12-109

Jankovic, J. (1997). Phenomenology and classification of tics. *Neurologic Clinics*, *15*(2), 267–275. https://doi.org/10.1016/S0733-8619(05)70311-X

JASP Team. (2022). *JASP* (Version 0.16.3).

Jenkinson, M., Bannister, P., Brady, M., & Smith, S. (2002). Improved Optimization for the Robust and Accurate Linear Registration and Motion Correction of Brain Images. *NeuroImage*, *17*(2), 825–841. https://doi.org/10.1006/NIMG.2002.1132

Jenkinson, M., Beckmann, C. F., Behrens, T. E. J., Woolrich, M. W., & Smith, S. M. (2012). FSL. *NeuroImage*, *62*(2), 782–790. https://doi.org/10.1016/j.neuroimage.2011.09.015

Jenkinson, N., & Brown, P. (2011). New insights into the relationship between dopamine, beta oscillations and motor function. In *Trends in Neurosciences* (Vol. 34, Issue 12, pp. 611–618). https://doi.org/10.1016/j.tins.2011.09.003

Jensen, O., & Mazaheri, A. (2010). Shaping functional architecture by oscillatory alpha activity: Gating by inhibition. *Frontiers in Human Neuroscience*, *4*. https://doi.org/10.3389/fnhum.2010.00186

Joundi, R. A., Jenkinson, N., Brittain, J. S., Aziz, T. Z., & Brown, P. (2012). Driving oscillatory activity in the human cortex enhances motor performance. *Current Biology*, *22*(5), 403–407. https://doi.org/10.1016/j.cub.2012.01.024

Juchem, C., & Rothman, D. L. (2014). Basis of Magnetic Resonance. In *Magnetic Resonance Spectroscopy* (pp. 3–14). Elsevier.

Jurkiewicz, M. T., Gaetz, W. C., Bostan, A. C., & Cheyne, D. (2006). Post-movement beta rebound is generated in motor cortex: Evidence from neuromagnetic recordings. *NeuroImage*, *32*(3), 1281–1289. https://doi.org/10.1016/j.neuroimage.2006.06.005

Kakigi, R. (1994). Somatosensory evoked magnetic fields following median nerve stimulation. *Neuroscience Research*, *20*(2), 165–174. https://doi.org/10.1016/0168-0102(94)90034-5

Kalanithi, P. S. A., Zheng, W., Kataoka, Y., DiFiglia, M., Grantz, H., Saper, C. B., Schwartz, M. L., Leckman, J. F., & Vaccarino, F. M. (2005). Altered parvalbumin-positive neuron distribution in basal ganglia of individuals with Tourette syndrome. *Proceedings of the National Academy of Sciences of the United States of America*, *102*(37), 13307–13312. https://doi.org/10.1073/pnas.0502624102

Kampe, K. K. W., Jones, R. A., & Auer, D. P. (2000). Frequency dependence of the functional MRI response after electrical median nerve stimulation. *Human Brain Mapping*, *9*(2), 106–114. https://doi.org/10.1002/(SICI)1097-0193(200002)9:2<106::AID-HBM5>3.0.CO;2-Y

Kataoka, Y., Kalanithi, P. S. A., Grantz, H., Schwartz, M. L., Saper, C., Leckman, J. F., & Vaccarino, F. M. (2010). Decreased number of parvalbumin and cholinergic interneurons in the striatum of individuals with tourette syndrome. *Journal of Comparative Neurology*, *518*(3), 277–291. https://doi.org/10.1002/cne.22206

Keitel, C., Quigley, C., & Ruhnau, P. (2014). Stimulus-driven brain oscillations in the alpha range: Entrainment of intrinsic rhythms or frequency-following response? In *Journal of Neuroscience* (Vol. 34, Issue 31, pp. 10137–10140). https://doi.org/10.1523/JNEUROSCI.1904-14.2014

Kelly, C., Toro, R., Di Martino, A., Cox, C. L., Bellec, P., Castellanos, F. X., & Milham, M. P. (2012). A convergent functional architecture of the insula emerges across imaging modalities. *NeuroImage*, *61*(4), 1129–1142. https://doi.org/10.1016/j.neuroimage.2012.03.021

Kleiner, M., Brainard, D., Pelli, D., Ingling, A., Murray, R., & Broussard, C. (2007). What's new in psychtoolbox-3. *Perception*, *36*(14), 1–16.

Kleiner, R., Koelle, D., Ludwig, F., & Clarke, J. (2004). Superconducting quantum interference devices: State of the art and applications. *Proceedings of the IEEE*, *92*(10), 1534–1548. https://doi.org/10.1109/JPROC.2004.833655

Kolasinski, J., Hinson, E. L., Divanbeighi Zand, A. P., Rizov, A., Emir, U. E., & Stagg, C. J. (2019). The dynamics of cortical GABA in human motor learning. *The Journal of Physiology*, *597*(1), 271–282. https://doi.org/10.1113/JP276626

Kundu, P., Brenowitz, N. D., Voon, V., Worbe, Y., Vértes, P. E., Inati, S. J., Saad, Z. S., Bandettini, P. A., & Bullmore, E. T. (2013). Integrated strategy for improving functional connectivity mapping using multiecho fMRI. *Proceedings of the National Academy of Sciences of the United States of America*, *110*(40), 16187–16192. https://doi.org/10.1073/PNAS.1301725110/SUPPL_FILE/PNAS.201301725SI.PDF

Kundu, P., Inati, S. J., Evans, J. W., Luh, W. M., & Bandettini, P. A. (2012). Differentiating BOLD and non-BOLD signals in fMRI time series using multi-echo EPI. *NeuroImage*, *60*(3), 1759–1770. https://doi.org/10.1016/J.NEUROIMAGE.2011.12.028

Kurth, F., Zilles, K., Fox, P. T., Laird, A. R., & Eickhoff, S. B. (2010). A link between the systems: functional differentiation and integration within the human insula revealed by meta-analysis. *Brain Structure & Function*, *214*(5–6), 519–534. https://doi.org/10.1007/s00429-010-0255-z

Kwak, C., Dat Vuong, K., & Jankovic, J. (2003). Premonitory sensory phenomenon in Tourette's syndrome. *Movement Disorders*, *18*(12), 1530–1533. https://doi.org/10.1002/mds.10618

Kwon, H. J., Lim, W. S., Lim, M. H., Lee, S. J., Hyun, J. K., Chae, J. H., & Paik, K. C. (2011). 1-Hz low frequency repetitive transcranial magnetic stimulation in children with Tourette's syndrome. *Neuroscience Letters*, *492*(1), 1–4. https://doi.org/10.1016/j.neulet.2011.01.007

Le, K., Liu, L., Sun, M., Hu, L., & Xiao, N. (2013). Transcranial magnetic stimulation at 1 Hertz improves clinical symptoms in children with Tourette syndrome for at least 6 months. *Journal of Clinical Neuroscience*, *20*(2), 257–262. https://doi.org/10.1016/j.jocn.2012.01.049

Leckman, J. F. (2002). Tourette's syndrome. *Lancet*, *360*(9345), 1577–1586. https://doi.org/10.1016/S0140-6736(02)11526-1

Leckman, J. F., Michael, M. H., Smith, M. E., Larabi, D., & Hampson, M. (2010). Neurobiological substrates of Tourette's disorder. In *Journal of Child and Adolescent Psychopharmacology* (Vol. 20, Issue 4, pp. 237–247). https://doi.org/10.1089/cap.2009.0118

Leckman, J. F., & Riddle, M. A. (2000). Tourette's syndrome: When habit-forming systems form habits of their own? In *Neuron* (Vol. 28, Issue 2, pp. 349–354). https://doi.org/10.1016/S0896-6273(00)00114-8

Leckman, J. F., Riddle, M. A., Hardin, M. T., Ort, S. I., Swartz, K. L., Stevenson, J., & Cohen, D. J. (1989). The Yale Global Tic Severity Scale: Initial Testing of a Clinician-Rated Scale of Tic Severity. *Journal of the American Academy of Child and Adolescent Psychiatry*, *28*(4), 566–573. https://doi.org/10.1097/00004583-198907000-00015

Leckman, J. F., Vaccarino, F. M., Kalanithi, P. S. A., & Rothenberger, A. (2006). Annotation: Tourette syndrome: A relentless drumbeat - Driven by misguided brain oscillations. In *Journal of Child Psychology*

and Psychiatry and Allied Disciplines (Vol. 47, Issue 6, pp. 537–550). https://doi.org/10.1111/j.1469-7610.2006.01620.x

Leckman, J. F., Zhang, H., Vitale, A., Lahnin, F., Lynch, K., Bondi, C., Kim, Y. S., & Peterson, B. S. (1998). Course of tic severity in Tourette syndrome: The first two decades. *Pediatrics*, *102*(1 I), 14–19. https://doi.org/10.1542/peds.102.1.14

Leckman, James. F., Walker, D. E., & Cohen, D. J. (1993). Premonitory urges in Tourette's syndrome. *American Journal of Psychiatry*, *150*(1), 98–102. https://doi.org/10.1176/ajp.150.1.98

Lerner, A., Bagic, A., Hanakawa, T., Boudreau, E. A., Pagan, F., Mari, Z., Bara-Jimenez, W., Aksu, M., Sato, S., Murphy, D. L., & Hallett, M. (2009). Involvement of insula and cingulate cortices in control and suppression of natural urges. *Cerebral Cortex*, *19*(1), 218–223. https://doi.org/10.1093/cercor/bhn074

Loued-Khenissi, L., Döll, O., & Preuschoff, K. (2019). An Overview of Functional Magnetic Resonance Imaging Techniques for Organizational Research. *Organizational Research Methods*, *22*(1), 17–45. https://doi.org/10.1177/1094428118802631

Ly, A., Stefan, A., van Doorn, J., Dablander, F., van den Bergh, D., Sarafoglou, A., Kucharský, S., Derks, K., Gronau, Q. F., Raj, A., Boehm, U., van Kesteren, E. J., Hinne, M., Matzke, D., Marsman, M., & Wagenmakers, E. J. (2020). The Bayesian Methodology of Sir Harold Jeffreys as a Practical Alternative to the P Value Hypothesis Test. *Computational Brain and Behavior*, *3*(2), 153–161. https://doi.org/10.1007/s42113-019-00070-x

Maiquez, B. M., Smith, C., Dyke, K., Chou, C.-P., Kasbia, B., McCready, C., Wright, H., Jackson, J. K., Farr, I., Badinger, E., Jackson, G. M., & Jackson, S. R. (2023). A double-blind, sham-controlled, trial of home-administered rhythmic 10Hz median nerve stimulation for the reduction of tics, and suppression of the urge-to-tic, in individuals with Tourette syndrome and chronic tic disorder. *MedRxiv*, 2023.03.06.23286799. https://doi.org/10.1101/2023.03.06.23286799

Manganotti, P., Formaggio, E., Storti, S. F., Avesani, M., Acler, M., Sala, F., Magon, S., Zoccatelli, G., Pizzini, F., Alessandrini, F., Fiaschi, A., &

Beltramello, A. (2009). Steady-state activation in somatosensory cortex after changes in stimulus rate during median nerve stimulation. *Magnetic Resonance Imaging*, *27*(9), 1175–1186. https://doi.org/10.1016/j.mri.2009.05.009

Martínez-Cagigal, V. (2020). *Shaded area error plot*. https://uk.mathworks.com/matlabcentral/fileexchange/58262-shaded-area-error-bar-plot

Mazumder, A., & Dubey, D. K. (2013). Nuclear Magnetic Resonance (NMR) Spectroscopy. In *Reference Module in Chemistry, Molecular Sciences and Chemical Engineering*. Elsevier. https://doi.org/10.1016/b978-0-12-409547-2.05891-1

Mazzone, L., Yu, S., Blair, C., Gunter, B. C., Wang, Z., Marsh, R., & Peterson, B. S. (2010). An fMRI study of frontostriatal circuits during the inhibition of eye blinking in persons with Tourette syndrome. *American Journal of Psychiatry*, *167*(3), 341–349. https://doi.org/10.1176/appi.ajp.2009.08121831

McCairn, K. W., Bronfeld, M., Belelovsky, K., & Bar-Gad, I. (2009). The neurophysiological correlates of motor tics following focal striatal disinhibition. *Brain*, *132*(8), 2125–2138. https://doi.org/10.1093/brain/awp142

McCairn, K. W., Nagai, Y., Hori, Y., Ninomiya, T., Kikuchi, E., Lee, J. Y., Suhara, T., Iriki, A., Minamimoto, T., Takada, M., Isoda, M., & Matsumoto, M. (2016). A Primary Role for Nucleus Accumbens and Related Limbic Network in Vocal Tics. *Neuron*, *89*(2), 300–307. https://doi.org/10.1016/j.neuron.2015.12.025

Miller, E. K., & Cohen, J. D. (2001). An integrative theory of prefrontal cortex function. In *Annual Review of Neuroscience* (Vol. 24, Issue 1, pp. 167–202). https://doi.org/10.1146/annurev.neuro.24.1.167

Mink, J. W. (2001). Basal ganglia dysfunction in Tourette's syndrome: A new hypothesis. In *Pediatric Neurology* (Vol. 25, Issue 3, pp. 190–198). https://doi.org/10.1016/S0887-8994(01)00262-4

Morera Maiquez, B., Jackson, G., & Jackson, S. (2020). Entraining movement-related brain oscillations using rhythmic median nerve stimulation. *[Preprint]*. https://doi.org/10.1101/2020.03.30.016097

Morera Maiquez, B., Jackson, G. M., & Jackson, S. R. (2022). Examining the neural antecedents of tics in Tourette syndrome using electroencephalography. *Journal of Neuropsychology*, *16*(1), 1–20. https://doi.org/10.1111/jnp.12245

Morera Maiquez, B., Sigurdsson, H. P., Dyke, K., Clarke, E., McGrath, P., Pasche, M., Rajendran, A., Jackson, G. M., & Jackson, S. R. (2020). Entraining Movement-Related Brain Oscillations to Suppress Tics in Tourette Syndrome. *Current Biology*, *30*(12), 2334-2342.e3. https://doi.org/10.1016/j.cub.2020.04.044

Mosher, J. C., Leahy, R. M., & Lewis, P. S. (1999). EEG and MEG: Forward Solutions for Inverse Methods. In *IEEE TRANSACTIONS ON BIOMEDICAL ENGINEERING* (Vol. 46, Issue 3).

Motion-related artefacts in fMRI. (2018, May). https://wiki.cam.ac.uk/bmuwiki/FMRI#Framewise_Displacement

Mrakic-Sposta, S., Marceglia, S., Mameli, F., Dilena, R., Tadini, L., & Priori, A. (2008). Transcranial direct current stimulation in two patients with Tourette syndrome. *Movement Disorders*, *23*(15), 2259–2261. https://doi.org/10.1002/mds.22292

Münchau, A., Colzato, L. S., AghajaniAfjedi, A., & Beste, C. (2021). A neural noise account of Gilles de la Tourette syndrome. In *NeuroImage: Clinical* (Vol. 30). Elsevier Inc. https://doi.org/10.1016/j.nicl.2021.102654

Murphy, K. A., & Morrisonponce, D. (2022). Anatomy, Shoulder and Upper Limb, Median Nerve. *StatPearls*.

Muthukumaraswamy, S. D. (2014). The use of magnetoencephalography in the study of psychopharmacology (pharmaco-MEG). In *Journal of Psychopharmacology* (Vol. 28, Issue 9, pp. 815–829). SAGE Publications Ltd. https://doi.org/10.1177/0269881114536790

Nahab, F. B., Hattori, N., Saad, Z. S., & Hallett, M. (2009). Contagious yawning and the frontal lobe: An fMRI study. *Human Brain Mapping*, *30*(5), 1744–1751. https://doi.org/10.1002/hbm.20638

Nakano, T., Kato, M., Morito, Y., Itoi, S., & Kitazawa, S. (2013). Blink-related momentary activation of the default mode network while viewing videos. *Proceedings of the National Academy of Sciences of*

the United States of America, *110*(2), 702–706. https://doi.org/10.1073/pnas.1214804110

Naqvi, N. H., Rudrauf, D., Damasio, H., & Bechara, A. (2007). Damage to the insula disrupts addiction to cigarette smoking. *Science*, *315*(5811), 531–534. https://doi.org/10.1126/science.1135926

Near, J., Edden, R., Evans, C. J., Paquin, R., Harris, A., & Jezzard, P. (2015). Frequency and phase drift correction of magnetic resonance spectroscopy data by spectral registration in the time domain. *Magnetic Resonance in Medicine*, *73*(1), 44–50. https://doi.org/10.1002/mrm.25094

Neuner, I., Werner, C. J., Arrubla, J., Stöcker, T., Ehlen, C., Wegener, H. P., Schneider, F., & Jon Shah, N. (2014). Imaging the where and when of tic generation and resting state networks in adult Tourette patients. *Frontiers in Human Neuroscience*, *8*(MAY). https://doi.org/10.3389/fnhum.2014.00362

Neuper, C., & Pfurtscheller, G. (2001). Evidence for distinct beta resonance frequencies in human EEG related to specific sensorimotor cortical areas. *Clinical Neurophysiology*, *112*(11), 2084–2097. https://doi.org/10.1016/S1388-2457(01)00661-7

Niccolai, V., Korczok, S., Finis, J., Jonas, M., Thomalla, G., Siebner, H. R., Müller-Vahl, K., Münchau, A., Schnitzler, A., & Biermann-Ruben, K. (2019). A peek into premonitory urges in Tourette syndrome: Temporal evolution of neurophysiological oscillatory signatures. *Parkinsonism and Related Disorders*, *65*, 153–158. https://doi.org/10.1016/j.parkreldis.2019.05.039

Nichols, T., & Hayasaka, S. (2003). Controlling the familywise error rate in functional neuroimaging: A comparative review. *Statistical Methods in Medical Research*, *12*(5), 419–446. https://doi.org/10.1191/0962280203sm341ra

Notbohm, A., Kurths, J., & Herrmann, C. S. (2016). Modification of brain oscillations via rhythmic light stimulation provides evidence for entrainment but not for superposition of event-related responses. *Frontiers in Human Neuroscience*, *10*(FEB2016). https://doi.org/10.3389/fnhum.2016.00010

Nunez, P. L., & Srinivasan, R. (2006). *Electric Fields of the Brain: The neurophysics of EEG*. https://doi.org/10.1093/acprof:oso/9780195050387.001.0001

Nutt, D., Wilson, S., Lingford-Hughes, A., Myers, J., Papadopoulos, A., & Muthukumaraswamy, S. (2015). Differences between magnetoencephalographic (MEG) spectral profiles of drugs acting on GABA at synaptic and extrasynaptic sites: A study in healthy volunteers. *Neuropharmacology*, *88*, 155–163. https://doi.org/10.1016/j.neuropharm.2014.08.017

Oldfield, R. C. (1971). The assessment and analysis of handedness: The Edinburgh inventory. *Neuropsychologia*, *9*(1), 97–113. https://doi.org/10.1016/0028-3932(71)90067-4

O'Neill, G. C., Tewarie, P. K., Colclough, G. L., Gascoyne, L. E., Hunt, B. A. E., Morris, P. G., Woolrich, M. W., & Brookes, M. J. (2017). Measurement of dynamic task related functional networks using MEG. *NeuroImage*, *146*, 667–678. https://doi.org/10.1016/j.neuroimage.2016.08.061

Orth, M., Amann, B., Robertson, M. M., & Rothwell, J. C. (2005). Excitability of motor cortex inhibitory circuits in Tourette syndrome before and after single dose nicotine. *Brain*, *128*(6), 1292–1300. https://doi.org/10.1093/brain/awh473

Orth, M., & Rothwell, J. C. (2009). Motor cortex excitability and comorbidity in Gilles de la Tourette syndrome. *Journal of Neurology, Neurosurgery and Psychiatry*, *80*(1), 29–34. https://doi.org/10.1136/jnnp.2008.149484

Ostrowsky, K., Magnin, M., Ryvlin, P., Isnard, J., Guenot, M., & Mauguière, F. (2002). Representation of pain and somatic sensation in the human insula: A study of responses to direct electrical cortical stimulation. *Cerebral Cortex*, *12*(4), 376–385. https://doi.org/10.1093/cercor/12.4.376

Pappert, E. J., Goetz, C. G., Louis, E. D., Blasucci, L., & Leurgans, S. (2003). Objective assessments of longitudinal outcome in Gilles de la Tourette's syndrome. *Neurology*, *61*(7), 936–940. https://doi.org/10.1212/01.WNL.0000086370.10186.7C

Passmore, S. R., Murphy, B., & Lee, T. D. (2014). The origin, and application of somatosensory evoked potentials as a neurophysiological technique to investigate neuroplasticity. *Journal of the Canadian Chiropractic Association*, *58*(2), 170–183.

Peirce, J., Gray, J. R., Simpson, S., MacAskill, M., Höchenberger, R., Sogo, H., Kastman, E., & Lindeløv, J. K. (2019). PsychoPy2: Experiments in behavior made easy. *Behavior Research Methods*, *51*(1), 195–203. https://doi.org/10.3758/s13428-018-01193-y

Penfield, W., & Faulk, M. E. (1955). The insula: Further observations on its function. *Brain*, *78*(4), 445–470. https://doi.org/10.1093/brain/78.4.445

Penny, W., Friston, K., Ashburner, J., Kiebel, S., & Nichols, T. (2007). Statistical Parametric Mapping: The Analysis of Functional Brain Images. *Statistical Parametric Mapping: The Analysis of Functional Brain Images*. https://doi.org/10.1016/B978-0-12-372560-8.X5000-1

Pépés, S. E., Draper, A., Jackson, G. M., & Jackson, S. R. (2016). Effects of age on motor excitability measures from children and adolescents with Tourette syndrome. *Developmental Cognitive Neuroscience*, *19*, 78–86. https://doi.org/10.1016/j.dcn.2016.02.005

Peterson, B. S., Skudlarski, P., Andersen, A. W., Zhang, H., Gatenby, J. C., Lacadie, C. M., Leckman, J. F., & Gore, J. C. (1998). A functional magnetic resonance imaging study of tic suppression in tourette syndrome. *Archives of General Psychiatry*, *55*(4), 326–333. https://doi.org/10.1001/archpsyc.55.4.326

Pfurtscheller, G. (1981). Central beta rhythm during sensorimotor activities in man. *Electroencephalography and Clinical Neurophysiology*, *51*(3), 253–264. https://doi.org/10.1016/0013-4694(81)90139-5

Pfurtscheller, G., & Aranibar, A. (1979). Evaluation of event-related desynchronization (ERD) preceding and following voluntary self-paced movement. *Electroencephalography and Clinical Neurophysiology*, *46*(2), 138–146. https://doi.org/10.1016/0013-4694(79)90063-4

Pfurtscheller, G., & Berghold, A. (1989). Patterns of cortical activation during planning of voluntary movement. *Electroencephalography and*

Clinical Neurophysiology, *72*(3), 250–258. https://doi.org/10.1016/0013-4694(89)90250-2

Pfurtscheller, G., & Lopes Da Silva, F. H. (1999). Event-related EEG/MEG synchronization and desynchronization: Basic principles. In *Clinical Neurophysiology* (Vol. 110, Issue 11, pp. 1842–1857). https://doi.org/10.1016/S1388-2457(99)00141-8

Pfurtscheller, G., Stancák, A., & Neuper, C. (1996). Post-movement beta synchronization. A correlate of an idling motor area? *Electroencephalography and Clinical Neurophysiology*, *98*(4), 281–293. https://doi.org/10.1016/0013-4694(95)00258-8

Picazio, S., & Koch, G. (2015). Is Motor Inhibition Mediated by Cerebello-cortical Interactions? In *Cerebellum* (Vol. 14, Issue 1, pp. 47–49). https://doi.org/10.1007/s12311-014-0609-9

Pikovsky, A., Rosenblum, M., & Kurths, J. (2003). *Synchronization: A universal concept in nonlinear sciences* (B. Chirikov, F. Moss, P. Cvitanovic, & H. Swinney, Eds.; 1st paperb). Cambridge Univ. Press.

Pogosyan, A., Gaynor, L. D., Eusebio, A., & Brown, P. (2009). Boosting Cortical Activity at Beta-Band Frequencies Slows Movement in Humans. *Current Biology*, *19*(19), 1637–1641. https://doi.org/10.1016/j.cub.2009.07.074

Poldrack, R. A., Nichols, T., & Mumford, J. (2011). Handbook of Functional MRI Data Analysis. In *Handbook of Functional MRI Data Analysis*. Cambridge University Press. https://doi.org/10.1017/cbo9780511895029

Poole, W., Gibbs, D. L., Shmulevich, I., Bernard, B., & Knijnenburg, T. A. (2016). Combining dependent P-values with an empirical adaptation of Brown's method. *Bioinformatics*, *32*(17), i430–i436. https://doi.org/10.1093/bioinformatics/btw438

Provencher, S. W. (2001). Automatic quantitation of localized in vivo 1H spectra with LCModel. *NMR in Biomedicine*, *14*(4), 260–264. https://doi.org/10.1002/nbm.698

Puts, N. A. J., & Edden, R. A. E. (2012). In vivo magnetic resonance spectroscopy of GABA: A methodological review. In *Progress in Nuclear Magnetic Resonance Spectroscopy* (Vol. 60, pp. 29–41). https://doi.org/10.1016/j.pnmrs.2011.06.001

Quinn, A., Lopes-dos-Santos, V., Dupret, D., Nobre, A., & Woolrich, M. (2021). EMD: Empirical Mode Decomposition and Hilbert-Huang Spectral Analyses in Python. In *Journal of Open Source Software* (Vol. 6, Issue 59, p. 2977). https://doi.org/10.21105/joss.02977

Rae, C. D. (2014). A guide to the metabolic pathways and function of metabolites observed in human brain 1H magnetic resonance spectra. *Neurochemical Research*, *39*(1), 1–36. https://doi.org/10.1007/S11064-013-1199-5/FIGURES/9

Raines, J. M., Edwards, K. R., Sherman, M. F., Higginson, C. I., Winnick, J. B., Navin, K., Gettings, J. M., Conteh, F., Bennett, S. M., & Specht, M. W. (2018). Premonitory Urge for Tics Scale (PUTS): replication and extension of psychometric properties in youth with chronic tic disorders (CTDs). *Journal of Neural Transmission*, *125*(4), 727–734. https://doi.org/10.1007/s00702-017-1818-4

Regan, D. (1966). Some characteristics of average steady-state and transient responses evoked by modulated light. *Electroencephalography and Clinical Neurophysiology*, *20*(3), 238–248. https://doi.org/10.1016/0013-4694(66)90088-5

Robertson, M. M. (2008). The prevalence and epidemiology of Gilles de la Tourette syndrome. Part 1: The epidemiological and prevalence studies. In *Journal of Psychosomatic Research* (Vol. 65, Issue 5, pp. 461–472). https://doi.org/10.1016/j.jpsychores.2008.03.006

Robertson, M. M. (2011). Gilles de la tourette syndrome: The complexities of phenotype and treatment. *British Journal of Hospital Medicine*, *72*(2), 100–107. https://doi.org/10.12968/hmed.2011.72.2.100

Romei, V., Bauer, M., Brooks, J. L., Economides, M., Penny, W., Thut, G., Driver, J., & Bestmann, S. (2016). Causal evidence that intrinsic beta-frequency is relevant for enhanced signal propagation in the motor system as shown through rhythmic TMS. *NeuroImage*, *126*, 120–130. https://doi.org/10.1016/j.neuroimage.2015.11.020

Rouder, J. N., Morey, R. D., Speckman, P. L., & Province, J. M. (2012). Default Bayes factors for ANOVA designs. *Journal of Mathematical Psychology*, *56*(5), 356–374. https://doi.org/10.1016/j.jmp.2012.08.001

Salenius, S., Schnitzler, A., Salmelin, R., Jousmäki, V., & Hari, R. (1997). Modulation of Human Cortical Rolandic Rhythms during Natural Sensorimotor Tasks. *NeuroImage*, *5*(3), 221–228. https://doi.org/10.1006/NIMG.1997.0261

Salmelin, R., Hämäläinen, M., Kajola, M., & Hari, R. (1995). Functional segregation of movement-related rhythmic activity in the human brain. *NeuroImage*, *2*(4), 237–243. https://doi.org/10.1006/nimg.1995.1031

Salmelin, R., & Hari, R. (1994). Spatiotemporal characteristics of sensorimotor neuromagnetic rhythms related to thumb movement. *Neuroscience*, *60*(2), 537–550. https://doi.org/10.1016/0306-4522(94)90263-1

Sander, T. H., Preusser, J., Mhaskar, R., Kitching, J., Trahms, L., & Knappe, S. (2012). Magnetoencephalography with a chip-scale atomic magnetometer. *Biomedical Optics Express*, *3*(5), 981. https://doi.org/10.1364/boe.3.000981

Sarvas, J. (1987). Basic mathematical and electromagnetic concepts of the biomagnetic inverse problem. *Physics in Medicine and Biology*, *32*(1), 11–22. https://doi.org/10.1088/0031-9155/32/1/004

Savica, R., Stead, M., Mack, K. J., Lee, K. H., & Klassen, B. T. (2012). Deep brain stimulation in Tourette syndrome: A description of 3 patients with excellent outcome. *Mayo Clinic Proceedings*, *87*(1), 59–62. https://doi.org/10.1016/j.mayocp.2011.08.005

Scahill, L., Erenberg, G., Berlin, C. M., Budman, C., Coffey, B. J., Jankovic, J., Kiessling, L., King, R. A., Kurlan, R., Lang, A., Mink, J., Murphy, T., Zinner, S., & Walkup, J. (2006). Contemporary Assessment and Pharmacotherapy of Tourette Syndrome. *NeuroRx*, *3*(2), 192–206. https://doi.org/10.1016/j.nurx.2006.01.009

Schaefer, A., Kong, R., Gordon, E. M., Laumann, T. O., Zuo, X.-N., Holmes, A. J., Eickhoff, S. B., & Yeo, B. T. T. (2018). Local-Global Parcellation of the Human Cerebral Cortex from Intrinsic Functional Connectivity MRI. *Cerebral Cortex*, *28*, 3095–3114. https://doi.org/10.1093/cercor/bhx179

Schaller, B., Xin, L., O'Brien, K., Magill, A. W., & Gruetter, R. (2014). Are glutamate and lactate increases ubiquitous to physiological activation?

A 1H functional MR spectroscopy study during motor activation in human brain at 7Tesla. *NeuroImage*, *93*(P1), 138–145. https://doi.org/10.1016/j.neuroimage.2014.02.016

Schomer, D. L., Lopes Da Silva, F. H., & Niedermeyer, E. (2018). *Niedermeyer's electroencephalography: basic principles, clinical applications, and related fields* (6th ed.).

Sederman, A. J. (2015). Magnetic resonance imaging. In *Industrial Tomography: Systems and Applications* (pp. 109–133). Elsevier. https://doi.org/10.1016/B978-1-78242-118-4.00004-6

Sekihara, K., Hild, K. E., Dalal, S. S., Timer, J. M., Wipf, D., Attias, H. T., & Nagarajan, S. S. (2007). Adaptive spatial filter and adaptive inverse modeling for electromagnetic source imaging. *Proc. of 2007 Joint Meet. of the 6th Int. Symp. on Noninvasive Functional Source Imaging of the Brain and Heart and the Int. Conf. on Functional Biomedical Imaging, NFSI and ICFBI 2007*, 190–191. https://doi.org/10.1109/NFSI-ICFBI.2007.4387723

Seuwen, A., Schroeter, A., Grandjean, J., Schlegel, F., & Rudin, M. (2019). Functional spectroscopic imaging reveals specificity of glutamate response in mouse brain to peripheral sensory stimulation. *Scientific Reports 2019 9:1*, *9*(1), 1–9. https://doi.org/10.1038/s41598-019-46477-1

Simpson, R., Devenyi, G. A., Jezzard, P., Hennessy, T. J., & Near, J. (2017). Advanced processing and simulation of MRS data using the FID appliance (FID-A)—An open source, MATLAB-based toolkit. *Magnetic Resonance in Medicine*, *77*(1), 23–33. https://doi.org/10.1002/mrm.26091

Singer, H. S., & Minzer, K. (2003). Neurobiology of Tourette's syndrome: Concepts of neuroanatomic localization and neurochemical abnormalities. *Brain and Development*, *25*(SUPPL. 1), 70–84. https://doi.org/10.1016/S0387-7604(03)90012-X

Spooner, R. K., Wiesman, A. I., & Wilson, T. W. (2022). Peripheral Somatosensory Entrainment Modulates the Cross-Frequency Coupling of Movement-Related Theta-Gamma Oscillations. *Https://Home.Liebertpub.Com/Brain*, *12*(6), 524–537. https://doi.org/10.1089/BRAIN.2021.0003

Sprawls, P. (2000). *Magnetic resonance imaging: principles, methods, and techniques*. Medical Physics Publishing.

Stagg, C. J., Bachtiar, V., & Johansen-Berg, H. (2011). What are we measuring with GABA Magnetic Resonance Spectroscopy? *Communicative & Integrative Biology*, *4*(5), 573–575. https://doi.org/10.4161/cib.16213

Stagg, C. J., Bestmann, S., Constantinescu, A. O., Moreno Moreno, L., Allman, C., Mekle, R., Woolrich, M., Near, J., Johansen-Berg, H., & Rothwell, J. C. (2011). Relationship between physiological measures of excitability and levels of glutamate and GABA in the human motor cortex. *Journal of Physiology*, *589*(23), 5845–5855. https://doi.org/10.1113/jphysiol.2011.216978

Stern, E. R., Brown, C., Ludlow, M., Shahab, R., Collins, K., Lieval, A., Tobe, R. H., Iosifescu, D. V., Burdick, K. E., & Fleysher, L. (2020). The buildup of an urge in obsessive–compulsive disorder: Behavioral and neuroimaging correlates. *Human Brain Mapping*, *41*(6), 1611–1625. https://doi.org/10.1002/hbm.24898

Stolk, A., Todorovic, A., Schoffelen, J. M., & Oostenveld, R. (2013). Online and offline tools for head movement compensation in MEG. *NeuroImage*, *68*, 39–48. https://doi.org/10.1016/j.neuroimage.2012.11.047

Storch, E. A., Murphy, T. K., Geffken, G. R., Sajid, M., Allen, P., Goodman, W. K., & Roberti, J. W. (2005). Reliability and validity of the Yale Global Tic Severity Scale. *Psychological Assessment*, *17*(4), 486–491. https://doi.org/10.1037/1040-3590.17.4.486

Sukhodolsky, D. G., Leckman, J. F., Rothenberger, A., & Scahill, L. (2007). The role of abnormal neural oscillations in the pathophysiology of co-occurring Tourette syndrome and attention-deficit/hyperactivity disorder. In *European Child and Adolescent Psychiatry* (Vol. 16, Issue SUPPL. 1, pp. 51–59). https://doi.org/10.1007/s00787-007-1007-3

Thut, G., Schyns, P. G., & Gross, J. (2011). Entrainment of perceptually relevant brain oscillations by non-invasive rhythmic stimulation of the human brain. In *Frontiers in Psychology* (Vol. 2, Issue JUL). https://doi.org/10.3389/fpsyg.2011.00170

Thut, G., Veniero, D., Romei, V., Miniussi, C., Schyns, P., & Gross, J. (2011). Rhythmic TMS causes local entrainment of natural oscillatory signatures. *Current Biology*, *21*(14), 1176–1185. https://doi.org/10.1016/j.cub.2011.05.049

Tierney, T. M., Holmes, N., Mellor, S., López, J. D., Roberts, G., Hill, R. M., Boto, E., Leggett, J., Shah, V., Brookes, M. J., Bowtell, R., & Barnes, G. R. (2019). Optically pumped magnetometers: From quantum origins to multi-channel magnetoencephalography. In *NeuroImage* (Vol. 199, pp. 598–608). https://doi.org/10.1016/j.neuroimage.2019.05.063

Tinaz, S., Malone, P., Hallett, M., & Horovitz, S. G. (2015). Role of the right dorsal anterior insula in the urge to tic in tourette syndrome. *Movement Disorders*, *30*(9), 1190–1197. https://doi.org/10.1002/mds.26230

Tkáč, I. (2008). Refinement of simulated basis set for LCModel analysis [abstr]. *Proceedings of the Sixteenth Meeting of the International Society for Magnetic Resonance in Medicine*.

Tkáč, I., Starčuk, Z., Choi, I. Y., & Gruetter, R. (1999). In vivo 1H NMR spectroscopy of rat brain at 1 ms echo time. *Magnetic Resonance in Medicine*, *41*(4), 649–656. https://doi.org/10.1002/(SICI)1522-2594(199904)41:4<649::AID-MRM2>3.0.CO;2-G

Tokimura, H., Di Lazzaro, V., Tokimura, Y., Oliviero, A., Profice, P., Insola, A., Mazzone, P., Tonali, P., & Rothwell, J. C. (2000). Short latency inhibition of human hand motor cortex by somatosensory input from the hand. *Journal of Physiology*, *523*(2), 503–513. https://doi.org/10.1111/j.1469-7793.2000.t01-1-00503.x

Tremblay, S., Beaulé, V., Proulx, S., de Beaumont, L., Marjá nska, M., Doyon, J., Pascual-Leone, A., Lassonde, M., Théoret, H., Beaumont, de L., & Rela, T. H. (2013). Relationship between transcranial magnetic stimulation measures of intracortical inhibition and spectroscopy measures of GABA and glutamate+glutamine. *J Neurophysiol*, *109*, 1343–1349. https://doi.org/10.1152/jn.00704.2012.-Trans

Tzourio-Mazoyer, N., Landeau, B., Papathanassiou, D., Crivello, F., Etard, O., Delcroix, N., Mazoyer, B., & Joliot, M. (2002). Automated

anatomical labeling of activations in SPM using a macroscopic anatomical parcellation of the MNI MRI single-subject brain. *NeuroImage*, *15*(1), 273–289. https://doi.org/10.1006/nimg.2001.0978

Ugawa, Y., Uesaka, Y., Terao, Y., Hanajima, R., & Kanazawa, I. (1995). Magnetic stimulation over the cerebellum in humans. *Annals of Neurology*, *37*(6), 703–713. https://doi.org/10.1002/ana.410370603

Uruñuela, E. (2021). *ME-ICA/rica: v1.0.6*. https://doi.org/10.5281/ZENODO.5788350

Uruñuela, E., Bolton, T. A. W., van de Ville, D., & Caballero-Gaudes, C. (2021). *Hemodynamic Deconvolution Demystified: Sparsity-Driven Regularization at Work*. http://arxiv.org/abs/2107.12026

Uruñuela, E., Jones, S., Crawford, A., Shin, W., Oh, S., Lowe, M., & Caballero-Gaudes, C. (2020). Stability-Based Sparse Paradigm Free Mapping Algorithm for Deconvolution of Functional MRI Data. *Proceedings of the Annual International Conference of the IEEE Engineering in Medicine and Biology Society, EMBS*, *2020-July*, 1092–1095. https://doi.org/10.1109/EMBC44109.2020.9176137

van der Salm, S. M. A., van der Meer, J. N., Cath, D. C., Groot, P. F. C., van der Werf, Y. D., Brouwers, E., de Wit, S. J., Coppens, J. C., Nederveen, A. J., van Rootselaar, A. F., & Tijssen, M. A. J. (2018). Distinctive tics suppression network in Gilles de la Tourette syndrome distinguished from suppression of natural urges using multimodal imaging. *NeuroImage: Clinical*, *20*(August), 783–792. https://doi.org/10.1016/j.nicl.2018.09.014

Van Eimeren, T., Boecker, H., Konkiewitz, E. C., Schwaiger, M., Conrad, B., & Ceballos-Baumann, A. O. (2001). Right lateralized motor cortex activation during volitional blinking. *Annals of Neurology*, *49*(6), 813–816. https://doi.org/10.1002/ANA.1063

Van Veen, B. D., Van Drongelen, W., Yuchtman, M., & Suzuki, A. (1997). Localization of brain electrical activity via linearly constrained minimum variance spatial filtering. *IEEE Transactions on Biomedical Engineering*, *44*(9), 867–880. https://doi.org/10.1109/10.623056

Veniero, D., Vossen, A., Gross, J., & Thut, G. (2015). Lasting EEG/MEG aftereffects of rhythmic transcranial brain stimulation: Level of control

over oscillatory network activity. *Frontiers in Cellular Neuroscience*, *9*(DEC), 1–17. https://doi.org/10.3389/fncel.2015.00477

Vialatte, F. B., Maurice, M., Dauwels, J., & Cichocki, A. (2010). Steady-state visually evoked potentials: Focus on essential paradigms and future perspectives. In *Progress in Neurobiology* (Vol. 90, Issue 4, pp. 418–438). https://doi.org/10.1016/j.pneurobio.2009.11.005

Volovyk, O., & Tal, A. (2020). Increased Glutamate concentrations during prolonged motor activation as measured using functional Magnetic Resonance Spectroscopy at 3T. *NeuroImage*, *223*(September). https://doi.org/10.1016/j.neuroimage.2020.117338

Vrba, J. (2002). Magnetoencephalography: The art of finding a needle in a haystack. *Physica C: Superconductivity and Its Applications*, *368*(1–4), 1–9. https://doi.org/10.1016/S0921-4534(01)01131-5

Vrba, J., & Robinson, S. E. (2001). Signal processing in magnetoencephalography. *Methods*, *25*(2), 249–271. https://doi.org/10.1006/meth.2001.1238

Wang, Z., Maia, T. V., Marsh, R., Colibazzi, T., Gerber, A., & Peterson, B. S. (2011). The neural circuits that generate tics in Tourette's syndrome. *American Journal of Psychiatry*, *168*(12), 1326–1337. https://doi.org/10.1176/appi.ajp.2011.09111692

Whalen, C., Maclin, E. L., Fabiani, M., & Gratton, G. (2008). Validation of a method for coregistering scalp recording locations with 3D structural MR images. *Human Brain Mapping*, *29*(11), 1288–1301. https://doi.org/10.1002/hbm.20465

Williams, M. (2016). An Introduction to the Nucleus Accumbens in schizophrenia. *Oruen - The CNS Journal*, *2*(January), 29. http://dx.doi.org/10.3389/fnins.2014.00230

Woods, D. W., Conelea, C. A., & Himle, M. B. (2010). Behavior Therapy for Tourette's Disorder: Utilization in a Community Sample and an Emerging Area of Practice for Psychologists. *Professional Psychology: Research and Practice*, *41*(6), 518–525. https://doi.org/10.1037/a0021709

Woods, D. W., Piacentini, J., Himle, M. B., & Chang, S. (2005). Premonitory Urge for Tics Scale (PUTS): Initial psychometric results and examination of the premonitory urge phenomenon in youths with tic

disorders. *Journal of Developmental and Behavioral Pediatrics*, *26*(6), 397–403. https://doi.org/10.1097/00004703-200512000-00001

Wu, J., Liu, H., Xiong, H., Cao, J., & Chen, J. (2015). K-means-based consensus clustering: A unified view. *IEEE Transactions on Knowledge and Data Engineering*, *27*(1), 155–169. https://doi.org/10.1109/TKDE.2014.2316512

Wu, S. W., Maloney, T., Gilbert, D. L., Dixon, S. G., Horn, P. S., Huddleston, D. A., Eaton, K., & Vannest, J. (2014). Functional MRI-navigated repetitive transcranial magnetic stimulation over supplementary motor area in chronic tic disorders. *Brain Stimulation*, *7*(2), 212–218. https://doi.org/10.1016/j.brs.2013.10.005

Yoon, H. W., Chung, J.-Y., Song, M. S., & Park, H. (2005). Neural correlates of eye blinking; improved by simultaneous fMRI and EOG measurement. *Neuroscience Letters*, *381*(1–2), 26–30. https://doi.org/10.1016/j.neulet.2005.01.077

Zapparoli, L., Macerollo, A., Joyce, E. M., Martino, D., & Kilner, J. M. (2019). Voluntary tic suppression and the normalization of motor cortical beta power in Gilles de la Tourette syndrome: an EEG study. *European Journal of Neuroscience*, *50*(12), 3944–3957. https://doi.org/10.1111/ejn.14548

Zhang, R., Geng, X., & Lee, T. M. C. (2017). Large-scale functional neural network correlates of response inhibition: an fMRI meta-analysis. *Brain Structure and Function*, *222*(9), 3973–3990. https://doi.org/10.1007/s00429-017-1443-x

Zhang, X. H., Li, J. Y., Zhang, Y. Q., & Li, Y. J. (2016). Deep brain stimulation of the globus pallidus internus in patients with intractable tourette syndrome: A 1-year follow-up study. *Chinese Medical Journal*, *129*(9), 1022–1027. https://doi.org/10.4103/0366-6999.180512

Ziemann, U., Lönnecker, S., Steinhoff, B. J., & Paulus, W. (1996). The effect of lorazepam on the motor cortical excitability in man. *Experimental Brain Research*, *109*(1), 127–135. https://doi.org/10.1007/BF00228633

Ziemann, U., Paulus, W., & Rothenberger, A. (1997). Decreased motor inhibition in Tourette's disorder: Evidence from transcranial magnetic

stimulation. *American Journal of Psychiatry*, *154*(9), 1277–1284. https://doi.org/10.1176/ajp.154.9.1277

Zimmerman, J. E., Thiene, P., & Harding, J. T. (1970). Design and operation of stable rf-biased superconducting point-contact quantum devices, and a note on the properties of perfectly clean metal contacts. *Journal of Applied Physics*, *41*(4), 1572–1580. https://doi.org/10.1063/1.1659074

Zoefel, B., ten Oever, S., & Sack, A. T. (2018). The involvement of endogenous neural oscillations in the processing of rhythmic input: More than a regular repetition of evoked neural responses. In *Frontiers in Neuroscience* (Vol. 12, Issue MAR, p. 95). https://doi.org/10.3389/fnins.2018.00095

Appendix A: Temporal Signal-to-Noise Ratio (tSNR)

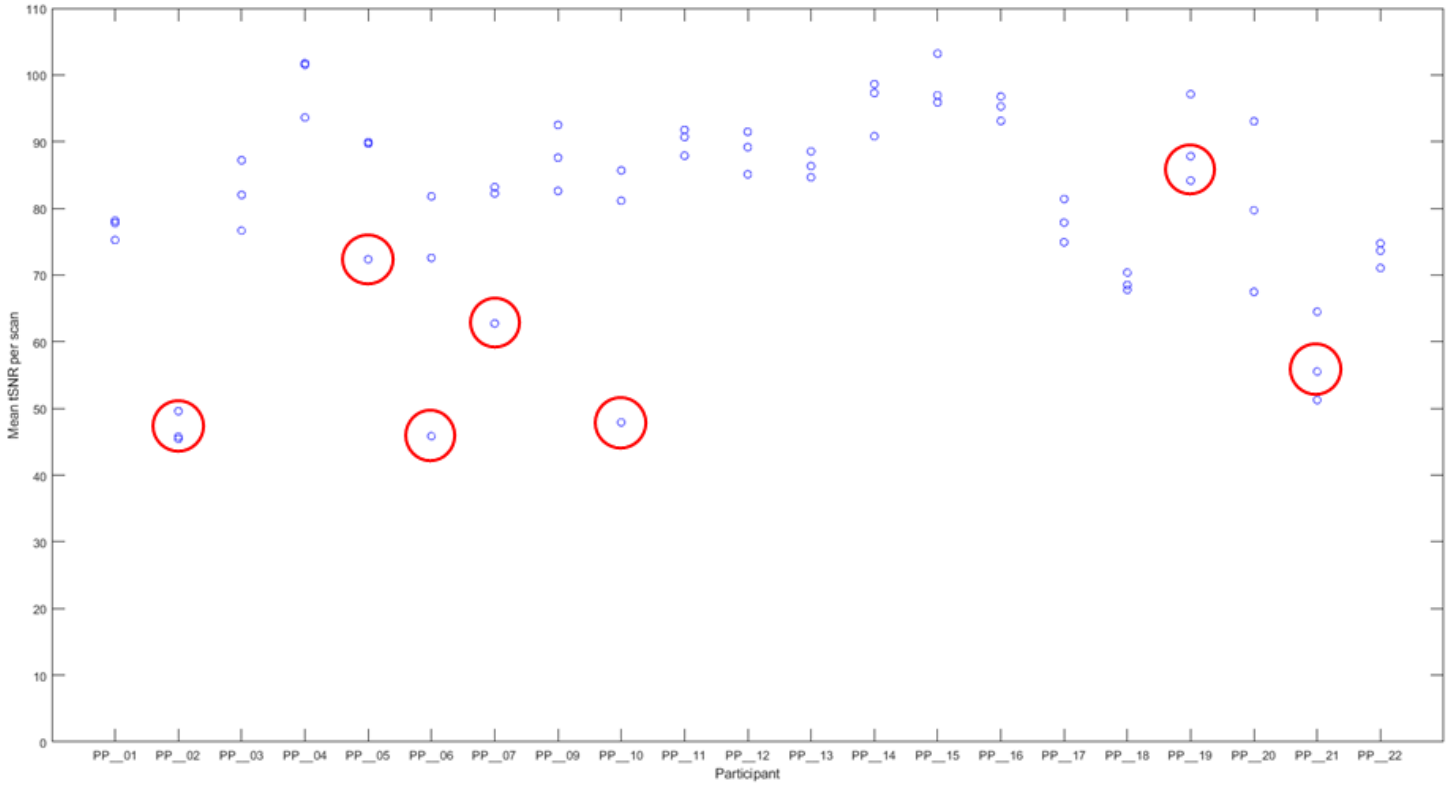

Figure A.1. *A graph showing the mean tSNR for each fMRI run of the blink suppression paradigm, where scans encircled in red were excluded due to a maintained absolute mean displacement over 1.5mm. If found, scans with a tSNR below 30 would have been excluded.*

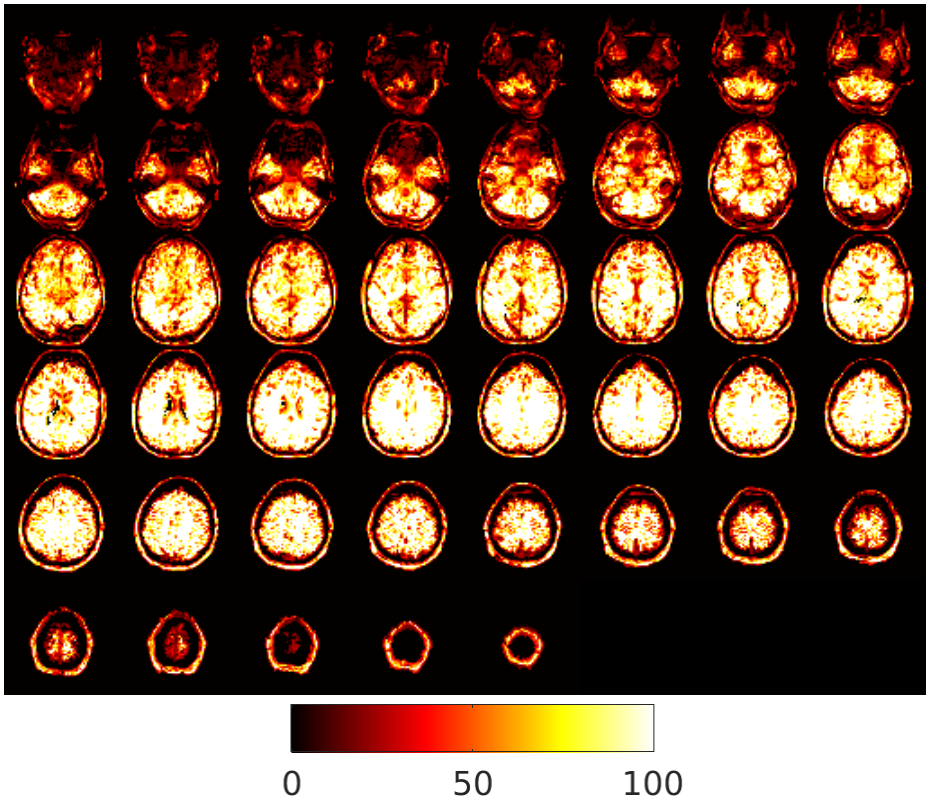

***Figure A.2**. An example (Sub01 run01) fMRI image with high tSNR.*

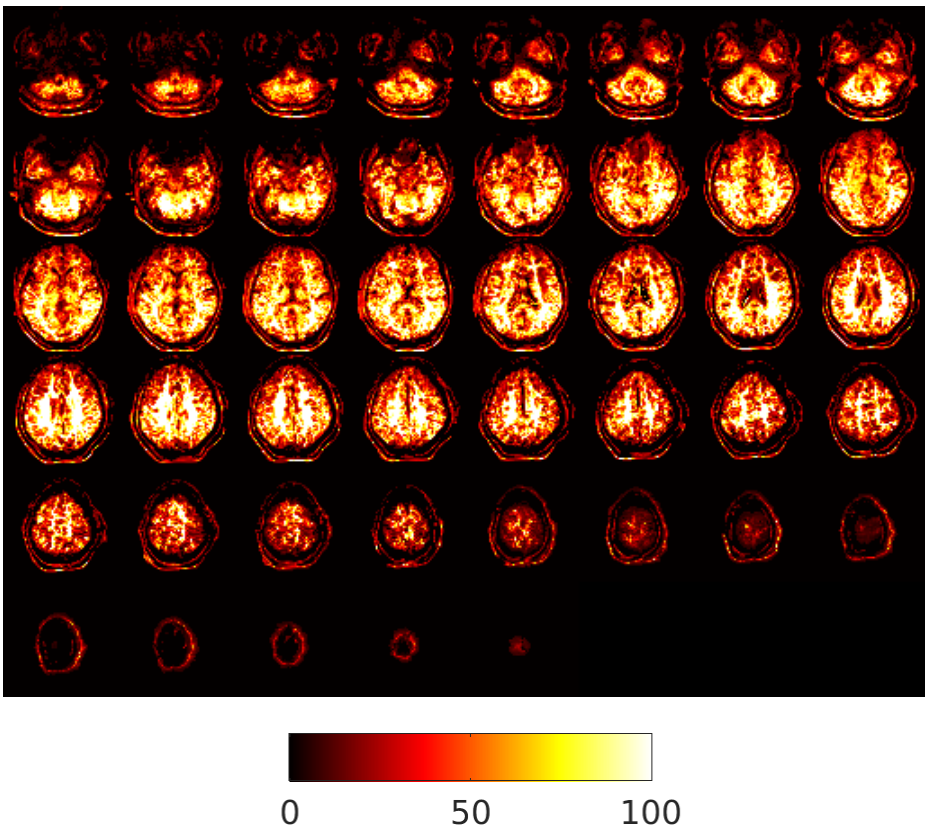

***Figure A.3.** An example (Sub02 run01) fMRI scan which was excluded due to a maintained absolute mean displacement over 1.5mm which caused a drop in tSNR.*

Appendix B: Local Maxima Cluster Index

Table B.1. *Local maxima cluster index for 'Suppress' blocks.*

Cluster Size	Region	Z-score	MNI Coordinates		
			X	Y	Z
Positive					
2394	Left precentral gyrus	6.53	-36	-21	54
	Left postcentral gyrus	6.22	-57	-24	45
	Left precentral gyrus	6.18	-33	-12	66
	Left postcentral gyrus	6.15	-42	-33	60
	Left postcentral gyrus	6.12	-48	-27	45
	Left superior parietal lobule	5.74	-33	-48	57
1090	Right anterior supramarginal gyrus	6.3	57	-24	45
	Right postcentral gyrus	5.98	45	-33	51
	Right postcentral gyrus	5.8	36	-33	48
	Right superior lateral occipital cortex	5.71	18	-69	63
	Right postcentral gyrus	4.95	60	-18	33
	Right superior parietal lobule	4.41	39	-48	63
525	Right I-IV	6.41	6	-51	-15
	Right V	6.3	3	-57	-12
	Right V	6.28	15	-51	-18
	Vermis VIIIa	4.79	0	-69	-36
	Left I-IV	3.9	0	-45	-3
	Right crus I	3.31	42	-51	-27
442	Right inferior lateral occipital cortex	5.96	45	-66	6
	Right inferior lateral occipital cortex	4.89	51	-60	-6
	Right inferior lateral occipital cortex	4.69	45	-69	-6
	Right inferior lateral occipital cortex	3.62	33	-81	6
	Right inferior temporal gyrus	3.57	42	-48	-6
236	Left inferior lateral occipital cortex	6.2	-48	-75	6
	Left inferior lateral occipital cortex	5.02	-48	-63	6
217	Right precentral gyrus	5.49	57	12	27
	Right insular cortex	5.16	39	0	9
103	Left precentral gyrus	5.21	-54	3	36
	Left inferior frontal gyrus, pars opercularis	3.54	-54	9	18
	Left precentral gyrus	3.5	-60	12	21
61	Left thalamus	5.35	-15	-21	9
57	Left central opercular cortex	5.33	-39	-3	15
52	Left VI	4.26	-36	-36	-33
	Left VI	4.2	-33	-51	-27
	Left VI	3.9	-33	-39	-39

	Left VI	3.87	-24	-57	-21
Negative					
5690	Left cuneal cortex	7.52	-6	-87	30
	Right lingual gyrus	6.61	9	-60	3
	Right precuneous cortex	6.44	3	-54	15
	Left lingual gyrus	6.36	-18	-42	-6
	Left lingual gyrus	6.28	-12	-60	3
	Right cuneal cortex	6.21	3	-75	27
956	Right anterior superior temporal gyrus	5.7	57	-3	-12
	Right anterior middle temporal gyrus	5.29	63	-6	-9
	Right planum polare	5.21	60	0	3
	Right Heschl's gyrus	5.08	45	-12	0
	Right posterior superior temporal gyrus	4.91	66	-24	0
	Right anterior superior temporal gyrus	4.88	63	-6	0
544	Right frontal pole	4.89	21	60	0
	Left frontal pole	4.74	-6	63	3
	Left frontal pole	4.5	-6	57	3
	Right frontal pole	4.37	6	60	-3
	Right paracingulate gyrus	4.31	6	42	24
	Right frontal pole	4.29	12	66	0
202	Right angular gyrus	5.62	57	-57	27
	Right angular gyrus	4.49	51	-54	36
146	Left crus I	5.35	-21	-78	-33
	Left crus II	4.78	-9	-81	-33
	Left crus I	3.69	-42	-75	-36
109	Right superior frontal gyrus	4.32	21	33	39
	Right frontal pole	4.31	24	36	48
	Right middle frontal gyrus	4.04	27	30	48
	Right superior frontal gyrus	3.96	24	30	54
	Right middle frontal gyrus	3.89	27	27	42
	Right superior frontal gyrus	3.87	27	24	57
74	Left middle frontal gyrus	4.12	-27	15	48
	Left middle frontal gyrus	4.11	-27	21	51
	Left superior frontal gyrus	3.68	-18	27	39
	Left superior frontal gyrus	3.58	-24	18	39
	Left middle frontal gyrus	3.48	-27	27	45
55	Left IX	5.04	6	-45	-39
	Left IX	3.91	-6	-54	-39

***Table B.2**. Local maxima cluster index for 'Okay to blink' blocks.*

Cluster Size	Region	Z-score	MNI Coordinates		
			X	Y	Z
Positive					
1259	Left postcentral gyrus	5.73	-57	-27	48
	Left postcentral gyrus	5.46	-39	-36	54
	Left postcentral gyrus	5.39	-45	-27	45
	Left precentral gyrus	5.3	-42	-21	60
	Left postcentral gyrus	5.22	-36	-36	45
	Left superior parietal lobule	5.14	-33	-45	54
797	Right precentral gyrus	5.92	54	-21	42
	Right postcentral gyrus	5.56	42	-30	48
	Right superior lateral occipital cortex	4.8	18	-63	63
	Right superior parietal lobule	4.71	39	-48	63
460	Right inferior lateral occipital cortex	5.48	45	-69	6
	Right inferior lateral occipital cortex	4.94	54	-60	-6
	Right inferior lateral occipital cortex	4.45	45	-69	-6
	Right superior lateral occipital cortex	4.12	30	-84	9
	Right inferior temporal gyrus	4	45	-48	-6
	Right cerebral white matter (superior longitudinal fasciculus)	3.85	42	-51	3
212	Right precentral gyrus	5.07	33	-6	57
	Right precentral gyrus	3.63	15	-12	72
	Right supplementary motor area	3.24	12	-9	54
165	Left inferior lateral occipital cortex	6.23	-45	-72	6
	Left cerebral white matter (inferior longitudinal fasciculus)	3.84	-36	-63	9
135	Right V	4.7	12	-51	-18
	Right V	4.46	24	-42	-30
96	Right precentral gyrus	5.09	57	12	27
Negative					
4237	Left cuneal cortex	6.57	-6	-87	27
	Left lingual gyrus	6.42	-12	-60	3
	Left cuneal cortex	6.42	-9	-87	18
	Left intracalcarine cortex	6.22	-12	-75	15
	Right lingual gyrus	6.21	12	-60	3
	Right precuneous cortex	6.14	18	-57	9
903	Right central opercular cortex	5.46	60	-3	6
	Right anterior superior temporal gyrus	5	57	-3	-9
	Right temporal pole	4.65	54	6	-15
	Right planum polare	4.57	42	0	-15
	Right middle temporal gyrus	4.51	66	-39	3
	Right planum polare	4.49	63	-18	3

311	Right angular gyrus	5.49	57	-54	24
	Right angular gyrus	4.91	57	-54	36
	Right posterior supramarginal gyrus	3.82	48	-39	21
	Right angular gyrus	3.74	39	-51	21
	Right angular gyrus	3.59	54	-54	51
283	Right frontal pole	5.12	27	54	36
	Right frontal pole	4.54	18	72	6
	Right frontal pole	4.25	21	63	0
	Right frontal pole	4.2	30	48	30
	Right frontal pole	4.04	30	57	18
	Right frontal pole	4.02	27	45	39
175	Left insular cortex	4.54	-42	-6	-9
	Left planum temporale	4.34	-60	-9	3
	Left central opercular cortex	4.04	-51	-6	12
	Left insular cortex	4.01	-33	12	-18
	Left planum polare	4.01	-54	0	-6
	Left temporal pole	3.49	-30	6	-21
172	Anterior cingulate cortex	4.44	6	12	39
	Paracingulate gyrus	3.99	6	33	30
	Anterior cingulate cortex	3.96	-6	39	18
	Anterior cingulate cortex	3.95	0	33	24
	Anterior cingulate cortex	3.85	3	39	21
	Anterior cingulate cortex	3.42	6	45	6
162	Left crus I	5.65	-18	-78	-33
	Left crus I	3.9	-15	-90	-24
	Left VI	3.78	-9	-72	-24
	Vermis VI	3.58	3	-72	-21
102	Left posterior supramarginal gyrus	4.9	-54	-48	18
	Left middle temporal gyrus	3.97	-57	-48	6
	Left middle temporal gyrus	3.7	-66	-54	6
	Left posterior supramarginal gyrus	3.52	-57	-45	33
	Left planum temporale	3.36	-57	-33	15
30	Right middle frontal gyrus	3.9	39	27	33

***Table B.3**. Local maxima cluster index for 'Random' active baseline blocks.*

Cluster Size	Region	Z-score	MNI Coordinates		
			X	Y	Z
Positive					
1986	Left postcentral gyrus	6.26	-57	-24	45
	Left precentral gyrus	6.18	-36	-21	54
	Left postcentral gyrus	6.13	-42	-33	60
	Left precentral gyrus	6.03	-33	-12	63
	Left postcentral gyrus	6.01	-48	-27	45
	Left superior parietal lobule	5.73	-33	-48	57
939	Right anterior supramarginal gyrus	5.96	57	-24	45
	Right postcentral gyrus	5.75	42	-33	48
	Right postcentral gyrus	5.68	33	-36	48
	Right superior lateral occipital cortex	5.16	18	-66	63
	Right postcentral gyrus	5.12	60	-15	33
	Right superior parietal lobule	4.38	39	-48	60
500	Right inferior lateral occipital cortex	5.89	45	-69	6
	Right inferior lateral occipital cortex	4.91	51	-60	-6
	Right inferior lateral occipital cortex	4.59	45	-69	-6
	Right cerebral white matter (inferior longitudinal fasciculus)	4.4	39	-60	-3
	Right superior lateral occipital cortex	4.36	30	-84	9
	Right inferior temporal cortex	3.85	42	-48	-6
364	Right V	6.09	15	-51	-18
	Right I-IV	5.87	6	-51	-15
	Right V	5.59	3	-57	-12
	Left I-IV	3.4	0	-45	-3
205	Left inferior lateral occipital cortex	6.45	-48	-75	6
	Left inferior lateral occipital cortex	4.63	-48	-63	6
123	Right precentral gyrus	5.49	57	12	27
102	Left precentral gyrus	5.23	-54	3	33
66	Vermis VIIIa	4.7	3	-66	-36
50	Left thalamus	4.98	-15	-24	9
39	Left inferior lateral occipital cortex	4.14	-27	-90	6
36	Left central opercular cortex	5.19	-39	-3	15
Negative					
4473	Left cuneal cortex	7.33	-6	-87	30
	Left lingual gyrus	6.87	-12	-60	3
	Left intracalcarine cortex	6.73	-6	-75	15
	Right cuneal cortex	6.71	3	-75	27
	Left lingual gyrus	6.63	-18	-42	-6
	Right lingual gyrus	6.58	12	-60	3

1007	Right central opercular cortex	5.95	60	0	6
	Right anterior superior temporal gyrus	5.54	57	0	-15
	Right temporal pole	4.99	45	9	-27
	Right Heschl's gyrus	4.95	45	-12	0
	Right planum polare	4.86	45	-3	-12
	Right temporal pole	4.85	45	15	-15
571	Right paracingulate gyrus	4.54	6	42	21
	Right frontal pole	4.44	21	60	0
	Right paracingulate gyrus	4.29	12	42	18
	Right frontal pole	4.27	24	54	12
	Right frontal pole	4.19	24	57	27
	Right frontal pole	4.13	24	54	-3
313	Right angular gyrus	5.72	57	-54	24
	Right angular gyrus	4.87	51	-54	36
	Right angular gyrus	3.88	54	-54	51
	Right angular gyrus	3.78	39	-51	21
	Right posterior supramarginal gyrus	3.49	48	-39	21
279	Left planum polare	4.69	-51	-3	-6
	Left insular cortex	4.59	-42	-3	-12
	Left planum polare	4.38	-57	-9	3
	Left frontal orbital cortex	4.25	-33	12	-21
	Left anterior superior temporal gyrus	4.24	-63	-12	0
	Left anterior superior temporal gyrus	4.1	-54	-12	-6
240	Left angular gyrus	5.2	-54	-51	18
	Left posterior superior temporal gyrus	4.13	-48	-33	3
	Left planum polare	3.98	-60	-33	15
	Left posterior supramarginal gyrus	3.97	-63	-48	21
	Left superior lateral occipital cortex	3.85	-57	-63	21
	Left posterior middle temporal gyrus	3.7	-45	-42	3
229	Right middle frontal gyrus	4.59	39	9	45
	Right superior frontal gyrus	4.43	21	33	39
	Right middle frontal gyrus	4.17	27	33	48
	Right superior frontal gyrus	3.96	24	24	51
	Right middle frontal gyrus	3.9	36	12	33
	Right superior frontal gyrus	3.88	27	24	57
152	Left crus I	5.38	-21	-81	-30
	Left crus II	4.96	-9	-78	-33
64	Left insular cortex	4.06	-36	18	-3
	Left insular cortex	3.97	-27	27	0
	Left frontal operculum cortex	3.64	-30	27	9
	Left putamen	3.55	-21	18	-3
	Left cerebral white matter (inferior fronto-occipital fasciculus)	3.49	-24	27	12

50	Left crus I	4.13	-42	-66	-42
	Left crus II	3.87	-36	-72	-42
	Left crus I	3.8	-42	-75	-36
	Left crus I	3.73	-54	-63	-30
49	Right IX	4.59	3	-45	-42
	Left IX	3.84	-9	-51	-33
31	Right thalamus	4.07	6	-9	12
	Right thalamus	3.52	3	-21	3
	Left thalamus	3.41	-3	-6	6

Table B.4. *Local maxima cluster index for blinks.*

Cluster Size	Region	Z-score	MNI Coordinates		
			X	Y	Z
Positive					
4484	Left lingual gyrus	6.39	-21	-51	-3
	Left intracalcerine cortex	6.37	-12	-72	12
	Left intracalcerine cortex	6.29	-12	-63	6
	Right lingual gyrus	6.16	15	-45	-3
	Right lingual gyrus	6.1	21	-51	-6
	Right intracalcerine cortex	5.87	15	-66	15
637	Left superior frontal gyrus	4.98	-12	-3	66
	Anterior cingulate cortex	4.6	6	12	39
	Anterior cingulate cortex	4.56	3	18	36
	Anterior cingulate cortex	4.52	-6	12	39
	Left superior frontal gyrus	4.48	-15	6	72
	Left supplementary motor area	4.31	-6	0	54
588	Left precentral gyrus	5.96	-54	6	3
	Left central opercular cortex	5.38	-45	6	6
	Left central opercular cortex	4.92	-36	9	15
	Left insular cortex	4.74	-36	9	3
	Left postcentral gyrus	4.7	-57	-24	21
	Left central opercular cortex	4.62	-42	-9	9
263	Right insular cortex	4.94	36	9	9
	Right central opercular cortex	4.29	54	-6	15
	Right precentral gyrus	4.19	57	6	6
	Right central opercular cortex	4.18	48	6	6
	Right precentral gyrus	3.87	51	3	12
	Right central opercular cortex	3.86	42	-12	21
149	Left frontal pole	5.08	-30	51	30
	Left frontal pole	4.73	-42	48	27
	Left frontal pole	4.66	-36	42	24
	Left frontal pole	4.46	-30	45	21
67	Left precentral gyrus	4.7	-39	-9	51
	Left postcentral gyrus	4.34	-36	-18	39
	Left precentral gyrus	3.58	-51	-6	54
49	Right angular gyrus	4.02	54	-51	15
	Right posterior supramarginal gyrus	3.99	60	-39	27
	Right angular gyrus	3.65	48	-48	24
39	Right precentral gyrus	3.81	48	0	54
	Right precentral gyrus	3.7	42	-6	57
	Right precentral gyrus	3.7	45	0	48
36	Right frontal pole	4.2	36	51	21

	Right frontal pole	3.85	30	48	39
	Right frontal pole	3.62	27	45	30
	Right frontal pole	3.28	24	48	24
Negative					
85	Right angular gyrus	4.46	36	-54	39
	Right superior lateral occipital cortex	4.1	33	-57	66
	Right superior lateral occipital cortex	3.75	39	-60	60
	Right superior parietal lobule	3.52	39	-45	48
	Right superior parietal lobule	3.51	36	-39	48

Table B.5. *Local maxima cluster index related to the subjective urge ratings.*

Cluster Size	Region	Z-score	MNI Coordinates		
			X	Y	Z
Positive					
1317	Right anterior thalamic radiation	4.91	3	-30	3
	Left thalamus	4.61	-6	-33	3
	Left intracalcarine cortex	4.49	-12	-72	15
	Left lingual gyrus	4.42	-12	-78	-3
	Right occipital pole	4.35	9	-99	9
	Right thalamus	4.32	18	-27	0
110	Left insular cortex	4.58	-42	-9	0
	Left insular cortex	4.52	-39	-15	6
69	Right planum polare	4.02	48	-9	-3
	Right insular cortex	3.99	39	-9	0
	Right planum polare	3.78	48	3	-3
	Right Heschl's gyrus	3.73	42	-18	3
	Right planum polare	3.49	45	-3	-9
50	Left insular cortex	3.9	-30	12	-12
	Left putamen	3.88	-21	6	-9
	Left putamen	3.36	-15	12	-9
41	Paracingulate gyrus	3.98	-3	33	33
	Anterior cingulate gyrus	3.87	0	24	33
37	Right central opercular cortex	3.79	48	-6	9
	Right insular cortex	3.66	33	-12	18
Negative					
49	Right superior lateral occipital cortex	4.29	18	-75	57
	Right superior lateral occipital cortex	3.89	27	-72	57
	Right precuneous cortex	3.47	9	-69	54
42	Right posterior supramarginal gyrus	4.18	39	-45	39
	Right posterior supramarginal gyrus	3.99	36	-39	36
33	Left superior lateral occipital cortex	3.96	-21	-63	51
	Left precuneous cortex	3.68	-6	-69	51

Table B.6. *Local maxima cluster index when contrasting 'Suppress' > 'Okay to blink' blocks.*

Cluster Size	Region	Z-score	MNI Coordinates		
			X	Y	Z
721	Right superior frontal gyrus	4.81	27	12	66
	Anterior cingulate cortex	4.62	-6	21	30
	Right superior frontal gyrus	4.62	6	12	63
	Paracingulate gyrus	4.53	0	12	45
	Paracingulate gyrus	4.5	-9	15	42
	Right superior frontal gyrus	4.38	12	6	66
459	Vermis VIIIa	5.06	-3	-69	-36
	Vermis VIIIa	4.6	-3	-63	-33
	Left I-IV	4.53	0	-45	-15
	Left VI	4.52	-6	-72	-12
	Right V	4.33	6	-60	-6
	Vermis VI	4.27	0	-72	-12
362	Left crus I	4.85	-54	-51	-36
	Left VI	4.56	-36	-57	-27
	Left VI	4.49	-27	-57	-21
	Left VI	4.46	-18	-72	-18
	Left crus I	4.43	-48	-45	-36
	Left VI	4.43	-24	-66	-27
337	Right frontal operculum	4.92	36	21	9
	Right inferior frontal gyrus, pars opercularis	4.76	48	6	15
	Right frontal operculum cortex	4.68	42	15	9
	Right insular cortex	4.13	36	6	3
	Right inferior frontal gyrus, pars opercularis	3.9	57	12	9
	Rightinferior frontal gyrus, pars opercularis	3.88	54	15	21
281	Right posterior SMG	4.33	60	-39	33
	Right posterior SMG	4.1	48	-42	60
	Right posterior SMG	4.05	66	-39	27
	Right middle temporal gyrus	4.03	45	-54	12
	Right angular gyrus	3.93	48	-48	21
	Right anterior supramarginal gyrus	3.89	54	-30	39
250	Left superior lateral occipital	4.26	-18	-63	63
	Left superior parietal lobule	4.23	-27	-54	60
	Left superior lateral occipital cortex	4.18	-12	-63	63
	Left superior lateral occipital	4.12	-15	-60	54
	Left superior lateral occipital	4.09	-18	-63	45
	Left superior lateral occipital	4.09	-15	-75	48
236	Left frontal operculum	4.7	-36	12	12
	Left frontal operculum	4.69	-33	18	12

	Left precentral gyrus	4.12	-54	6	9
	Left inferior frontal gyrus, pars opercularis	4.02	-57	12	0
	Left central opercular cortex	3.91	-48	-3	6
193	Right frontal pole	5.72	36	57	21
	Right frontal pole	4.6	27	57	30
	Right frontal pole	4.14	33	48	39
188	Right superior lateral occipital	4.29	15	-60	54
	Right superior lateral occipital	4.15	12	-72	48
	Right superior lateral occipital	3.96	9	-60	72
	Right superior lateral occipital	3.78	15	-72	63
	Right precuneous cortex	3.64	18	-66	42
	Right superior parietal lobule	3.49	24	-54	51
120	Right cerebellum	4.81	21	-45	-42
	Right VI	4.25	39	-45	-33
	Right VI	4.15	30	-51	-30
	Right VI	3.77	30	-39	-33
	Right crus II	3.65	33	-48	-42
109	Left superior frontal gyrus	4.45	-24	3	57
	Left superior frontal gyrus	3.93	-12	-6	72
	Left superior frontal gyrus	3.91	-18	6	69
	Left superior frontal gyrus	3.59	-27	-6	72
91	Left frontal pole	4.48	-36	45	18
	Left frontal pole	3.99	-33	51	24
	Left frontal pole	3.95	-36	51	30
	Left frontal pole	3.91	-33	57	21
60	Left inferior lateral occipital	4.56	-45	-78	12
	Left inferior lateral occipital	3.57	-54	-66	12
	Left middle temporal gyrus	3.55	-45	-60	6
59	Left precentral gyrus	4.3	-12	-21	42
	Left precentral gyrus	4.25	-15	-33	45
	Left postcentral gyrus	3.86	-18	-42	54
42	Posterior cingulate cortex	4.24	9	-30	45
	Posterior cingulate cortex	4.21	6	-21	45
	Right precuneous cortex	3.67	15	-36	45
	Right postcentral gyrus	3.56	21	-42	51

Table B.7. *Local maxima cluster index when contrasting 'Okay to blink' > 'Suppress' blocks.*

Cluster Size	Region	Z-score	MNI Coordinates		
			X	Y	Z
261	Posterior cingulate cortex	5	3	-48	21
	Posterior cingulate cortex	4.25	-9	-51	21
	Posterior cingulate cortex	4.04	0	-42	36
	Posterior cingulate cortex	4.02	-6	-45	12
	Left precuneous cortex	3.84	-3	-60	36
207	Left middle frontal gyrus	4.6	-27	18	48
	Left middle frontal gyrus	4.58	-33	18	54
	Left superior frontal gyrus	4.43	-15	24	48
	Left superior frontal gyrus	4.39	-21	27	48
	Left frontal lobe	3.86	-15	45	54
	Paracingulate gyrus	3.84	-3	39	36
203	Left superior lateral occipital	4.63	-42	-72	42
	Left superior lateral occipital	4.52	-39	-63	39
	Left superior lateral occipital	4.39	-45	-72	33
	Left superior lateral occipital	4.33	-36	-72	48
	Left angular gyrus	4.12	-42	-60	33
52	Frontal pole	4.55	0	63	-6
	Right frontal pole	4.48	6	63	-6
52	Left hippocampus	3.77	-36	-18	-12
	Left parahippocampal gyrus	3.58	-27	-33	-12
	Left amygdala	3.55	-27	-9	-18
51	Left frontal orbital cortex	4.61	-48	36	-9
	Left frontal pole	4.03	-42	45	-6
44	Right frontal pole	4.04	18	36	48
	Right superior frontal gyrus	3.79	18	36	57
42	Right crus I	4.04	27	-81	-24
	Right crus II	3.93	24	-84	-36
	Right crus I	3.84	30	-84	-30
	Right crus I	3.67	39	-81	-27
	Right crus II	3.54	15	-84	-36

Table B.8. *Local maxima cluster index when contrasting 'Random' > Urge blocks.*

Cluster Size	Region	Z-score	MNI Coordinates		
			X	Y	Z
1660	Left precentral gyrus	6.53	-36	-21	54
	Left postcentral gyrus	6.37	-57	-24	45
	Left postcentral gyrus	6.19	-42	-33	60
	Left postcentral gyrus	6.19	-48	-27	45
	Left precentral gyrus	6.07	-33	-12	63
	Left superior parietal lobule	5.76	-33	-48	57
953	Right anterior SMG	6.26	57	-24	45
	Right postcentral gyrus	5.78	45	-33	51
	Right postcentral gyrus	5.72	36	-33	48
	Right superior lateral occipital	5.47	18	-69	63
	Right postcentral gyrus	4.84	60	-15	33
	Right superior parietal lobule	4.32	39	-48	60
437	Right inferior lateral occipital	6.02	45	-69	6
	Right inferior temporal gyrus	4.96	51	-57	-6
	Right inferior temporal gyrus	4.13	42	-48	-6
	Right superior lateral occipital	3.78	30	-84	9
386	Right V	6.48	15	-51	-18
	Right I-IV	6.3	6	-51	-15
	Right VI	3.83	15	-63	-21
	Left I-IV	3.59	0	-45	-3
386	Right precentral gyrus	5.05	27	-9	51
	Right precentral gyrus	4.82	27	-9	57
	Right precentral gyrus	4.75	27	-12	63
	Right precentral gyrus	4.67	33	-12	60
	Right superior frontal gyrus	4.43	24	3	60
	Right precentral gyrus	3.6	15	-9	63
205	Left inferior lateral occipital	6.47	-45	-72	6
	Left inferior lateral occipital	4.87	-48	-63	6
120	Right precentral gyrus	5.56	57	12	27
85	Left precentral gyrus	5.19	-54	3	36
72	Vermis VIIIa	4.72	3	-66	-36
47	Left thalamus	4.93	-18	-21	9
31	Left central opercular cortex	5.07	-39	-3	15

Table B.9. *Local maxima cluster index when contrasting Urge > 'Random' blocks.*

Cluster Size	Region	Z-score	MNI Coordinates		
			X	Y	Z
5595	Left cuneal cortex	8.05	-6	-87	30
	Left lingual gyrus	6.87	-18	-42	-6
	Left lingual gyrus	6.8	-12	-60	3
	Left intracalcarine cortex	6.79	-6	-75	15
	Right cuneal cortex	6.73	3	-75	27
	Right lingual gyrus	6.68	9	-60	3
1176	Right central opercular cortex	5.99	60	0	6
	Right anterior superior temporal gyrus	5.69	57	0	-15
	Right Heschl's gyrus	5.21	45	-12	0
	Right temporal pole	5.05	45	9	-27
	Right temporal pole	4.93	45	15	-15
	Right temporal pole	4.91	36	6	-18
665	Paracingulate cortex	4.76	6	42	21
	Paracingulate cortex	4.57	0	42	27
	Right frontal pole	4.49	21	60	0
	Anterior cingulate cortex	4.42	-3	33	24
	Paracingulate cortex	4.38	12	42	18
	Left frontal pole	4.33	-6	57	3
291	Right angular gyrus	5.52	57	-54	24
	Right angular gyrus	4.74	51	-54	36
	Right angular gyrus	3.76	39	-51	21
	Right angular gyrus	3.67	45	-45	21
	Right angular gyrus	3.66	54	-54	51
	Right posterior supramarginal gyrus	3.66	48	-39	21
132	Left Crus I	5.25	-21	-78	-33
	Left Crus II	4.65	-9	-78	-33
94	Right superior frontal gyrus	4.13	21	33	39
	Right middle frontal gyrus	4.06	27	33	48
	Right superior frontal gyrus	3.7	27	24	57
	Right superior frontal gyrus	3.62	24	24	51
61	Right IX	5.14	3	-45	-42
	Left IX	4.22	-6	-51	-33
47	Right middle frontal gyrus	4.87	39	9	45
	Right middle frontal gyrus	3.95	36	12	33
	Right middle frontal gyrus	3.36	42	24	33
	Right middle frontal gyrus	3.25	45	24	42

Table B.10. *Local maxima cluster index when contrasting Blinks > Urge blocks.*

Cluster Size	Region	Z-score	MNI Coordinates		
			X	Y	Z
4149	Left lingual gyrus	6.18	-21	-51	-3
	Left intracalcerine cortex	6.05	-12	-63	6
	Left intracalcerine cortex	6.05	-12	-72	12
	Right lingual gyrus	5.98	15	-45	-3
	Left lingual gyrus	5.77	-9	-57	0
	Right precuneous cortex	5.74	18	-60	12
538	Left superior frontal gyrus	4.97	-12	-3	66
	Anterior cingulate cortex	4.52	-6	12	39
	Left superior frontal gyrus	4.45	-18	6	72
	Anterior cingulate cortex	4.42	3	12	39
	Anterior cingulate cortex	4.36	3	18	36
	Right superior frontal gyrus	4.29	12	0	63
502	Left central opercular cortex	5.5	-45	6	6
	Left precentral gyrus	5.45	-57	6	3
	Left frontal opercular cortex	5.15	-45	12	0
	Left postcentral gyrus	5.12	-57	-24	21
	Left frontal opercular cortex	4.92	-36	12	15
	Left insular cortex	4.6	-36	9	3
201	Right insular cortex	4.73	36	9	9
	Right central opercular cortex	4.24	54	-6	15
	Right precentral gyrus	4.03	57	6	6
	Right central opercular cortex	3.94	48	6	6
	Right precentral gyrus	3.84	51	3	12
	Right central opercular cortex	3.66	42	-12	21
138	Left frontal pole	5.07	-30	51	30
	Left frontal pole	4.73	-30	45	21
	Left frontal pole	4.59	-42	48	27
	Left frontal pole	4.22	-24	60	33
54	Left postcentral gyrus	4.71	-36	-18	39
	Left precentral gyrus	4.68	-42	-9	51
37	Right frontal pole	4.43	36	51	21
	Right frontal pole	3.89	30	48	36
	Right frontal pole	3.68	27	45	30

Appendix C: Activation Time Series

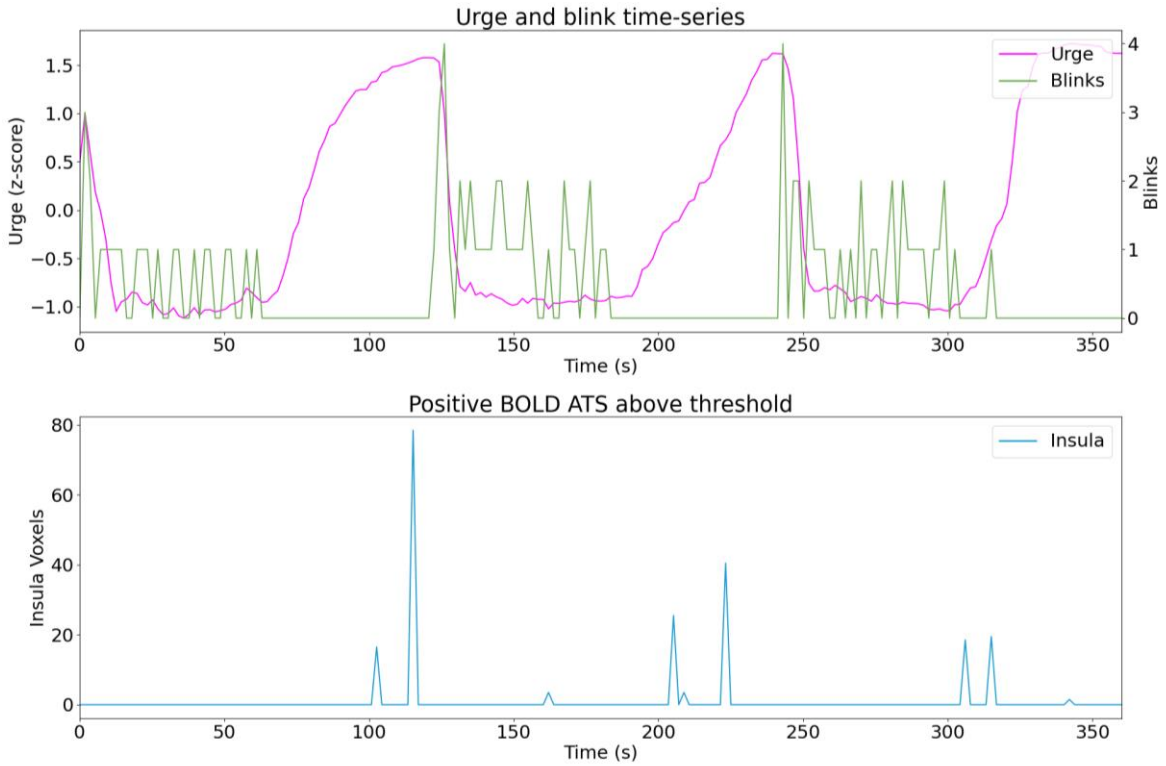

Figure C.1. *Sub01 run01*

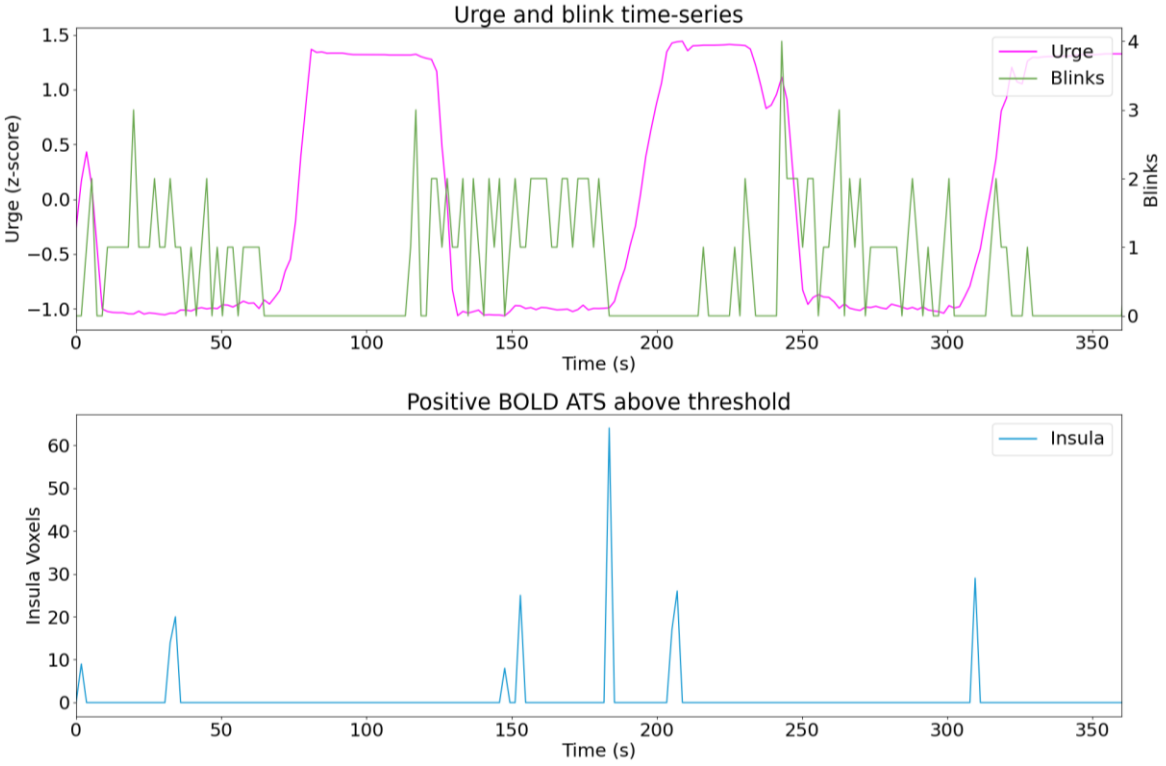

Figure C.2. *Sub01 run02*

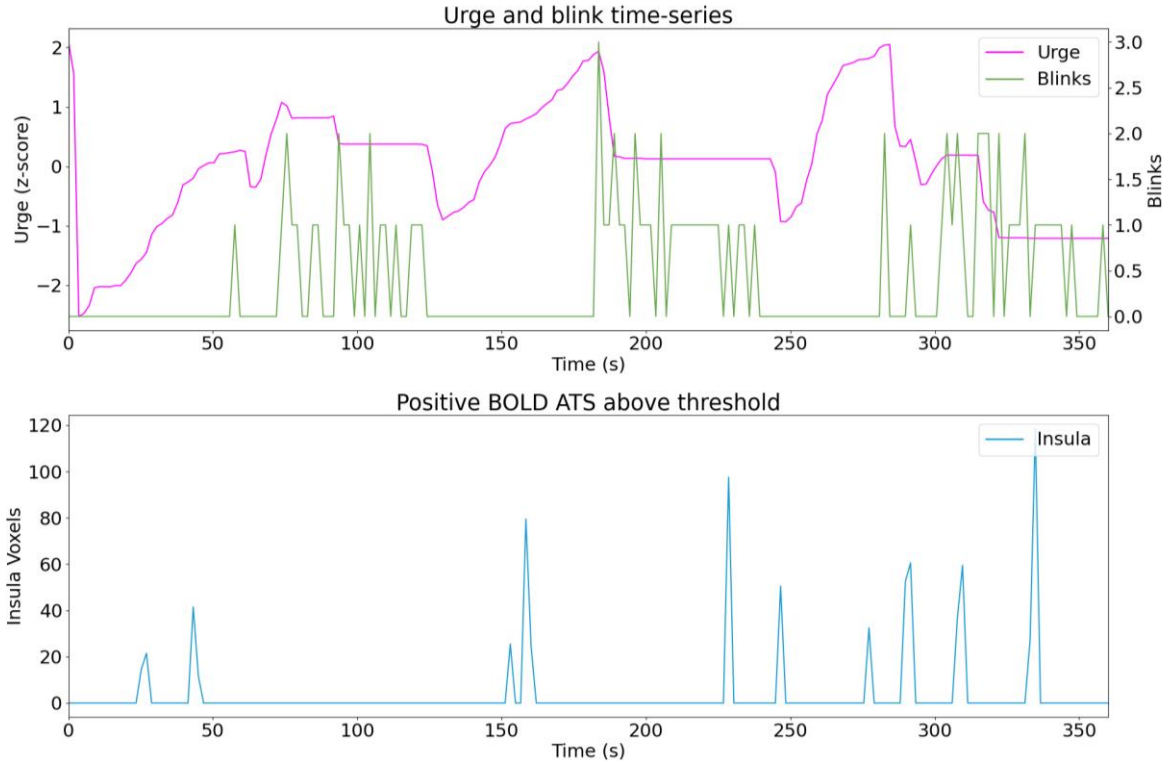

Figure C.3. *Sub03 run01*

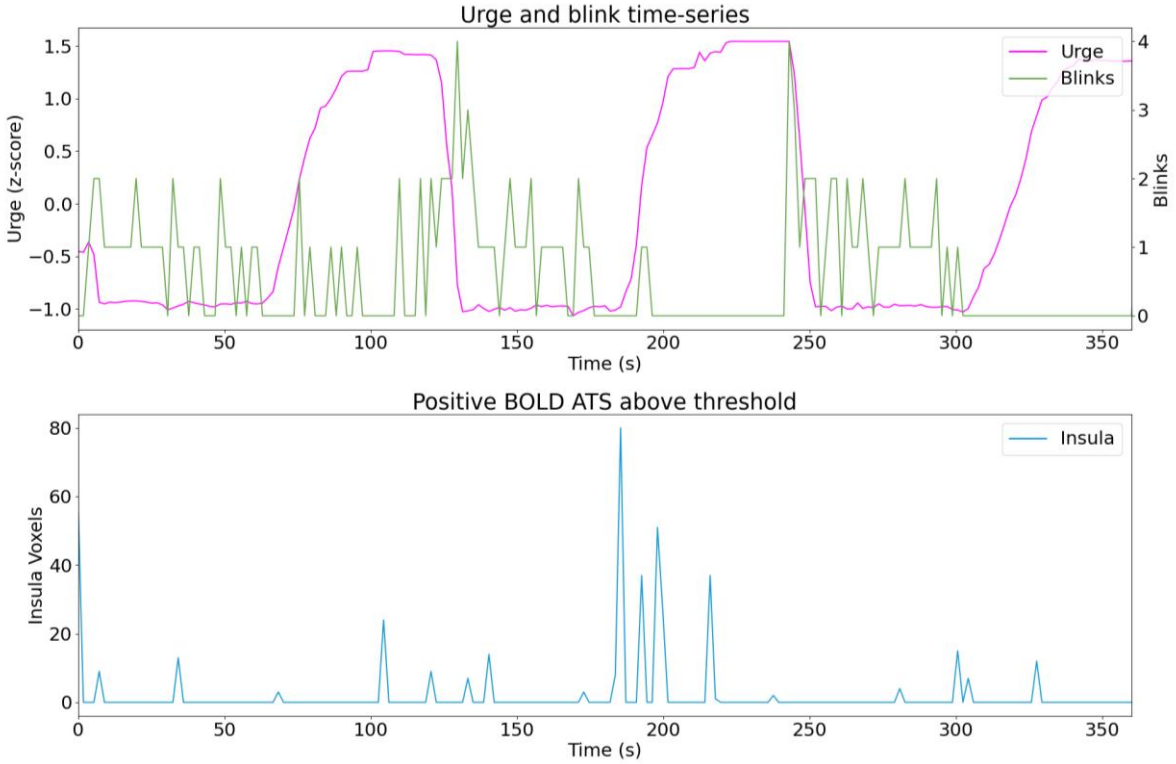

Figure C.4. *Sub01 run03*

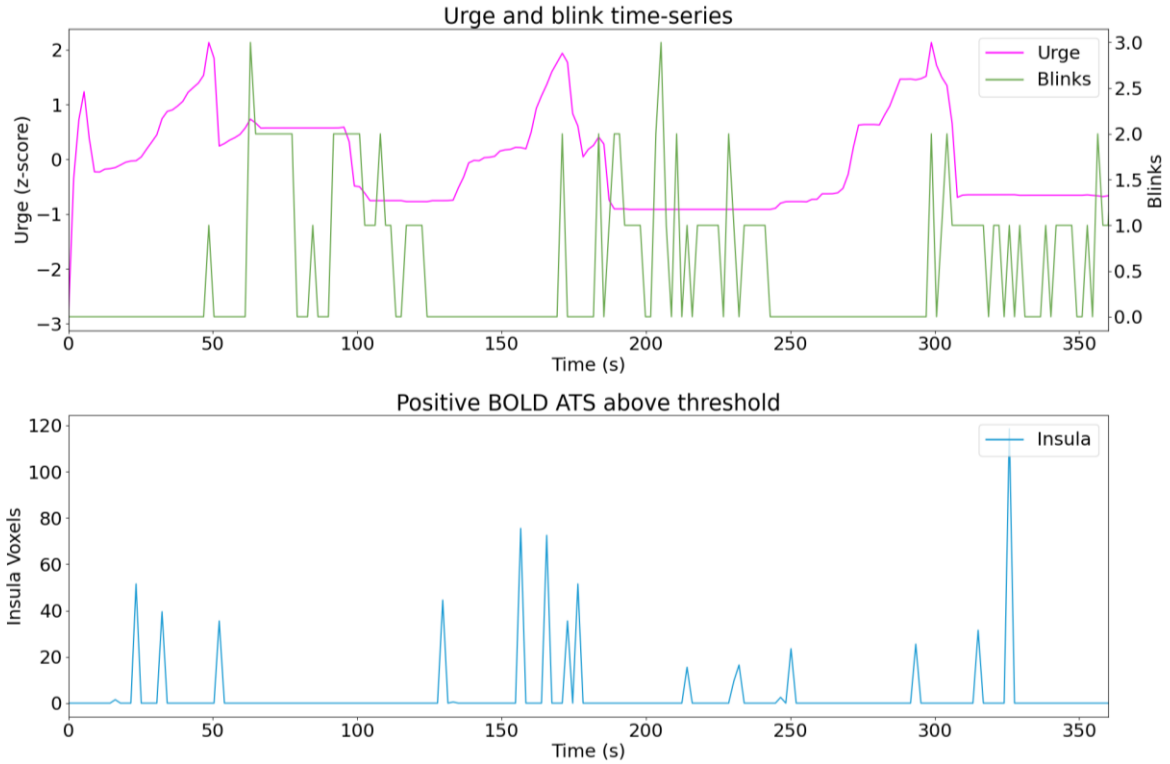

Figure C.5. *Sub03 run03*

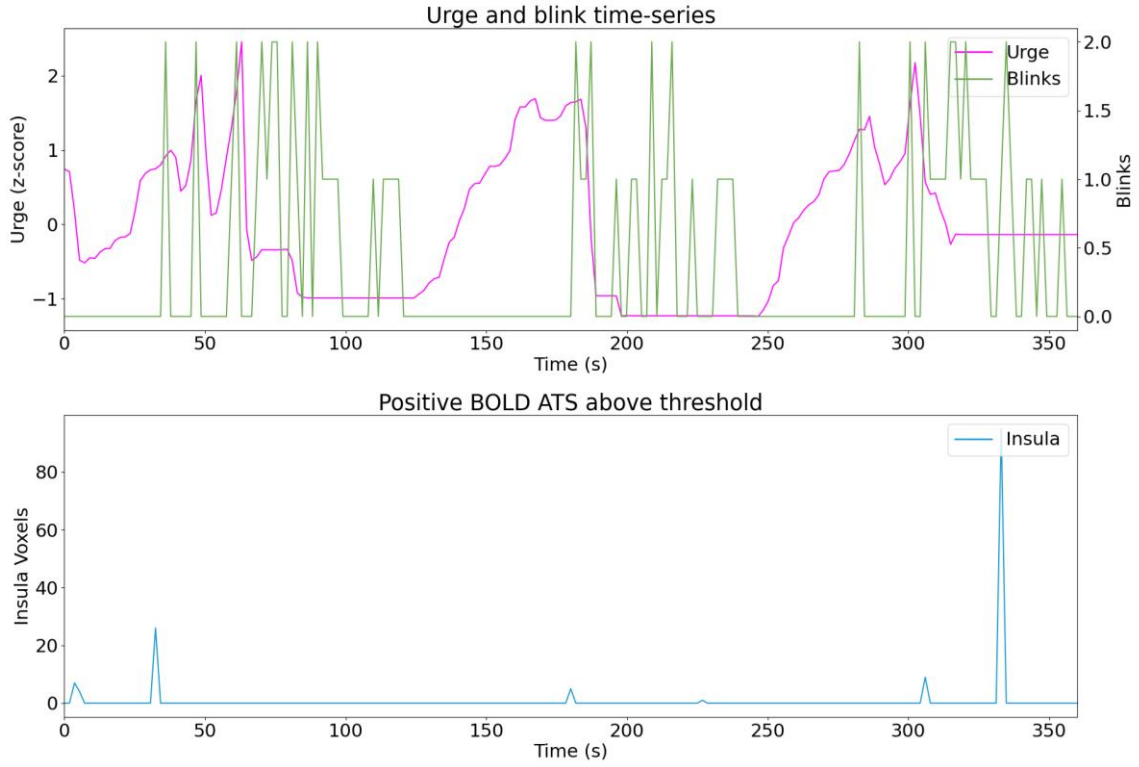

Figure C.6. *Sub03 run02*

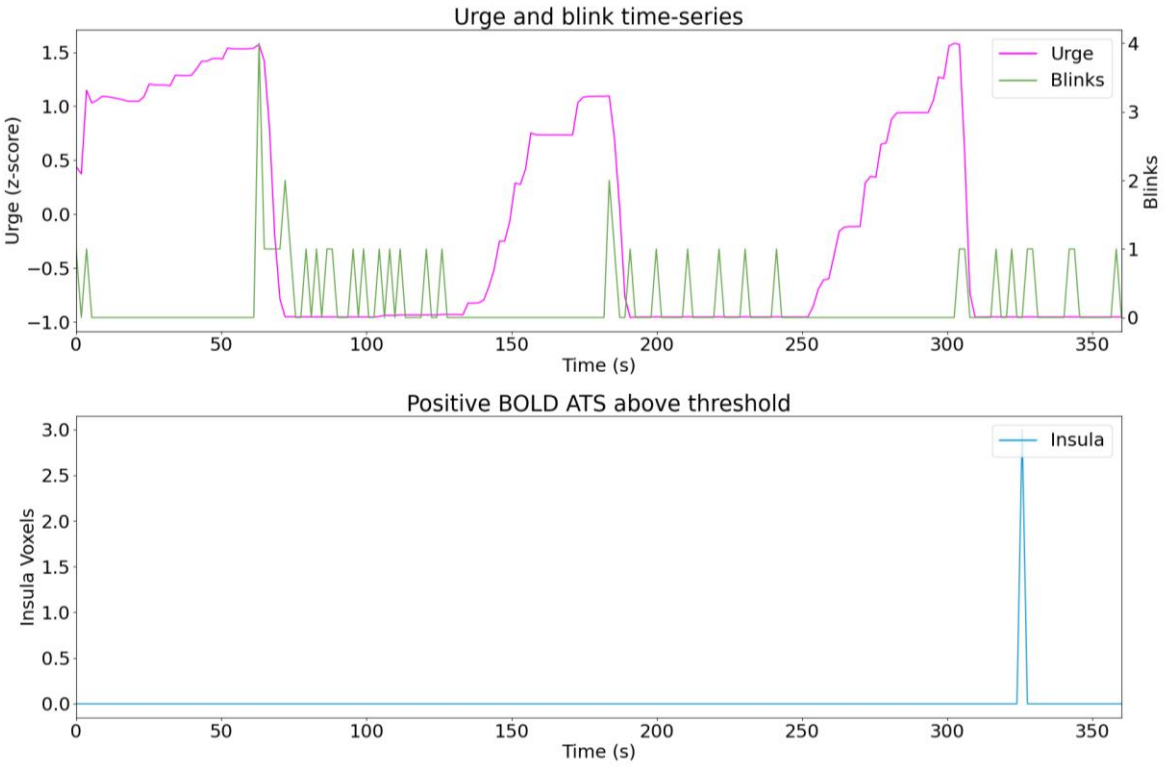

Figure C.7. *Sub04 run01*

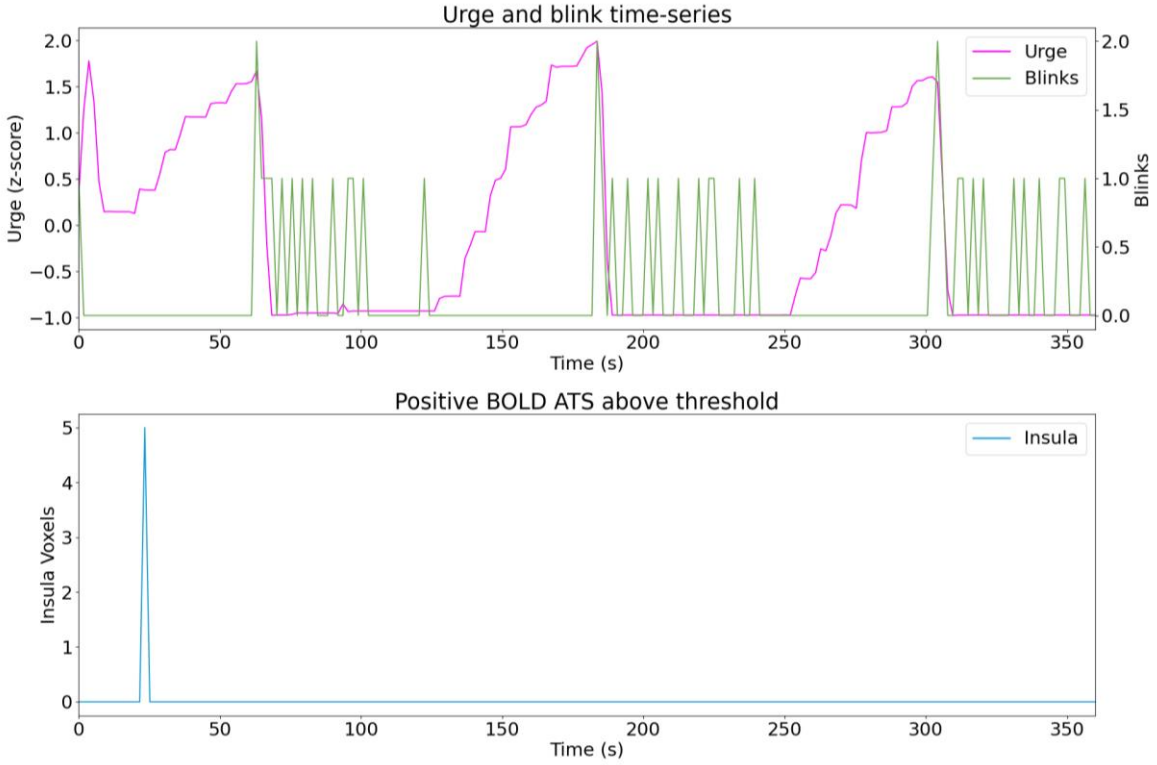

Figure C.8. *Sub04 run02*

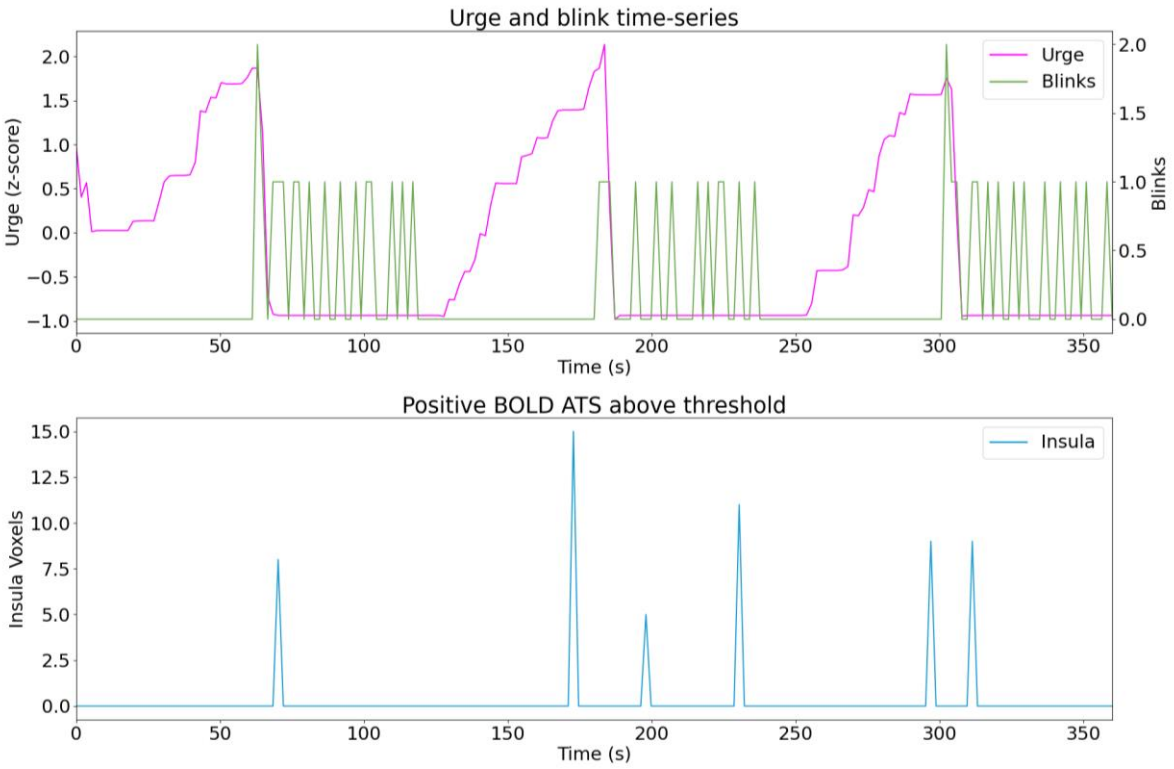

Figure C.9. *Sub04 run03*

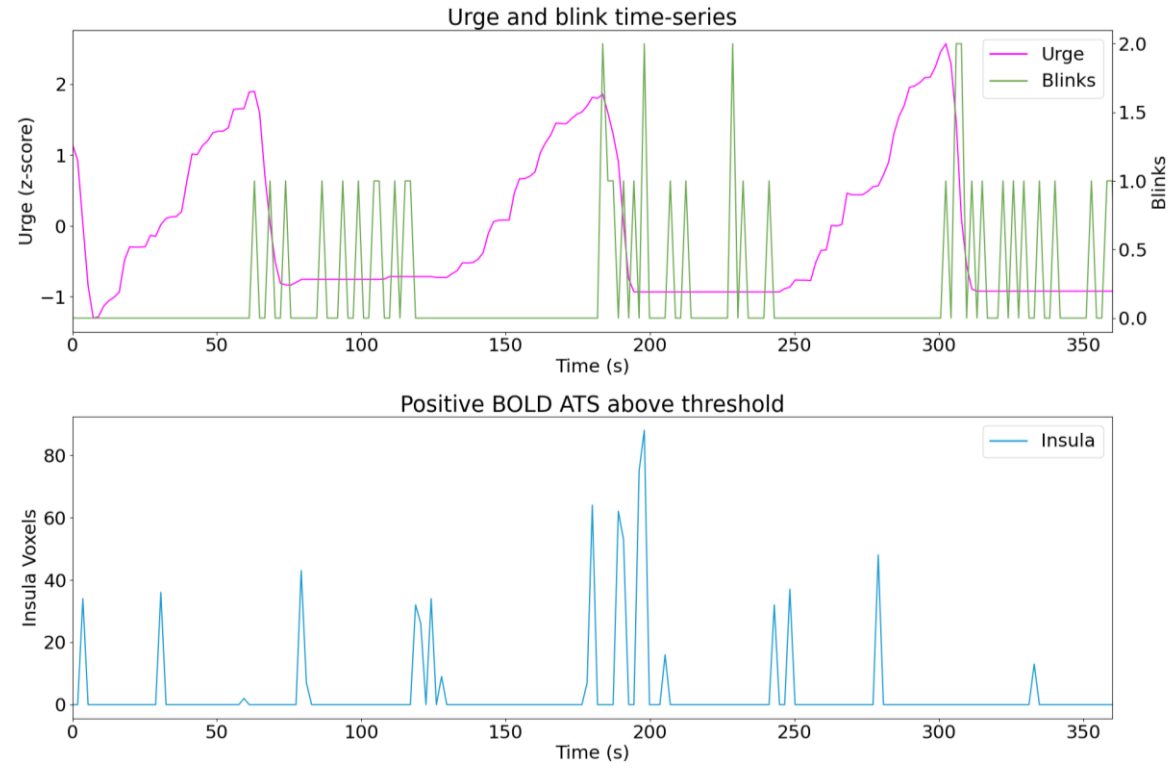

Figure C.10. *Sub05 run02*

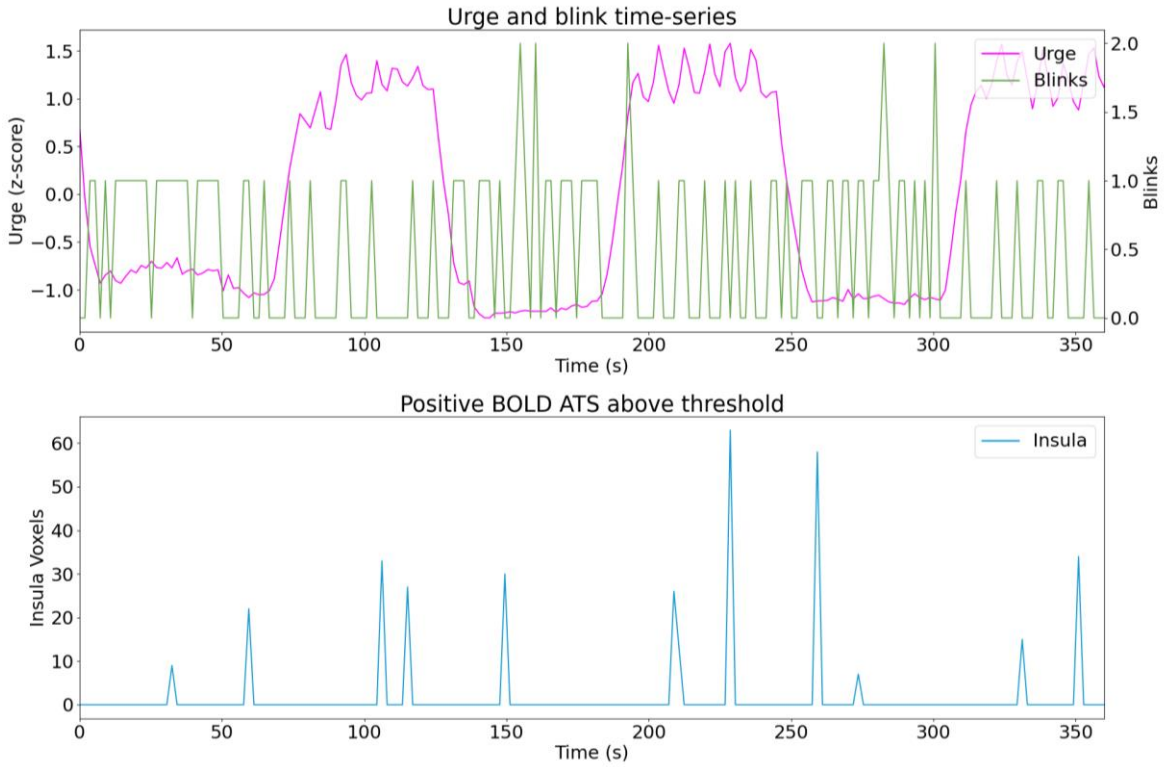

Figure C.11. *Sub06 run02*

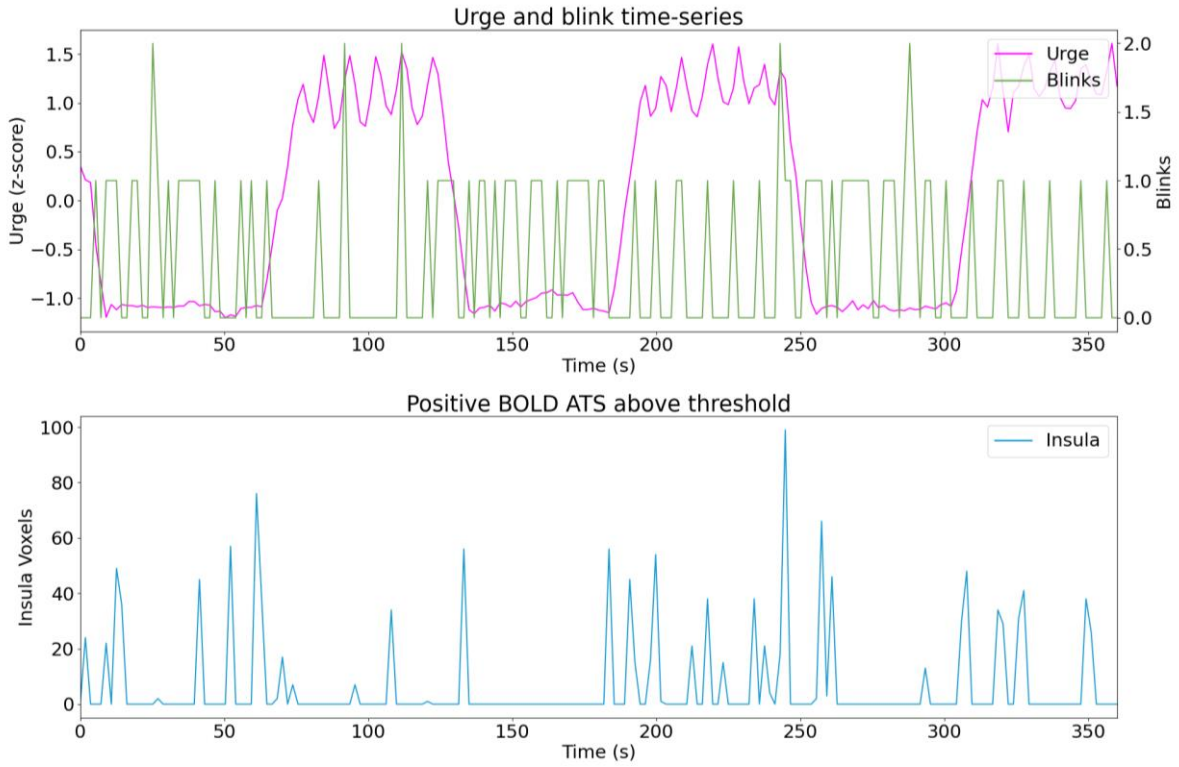

Figure C.12. *Sub06 run03*

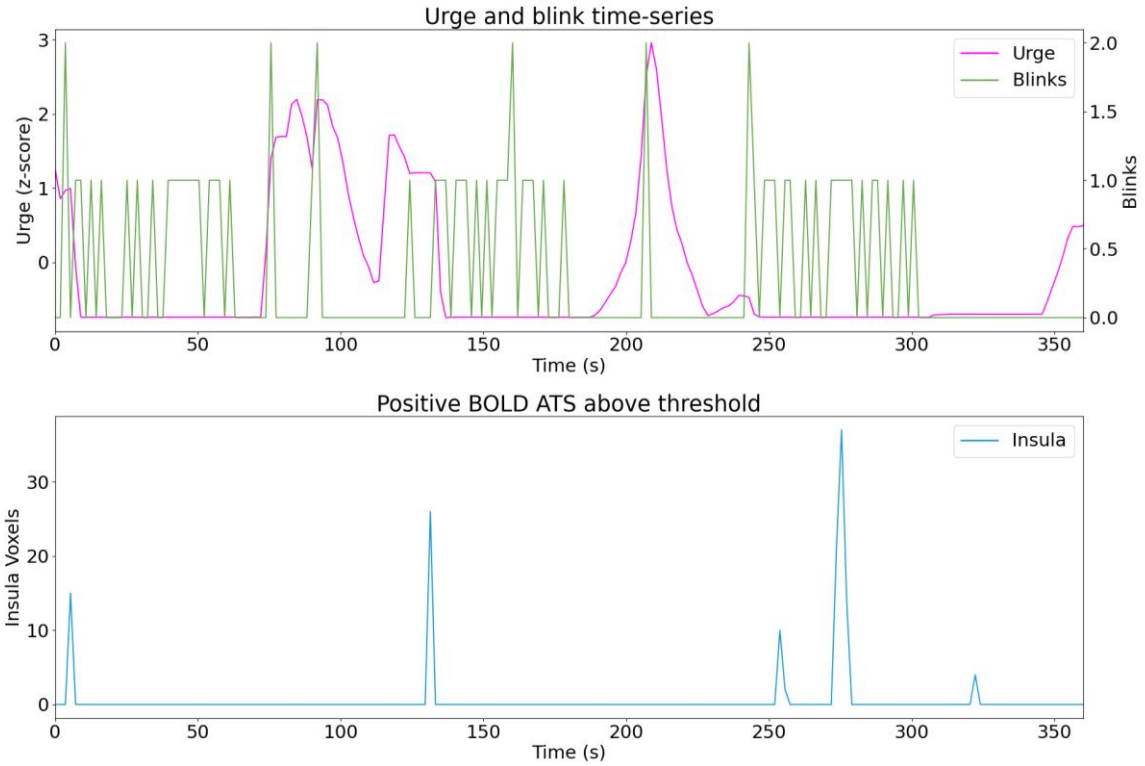

Figure C.13. *Sub07 run01*

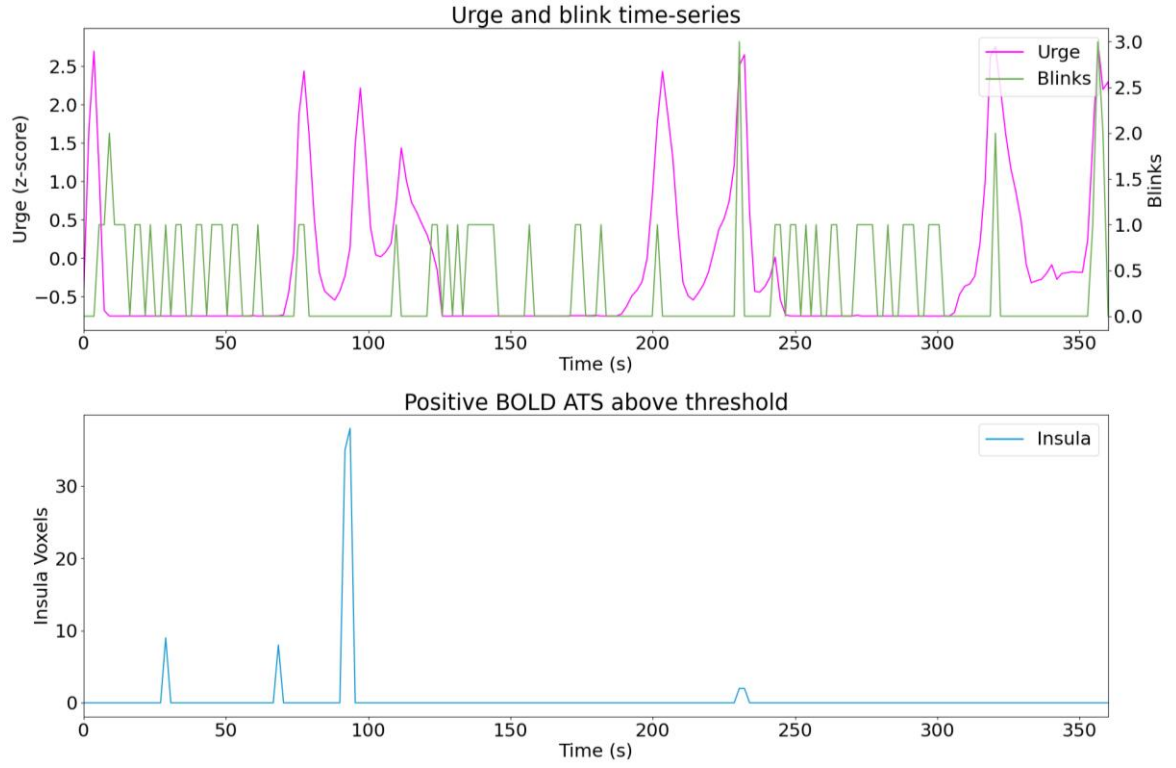

Figure C.14. *Sub07 run02*

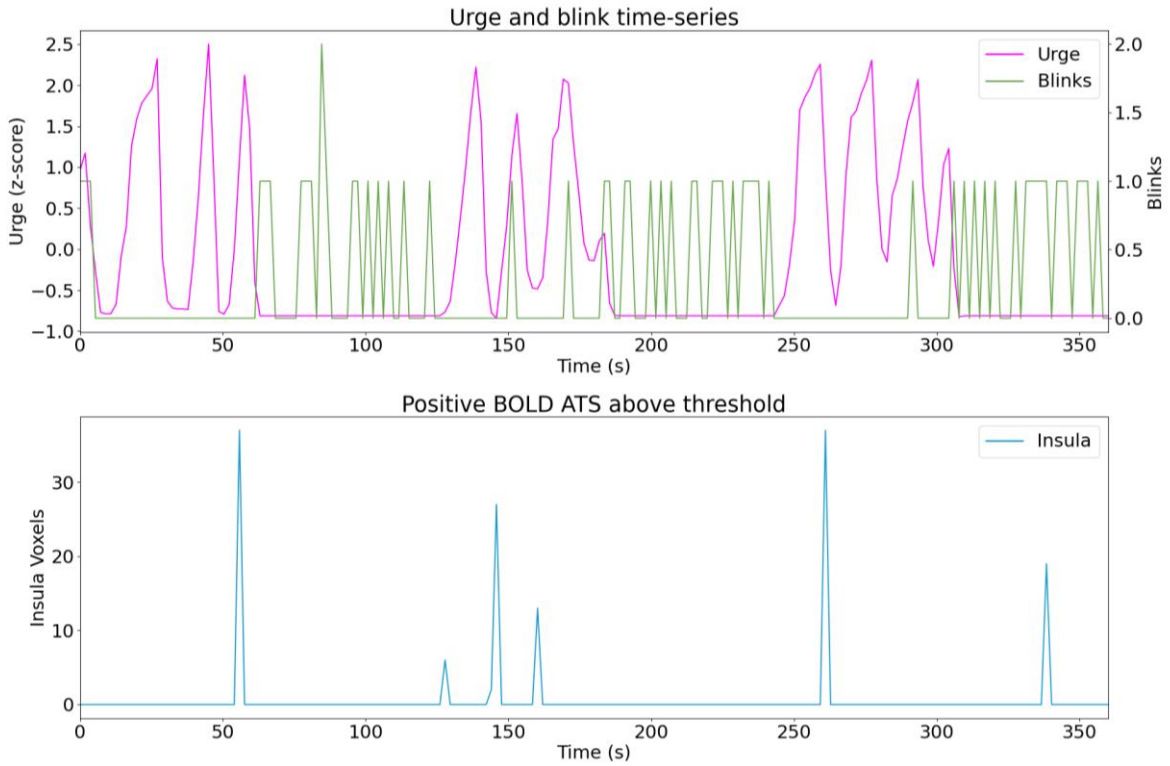

Figure C.15. *Sub09 run01*

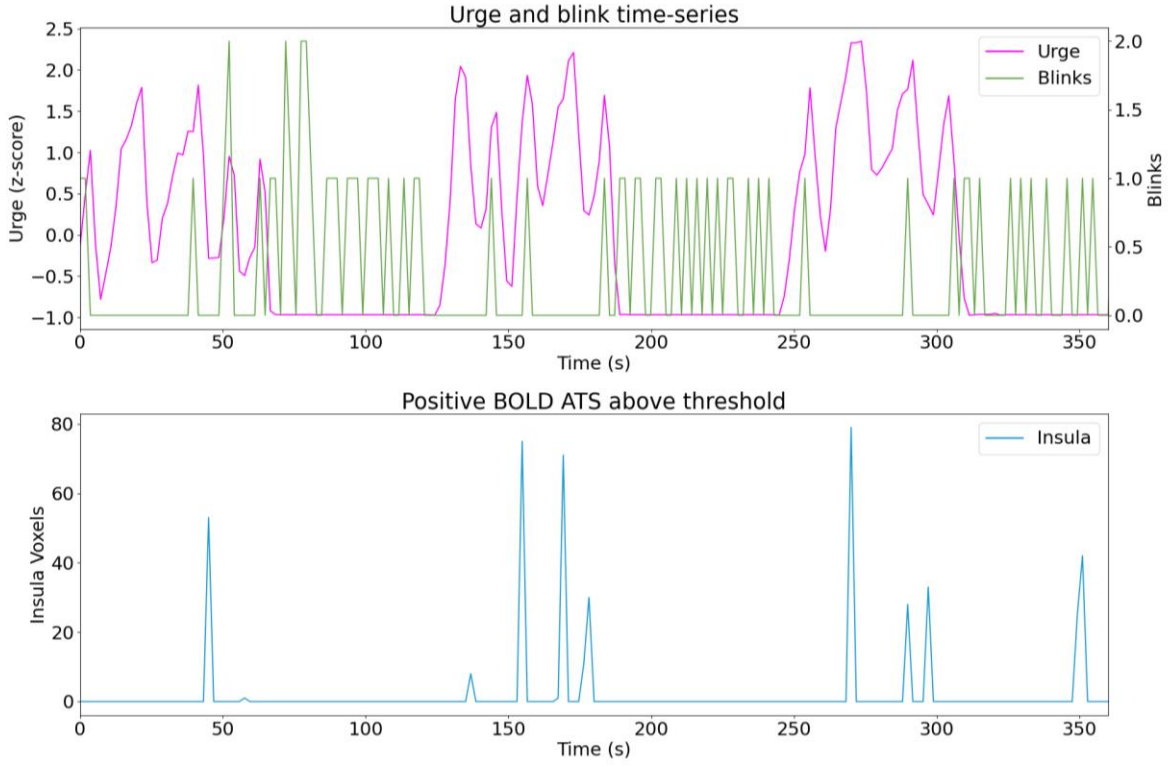

Figure C.16. *Sub09 run02*

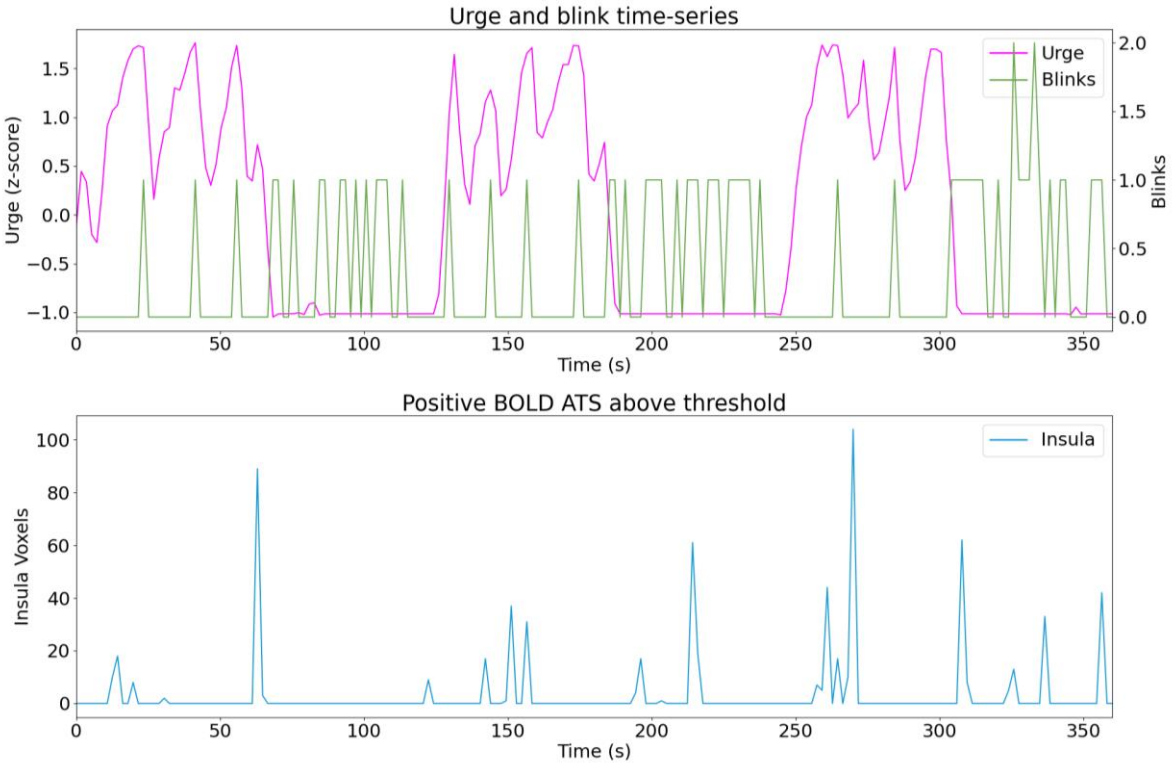

Figure C.17. *Sub09 run03*

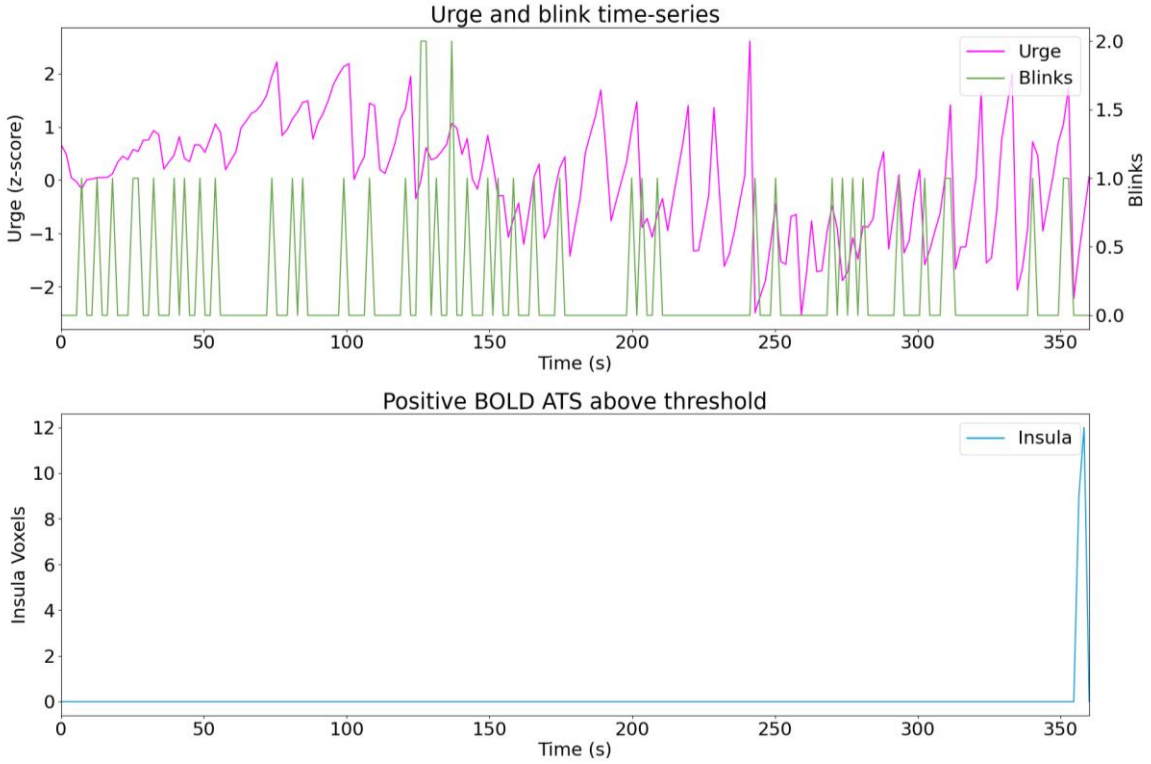

Figure C.18. *Sub10 run01*

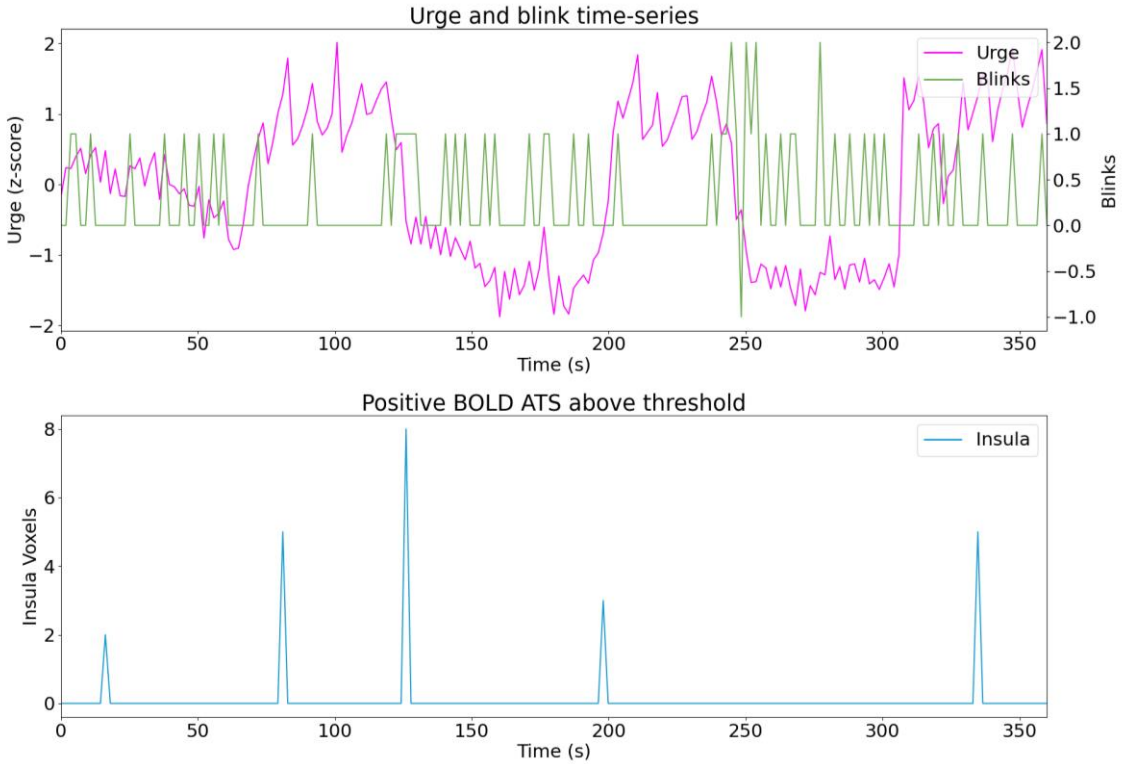

Figure C.19. *Sub10 run02*

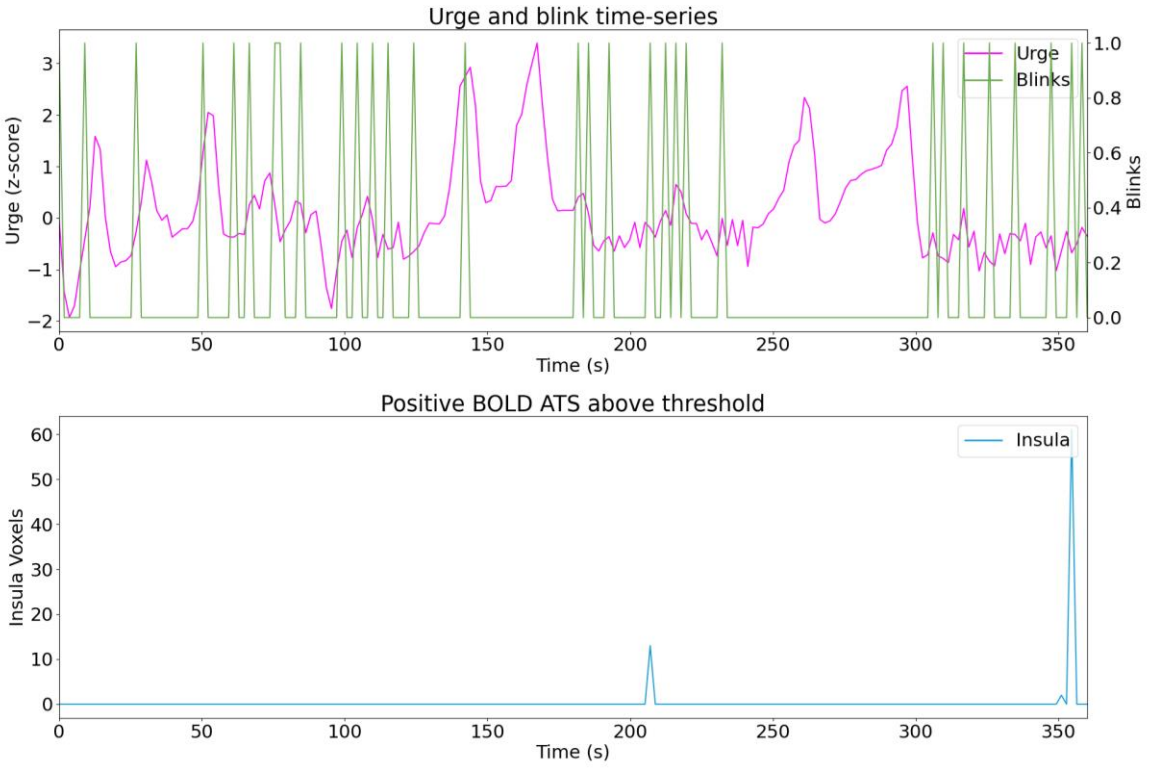

Figure C.20. *Sub11 run01*

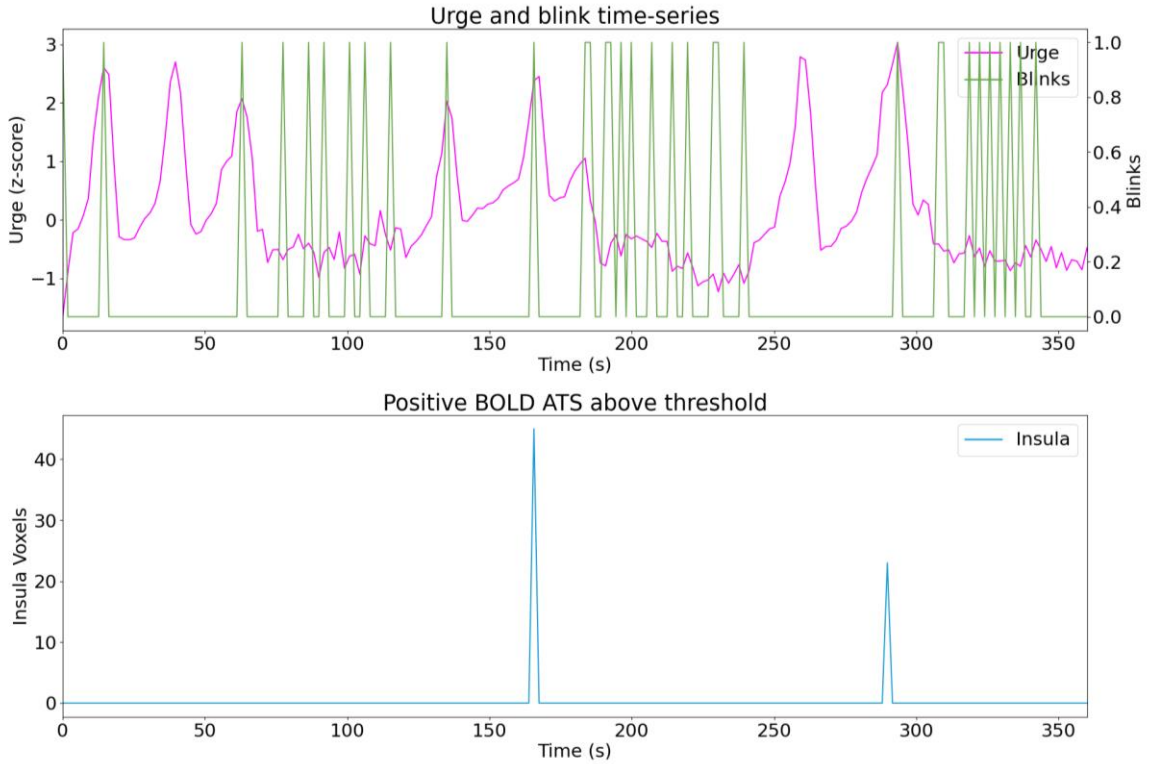

Figure C.21. *Sub11 run02*

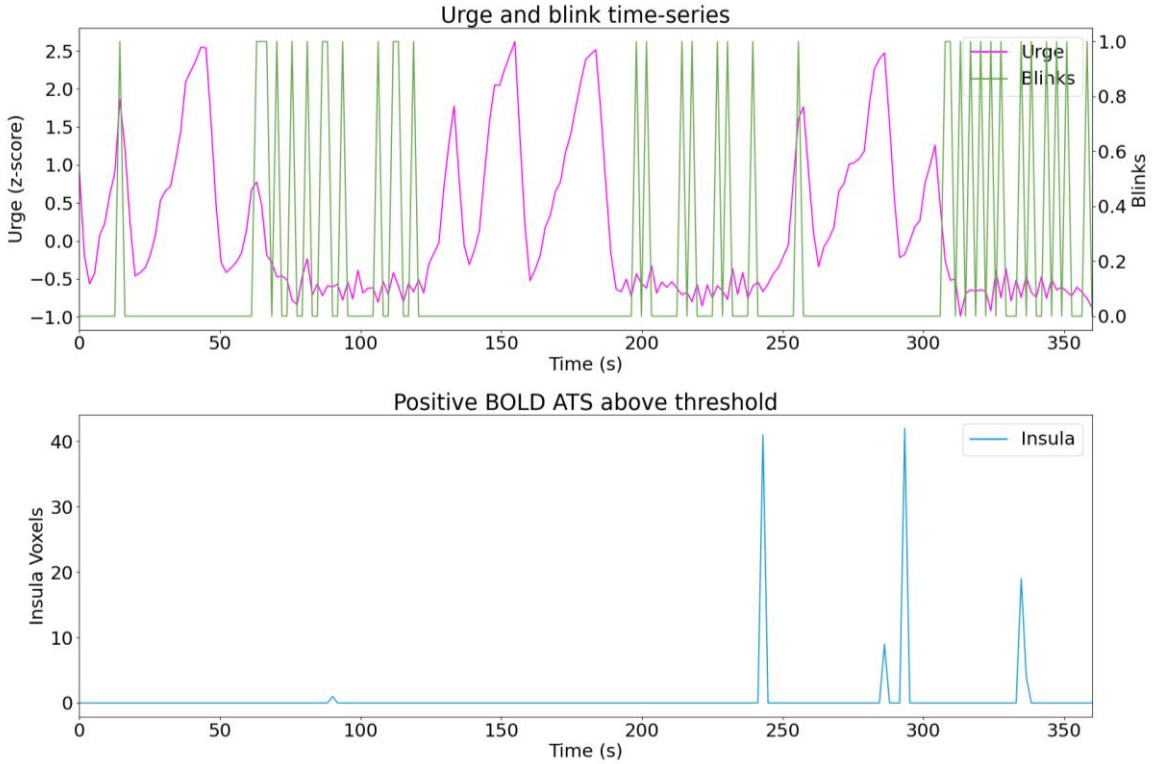

Figure C.22. *Sub11 run03*

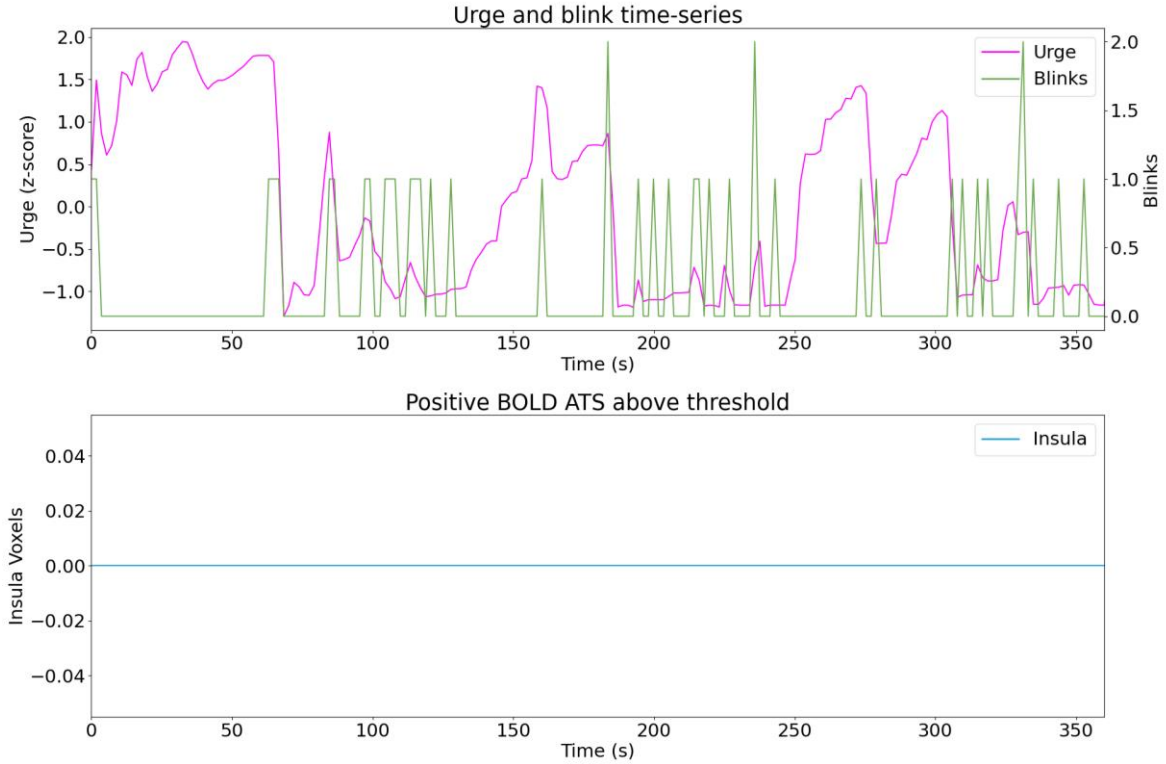

Figure C.23. *Sub12 run01*

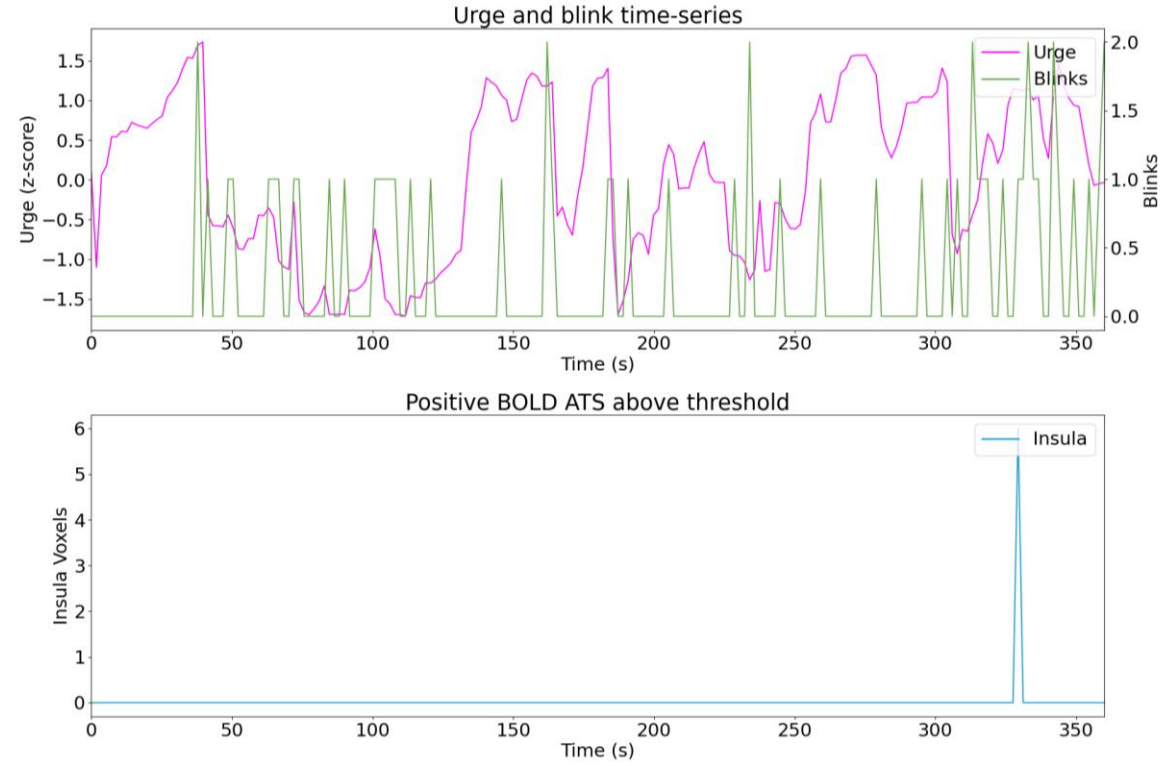

Figure C.24. *Sub12 run02*

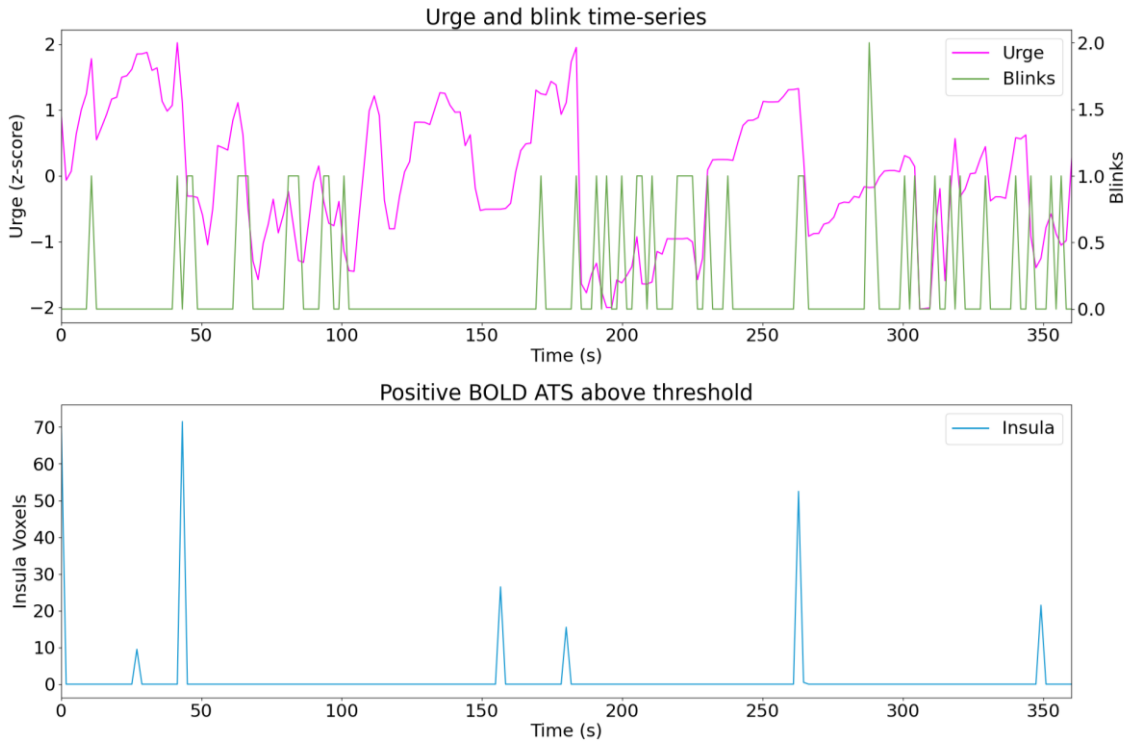

Figure C.25. *Sub12 run03*

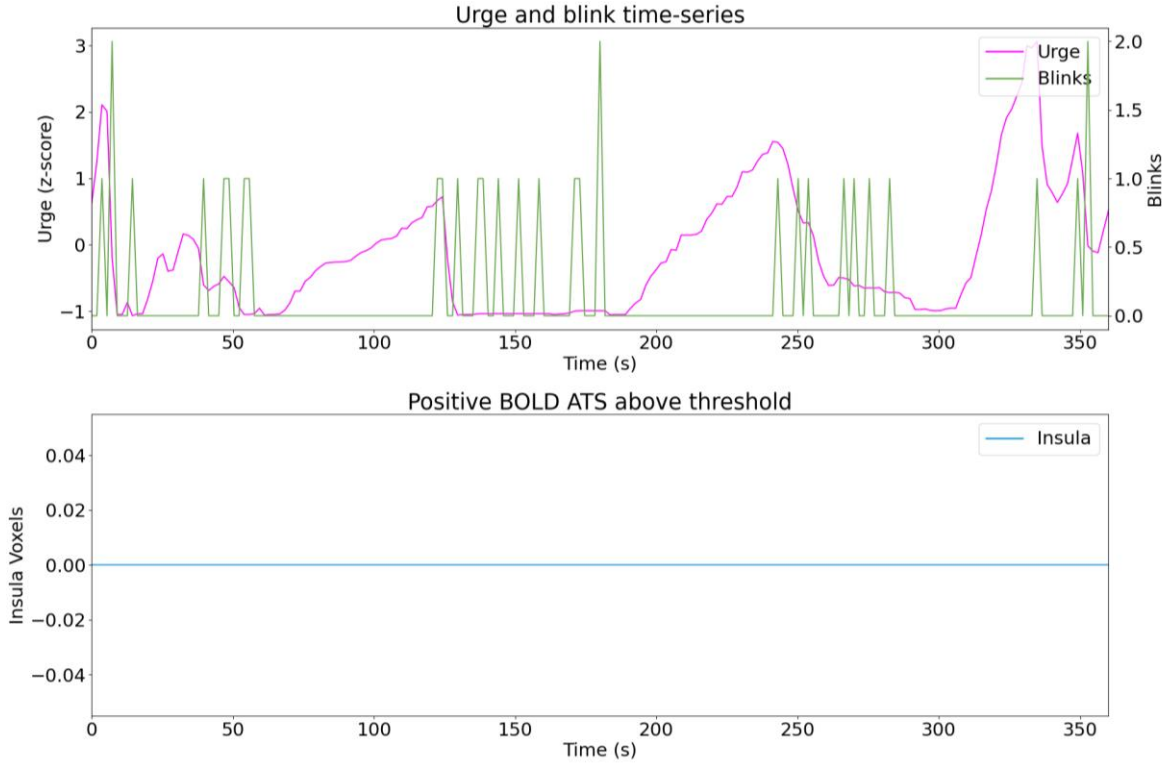

Figure C.26. *Sub13 run01*

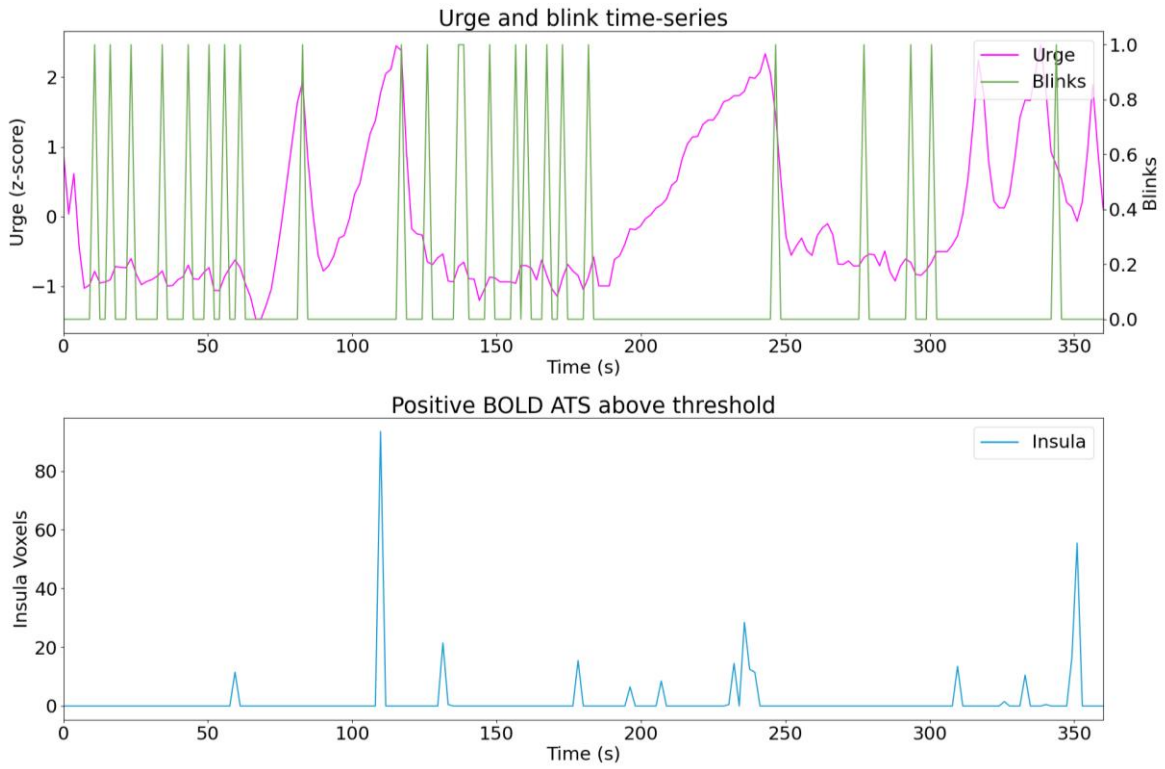

Figure C.27. *Sub13 run02*

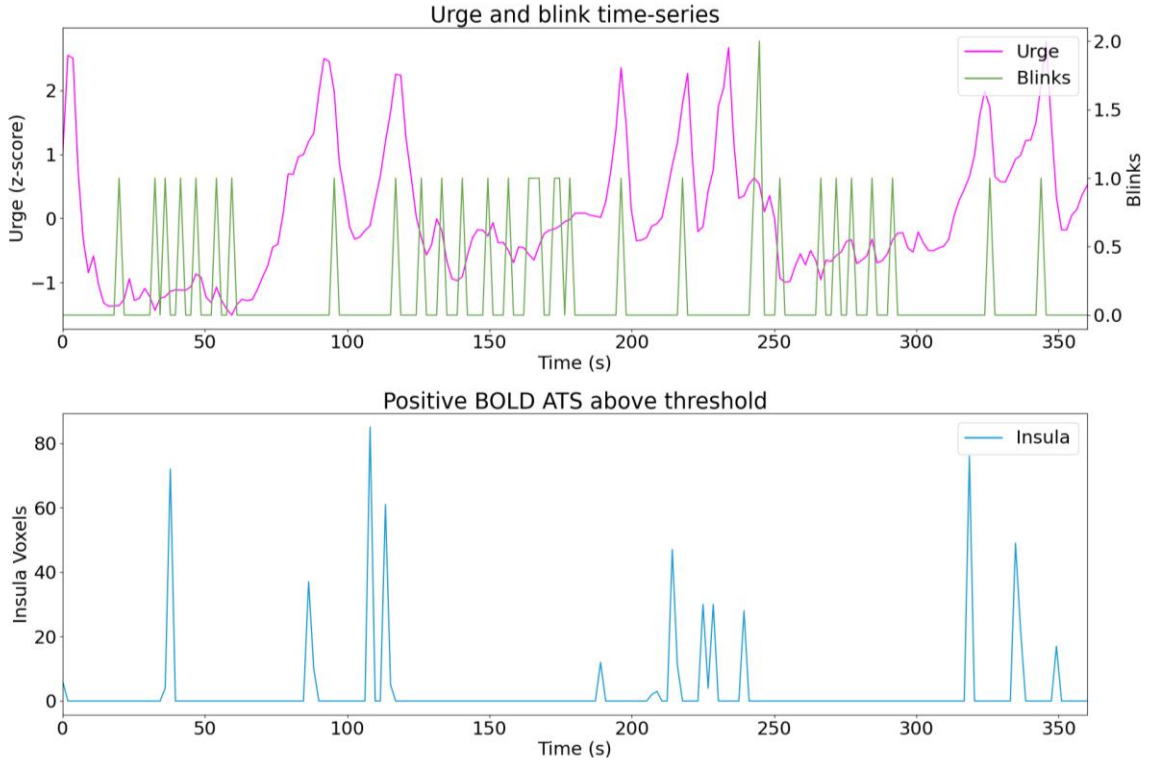

Figure C.28. *Sub13 run03*

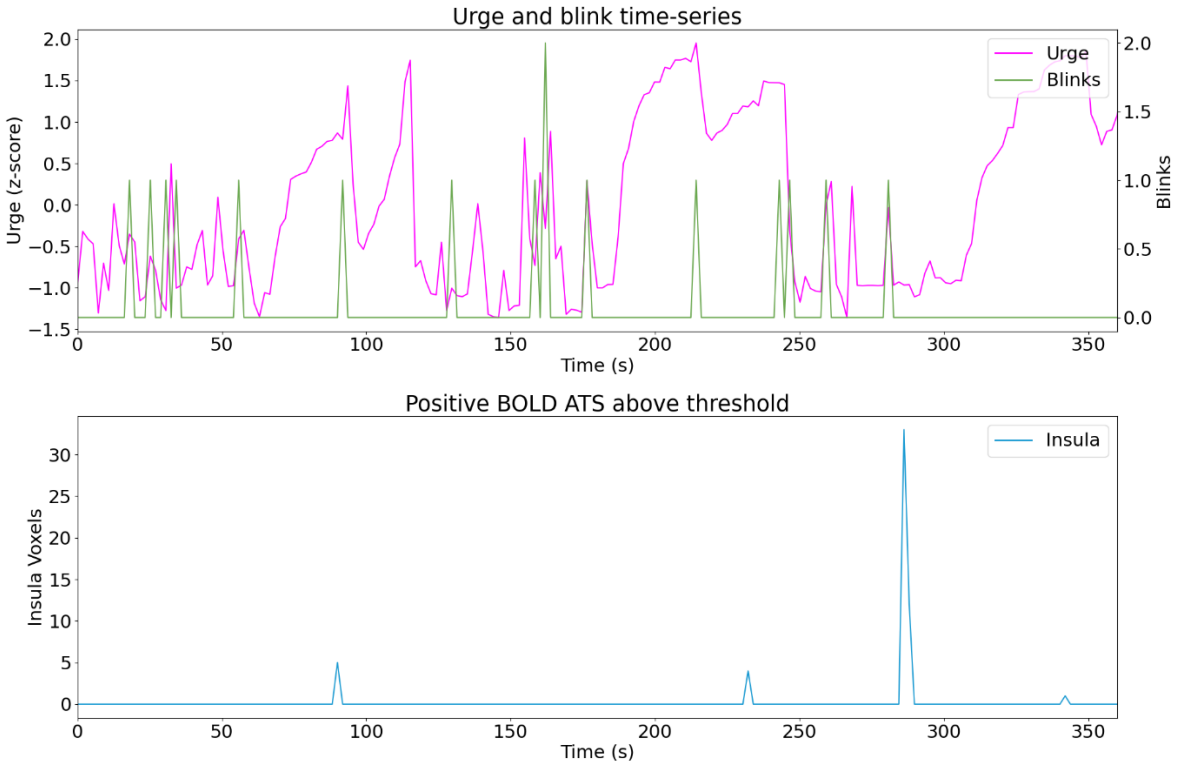

Figure C.29. *Sub14 run01*

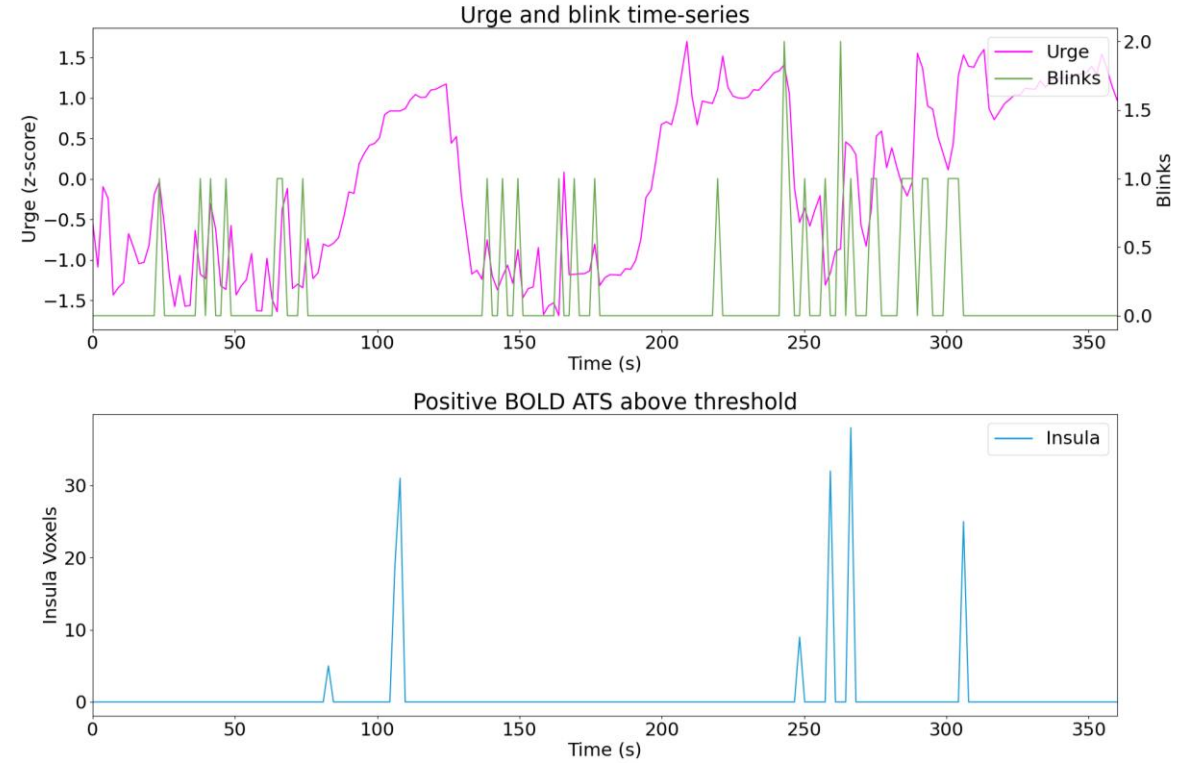

Figure C.30. *Sub14 run02*

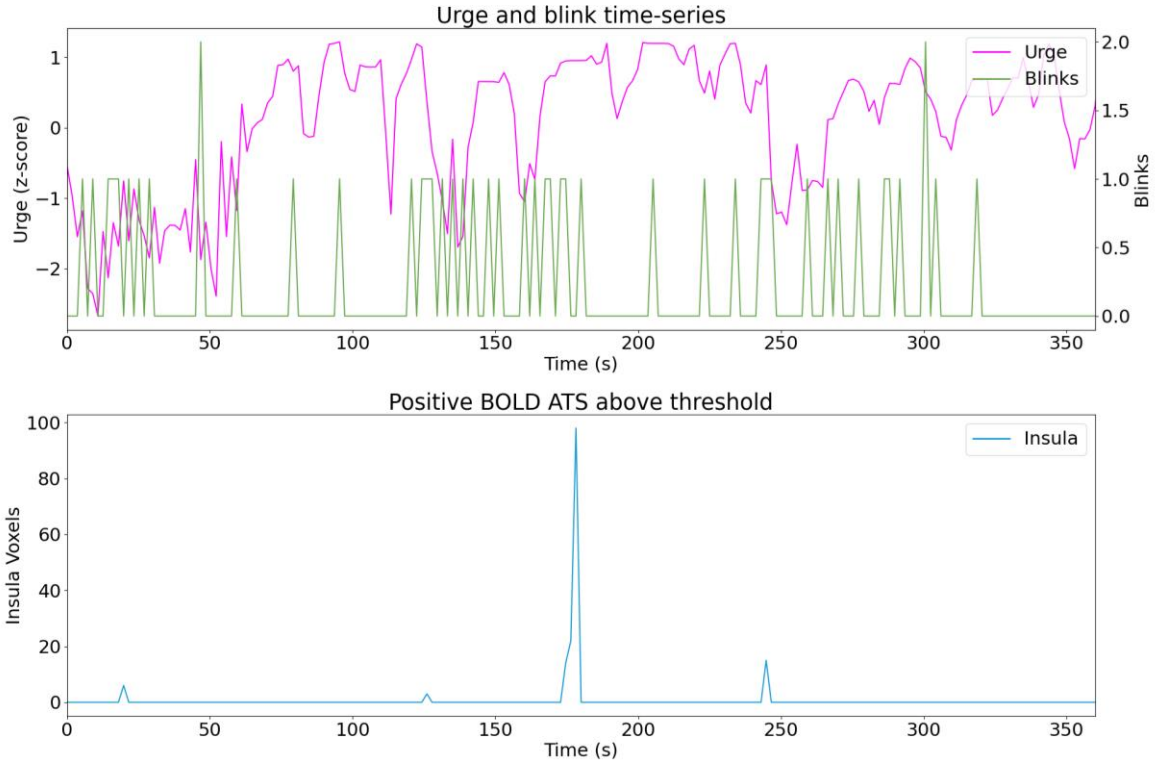

Figure C.31. *Sub14 run03*

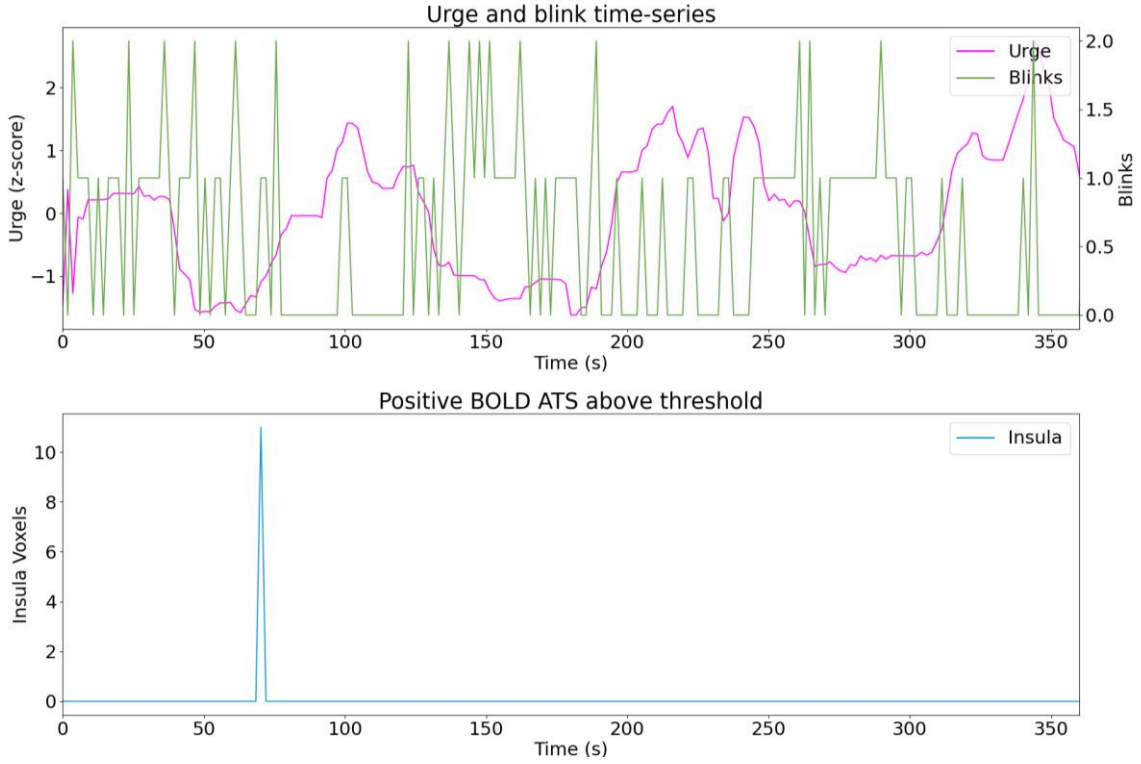

Figure C.32. *Sub15 run01*

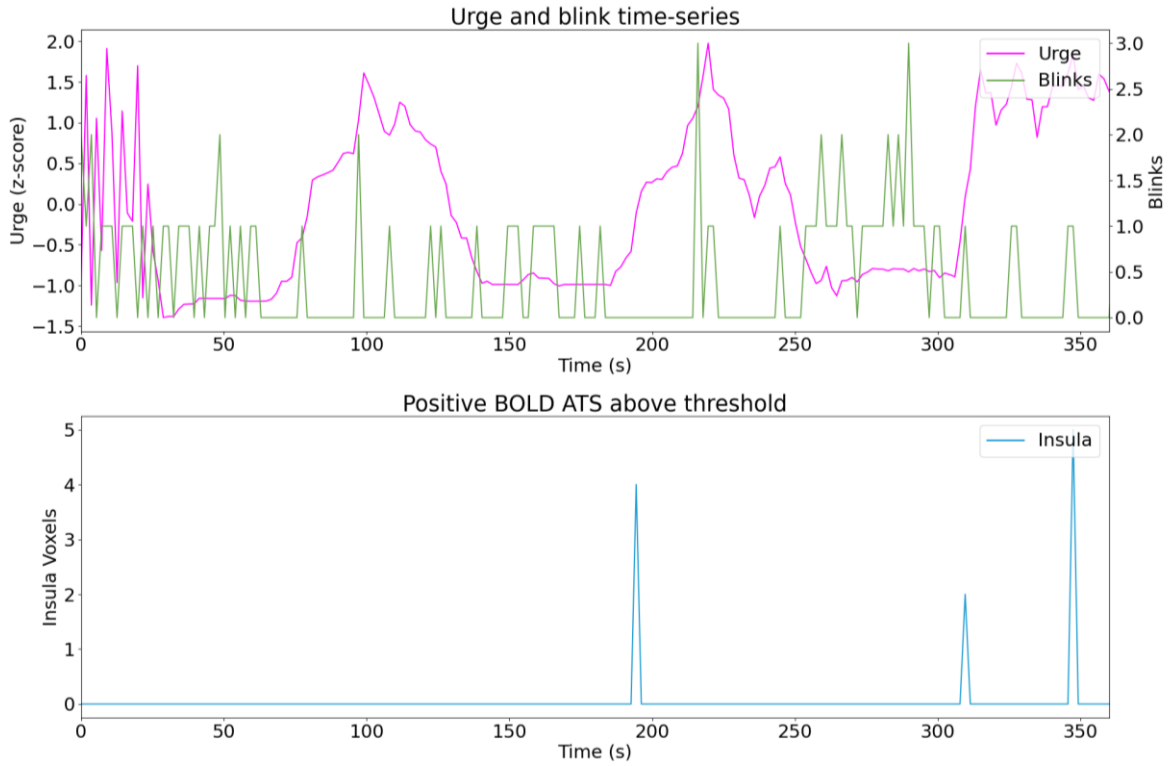

Figure C.33. *Sub15 run02*

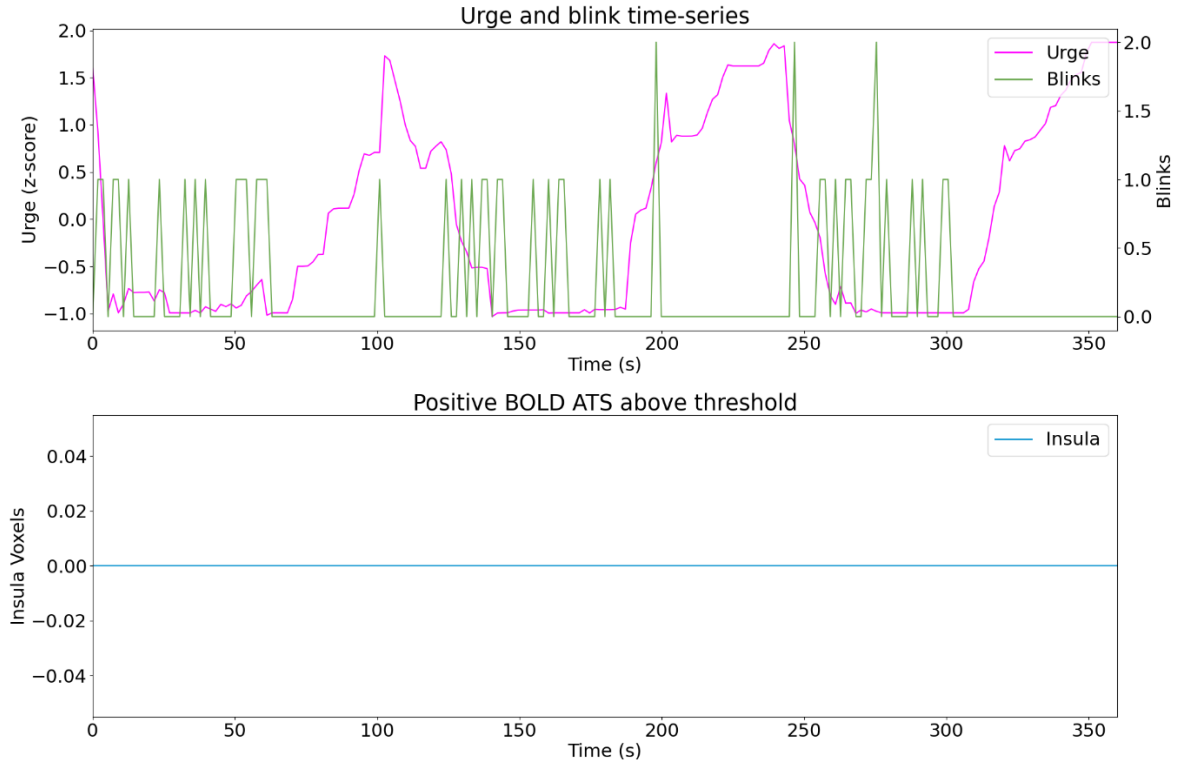

Figure C.34. *Sub15 run03*

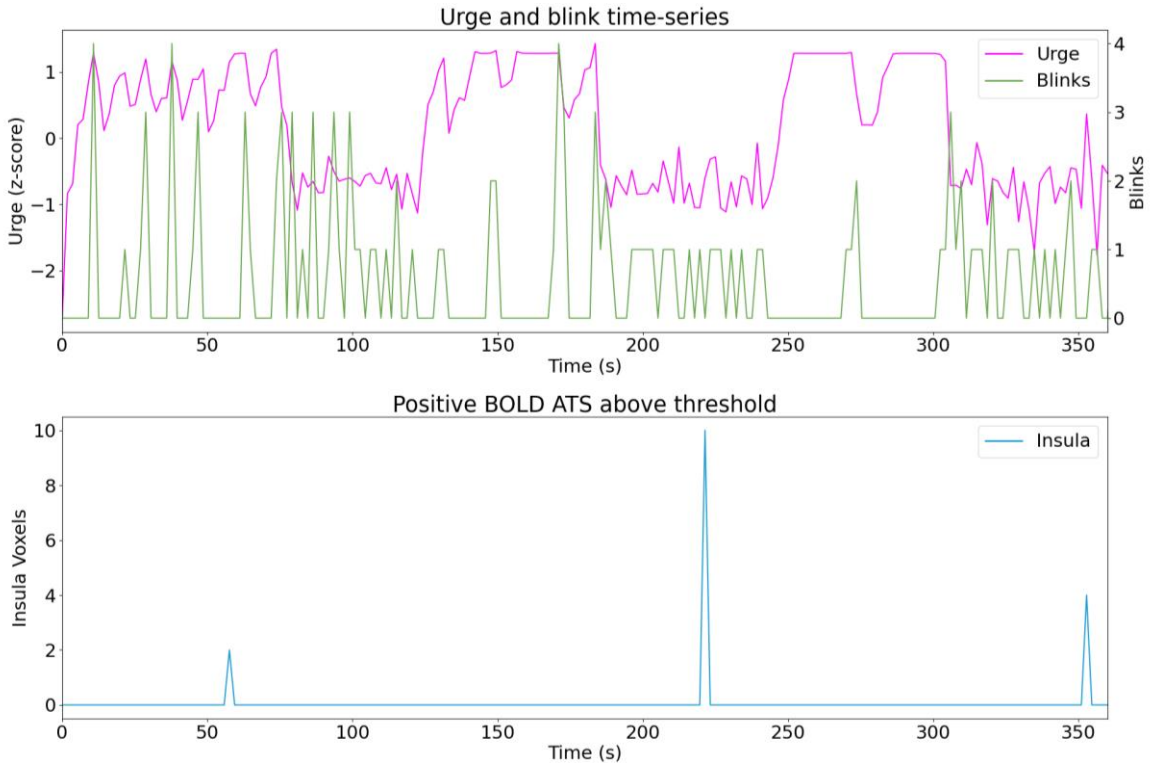

Figure C.35. *Sub16 run01*

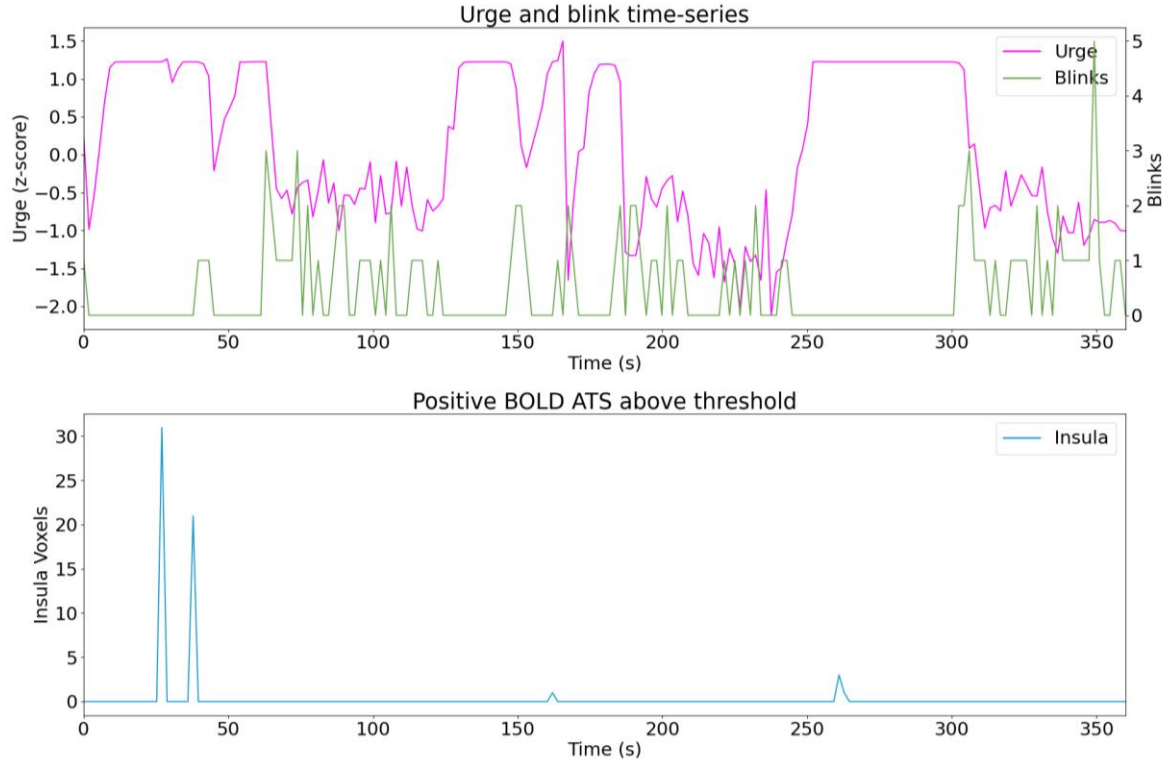

Figure C.36. *Sub16 run02*

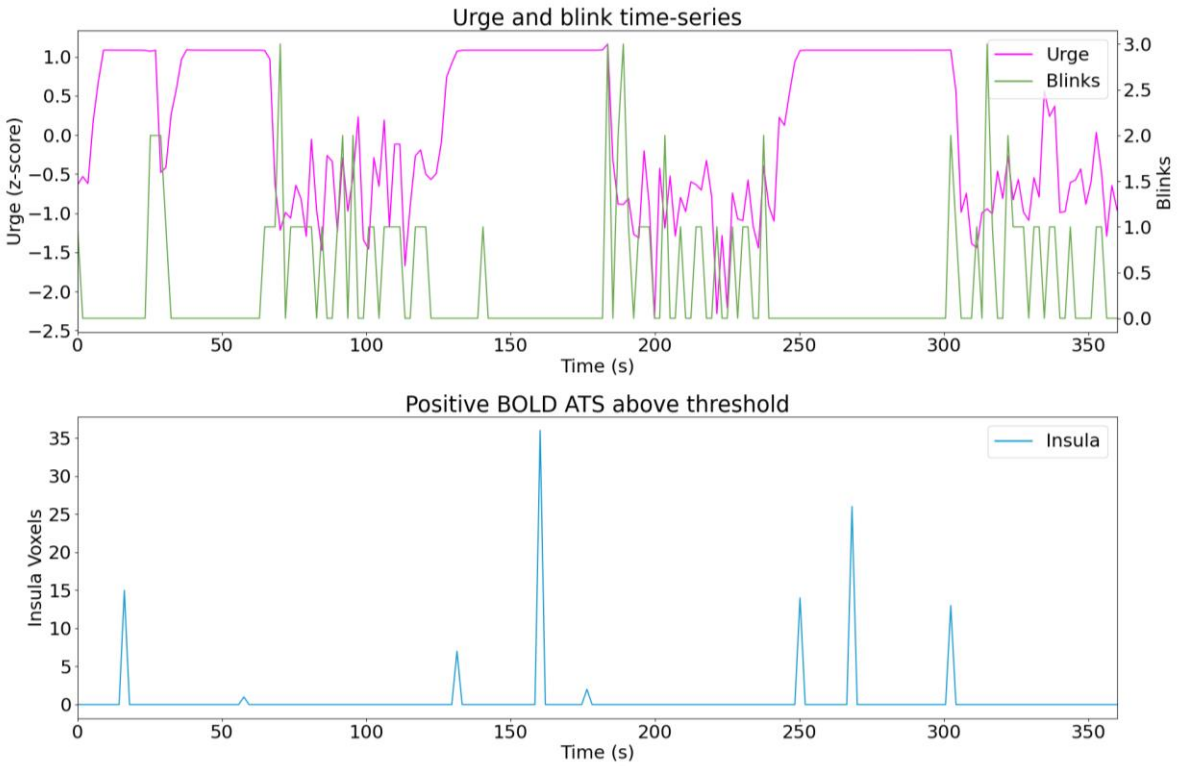

Figure C.37. *Sub16 run03*

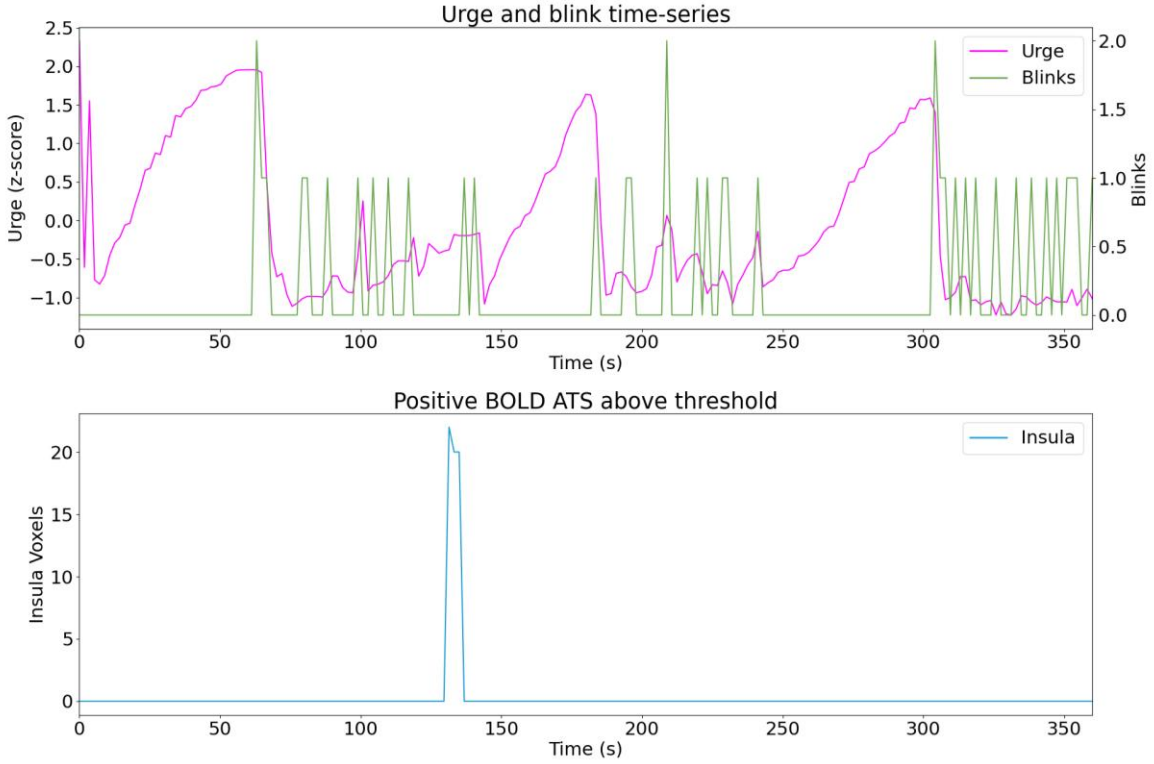

Figure C.38. *Sub17 run01*

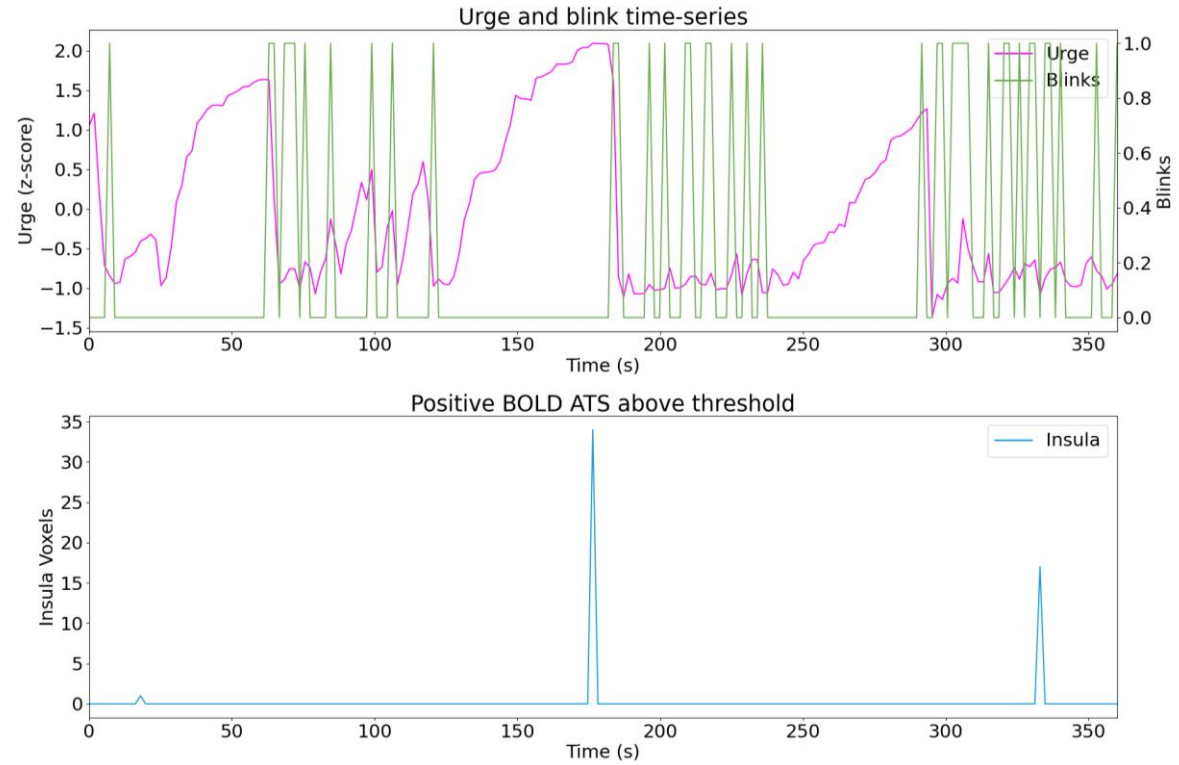

Figure C.39. *Sub17 run02*

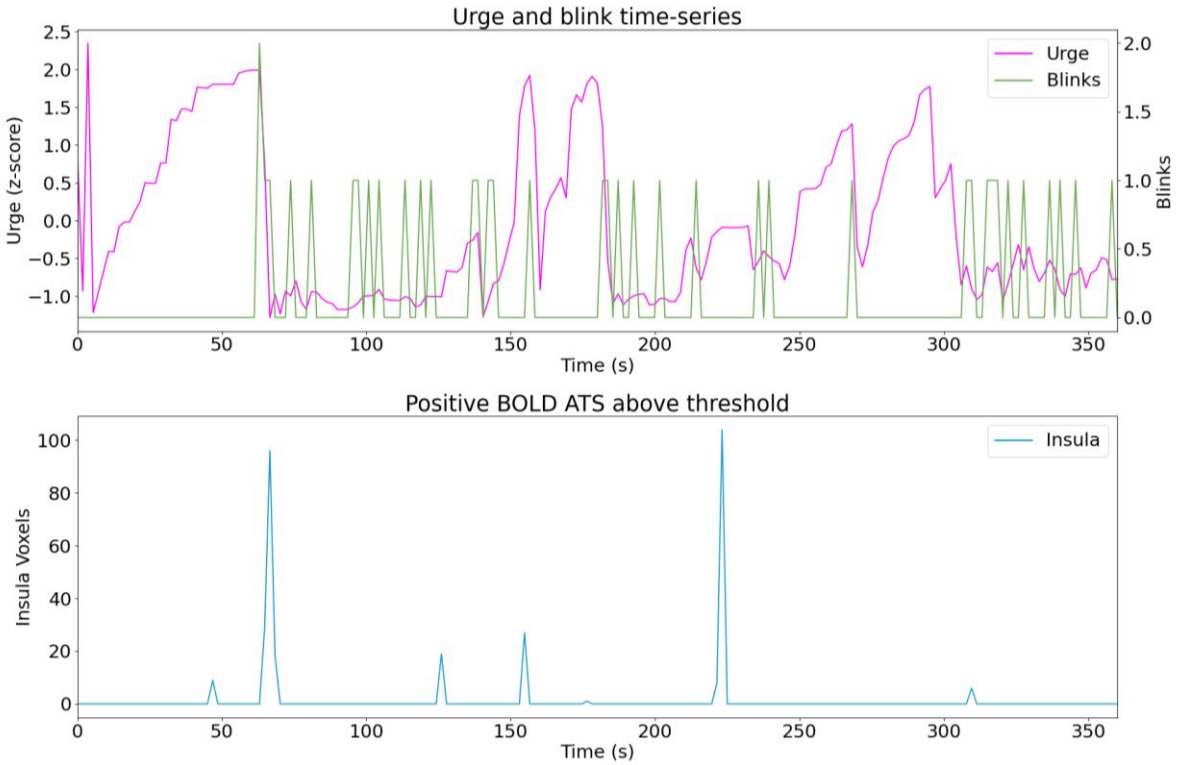

Figure C.40. *Sub17 run03*

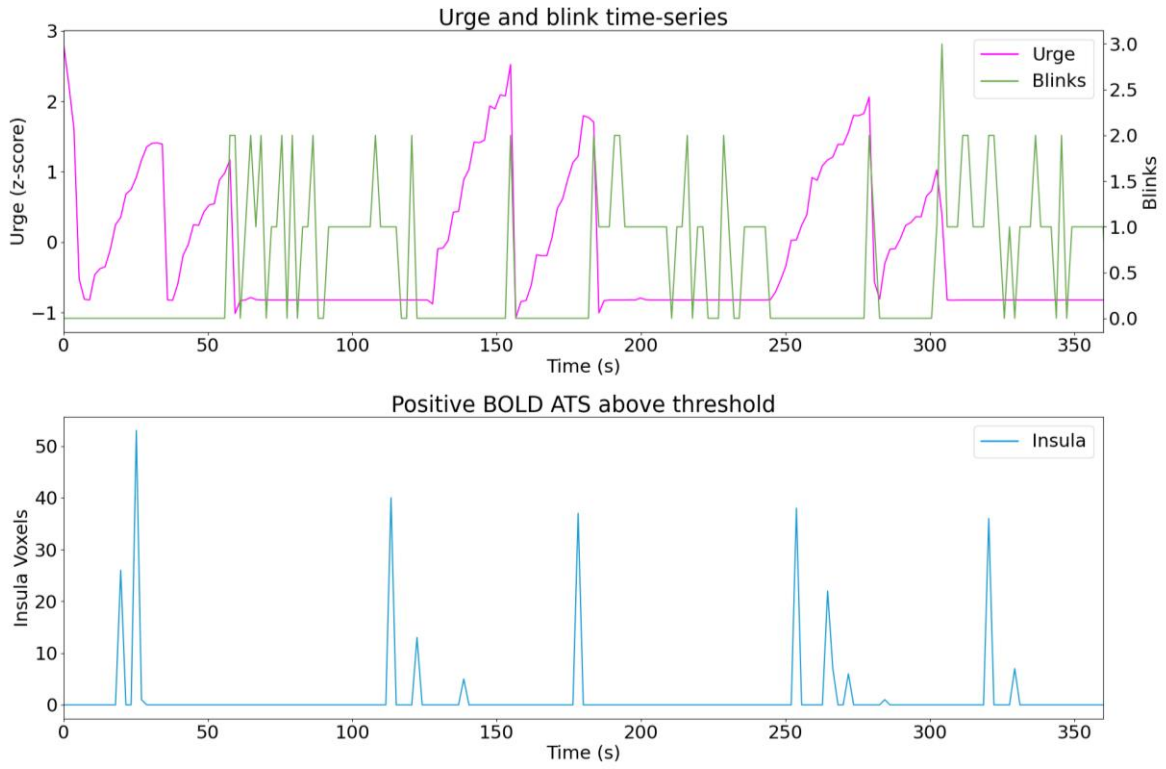

Figure C.41. *Sub18 run01*

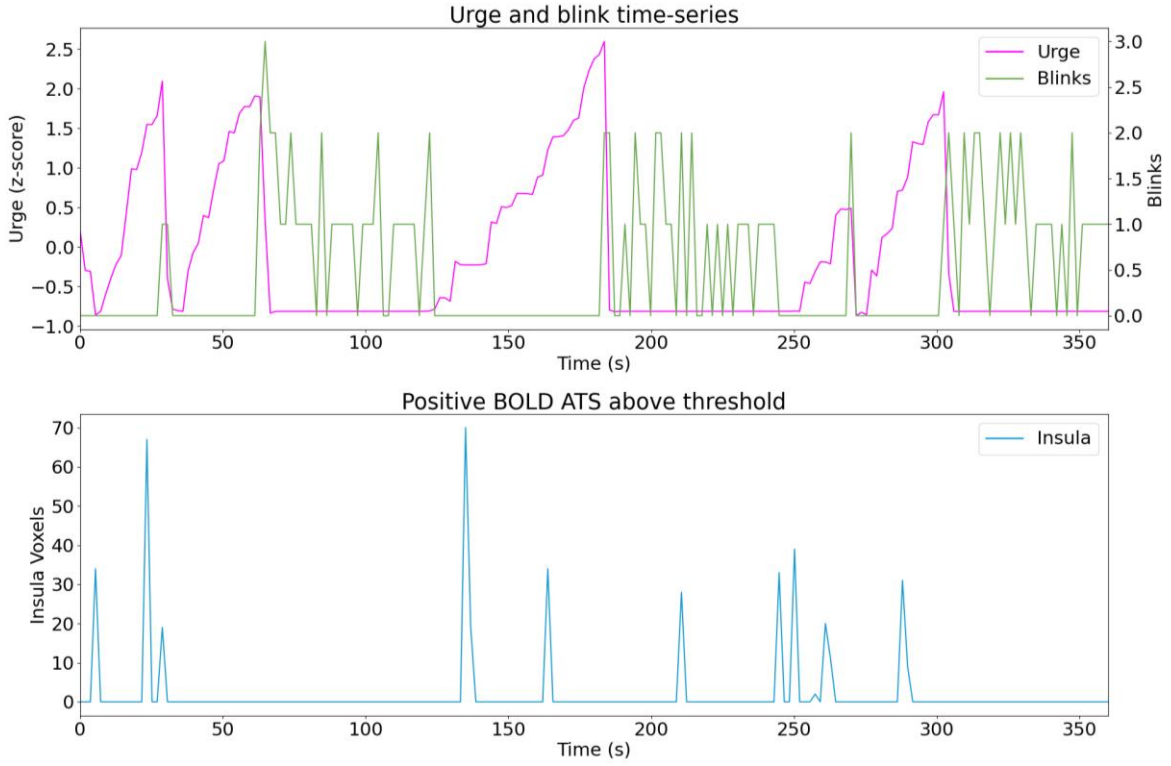

Figure C.42. *Sub18 run02*

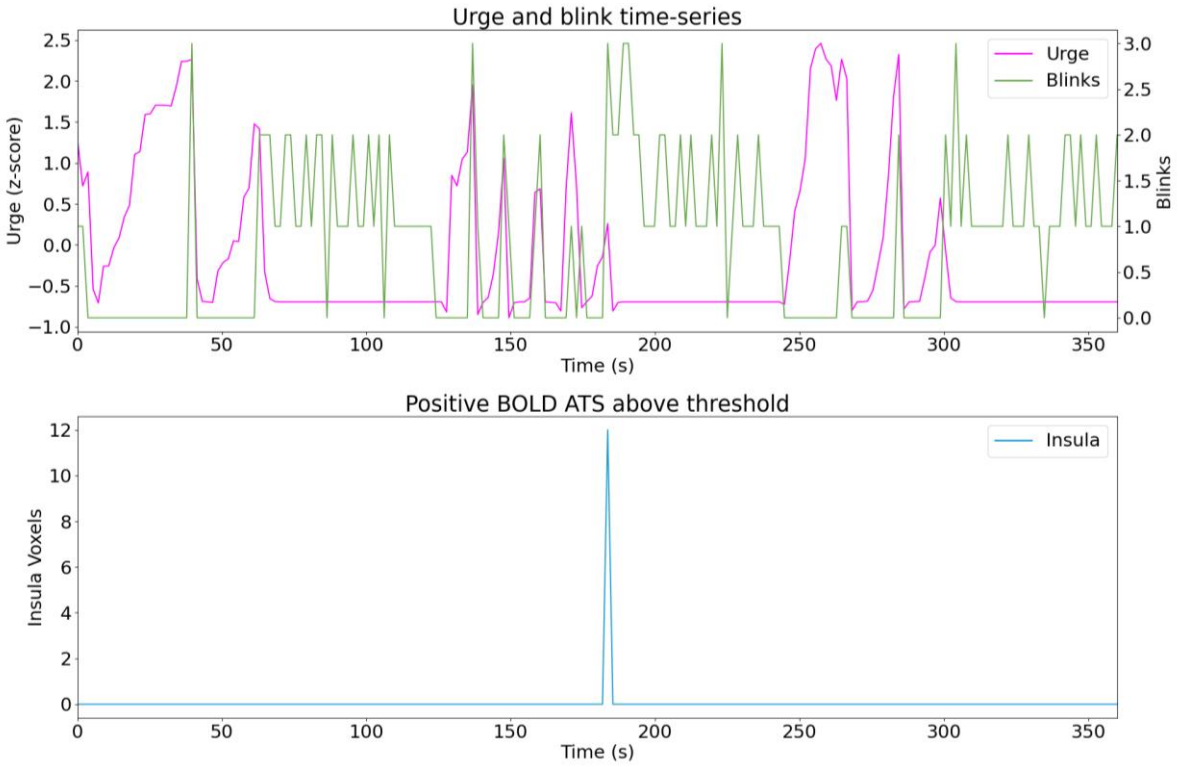

Figure C.43. *Sub18 run03*

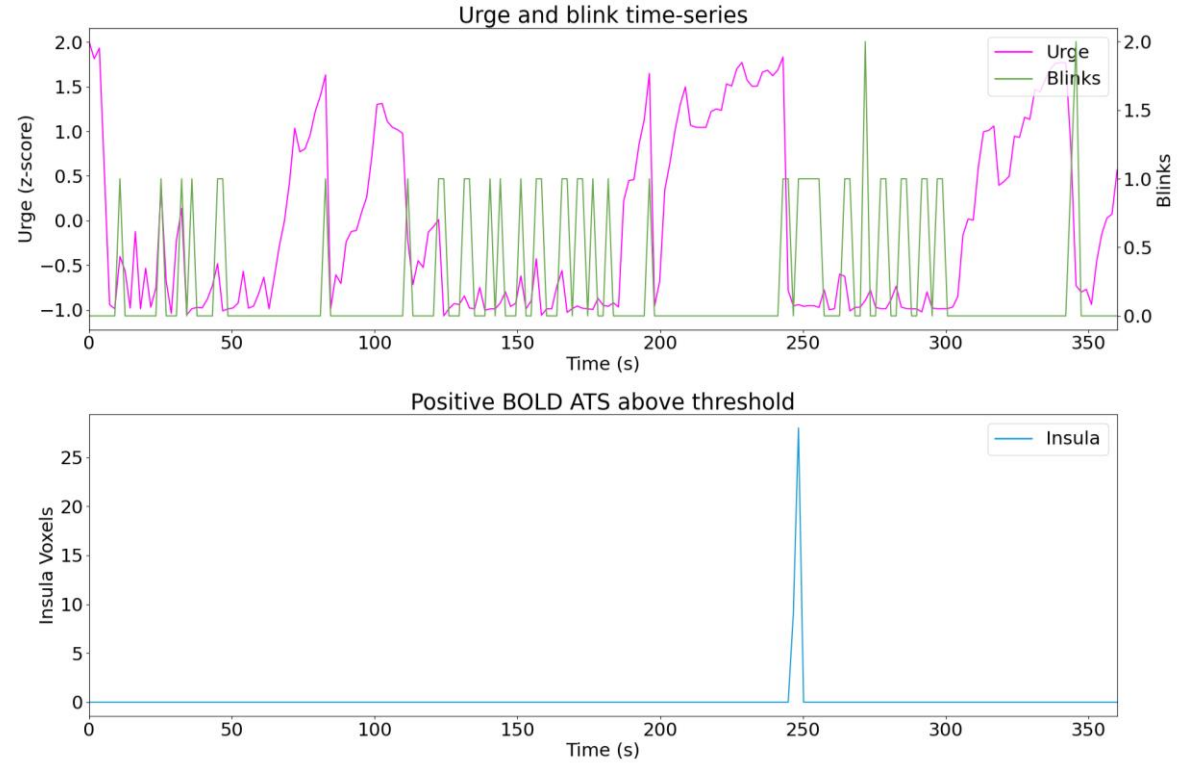

Figure C.44. *Sub19 run01*

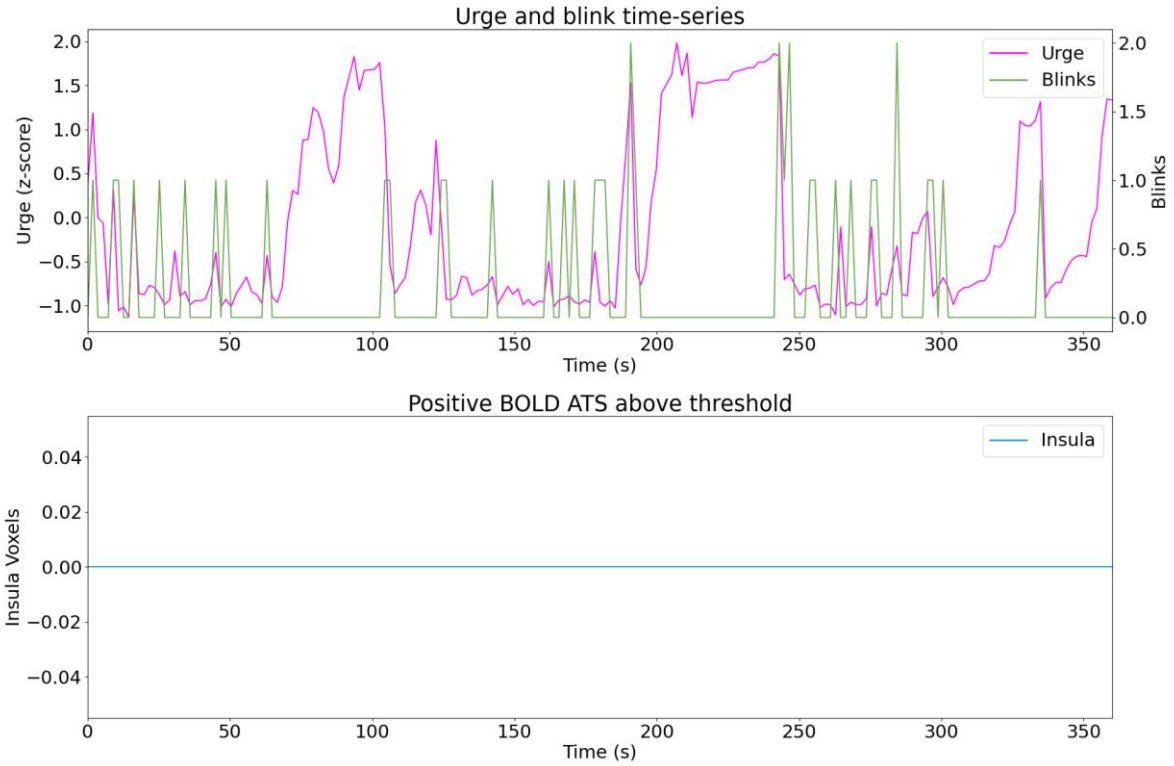

Figure C.45. *Sub19 run03*

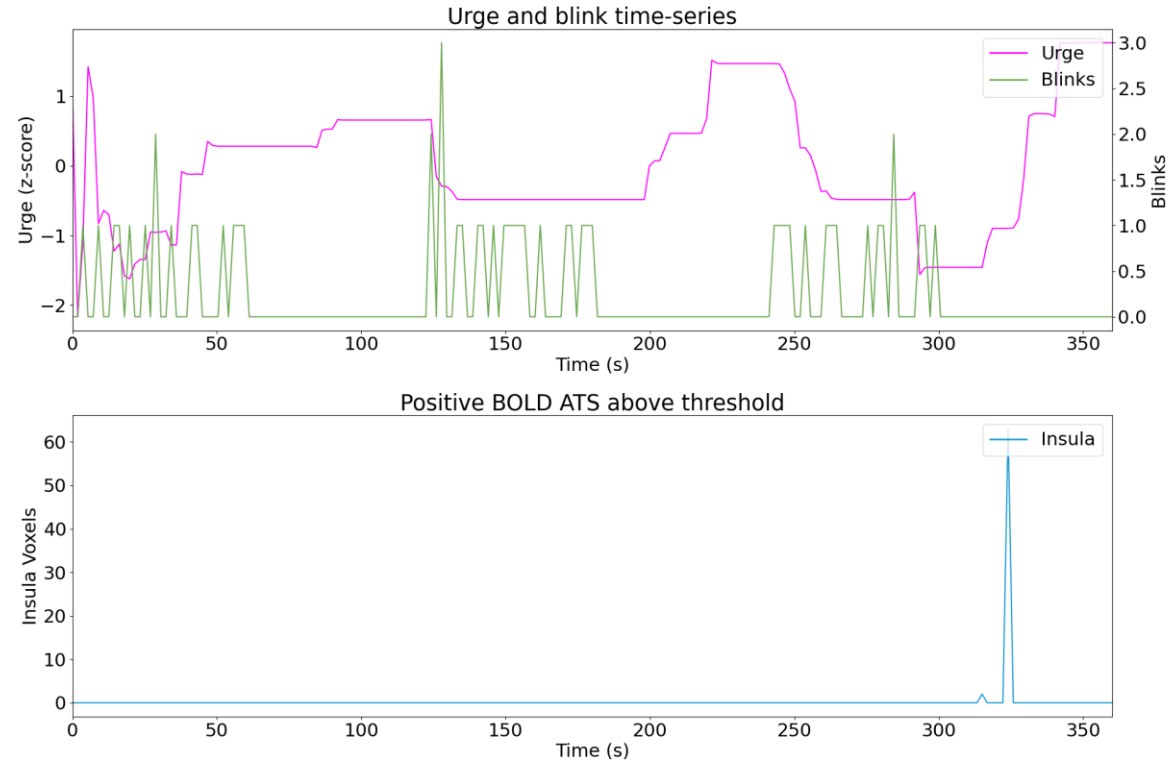

Figure C.46. *Sub20 run01*

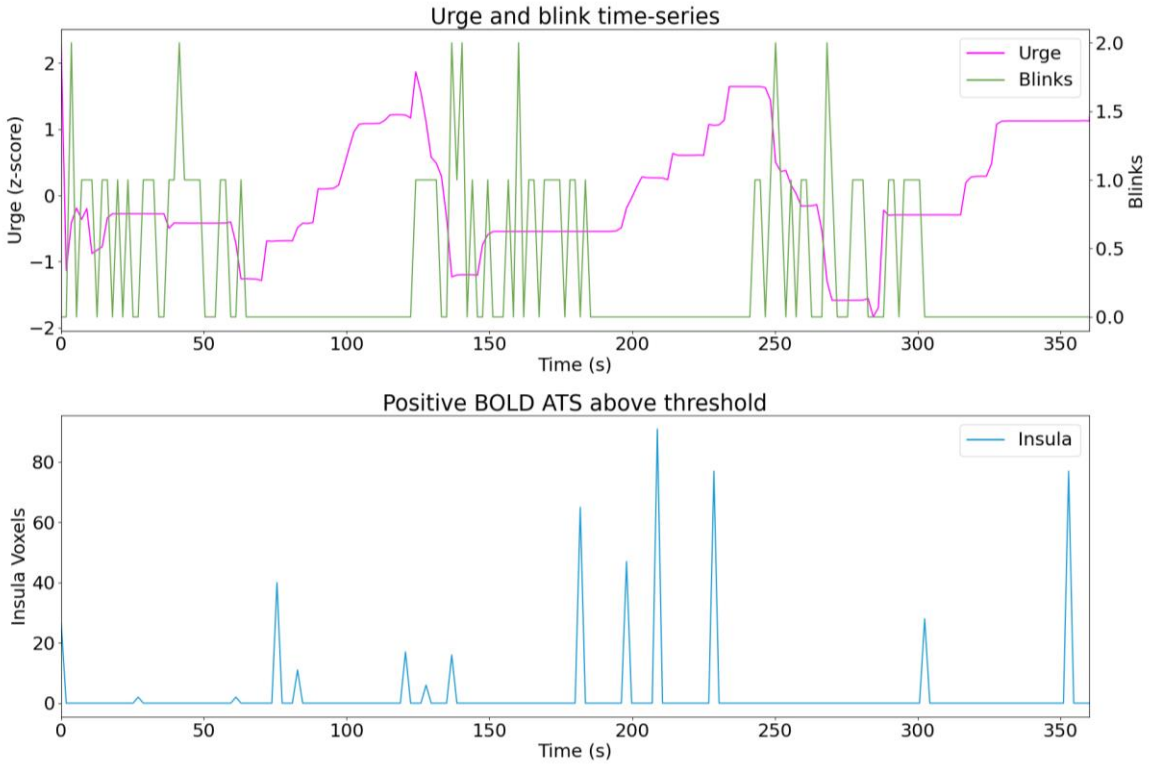

Figure C.47. *Sub20 run02*

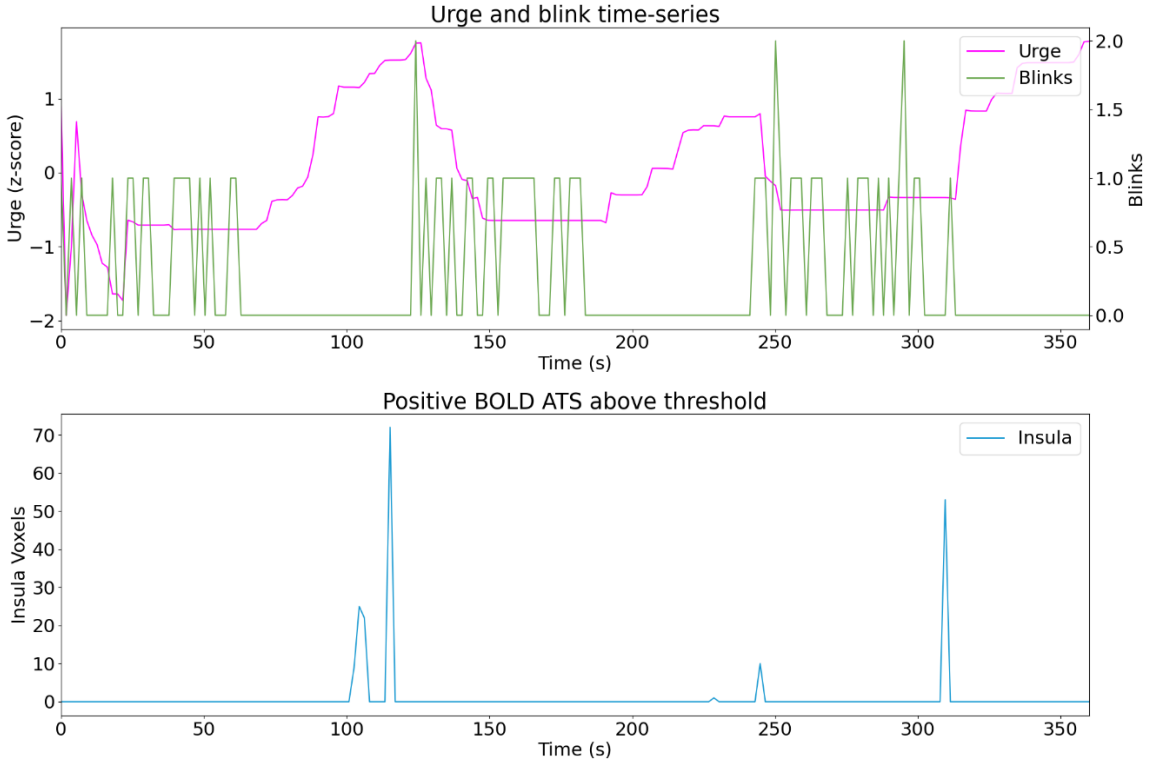

Figure C.48. *Sub20 run03*

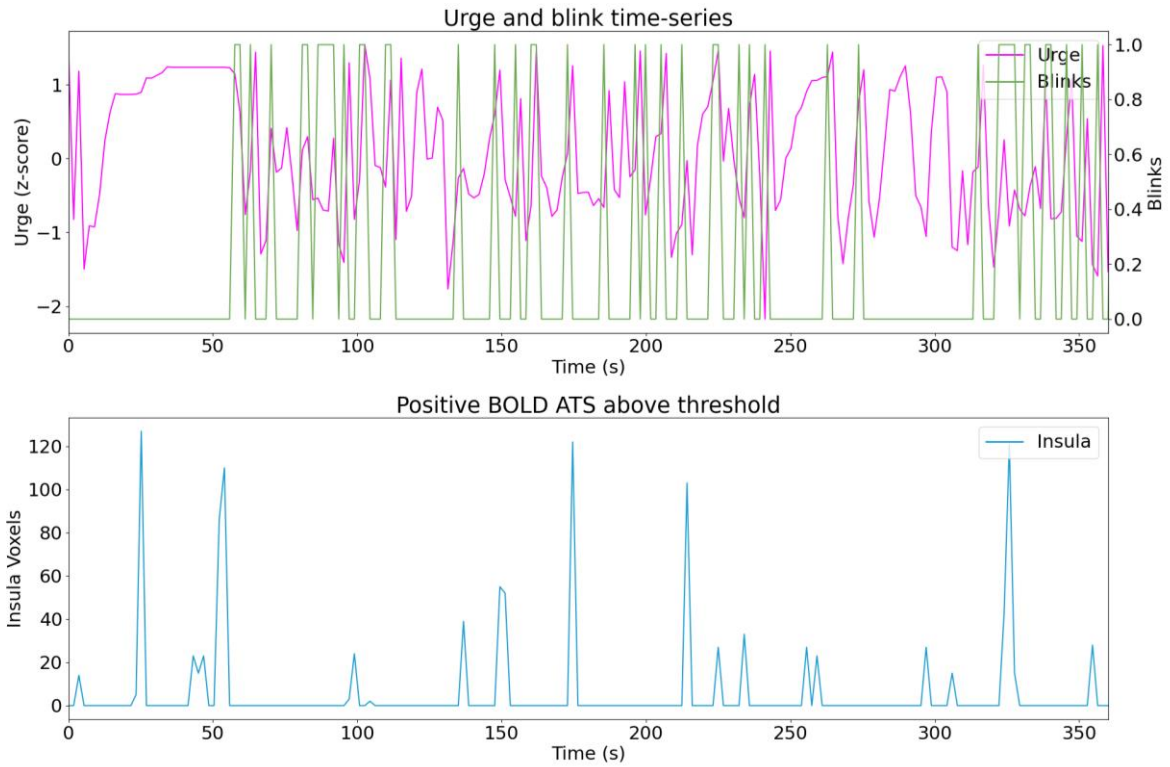

Figure C.49. *Sub21 run03*

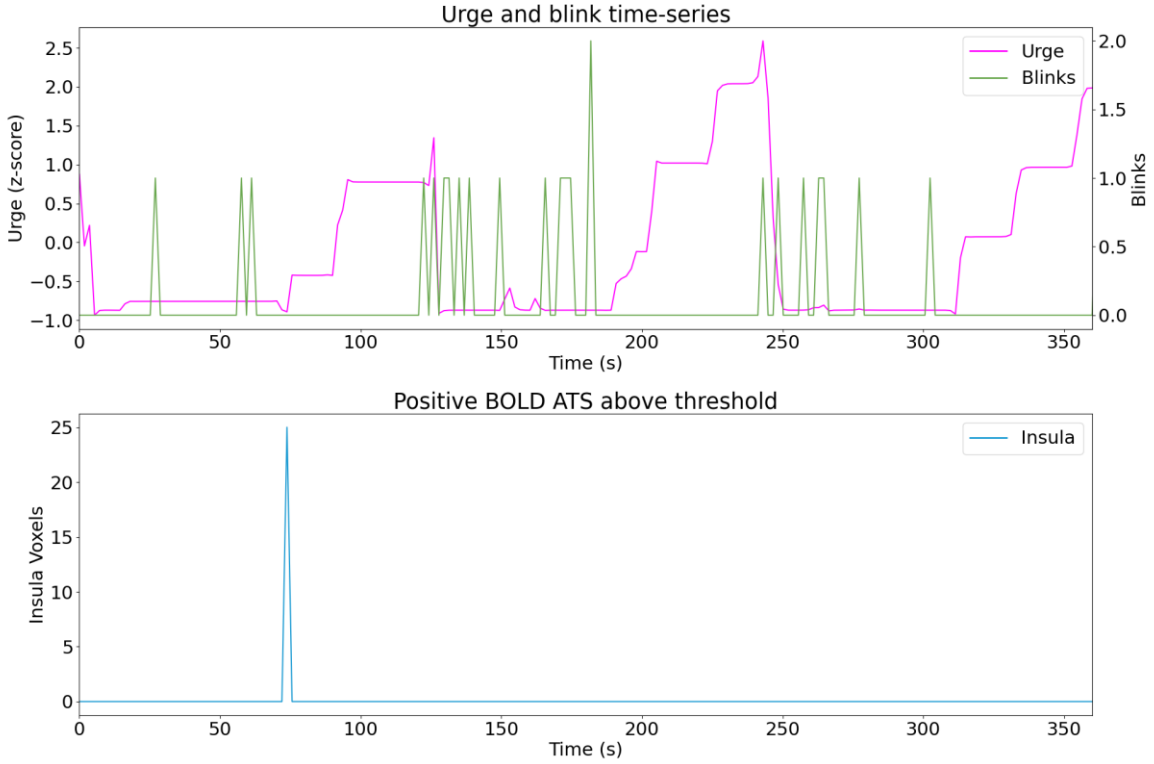

Figure C.50. *Sub22 run01*

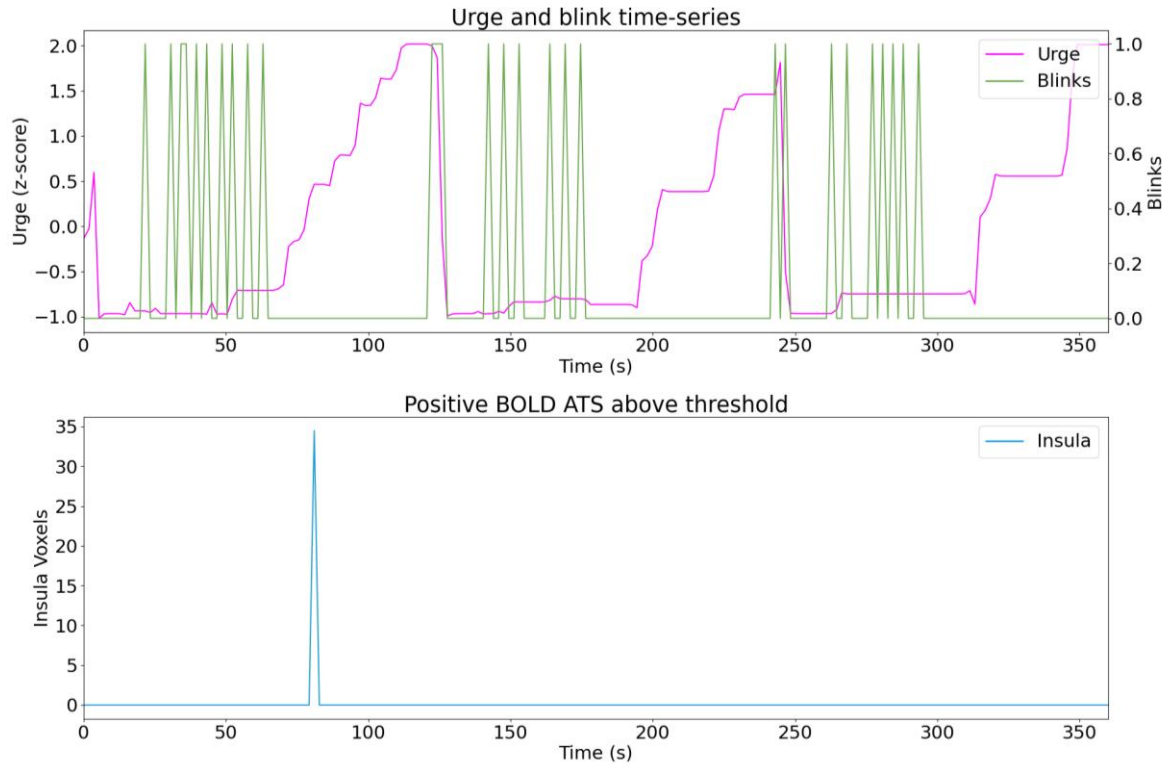

Figure C.51. *Sub22 run02*

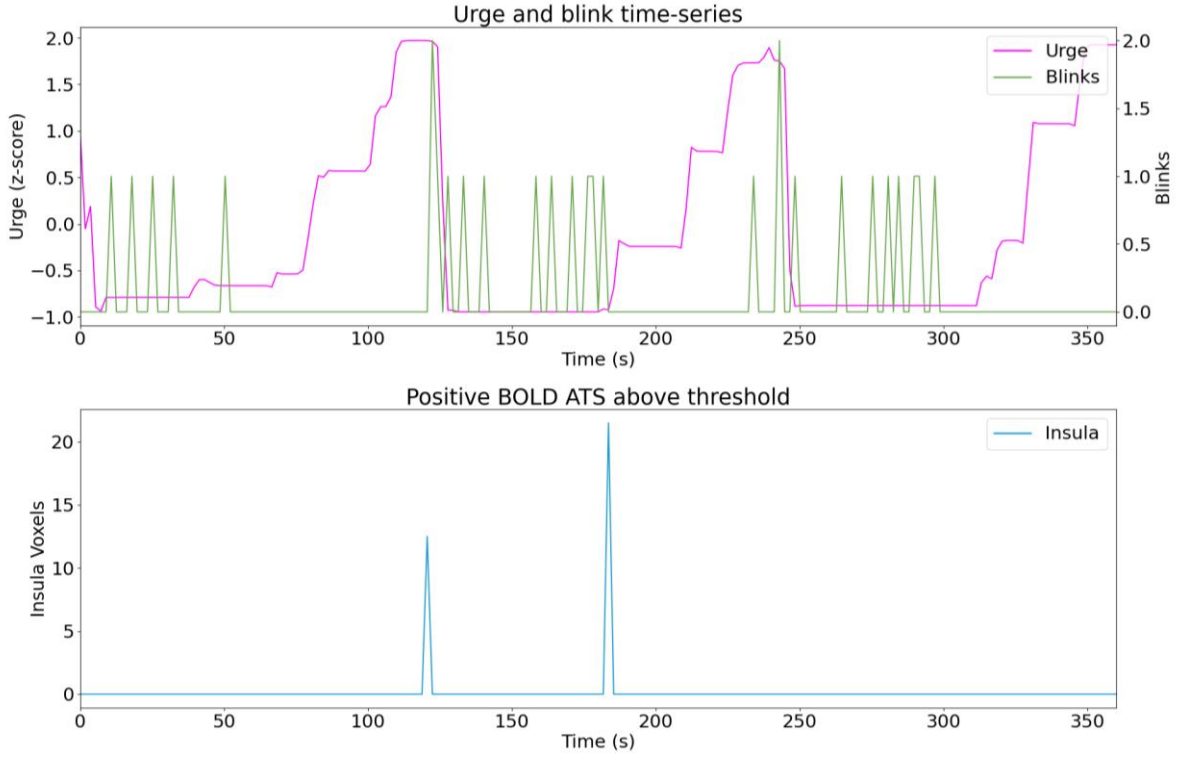

Figure C.52. *Sub22 run03*

Appendix D: Additional MEG Analysis

Analysis of amplitude (Figure D.1) and ITPC (Figure D.2) within the contralateral motor cortex shows similar results to those seen for the sensory cortex in Chapter 5, with an increase during the rhythmic pattern of stimulation for both the 12 and 20Hz conditions. As in the Chapter 5, both the instantaneous amplitude and ITPC timecourses were filtered according to the frequency of stimulation (11-13 Hz or 19-21 Hz) and were statistically compared using a one-tailed Wilcoxon signed rank test at each timepoint.

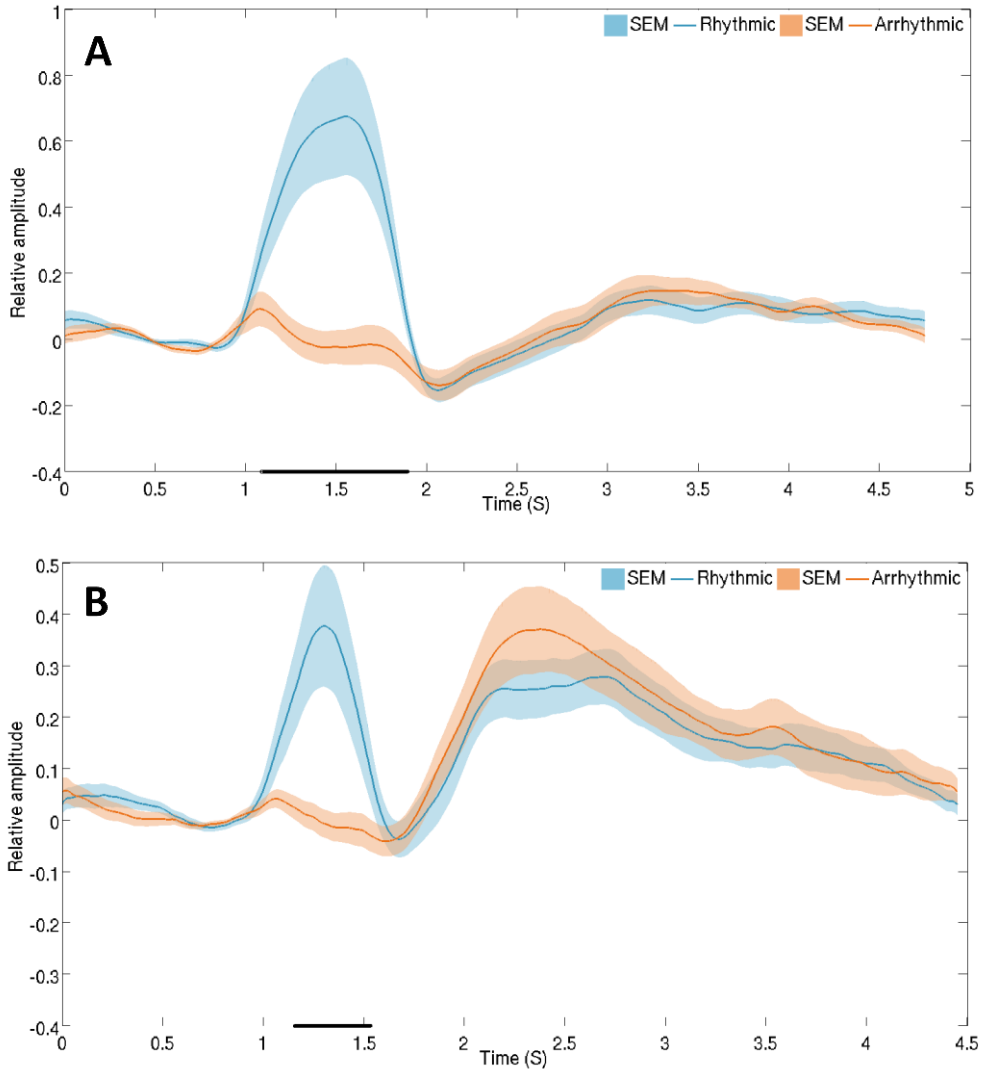

Figure D.1. *Comparison between rhythmic and arrhythmic amplitude changes in the contralateral motor cortex.*

Graphs showing the difference in the relative A) 12Hz amplitude and B) 20Hz amplitude in the rhythmic and arrhythmic conditions. A black line along the x-axis marks timepoints where a significant difference ($p \leq 0.05$) is seen (FDR corrected).

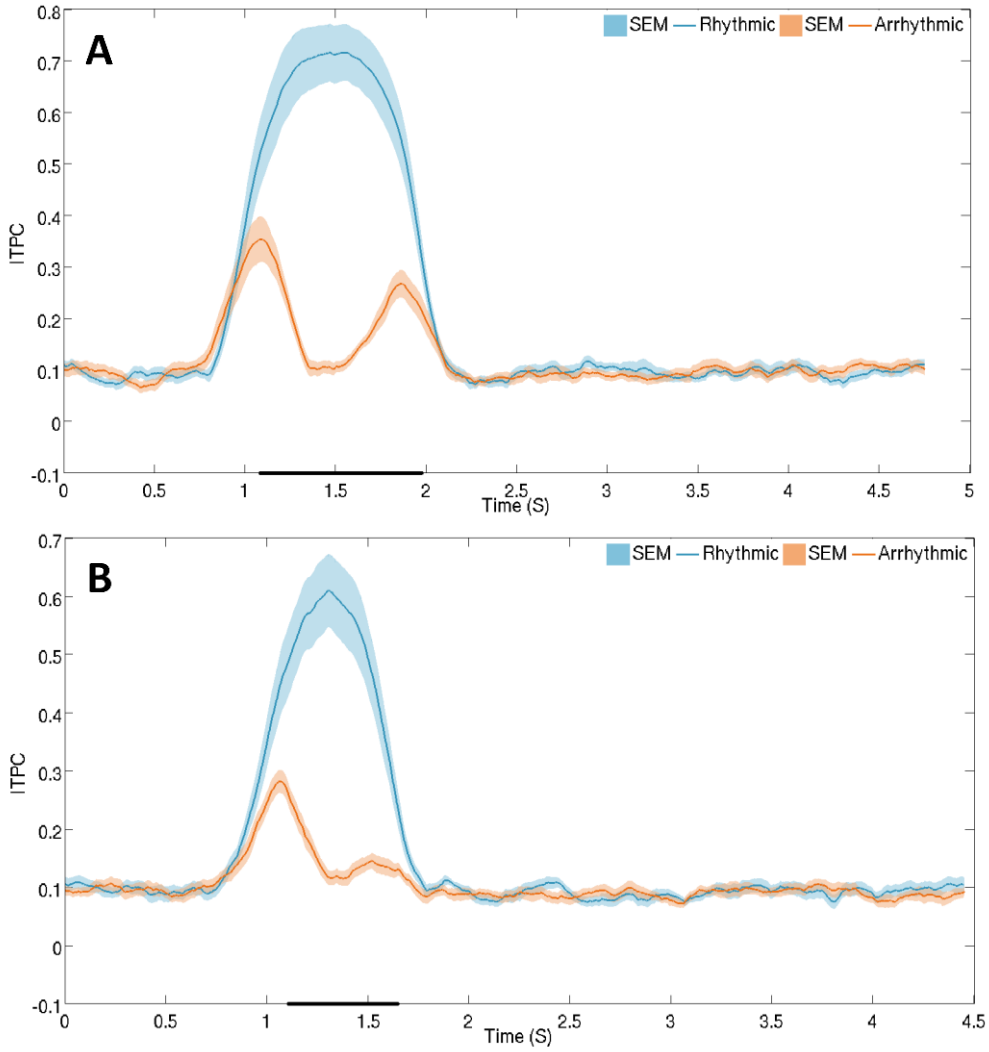

Figure D.2. *Inter-trial phase coherence in the contralateral motor cortex.*

A graph showing the difference between ITPC in the rhythmic and arrhythmic conditions during A) 12Hz and B) 20Hz stimulation. A black line along the x-axis marks timepoints where a significant difference ($p \leq 0.05$) is seen (FDR corrected).

Examples of model fit in individual subjects

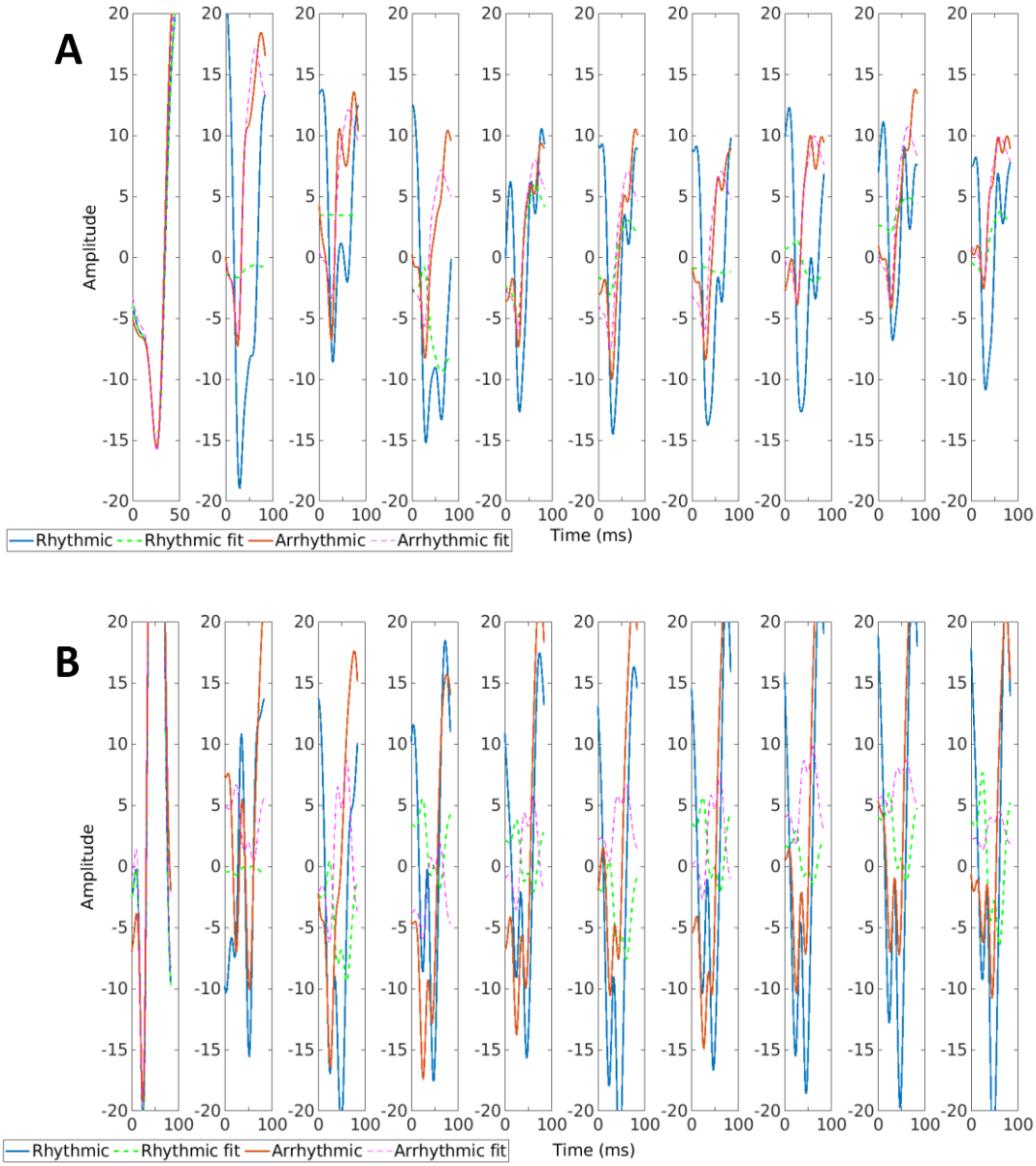

Figure D.3. *Example model fit for two subjects.*

A figure showing the model fit for two subjects for the 12 Hz stimulation.

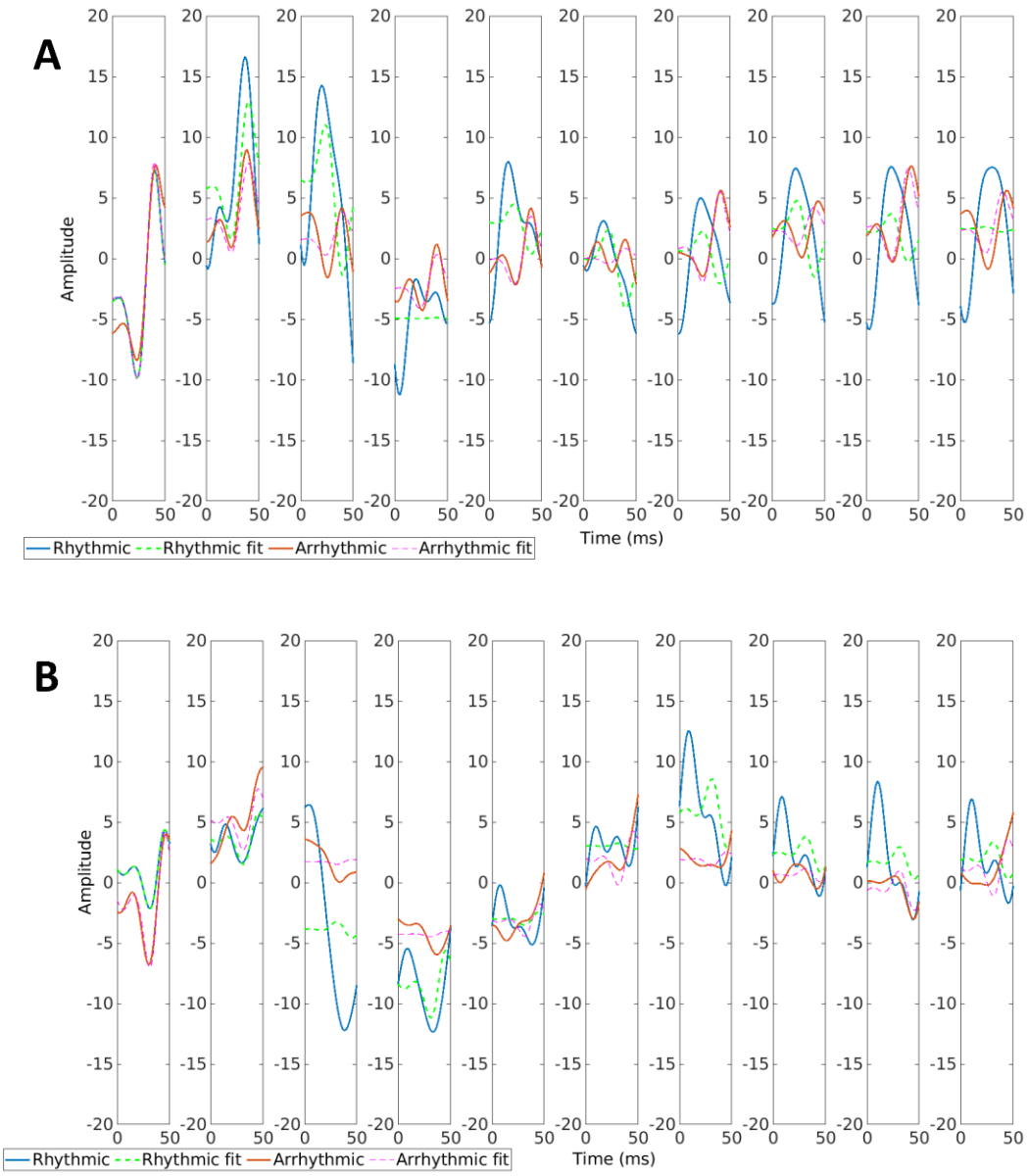

Figure D.4. *Example model fit for two subjects.*

A figure showing the model fit for two subjects for the 20 Hz stimulation.

Appendix E: Optically pumped magnetometers

Background

Although SQUIDs are sensitive enough to detect magnetic fields induced by neural activity, they need to be cooled in a dewar of liquid helium, which constrains several aspects of MEG experimentation. Firstly, the standardised helmet used has a brain-to-sensor distance of around 1.7cm, even when the helmet is a perfect fit, which is increased in subjects with smaller heads (Boto et al., 2020). Secondarily, head movement of ~5mm or more will greatly affect data quality (Handy, 2009). As a consequence, children and certain patient groups cannot be scanned and the movement-related paradigms implemented are by necessity unnatural (Boto et al., 2018).

Optically pumped magnetometers (OPMs) are quantum sensors that have recently been used as an alternative to SQUIDs for MEG due to developments allowing them to be mounted on the scalp (Sander et al., 2012). The type of sensors (QuSpin, Louisville, CO) used in this thesis contain a glass cell of gaseous ^{87}Rb, the atoms of which are spin-polarised in a process known as optical pumping (Figure E.1) (Boto et al., 2018, 2020). During optical pumping, the orientations of the magnetic moments of the ^{87}Rb atoms are aligned along the axis of a circularly polarised 795nm laser making the gas magnetically sensitive (Figure E.1) (Boto et al., 2020). Once aligned, no more light can be absorbed by the atoms and so the photodetector signal is maximal (Boto et al., 2020). Disruption of this alignment due to the presence of a magnetic field (B_0) means the atoms can once again absorb laser light and the signal detected will decrease.

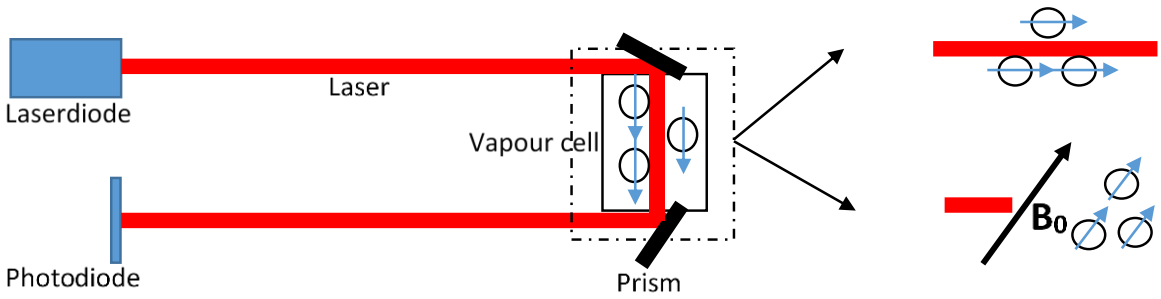

Figure E.1. *A diagram of an OPM sensor.*

Optical pumping using left circularly polarised light causes alignment of the magnetic moments of rubidium atoms. In the presence of an external magnetic field B_0 the spins reorientate to precess at the Larmor frequency around the field vector. Based on Boto et al., 2020.

Quantum basis of optical pumping

Optical pumping involves the promotion of electrons to a higher energy state through the use of light. The orbital angular momentum of an electron is the magnitude at which it moves in a circle about the nucleus, while spin angular momentum is the magnitude at which it spins about its own axis (Boto et al., 2020). For the valence electron in rubidium the orbital angular momentum ***L*** at its ground state is 0 and if excited with sufficient energy, it will transition to a higher energy state with an orbital angular momentum equal to 1 (Boto et al., 2020). However, interactions within the rubidium atoms complicate this scenario, to understand the physics behind optical pumping these interactions are outlined briefly below (for a more in-depth explanation please see (Boto et al., 2020; Tierney et al., 2019)).

Fine structure

All moving charged particles generate a magnetic field. The positively charged nucleus can be thought of as orbiting around the valence electron, producing a current loop which in turn generates a magnetic field passing through the electron (Boto et al., 2020). The negatively charged electron also produces a magnetic field due to its intrinsic spin (Boto et al., 2020). The interaction of these fields means that the electron can undergo either a D1 or D2 transition to a higher energy state, each of which needs absorption of a different amount of energy (Boto et al., 2020). In QuSpin

OPM sensors the D1 transition is used, which requires the photon energy of the laser to be tuned to 795nm (QuSpin, Louisville, CO) (Boto et al., 2020).

Hyperfine and Zeeman splitting

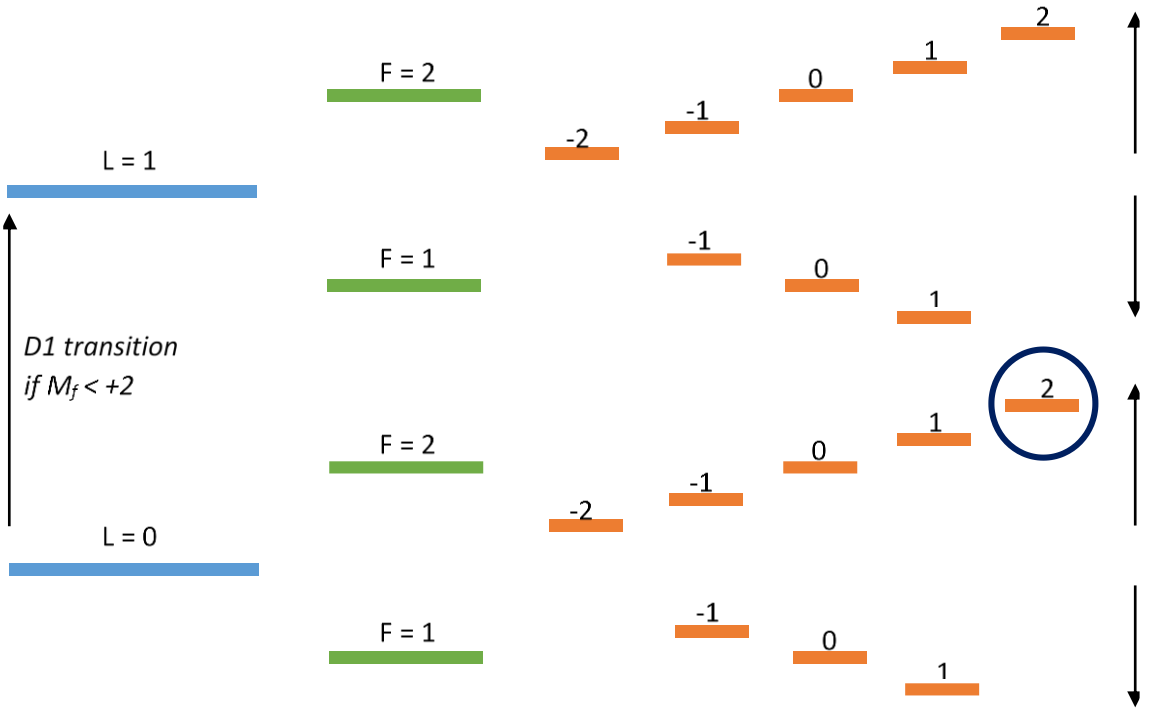

Figure E.2. *A schematic diagram of the energy sublevels within an ^{87}Rb atom. The diagram depicts the principle of optical pumping of valence electrons into the L=0, F=2, M_f=+2 state (blue circle) Based on Boto et al., 2020.*

Like the valence electron, the spin of the ^{87}Rb nucleus generates a magnetic field and the interaction between these spin generated fields is known as hyperfine splitting (Boto et al., 2020). For both the ground and higher energy state there are two energy levels denoted by the total atomic angular momentum ***F*** (F=1 and F=2) (Boto et al., 2020; Tierney et al., 2019). The total angular momentum is the sum of the orbital and spin angular momentum of the electron and the orbital angular momentum of the nucleus (Tierney et al., 2019). In a zero magnetic field the effect of hyperfine splitting is negligible, however in the presence of an external magnetic field the orientation of the angular momentum ***Mf*** with respect to the magnetic field is quantised (Mf =-F to F) (Boto et al., 2020). As a

result, Zeeman splitting is seen where each of the energy states is further split into sublevels.

To account for the many atomic interactions which occur and to allow accurate recording using OPMs we need to ensure we control which sublevel we excite the valence electron to (Boto et al., 2020). Therefore, OPMs use circularly polarised light. Photons of left circularly polarised light have an angular momentum of +1 and when absorbed by the outer rubidium electron their angular momentums will be summed causing a transition to the higher energy state (Boto et al., 2020). However, atoms will spontaneously decay to the ground state through emission of light. Vitally while this process involves a reduction of orbital angular momentum ***L***, the orientation of angular momentum ***Mf*** has an equal probability of changing by 0, 1 or -1 (Tierney et al., 2019). Therefore, due to the D1 transition always involving an increase in ***Mf*** of +1 but the decay not always resulting in a change of ***Mf***, the net effect of the combination of D1 transition and decay will result in the atoms residing in the ground state with the highest possible angular momentum (L=0, F=2, Mf=+2) (Figure E.2) (Boto et al., 2020; Tierney et al., 2019). As ***Mf*** denotes the orientation of angular momentum, the atomic magnetic moments are aligned making the vapour magnetically sensitive (Tierney et al., 2019).

After spin-polarisation the atom will be unaffected by the laser due to the lack of an energy sublevel with ***Mf*** higher than 2 (Boto et al., 2020; Tierney et al., 2019). Therefore the atom becomes transparent to the laser light and a photodetector measures the light intensity of the laser passing through the vapour cell (Boto et al., 2020). When there is a perpendicular magnetic field, as is present during MEG recording, it will cause Larmor precession around the B_0 axis (Boto et al., 2020). The rotation of atomic magnetic moments away from the axis of the laser and the associated redistribution amongst the atomic sublevels means the atoms can again absorb light causing a decrease in the light intensity measured by the photodetector (Boto et al., 2020).

Spin-exchange relaxation

Spin-exchange relaxation involves atom collisions which cause decoherence of their precession meaning the gas will no longer be magnetically sensitive (Boto et al., 2020). OPMs are operated in a spin-exchange relaxation (SERF) regime. This technique involves using a high atomic density vapour cell in an environment with a low magnetic field (Boto et al., 2020; Tierney et al., 2019). At high densities these collisions occur at a faster rate than the precession frequency meaning the net precession remains coherent. To ensure the high atomic density of rubidium in the cell, heaters are used to heat the vapour to 150°c. Despite this heating, the surface of the OPM is close to 37°c allowing them to be placed in close proximity to the scalp without causing harm (Boto et al., 2020). This proximity means that there is an increase in the magnitude of the signal measured compared to SQUIDs due to the magnetic field decaying according to the inverse square law (Boto et al., 2020). Furthermore, a system employing OPMs has shown improved spatial resolution in comparison to SQUIDs, both when a subject is still and when performing naturalistic movements (Boto et al., 2018).

Zero field recording

OPMs need to be operated in the zero-field as the dynamic range of OPMs is ±1.5nT and so the head-mounted sensors can become saturated during movement through the inhomogeneous field remaining in the shielded room (Boto et al., 2018; Holmes et al., 2018). Therefore along with the noise reduction provided by the shielded room, there are a set of coils surrounding the vapour cell within OPMs which measure the offset of the field and produce an equal and opposite magnetic field to zero the field in a particular orientation (x, y or z) (Holmes et al., 2018). A set of 6 bi-planar nulling coils are set up within the scan room which null this residual field around the participant's head by generating three spatially uniform fields (*Bx, By, Bz*) and reducing three field gradients (*dBx/dz*, *dBy/dz* and *dBz/dz*) (Holmes et al., 2018). The currents within the coils are set using 4 reference sensors located near to the head which measure the remnant magnetic fields and act as a feedback loop (Holmes et al., 2018). This setup is what allows recording during tasks involving head movement.

Why OPM-MEG?

OPM-MEG has a lower spread of the magnetic field due to the sensors being closer to the scalp in comparison to conventional MEG and the lack of spatial smearing in comparison to EEG. Therefore, the lead fields for the sources are less correlated meaning there is improved spatial resolution. Furthermore, as the sensors are closer to the scalp in comparison to CTF-MEG then the SNR is also higher, further improving the spatial resolution (Boto et al., 2020).

Assessing Clinical Measures in Tourette Syndrome

Yale Global Tic Severity Scale

The YGTSS is a semi-structured interview which evaluates the number, frequency, intensity, complexity and interference of the participant's motor and phonic tics over the previous week (Leckman et al., 1989). The global estimate of tic symptom severity is calculated through summation of the motor, phonic and impairment ratings. This scale is the most used measure to assess tic severity in clinical research. The initial description of the scale demonstrated good interrater agreement as well as high convergent validity of the subscales (Leckman et al., 1989). More recent assessment of YGTSS has shown that it is a valid and reliable measure which remains stable across time (Storch et al., 2005).

Premonitory Urge for Tics Scale – Revised

The majority of Tourette's patients experience an urge or sensation prior to tic onset (Kwak et al., 2003). This sensation can be assessed using the Premonitory Urge for Tics Scale – Revised (PUTS-R)(Baumung et al., 2021). The PUTS-R evaluates the participants' agreement with statements about common feelings prior to a tic using a 5-point Likert scale (0 = "Not at all", 4 = "Very much") (Baumung et al., 2021). These scores are then summed for the 24 statements to provide a total severity score out of 96, where a higher score indicates more urge related symptoms. Woods and colleagues showed that the original scale had both discriminant and concurrent validity, internal consistency and was stable across time (Woods et al., 2005). Moreover, a large sample of participants with chronic

tic disorders has been analysed to show the reliability of PUTS, particularly in patients over the age of 10 (Raines et al., 2018). A more recent study however showed good reliability in children under the age of 11, potentially due to parents helping young children with completion of the questionnaire (Baumung et al., 2021).

Pilot Experiment

Previous attempts to investigate the oscillatory dynamics of tics and urges in TS using OPM-MEG in 2019 were hampered by the use of a flexible cap, similar to that used with EEG. When tics occurred, the sensors would rattle resulting in a noise artefact at tic onset (Figure E.3). Recently, we piloted this experiment again using the new rigid 3D printed helmet which is currently in use at the University of Nottingham.

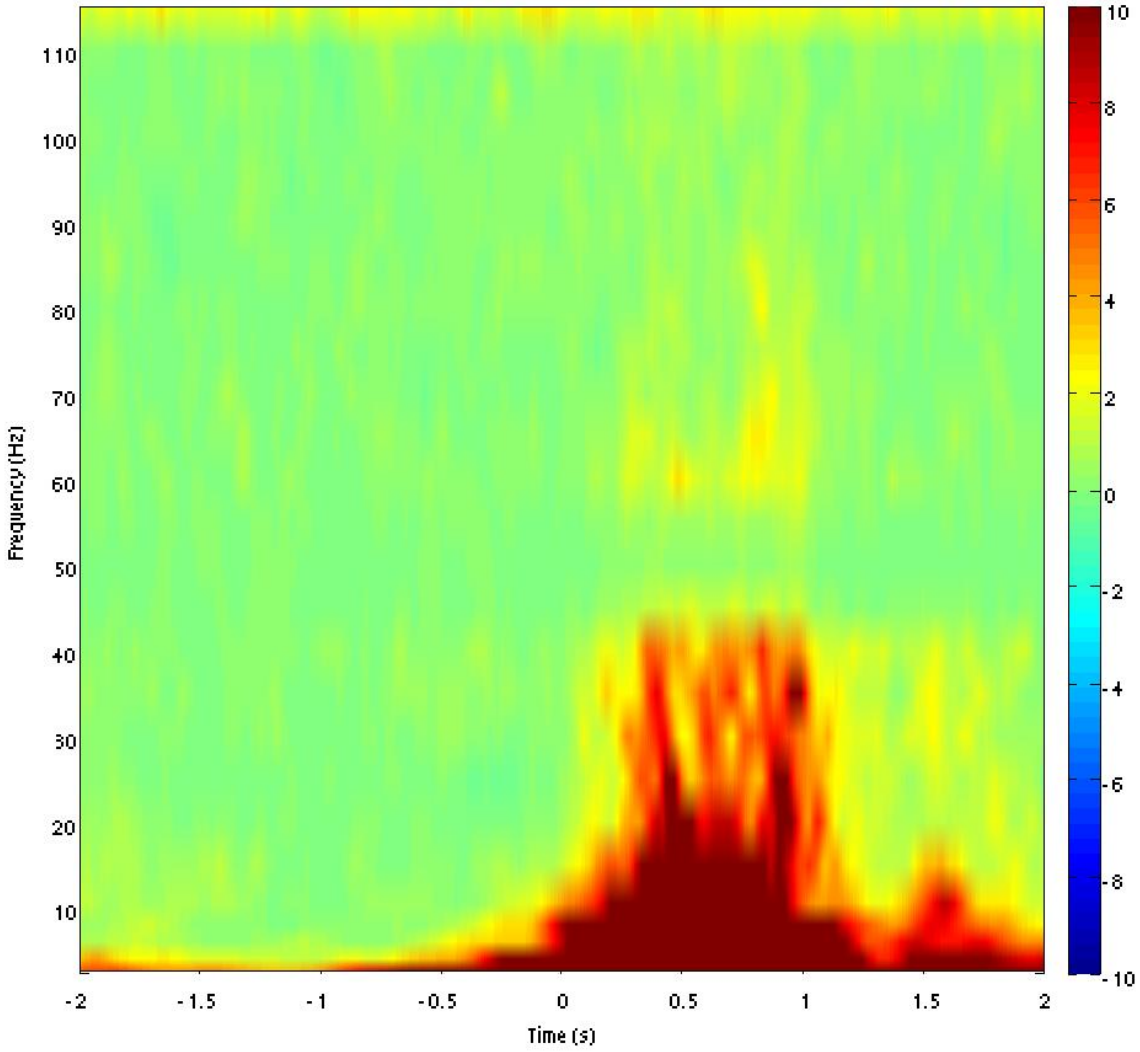

Figure E.3. *Time frequency spectra for gradiometers overlying the sensorimotor cortex, with tic bout onset at time 0.*

Method

Here I describe pilot data collected from a 35-year-old participant with a TS diagnosis (male, right-handed). The participants Yale total tic severity score was 36/50 and their PUTS-R score was 27/96. The participant was scanned using OPM-MEG with the sensors placed to give whole-head coverage. During the scan, video and audio recordings were collected to determine tic onsets during post-hoc analysis. Tics needed to be at least 2s apart to be classed as a different tic bout.

Voluntary movement

The first task involved a single cued right index finger abduction every 5-seconds for 60 trials. In-house Matlab code was used to compare movement to baseline resulting in a similar beta (13-30 Hz) timecourse to what would be expected in healthy participants with desynchronization during movement being localised to the contralateral sensorimotor cortex (Figure E.4A and B), followed by a post-movement beta rebound (Figure E.4B).

Tic suppression paradigm

For the second task the participant was asked to rest and freely express their tics during a 5-minute block followed by a period where they would attempt to suppress their tics for the duration of a 5-minute block, this was then repeated.

Due to the frequency of the participants tics, we were not able to get any trials during the rest block due to tics being constant within this period. Therefore, for suppression trials (N = 45) only we investigated the changes in oscillatory activity immediately preceding tics (active window -1s to 0s) compared with during tics (control window 0s to 1s) in the cingulate and insular cortices which were highlighted as regions of interest in Chapter 3. We would expect any urge related activity within these regions would be highest immediately preceding tics (Figure E.5A, B and C).

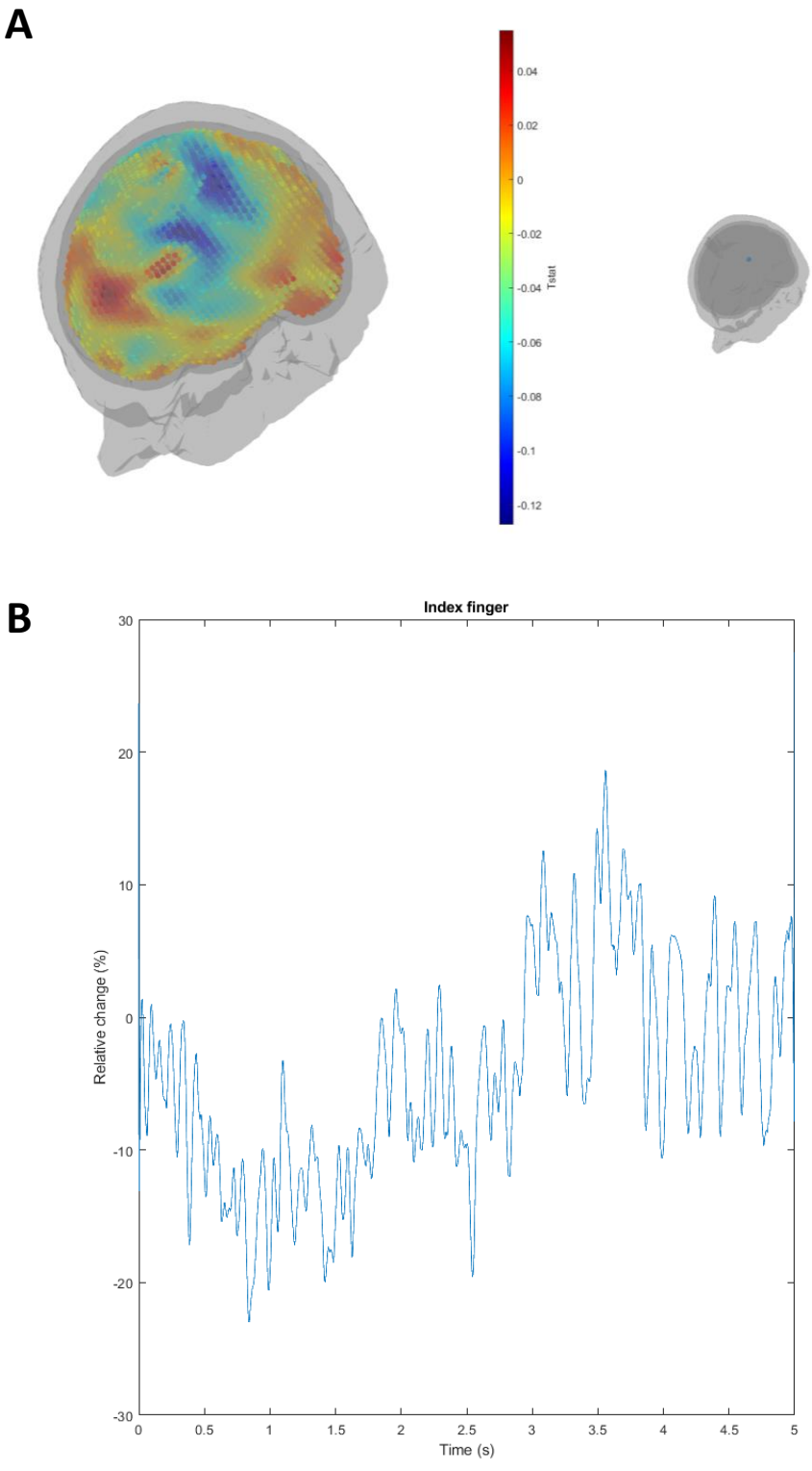

Figure E.4. *(A) A figure showing the lowest T-stat value in the beta (13-30 Hz) frequency range during voluntary finger abduction is within the contralateral sensorimotor cortex. (B) The timecourse of beta oscillatory changes within the voxel with the lowest T-stat value in the beta frequency band, showing a desynchronisation followed by a rebound.*

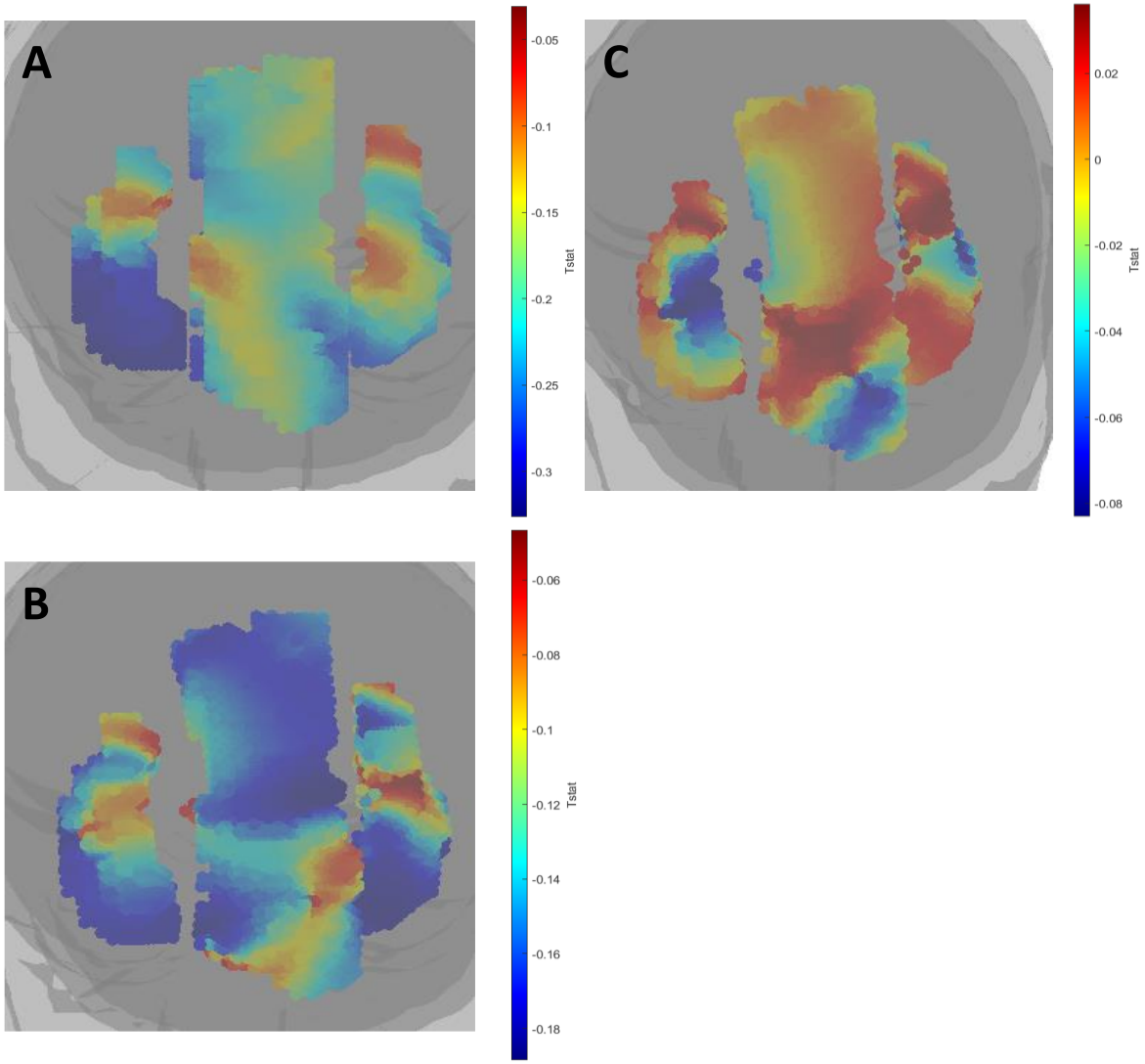

Figure E.5. *T-stat maps showing the differences within the cingulate and insular cortices prior to a tic compared to during a tic in the (A) theta (4-7 Hz), (B) alpha (8-12 Hz) and (C) Beta (13-30 Hz) frequency bands.*

Discussion

Due to the inclusion of only one participant, we cannot make any conclusions regarding the oscillatory changes preceding tics. However, we have demonstrated that when using the rigid 3D printed helmet, we are able to record good data from participants whilst they tic which can be beamformed to the regions of interest, the cingulate and insular cortices.